POTENTIAL SYNCHROTRON-COMPTON HIGH ENERGY BLAZARS AMONG UNIDENTIFIED *EGRET* GAMMA-RAY SOURCES

Thesis submitted in accordance with the requirements
for the award of the DEGREE of PHILOSOPHIAE DOCTOR
in the Faculty of Agricultural and Natural Sciences/Department of Physics
at the UNIVERSITY of the FREE STATE

by

Pheneas Nkundabakura
M.Sc (UFS)

Promoter: Prof. P.J. Meintjes (UFS)

November 2, 2010

Abstract

The synchrotron self-Compton (SSC), a process where synchrotron emitting electrons upscatter the same photons to high energies, remains one of the dominant mechanisms for γ-ray production inside homogeneous jets, explaining the observed broadband emission in blazars. Therefore, the synchrotron-Compton blazars can provide information regarding production mechanisms of Very High Energy (VHE) photons and possibly the acceleration mechanisms of particles to high energies.

Synchrotron-Compton blazars have been observed by γ-ray telescopes, both ground- and space-based, for example the *Energetic Gamma-Ray Experiment Telescope* (*EGRET*) on board the *Compton Gamma-Ray Observatory* (*CGRO*) and the *Large Area Telescope* (*LAT*) on board the Fermi Observatory and are believed to be radio-loud Active Galactic Nuclei (AGNs) with their jets oriented at relatively small angles with respect to the line of sight.

The main purpose of this study was to search for possible synchrotron-Compton blazars among the southern high galactic latitude sources among the unidentified *EGRET* sources with the aim to understand their nature. The identification of possible point sources, associated with the *EGRET* γ-ray sources, is complicated by the large *EGRET* gamma-ray error boxes, that is between 0.5–1.5 degrees, which can harbour several potential sources, especially at low galactic latitudes.

The initial phase of this study constituted the tedious search for extra-galactic flat spectrum radio counterparts in the online and published catalogues inside the *EGRET* error boxes of high galactic sources, with $|b| > 10°$. The strategy was to select sources with $|\alpha| < 0.7$ for further multi-wavelength studies. To enable the utilization of the 26-m radio telescope of the *Hartebeesthoek Radio Astronomical Observatory (HartRAO)*, only sources with the declination range $-70° < \mathrm{Dec} < +45°$ were considered. A further consideration was to single out only those flat spectrum sources with a flux density above 200 mJy at 12.4 GHz, the latter are those sources with rising nonthermal spectra towards high energies. Based upon the above-mentioned criteria, a selection of thirteen blazar-like candidates was made for further investigation.

In the second phase of this study, multi-wavelength photometric and spectroscopic observations of the selected sources were carried out in order to reconstruct their Spectral Energy Distributions (SEDs) which are the signature of the main emission mechanisms (that is the synchrotron and the inverse Compton processes) occurring in the jets. The main result of this

investigation has been the determination of the redshifts of two radio sources selected initially as radio counterparts of two unidentified *EGRET* sources, *3EG J0821-5814* and *3EG J0706-3837*. The Ca H & K line depression, occurring around 4000 Å (in the rest frame of the source), was used to diagnose the domination of the nonthermal emission in the sources which helped disentangle Flat Spectrum Radio Quasars (FSRQs) from normal radio galaxies.

In the third phase, the homogeneous synchrotron self-Compton model was used to constrain the physical parameters of the emitting plasma in the sources. Results show that the model can be successful, provided that there are sufficient data to pin down the observed parameters, such as the position of the peaks in emission as well the spectral indices in different parts of the SED. However, it has been pointed out that the SSC model could not provide a good fit for the synchrotron low-energy radio emission and it has been suggested subsequently to consider an inhomogeneous jet model. In the MeV to GeV energy range, the contribution of inverse Compton scattering from external photons has been considered to explain the SED satisfactorily.

Keywords: radiation mechanisms: non-thermal, line: identification, techniques: spectroscopic, galaxies: jets, BL Lacertae objects: general, quasars: general.

Samevatting

Synchrotron eie-Compton (SEC), die proses waar synchrotron fotone opwaarts verstrooi word na hoë energieë deur synchrotron-stralende elektrone, bly een van die dominante meganismes vir gammastraal produksie en verskaf 'n bevredigende verklaring vir die waargenome wye-band uitstraling van blasars van radio-tot Baie Hoë Energie (BHE) gammastrale. Synchrotron-Compton blasars kan dus inligting verskaf aangaande die produksie-meganismes van BHE fotone en moontlik op die versnellings-meganismes van deeltjies tot baie hoë energie.

Synchrotron-Compton blasars is waargeneem deur beide grond-en ruimte gammastraal teleskope, naamlik, die *Energetic Gamma-Ray Experiment Telescope (EGRET)* op die *Compton Gamma-Ray Observatory (CGRO)* asook die *Large Area Telescope (LAT)* op die Fermi Observatory. Daar word beweer dat synchrotron-Compton blasars sterk radio Aktiewe Galaktiese Kerne (AGKs) is waar 'n gas-spuit met relatiwistiese deeltjies vanaf 'n kompakte kern 'n relatiewe klein hoek vorm met betrekking tot die waarnemingslyn.

Die hoof doel van hierdie studie was die soektog na moontlike Synchrotron-Compton blasars tussen die suidelike hoë galaktiese breedtegraad bronne van die ongeïdentifiseerde *EGRET* populasie, met die doel om die aard en eienskappe van die bronne te ontrafel. Die identifikasie van moontlike puntbronne, wat geassosieer kan word met die *EGRET* gammastraal bronne, word bemoeilik deur die groot foutgrense (tussen 0.5 en 1.5 grade) van die EGRET bronne. Verskeie moontlike bronne kan binne hierdie grense val, veral by lae galaktiese breedtegrade. Die aanvanklike fase van hierdie studie het bestaan uit die noukeurige soektog na ekstra-galaktiese plat spektrum radio bronne uit webgebaseerde en gepubliseerde katalogusse, binne die *EGRET* foutgrense, van hoë galaktiese bronne, dit wil sê met $|b| > 10°$. Die strategie was om bronne te kies met $|\alpha| < 0.7$ vir verdere multi-golflengte studies. Om die benutting van die 26-m radio teleskoop by die *Hartebeesthoek Radio Sterrewag (HartRAO)* te verseker, is daar op bronne gekonsentreer met deklinasie hoeke tussen $-70° < Dec < +45°$. 'n Verdere oorweging vir die kies van bronne was om die bronne te identifiseer met 'n plat spektrum, dit wil sê met 'n vloeddigtheid bo 200 mJy by 12.4 GHz. Net bronne met stygende nie-termiese spektrum na hoër energieë. Gebaseer op bogenoemde kriteria, is 'n seleksie van 13 blasar-agtige kandidate gemaak vir verdere studie. In die tweede fase van hierdie studie is multi-golflengte fotometriese en spektrometriese waarnemings gedoen van die gekose bronne, om sodoende die Spektrale-Energie-Verdeling (SEVs) van die bronne te rekonstrueer. Hierdie SEVs is die kenteken van die hoof uitstralings-meganisme

betrokke in die spuit, dit wil sê die synchrotron en die inverse-Compton prosesse. Die hoof resultaat van die ondersoek was die bepaling van die rooiverskuiwing van twee radio bronne wat aanvanklik gekies was as radio eweknieë van twee ongeïdentifiseerde *EGRET* bronne, naamlik *3EG J0821-5814* en *3EG J0706-3837*. Die Ca H & K lyn depressie, wat rondom 4000 Å (in die russisteem van die bron) voorkom, was gebruik om die dominansie van die nie-termiese uitstraling van die bronne te bevestig. Dit het gehelp om die Plat Spektrum Radio kwasars (PSRQs) te onderskei van normale radio sterrestelsels. In die laaste fase was die homogene synchrotron eie-Compton model gebruik om die fisiese parameters van die stralende plasma in die bronne te begrens. Resultate dui dat die model suksesvol kan wees, mits daar genoeg data is om die waargenome parameters te begrens, soos byvoorbeeld die posisie van die stralingspieke in die spektrum, sowel as die spektraal-indekse in verskillende dele van die SEV. Daar is egter aangedui dat die SEC model nie 'n goeie verduideliking vir die lae-energie synchrotron radio uitstraling kan gee nie. As gevolg hiervan is 'n voorstel gemaak om 'n nie-homogene spuit model te oorweeg. In die MeV en GeV energië-band verskaf die bydrae van inverse-Compton verstrooing vanaf eksterne fotone 'n meer bevredigende meganisme om die SEV te beskryf.

Sleutelterme: stralingsmeganismes: nie-termies, lyn: identifisering, tegnieke: spektroskopie, sterrestelsels: strale, BL Lacertae: algemeen, kwasars: algemeen.

Acknowledgements

I would like to thank Professor Pieter Meintjes, my supervisor, for his guidance, support and encouragement for the duration of this project. I would also like to thank Dr David Thompson the Fermi Deputy Project Scientist and former member of the *EGRET* team, for many valuable discussions and kind answers to all of my many questions about *EGRET* and Fermi when I met him at the 11^{th} COSPAR workshop in India in February 2010. I thank the following people for their contribution towards the success of this thesis (in random order): Dr Michael Gaylard at the *HartRAO* observatory for his help in preliminary radio data reduction, Dr Petri Vaisanen at *SAAO* for his help in spectroscopy, Dr Encarni Romero at *SAAO* for her guidance in photometry with *SALT* data, Dr John Menzies for his technical assistance in running the 1.9-m and 1.0-m *SAAO* telescopes and Dr David Buckley for his constructive comments on my first *SALT* proposal.

Finally, I wish to extend my appreciation for the encouragement, love and support given by my wife and my children during my time as a graduate student.

This work was fully sponsored by the South African National Research Foundation via the South African Square Kilometer Array project. I am very grateful for the financial support.

Table of Contents

List of Figures

List of Tables

List of Acronyms

1FGL First Fermi Gamma-Ray Large Area Telescope Catalogue [p. 115]

2MASS Two Micron All Sky Survey catalogue [p. 71]

3EG Third *EGRET* catalogue [p. 1]

AGN Active Galactic Nucleus [p. 1]

BATSE Burst And Transient Source Experiment [p. 57]

BEL Broad Emission Line [p. 166]

BLR Broad Line Region [p. 2]

CCD Charge Coupled Device [p. 86]

CDQ Core-Dominated Quasar [p. 7]

CGRO Compton Gamma-Ray Observatory [p. 1]

COMPTEL Imaging Compton Telescope [p. 57]

CTIO Cerro Tololo Inter-American Observatory [p. 104]

ECC External Comptonisation of radiation from Clouds [p. 53]

ECD External Comptonisation of direct Disk radiation [p. 53]

EC External Compton scattering [p. 52]

EGRET Energetic Gamma-Ray Experiment Telescope [p. 1]

EGR *EGRET* Revised catalogue [p. 64]

FSRQ Flat Spectrum Radio Quasar [p. 6]

GBM Gamma-Ray Burst Monitor [p. 62]

GLAST Gamma-ray Large Area Space Telescope [p. 109]

GTI Good Time Interval [p. 115]

HartRAO Hartebeesthoek Radio Astronomical Observatory [p. 73]

HBL High-Energy Peaked BL Lac [p. 10]

HEAO-2 Second High Energy Astrophysical Observatory [p. 140]

HPQ Highly Polarized Quasar [p. 7]

HRS High Resolution Spectrograph [p. 86]

HSP-BL Lacs High Synchrotron Peaked BL Lacs [p. 10]

IRAF Image Reduction and Analysis Facility [p. 105]

ISM Interstellar Medium [p. 17]

ISP BL Lacs Intermediate Synchrotron Peaked BL Lacs [p. 10]

KAT Karoo Array Telescope [p. 73]

LAT Large Area Telescope [p. 12]

LBL Low-Energy Peaked BL Lac [p. 10]

LCP Left Circular Polarisation [p. 80]

LSP BL Lacs Low Synchrotron Peaked BL Lacs [p. 10]

MET Mission Elapsed Time [p. 115]

NED NASA/IPAC Extragalactic Database [p. 66]

NIR Near Infrared [p. 152]

NLR Narrow Line Region [p. 2]

NOAO National Optical Astronomy Observatory [p. 104]

NVSS NRAO VLA Sky Survey [p. 71]

OSSE Oriented Scintillation Spectrometer Experiment [p. 57]

OVV Optically Violently Variable [p. 7]

PFIS Prime Focus Imaging Spectrograph [p. 86]

PKS Parkes Radio Sources catalogue [p. 71]

PMN Parkes-MIT-NRAO catalogue [p. 172]

RCP Right Circular Polarisation [p. 80]

ROI Region of Interest [p. 115]

ROSAT Roentgen Satellite [p. 140]

RSS Robert Stobie Spectrograph [p. 71]

SAAO South African Astronomical Observatory [p. 71]

SAA South Atlantic Anomaly [p. 115]

SALTICAM SALT Imaging Camera [p. 86]

SALT Southern African Large Telescope [p. 71]

SAS-2 Small Astronomy Satellite-2 [p. 61]

SED Spectral Energy Distribution [p. 7]

SKA Square Kilometre Array [p. 73]

SOAR Southern Observatory for Astrophysical Research [p. 71]

SSC Synchrotron Self-Compton [p. 14]

SSRQ Steep Spectrum Radio Quasar [p. 6]

UV Ultra-Violet [p. 56]

VHP Volume Holographic Phase [p. 104]

Chapter 1

Introduction

The *Energetic Gamma-Ray Experiment Telescope (EGRET)* on board the *Compton Gamma-Ray Observatory (CGRO)*, during its 9 years of service between 1991 and 2000, produced the first all-sky γ-ray map above 100 MeV. In the Third *EGRET* catalogue (3EG) (Hartman et al. 1999), 271 sources have been reported of which 130 are still unidentified, i.e. not associated with any particular class of point source in the sky. Of the 130 unidentified sources, 69 are at high galactic latitudes, i.e. $|b| > 10$ degrees while the rest are confined in the galactic plane, probably associated with diffuse γ-ray emission from hydrogen gas clouds bombarded by high energy cosmic rays.

A serious complicating factor concerning possible identification of point sources that could possibly be associated with the *EGRET* γ-ray sources is the large field of view, i.e. between 0.5–1.5 degrees in the sky. This implies that the *EGRET* field could harbour several potential sources, especially at low galactic latitudes. This creates an intrinsic problem in the identification of possible radio/optical and X-ray counterparts for the detected *EGRET* sources.

Since the large majority of *EGRET*-detected sources have been associated with blazars (Hartman et al. 1999), it can be assumed that some of the unidentified *EGRET* sources may also be blazars, especially those at high galactic latitudes. The purpose of this study is therefore to search for possible blazars among selected high latitude southern unidentified *EGRET* sources.

1.1 General properties of blazars

An Active Galactic Nucleus (AGN) is a compact region at the center of a galaxy which has a much higher than normal luminosity over some, or all windows of the electromagnetic spectrum. A galaxy hosting an AGN is called an Active Galaxy. Galactic activity refers to one or more of the following phenomena (Landt 2003):

- a central compact core brighter than that of normal galaxies,
- continuum radiation of the central core component, extending from the radio to the X-ray,

and in some cases, to the γ-ray spectral bands,

- emission lines produced in the central regions (accretion disk and its corona, Broad Line Region (BLR) and Narrow Line Region (NLR)) by non-stellar processes,
- highly variable continuum and spectral line emission, and
- nonthermal radio emission emanating from the centre and collimated in the form of two opposite jets.

The name Active Galactic Nucleus (AGN) emphasizes the fact that the activity is confined mainly to the central region. Schematic diagrams illustrate the current understanding of the structure of an AGN in Figure 1.1 and Figure 1.2.

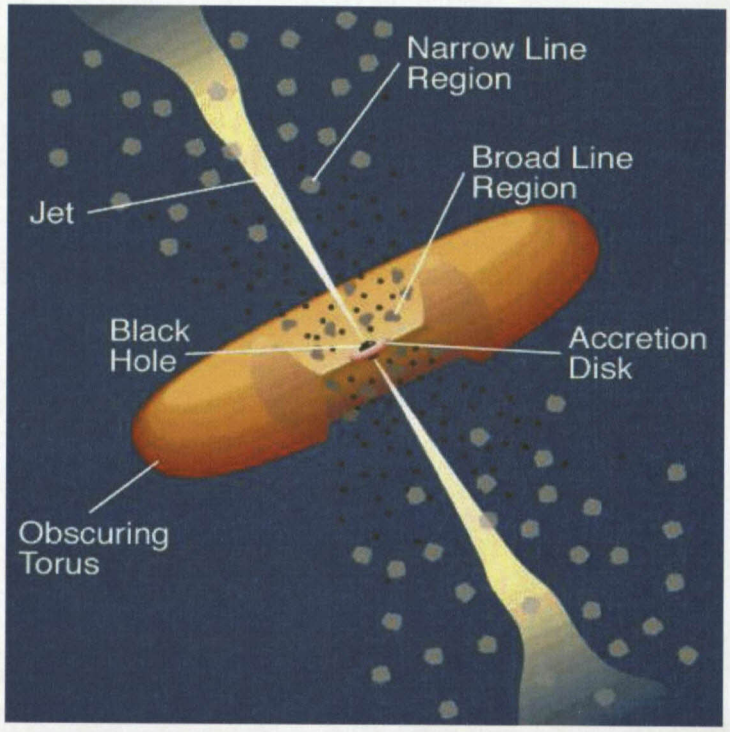

Figure 1.1: Illustration of the physical structure of an AGN (adapted from Urry and Padovani (1995)). The central black hole is surrounded by a luminous accretion disk. Broad and narrow emission lines are produced in clouds closer (dark blobs) and further away (grey blobs) from the central source respectively. A thick, dusty torus (or warped disk) obscures the broad-line region viewed edge-on. Powerful radio jets emanate from the region near the black hole in radio-loud AGN.

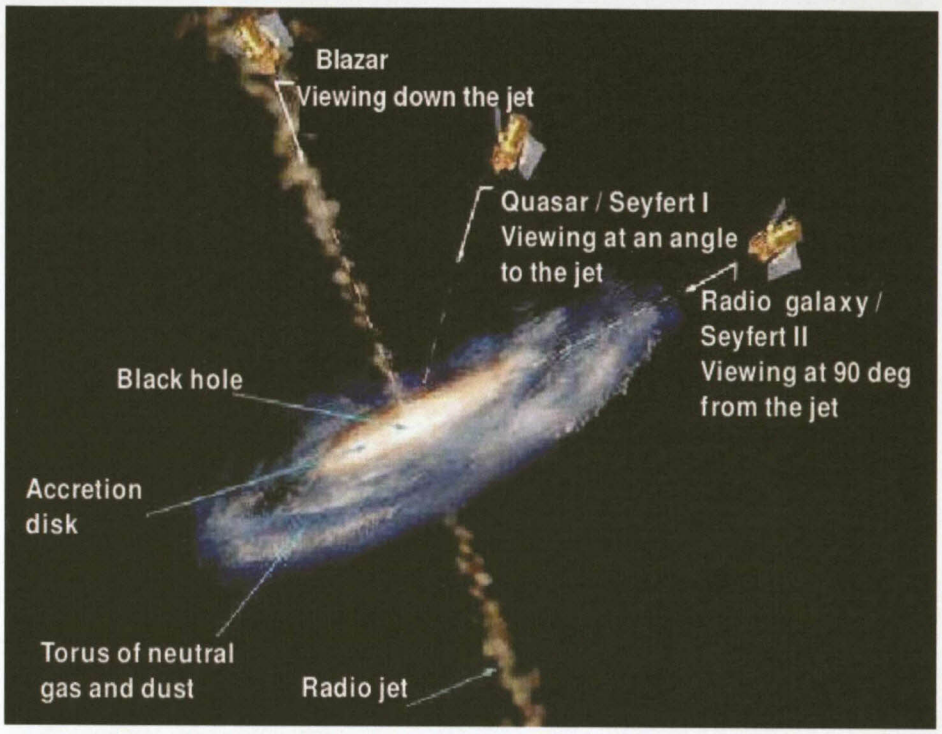

Figure 1.2: In terms of a unified model of AGNs, blazars are viewed face-on, implying a highly Doppler boosted jet being projected towards the observer, while the second jet is projected in the opposite direction. For blazars, the Broad Line Region (BLR) and inner accretion disc will not be obscured by the larger dusty accretion torus lying in a plane normal to the jet. The observed radio emission will be dominated by a one-sided jet that may be variable in intensity and apparently superluminal. At a slightly larger viewing angle (less than 45 degrees), if the optical AGN emission is much brighter than the starlight of the host galaxy, the object will be called a Quasi Stellar Object (QSO); otherwise a Seyfert I galaxy. If the inclination angle is larger than about 45°, the optical core may be obscured by the dusty torus and highly relativistic radio jets may be Doppler-dimmed, and we will see either a double-lobed radio galaxy or a Seyfert II galaxy (a Seyfert galaxy with only the narrow emission lines directly visible).

According to this model, a supermassive ($M \sim 10^6$–$10^{10} M_\odot$, where $M_\odot$ is the mass of the Sun) black hole lies at the centre, and its strong gravitational potential dominates the dynamics of the whole galaxy. For a $10^9\ M_\odot$ black hole, e.g. the blazar 3C453.3[1] ($M_{\rm BH} = 1.9 \times 10^9\ M_\odot$, $z = 0.859$ (Woo and Urry 2002)), the gravitational radius (Schwartzschild's radius) is $R_{\rm G} = \frac{GM}{c^2} \sim 5 \times 10^{-5}$ pc (comparable to the size of the orbit of the planet Saturn[2]), the accretion disk extends from $\sim$ 6–200 $R_{\rm G}$, i.e. 3–100 $\times 10^{-4}$ pc, the broad-line clouds are located between $\sim$ 5–50 $\times 10^{-2}$ pc of the black hole (Urry and Padovani 1995, Kaspi et al. 2000) and the inner radius of the dusty torus is approximately $\sim$ 1 pc. The narrow-line region extends approximately from 10 to a few times 10^4 pc and radio jets have been detected on scales from 1 to several Mpc (Fig. 1.3).

[1]The brightest gamma-ray source in the sky ($> 2.6 \times 10^{-6}$ photons cm^{-2} s^{-1} in high state at $z = 0.859$.)
[2]Saturn: aphelion: 1.519×10^{12} km $\sim 5 \times 10^{-5}$ pc

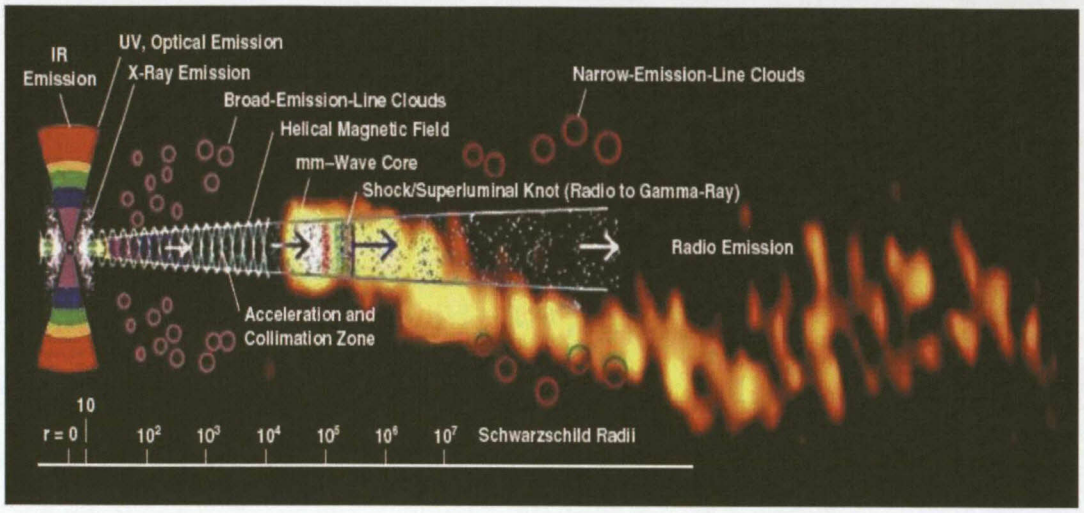

Figure 1.3: Illustration of the physical scale of different components of the AGN in the blazar 3C454.3. This is a 3mm radio image of the source adopted from Wehrle et al. (2009).

The multi-wavelength emission in these systems is directly related to the accretion of material into the supermassive black hole (e.g. Frank et al. (1992; p. 4)). Through the conservation of angular momentum, the in-falling material forms an accretion disk, which radiates through the conversion of potential to thermal energy as a result of viscous dissipation. It is through the highly efficient matter-to-energy conversion that AGNs can produce in tiny volumes ($\sim 10R_{\mathrm{G}}$) extraordinary (up to 10^{47} erg s^{-1}) luminosities, which are much higher than what can be achieved through ordinary, non-explosive stellar processes. The most common assumption about the state of the thermal plasma within the accretion disk is that it is optically thick. This then implies that the released energy extends roughly from optical through soft X-ray frequencies, with a substantial fraction emitted in the form of ultraviolet (UV) photons (blue bump).

In addition to the central black hole and the accretion disk surrounding it, massive clouds of gas move rapidly in the potential well of the black hole at somewhat larger distances. These clouds are illuminated by the radiation from the accretion disk and produce, mainly via the processes of photoionisation and collisional excitation, the strong emission lines characteristic of an AGN's spectrum (but enhanced in Seyfert galaxies). Clouds closer to the black hole ($\sim$ 0.01–1 pc) are denser and move more rapidly. These give rise to broad ($\geq$ a few 1000 km s^{-1}) emission lines in the object's spectrum, which are usually permitted transitions. The most prominent of these are the Hydrogen lines from the Balmer and Lyman series and transitions of Magnesium ions. These clouds are referred to as the Broad Line Region (BLR). Clouds located further out (up to a few kpc, e.g. Schmitt and Kinney (1996), Bennert et al. (2002)) have lower densities and velocities and form the so-called Narrow-Line Region (NLR). Narrow emission lines can be permitted and, taking advantage of the relatively low electron densities ($n_{\mathrm{e}} \sim 10^{10}$ m^{-3}, e.g. Safier (1992)), also forbidden lines. The strongest of the latter type are transitions of ionized Oxygen and Neon.

Since we do not observe broad emission lines in all AGNs, but almost always narrow emission lines, the existence of a thick, dusty torus (or warped disk) has been postulated. This feature is assumed to be located outside the accretion disk, obscuring the BLR at certain orientations of the AGN with respect to our line of sight.

Additionally, we observe in radio-loud AGNs (and sometimes also in radio-quiet AGNs, although on much smaller scales) the so-called "jets". These are streams of plasma (most likely electrons and positrons or electrons and protons) that are accelerated from the black hole and collimated by strong magnetic fields, thus radiating via the synchrotron process. The jets emanate from locations close to the central black hole at approximately 0.1 pc (e.g. Figure 1.4) and are feeding extended lobes at very large distances (up to several 100 kpc) to each side of the central nucleus.

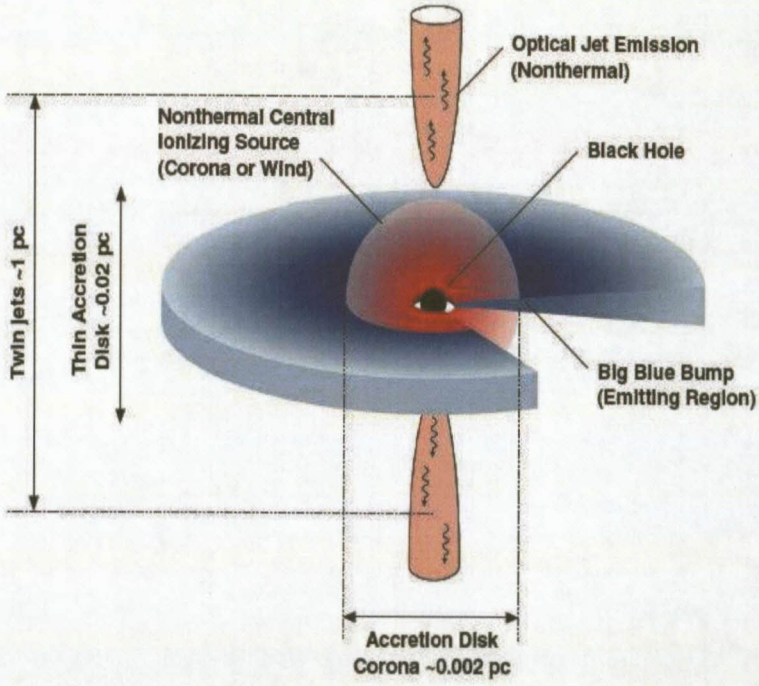

Figure 1.4: The jets emanate from locations close to the central black hole at $\sim$ 0.1–1 pc and feed extended lobes at very large distances (up to several 100 kpc) to each side of the central nucleus. Adopted from Wehrle et al. (2009).

Using their radio emission, AGNs are classified into radio-quiet and radio-loud (e.g. Figure 1.5). The radio-loud AGNs are objects with radio (5 GHz) to optical (B band) flux ratios above ten (they are $\sim$ 10% of the entire AGN population, e.g. Ivezić et al. (2002)). Within the class of radio-loud AGNs, 3 subdivisions can be made i.e.

- radio galaxies,
- quasars, and

- BL Lacertae objects (BL Lacs).

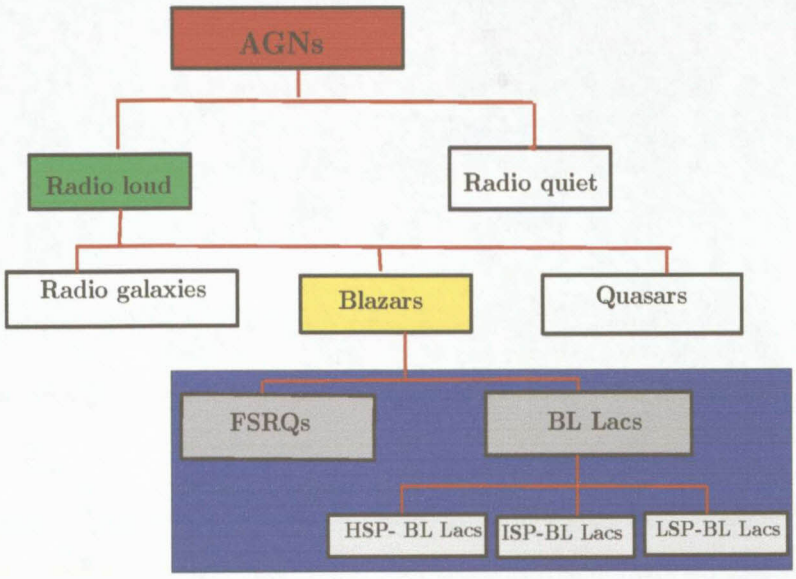

Figure 1.5: AGNs are subdivided into radio loud ($\frac{f_{radio-5GHz}}{f_{Opt-B}} > 10$) and radio quiet ($\frac{f_{radio-5GHz}}{f_{Opt-B}} < 10$). Radio loud are also subdivided into radio galaxies (extended radio sources with strong optical absorption lines), quasars (point-like sources at cosmological distances) and blazars (flat spectrum radio sources with jets oriented towards the Earth). Blazars are subdivided into BL Lacertae objects (BL Lacs, characterised by narrow emission lines) and Flat Spectrum Radio Quasars (FSRQs, characterised by strong emission lines). BL Lacs are subdivided into High Synchrotron Peaked BL Lacs (HSP-BL Lacs) [$\nu_{sync} > 10^{16}$ Hz], Intermediate Synchrotron Peaked BL Lacs (ISP BL Lacs) [$10^{14} < \nu_{sync} < 10^{16}$ Hz] and Low Synchrotron Peaked BL Lacs (LSP BL Lacs) [$\nu_{sync} < 10^{14}$) Hz].

Radio galaxies reach the largest linear dimensions at radio frequencies and their (optical) spectra show only narrow emission lines (if any at all), but more commonly absorption lines[3]. Therefore, these sources are believed to be oriented with their radio jets at relatively large angles with respect to our line of sight. Their BLR is then most likely obscured by the dusty torus. These galaxies present a radio luminosity of the order of 10^{25} W Hz^{-1} at low radio frequencies near 178 MHz (Urry and Padovani 1995).

BL Lacs and quasars are strong radio sources characterized by their distinct (optical) spectra. In fact, in BL Lacs we observe no (or very) weak emission lines and their continuum emission can often be fitted by a power-law, while in quasars both strong narrow and broad emission lines feature.

Using their radio spectral indices, within the quasars class we can further differentiate between Steep Spectrum Radio Quasars (SSRQs) and Flat Spectrum Radio Quasars (FSRQs), defined as quasars with radio spectral indices $\alpha_r > 0.5$ and $\alpha_r \leq 0.5$ respectively (where $S_\nu \propto \nu^{-\alpha}$).

[3]A forbidden line is a spectral line emitted by atoms undergoing energy transitions not normally allowed by the selection rules of quantum mechanics. However, such transitions do have small probability of their spontaneous occurrence, should an atom or molecule be raised to an excited state. Forbidden emission lines have only been observed in extremely low-density gases and plasmas in which atomic collisions are low so that atoms can stay relatively longer before being de-excited by collisions.

The differences in radio spectra are the signature of their distinct morphologies: SSRQs have weaker radio cores and show extended (steep spectrum) radio lobes similar to the ones of radio galaxies (although on smaller linear scales), whereas the emission of FSRQs is dominated by the (flat-spectrum) core component. The former Optically Violently Variable (OVV) quasars, Highly Polarized Quasars (HPQs) and Core-Dominated Quasars (CDQs) are now often grouped under the FSRQs class. In general, BL Lacs showed extreme properties more similar to the ones of FSRQs, which led to their common name of 'blazars'. The word '**blazar**' was suggested by Edward A. Spiegel [4] in 1978 and combines **BL** (Lac) with (qu)**asar**.

1.2 Classification of blazars

The two components of blazars (BL Lacs and FSRQs) are separated based on the strength of their emission lines.

The first blazar to be discovered and which gave it its name was BL Lacertae (BL Lac). This is a compact and highly variable radio source that had first been identified with a star. However, its optical spectrum is rather unusual, as it is featureless. Its spectrum could be explained as the signature of Doppler-boosted jet emission (Blandford and Rees 1978) observed at small viewing angles. At such orientations the core emission is strongly enhanced by relativistic beaming which outshines the extended emission from the host galaxy and is therefore lacking absorption lines. After the discovery of BL Lac other similar objects were found. Strittmatter et al. (1972) suggested that they formed a new class of extragalactic radio sources named BL Lacs. Attempts to classify blazars have been based on their optical spectroscopic features and on their Spectral Energy Distributions (SEDs) over the whole electromagnetic spectrum.

1.2.1 Optical spectra of blazars

Originally BL Lacs were found with completely featureless spectra, i.e. neither absorption nor emission lines. However, many BL Lacs turned out to have temporarily weak emission lines especially when in the low state. In order to separate BL Lacs from emission-line AGNs, BL Lacs were defined as flat-spectrum ($\alpha_r \leq 0.5$) radio sources with emission lines of Equivalent Widths $EW_\lambda < 5$ Å (Stocke et al. 1991) in the rest frame. The flat radio spectrum implies that the objects were relatively core-dominated and therefore beamed.

Separating BL Lacs from normal galaxies, the blazars' signature is a Ca II K & H (Calcium depression at ~ 4000 Å) break value $K_{4000} \leq 40\%$, in contrast to deeper depressions observed in normal radio galaxies[5]. As mentioned in the footnote this depression at ~ 4000 Å is the result

[4] Astronomy Department, Columbia University

[5] H & K lines are two absorption lines of singly ionised calcium Ca II in the intergalactic gas located between the source and the observer. They occur in the near-ultraviolet at wavelengths of H: 3969 Å and K: 3934 Å and result from the electronic transition from H: $4s\ ^2S_{\frac{1}{2}}$–$4p\ ^2P_{\frac{1}{2}}$ and K: $4s\ ^2S_{\frac{1}{2}}$–$4p\ ^2P_{\frac{3}{2}}$ (Goldberg 1964). The Ca II

of absorption of the thermal emission in the intergalactic gas. However, if the source has an additional multi-wavelength nonthermal spectrum, the depression will be shallower; therefore this can be used as a diagnostic tool to distinguish between blazars and other normal radio galaxies. A comparison of the K_{4000} depression in blazars (Figure 1.6) and in radio galaxies (Figure 1.7) are presented. This was based on the finding that this stellar absorption feature appears on average in $\sim 50\%$ of non-active elliptical galaxies (Dressler and Shectman, 1987). It is believed that any source with Ca II K & H break depression $K_{4000} \leq 40\%$ is likely to have an extra nonthermal emission component and should be classified as a blazar. Figure 1.7 illustrates how the depression caused by the Ca II K & H absorption is found to be deeper in radio galaxies than it is in blazars.

Dressler and Shectman (1987) pointed out that the strength of emission lines in radio-loud AGNs will depend strongly on the contribution from nonthermal jet emission, and, therefore on the Spectral Energy Distribution (SED).

depression at 4000 Å is calculated using the relation

$$K_{4000} = \frac{f^+ - f^-}{f^+}, \tag{1.1}$$

where f^- is the average flux between 3750 Å and 3950 Å and f^+ is the average flux between 4050 Å and 4250 Å in the rest frame (Caccianiga et al. 1999b). The depression materialises the absorption from Ca II ions around λ =4000 Å.

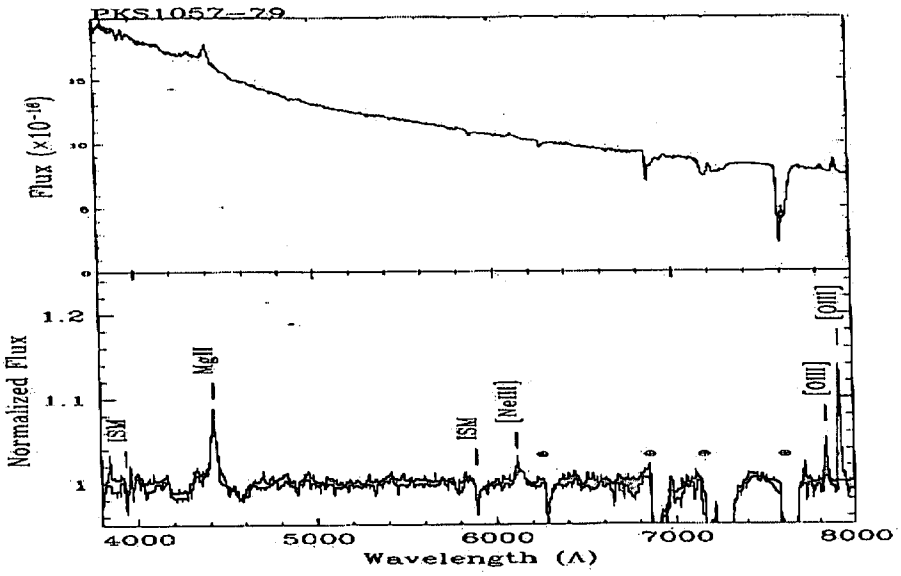

(a) RBS 1752 (BL Lac object). Adopted from Sbarufatti et al. (2008).

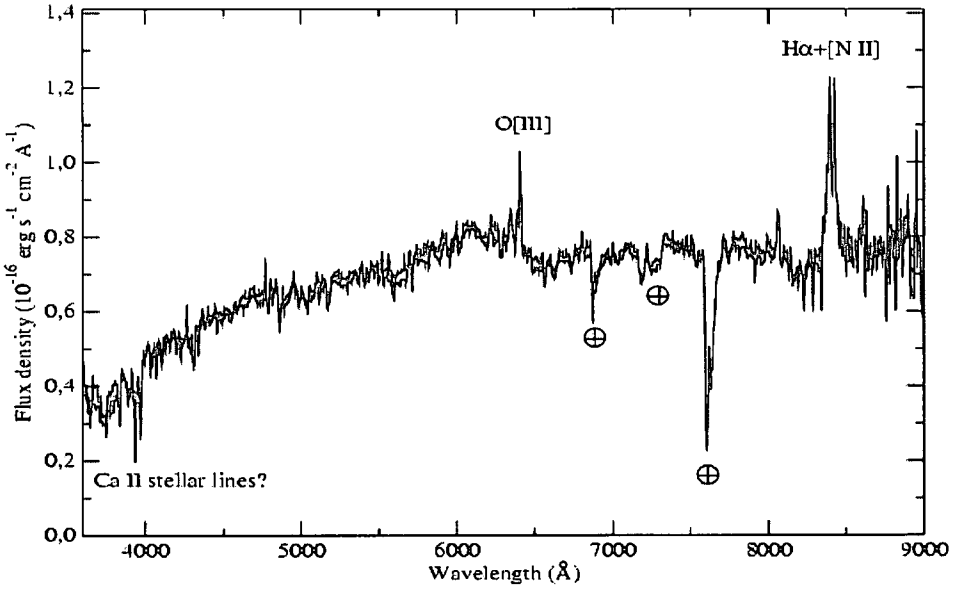

(b) 1RXS J072418.3-071508 (FSRQ)). Adopted from Martí et al. (2004).

Figure 1.6: (a) Optical spectrum of the BL Lac object RBS 1752 ($z = 0.449$) obtained with the *Focal Reducer and Low Dispersion Spectrograph-1 (FORS1)* at the *Very Large Telescope (VLT)*. Apart from telluric absorption lines, the spectrum consists of featureless nonthermal emission. Additional faint absorption lines are due to intergalactic absorption.
(b) Optical spectrum of the FSRQ 1RXS J072418.3-071508 with a redshift of $z = 0.270$. The presence of Ca II absorption lines close to their rest wavelength could be explained if a late type star is almost superposed on the quasar line-of-sight (Martí et al. 2004).

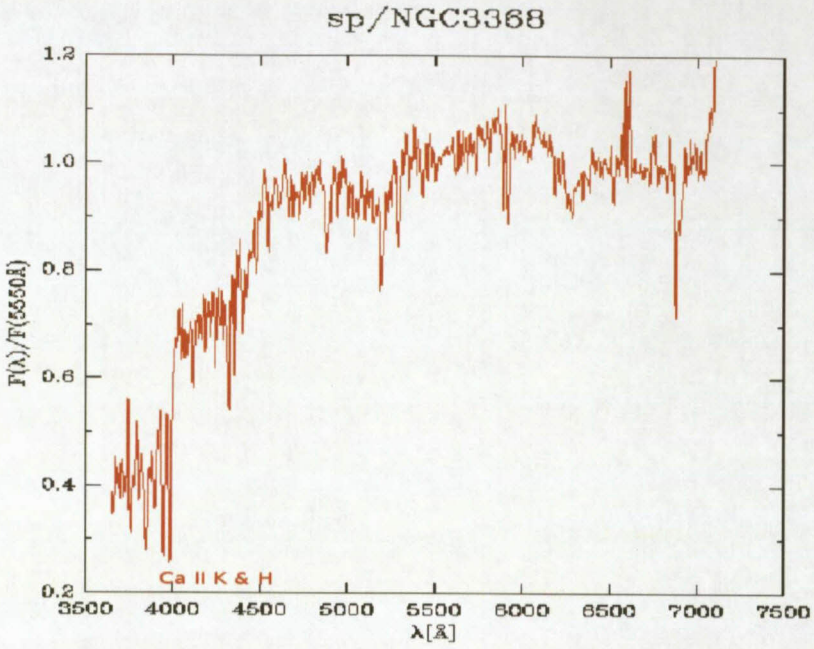

Figure 1.7: Optical spectrum of a normal radio galaxy NGC 3368 (RA = 10 h 46 m 45.8 s, Dec = +11 d 49 m 10 s; B = 10 mag; $z = 0.030$; Type: Sab). Adopted from Kennicutt (2004). Noticeable is the depression (known as 4000 Å break) caused by the Ca II K & H absorption lines (K: 3933 Å, and H: 3968.5 Å) here in the normal radio galaxy which is deeper than in the optical spectra of blazars represented in Fig. 1.6.

1.2.2 Spectral Energy Distribution (SED) of blazars

Initially, using their SEDs, BL Lacs were subdivided into Low-Energy Peaked BL Lacs (LBLs) and High-Energy Peaked BL Lacs (HBLs). Figure 1.8 displays the characteristic SED of each group. All exhibit two broad emission peaks - a lower-frequency one, attributed to synchrotron emission, and a higher-frequency one, produced by inverse Compton emission. LBLs and HBLs are defined as BL Lacs with a synchrotron emission peak located at IR/optical (LBLs) and UV/soft–X- ray (HBLs) frequencies respectively. A recent review of this classification (Abdo et al. 2010a), based on the 11-month Fermi data, introduces an intermediate subclass between LBLs and HBLs and now the three subclass denominations are: the High Synchrotron Peaked BL Lacs (HSP-BL Lacs) with $\nu_{sync} > 10^{16}$ Hz, the Intermediate Synchrotron Peaked BL Lacs (ISP BL Lacs) with $10^{14} < \nu_{sync} < 10^{16}$ Hz and the Low Synchrotron Peaked BL Lacs (LSP BL Lacs) with $\nu_{sync} < 10^{14}$ Hz.

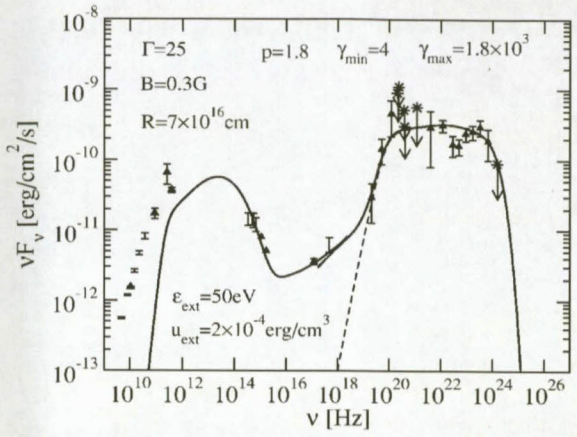

(a) *3C 279* (FSRQ)

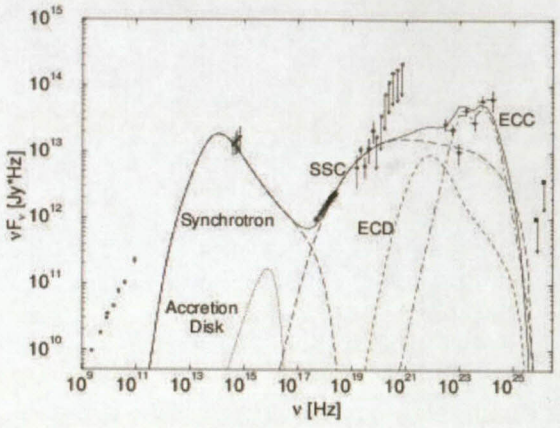

(b) *BL Lacertae* (LBL)

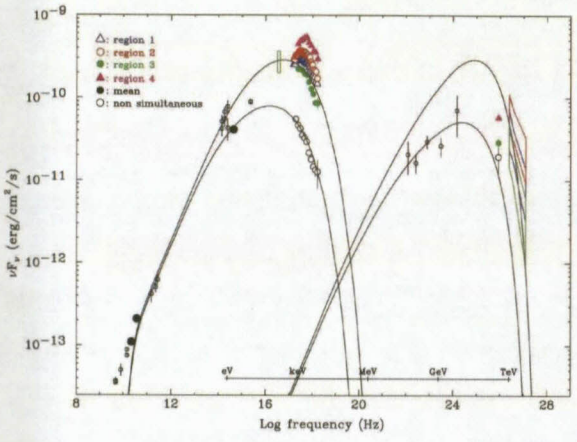

(c) *Mrk421* (HBL)

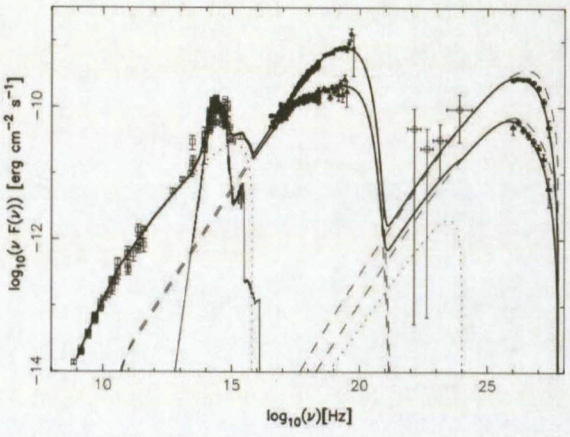

(d) *Mrk501* (HBL)

Figure 1.8: (a) *3C 279* (FSRQ) (Adopted from Kusunose et al. 2003), (b) *BL Lacertae* (LBL)(Adopted from Böttcher 2002), (c) *Mrk 421* (HBL) (Adopted from Takahashi et al. 2000) and (d) *Mrk 501* (HBL) (Adopted from Katarzyński et al. 2001). For FSRQs and LBLs the synchrotron peak is located in the IR-Optical part of the spectrum, with inverse Compton radiation contributing significantly in the spectrum above X-ray frequencies ($\simeq 10^{19}$ Hz). For *Mrk 421* (HBL) the synchrotron process still contributes significantly to the X-ray part of the spectrum, with the inverse Compton mechanism being responsible for the high energy emission. For *Mrk 501* the peak at $\simeq 10^{14}$ Hz represents the contribution of the stellar emission of the host galaxy. The two superimposed plots were obtained when the object was in high state (top) and low state (below).

In practice, however, the division between LBLs and HBLs is based on their X-ray-to-radio flux ratios. A value of $\frac{f_x}{f_r} = 10^{11.5}$ (with f_x (in erg cm^{-2} s^{-1}) in the energy range 0.3–3.5 keV, and f_r (in Jy) at 5 GHz) was proposed as a dividing line (Padovani and Giommi 1996).

1.2.3 Gamma-ray photon index in blazars

A review of the blazar classification based on 11 months of the *Fermi-Large Area Telescope (LAT)* data (Abdo et al. 2010a) shows that the γ-ray photon index ($F_\gamma \propto E^{-p}$) can be grouped as seen in Figure 1.9. Based upon the distribution of photon indices displayed in Figure 1.9, these authors grouped blazars subclasses together based upon the average photon indices displayed in Table 1.1.

Class	mean	rms
FSRQs	2.46	0.18
LSP-BL Lacs	2.21	0.16
ISP-BL Lacs	2.13	0.17
HSP-BL Lacs	1.86	0.17

Table 1.1: Distribution of photon index in blazar subclasses. FSRQs = Flat spectrum radio Quasars, LSP-BL Lacs = Low Synchrotron Peaked BL Lacs, ISP-BL Lacs = Intermediate Synchrotron Peaked BL Lacs and HSP-BL Lacs = High Synchrotron Peaked BL Lacs

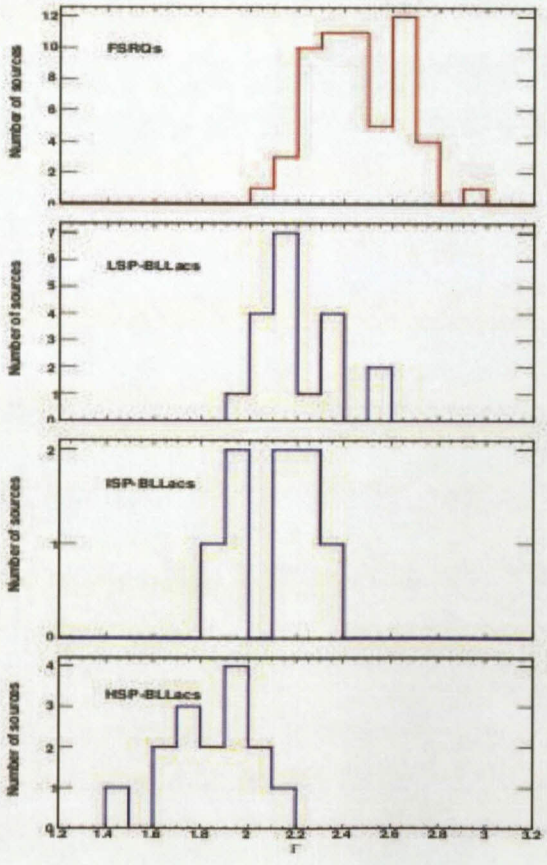

Figure 1.9: Classification of blazars based on the gamma-ray photon index.

A similar split for the more powerful blazar subclass, the FSRQs, does not exist so far. All known FSRQs were found to have SEDs similar to that of LBLs. Within the sequence FSRQs–LBLs–HBLs, the bolometric luminosity is decreasing in the radio to X-ray region. Also the frequency where the emission peaks increases in the spectral energy distribution of the source (Stecker et al. 1996). Table 1.2 summarises the differences within the blazars class.

Class	FSRQs	BL Lacs
Defining property	Strong emission lines	almost lineless
Environment	intense radiation field (disk, clouds, torus)	low radiation field
Power	$\sim 10^{46-48}$ erg/s	$\sim 10^{45-46}$ erg/s
Parent population	Fanaroff-Riley 2	Fanaroff-Riley 1
Synchrotron hump in SED	Peak in IR	Peak in UV/X-rays: HBL Peak in Opt/IR: LBL
Redshift of *EGRET* blazars	0.1–2.3	< 1

Table 1.2: Summary of differences between FSRQs and BL Lacs.

The synchrotron and the inverse Compton scattering emissions appear to be the main mechanisms explaining the multi-wavelength emission observed in blazars. A more detailed discussion, focussing on these mechanisms primarily, will be presented in the next chapter.

1.3 Motivation and structure of this thesis

The main objective of this study is the search for possible blazars among the high latitude unidentified *EGRET* sources. The methodology involves the search for flat spectrum ($\alpha < 0.7$) radio counterparts in the *EGRET* error boxes. Since it is believed that the γ-ray production in blazars involves a synchrotron self-Compton process, a more detailed discussion of the synchrotron and inverse Compton scattering processes will be presented in Chapter 2.

In Chapter 3, a brief discussion of *EGRET* and the methodology related to the search for the flat spectrum radio counterparts in the error boxes of the Unidentified *EGRET* sources, will be presented.

In Chapter 4, multi-wavelength observations of these sources and data analysis methods are presented.

In Chapter 5, different models used to fit the observed data and constraining the very high energy emission are described.

Finally, a final discussion and conclusions are presented in Chapter 6.

Chapter 2

Nonthermal Emission in Blazars

In Chapter 1, general properties of blazars have been discussed. It has been shown that the Spectral Energy Distribution (SED) of blazars exhibits two peaks resulting from the combined nonthermal synchrotron and inverse Compton scattering emission from highly relativistic electrons. This process is referred to as the Synchrotron Self-Compton (SSC) process. Nonthermal emission is produced by particles accelerated to relativistic velocities. The acceleration mechanisms in these objects are believed to be associated with strong shock waves in relativistic jet-like outflows originating from a region close to a compact object which is, in the case of blazars, a supermassive black hole.

The acceleration is the result of the scattering of particles off magnetic turbulence structures, or irregularities, where the magnetic irregularities act as magnetic mirrors (charged particles bounce back from the high-intensity magnetic field region). The acceleration is stochastic, and was introduced by Fermi in 1949 to show that high energy cosmic rays can be produced by charged particles colliding with clouds (scattering centres) in interstellar space (Fermi 1949).

Due to the fact that the jet axis is close to the line-of-sight, some relativistic effects such as the beaming effect and the blue shifting contribute to enhance the observed flux in blazars.

In this Chapter, a brief discussion of the acceleration of particles in blazar jets is presented. This is supplemented by a brief discussion of the influence of relativistic effects in the flow and cosmic expansion on the observed emission in the frame of reference of the observer.

2.1 Acceleration mechanisms in blazars

The total multi-wavelength emission of blazars from radio to γ-rays can be explained satisfactorily by an SSC model. It has been shown earlier (e.g. Section 1.2.2) that the entire spectrum from radio to VHE γ-rays is reconcilable with processes within the jets, accelerating a large population of electrons to energies between $\gamma_e \sim 10^3$–10^4. These electrons radiate in the jet magnetic field (via the synchrotron process), as well as scattering up the same synchrotron photons to high energies (see Figure 2.1). In this section, a brief discussion is presented of the relevant

particle acceleration processes in blazar jets.

It is believed that the signature of the multi-wavelength emission in blazars is reconcilable with a Fermi-like process, probably accompanied by an impulsive electrodynamic injection process, (e.g. Petrosian and Bykov 2008).

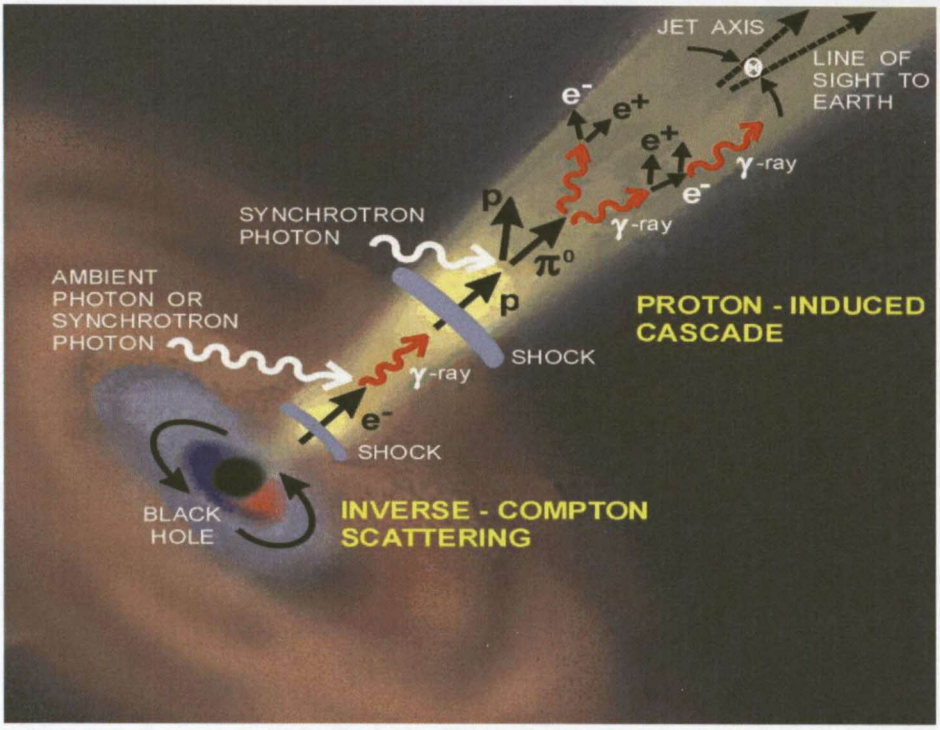

Figure 2.1: Graphical illustration of production of γ-rays. In both scenarios (inverse Compton scattering and hadronic cascade, particles are first accelerated to high energies by shock waves. Adopted from `http://inwfsun1.ugent.be/`.

2.1.1 Fermi acceleration mechanisms

In the Fermi acceleration process a fraction of particle kinetic energy is gained as a result of the elastic scattering off magnetic turbulence or magnetic irregularities in the flow where they are confined. As mentioned earlier, these irregularities act as moving magnetic mirrors in the flow. The Fermi process can be divided into two regimes, i.e. a fast acceleration process (first order Fermi process) as a result of scattering mainly head-on with scattering centres in strong shocks and a slow stochastic process (second order Fermi process) as a result of scattering off magnetised clouds. The original version of Fermi's theory is therefore known as second order Fermi acceleration. In both regimes, in order for the mechanism to be effective, the environment has to be collisionless, i.e.

$$\beta = \frac{P_{\rm gas}}{P_{\rm mag}} = \frac{nkT}{\frac{B^2}{8\pi}} \ll 1, \tag{2.1}$$

where $P_{\rm gas}$ and $P_{\rm mag}$ represent the gas pressure and magnetic pressure respectively. This is because frequent collisions with surrounding particles will result in severe energy loss and a resultant thermalisation of the medium instead of creating a nonthermal spectrum of accelerated particles. The attractive feature of the Fermi acceleration, first and second order, is the creation of a power-law spectrum $N(E) \propto E^{-p}$, which is the general signature of a nonthermal spectrum associated with virtually all nonthermal sources in the universe. A more detailed summary of both these processes will now be presented.

2.1.1.1 First order Fermi acceleration

The first order Fermi acceleration process occurs when charged particles are deflected off magnetic irregularities frozen into the plasma up- and downstream of strong shocks (e.g. Axford et al. (1977), Krymskii (1977), Bell (1978), Blandford and Rees (1978)).

The beauty of this process is that particles scattering back and forth across the shock will gain energy from mainly head-on collisions, which on average transfers energy (e.g. Bell (1978), Longair (1994) for discussion)

$$\langle \frac{dE}{E} \rangle \simeq \left(\frac{4}{3} \frac{V_s}{\rm c} \right), \tag{2.2}$$

where $V_{\rm s}$ represents the shock velocity and c the speed of light.

The key point of the acceleration process is that high energy particles hardly notice the shock at all since the thickness of the shock will normally be much smaller than the gyroradius of the high energy particles. Because of turbulence on both sides of the shock, particles are scattered when they pass through the shock in either direction, so that their velocity distribution rapidly becomes isotropic on either side of the shock with respect to the frame of reference in which the fluid is in rest.

The spectral signature of this process is a characteristic spectrum

$$dN(E) \sim E^{-p} dE, \tag{2.3}$$

with $p = \frac{\rho+2}{\rho-1}$ where $\rho = \dfrac{u_{\rm u}}{u_{\rm d}}$ represents the ratio of the flow velocities up- and downstream of the shock. For strong shocks $\rho \rightarrow 4$, resulting in $p \rightarrow 2$. However, the spectrum may be modulated by several physical processes (see Frank and Valenti (2007)) such as

- non-linear effects and multiple shocks which can harden the spectrum to indices $p < 2$ (e.g. Berezhko and Ellison (1999), White (1985)) and
- anomalous transport processes associated with magnetic field diffusion from the shock region resulting in $p \rightarrow 2.5$ (Kirk et al. 1996).

Electron acceleration in shocks is further complicated by rapid energy loss via synchrotron radiation in strong magnetic fields. For effective acceleration of electrons, a fast and effective pre-acceleration via electric fields is required for Lorentz factors $\gamma_e > \frac{m_p}{m_e}\frac{V_A}{c}$, where V_A represents the local Alfvén speed (Achterberg 2001, Longair 1994).

The first-order Fermi acceleration (diffusive shock acceleration) process represents the most efficient and plausible mechanism for the origin of the inferred nonthermal power-law distributions in most of the inner AGN jets (Frank and Valenti 2007).

2.1.1.2 Second order Fermi acceleration

In Fermi's original version of the theory, the particles scatter off moving magnetised clouds in a galaxy. In this process, the magnetic scattering centres are moving randomly with typical velocity V_s, resulting in an effective energy transfer of

$$\langle\frac{dE}{E}\rangle \simeq \left(\frac{8}{3}\frac{V_s}{c}\right)^2 \tag{2.4}$$

per scatter (e.g. Longair (1994) for a review). One can see on close inspection that the average energy increase is only second order in $\frac{V_s}{c}$, hence second order Fermi acceleration. This process is also significantly slower than the first order process since the random velocities in interstellar clouds in the Galaxy is very small, e.g. $\frac{V_s}{c} \rightarrow 10^{-4}$. However, this process can generate a power-law spectrum

$$dN(E) \propto E^{-p}dE \tag{2.5}$$

with $p = 1 + \frac{1}{\alpha t_{esc}}$, where t_{esc} represents the time the particle spends in the accelerating region, and $\alpha = \frac{4}{3}(\frac{V_s^2}{cL})$, with L being the mean free path between clouds (e.g. Longair (1994)).

The estimated mean free path of galactic cosmic rays in the Interstellar Medium (ISM) is roughly $L \sim 1\,\mathrm{pc}$, resulting in a collision rate of roughly one per year. This justifies second order Fermi acceleration being a very slow process, and certainly not an effective mechanism to accelerate the cosmic rays to the high energies.

2.1.2 Acceleration in electric fields

It has been mentioned earlier (e.g. Section 2.1.1.1) that for effective shock acceleration of electrons in strong shocks, an effective pre-acceleration is required. It is likely that electrons are pre-accelerated by electric fields induced in the plasma, for example, magnetic neutral sheets, double layers, as well as a betatron process where electric fields are induced according to Maxwell's

equation

$$\vec{\nabla} \times \vec{E} = -\frac{1}{c}\frac{\partial \vec{B}}{\partial t}. \tag{2.6}$$

In all these examples mentioned above the electric fields are dynamic, since static electric fields cannot be maintained in highly conducting ionised fluids. A brief discussion of the most relevant aspects surrounding electrodynamic particle acceleration in highly conducting fluids will be presented. The following discussion will focus mainly on processes that accelerate particles like electrons in the turbulent pre- and post-shock plasma of strong shocks.

2.1.2.1 Magnetic reconnection

Magnetic reconnection as a mechanism to accelerate particles through current dissipation in neutral sheets is well documented (e.g. Svestka (1976), Parker (1979) and references therein). This mechanism occurs if magnetic field lines of opposite polarity merge at a neutral point where $\vec{B} = 0$. Dissipation of current may then be converted to kinetic and thermal energy in the plasma under special conditions (e.g. Parker (1975), Lesch (1991)). The electric field induced through the merging of magnetic fields follows from the application of Faraday's induction law (e.g. Biskamp (1989), Lesch (1991)). In the pre-merging magnetic field of strong B, a particle spiralling in the field will find that the magnetic flux,

$$\phi_B = \pi R_{\rm L}^2 B, \tag{2.7}$$

that passes through a hypothetical surface bound by its orbit with radius $R_{\rm L}$, i.e. the Larmor radius, decreases at a rate

$$\frac{\partial \phi}{\partial t} \sim -\frac{\pi R_{\rm L}^2 B}{\tau_{\rm R}}, \tag{2.8}$$

where $\tau_R = \frac{R_{\rm L}}{V_{\rm m}}$ represents the reconnection time scale. By Faraday's induction law, the work done per unit charge (emf-electromotive force) in a single orbit is

$$\begin{aligned} \text{emf} &= 2\pi R_{\rm L} E \\ &= \frac{\pi B R_{\rm L} V_{\rm m}}{\rm c}, \end{aligned} \tag{2.9}$$

where $V_{\rm m} \sim 0.1 V_{\rm A}$ represents the speed with which field lines merge in the fluid, typically a fraction of the Alfvén speed in the magnetised fluid, which is

$$V_{\rm A} = \frac{B}{\sqrt{4\pi\rho}}. \tag{2.10}$$

The electric field induced in the merging region (MR) as a result of the $\overrightarrow{V} \times \overrightarrow{B}$ motion of charge accross the magnetic field is of the order

$$E_{\mathrm{MR}} \approx \frac{B\, V_{\mathrm{m}}}{\mathrm{c}}. \tag{2.11}$$

This field in the merging region must be of the same order as the electric field in the dissipation region, i.e. the current sheet, which is (e.g. Benz and Courvoisier (1994))

$$E_{\mathrm{DR}} = \frac{J}{\sigma} = \frac{D}{c}\left(\frac{\partial B}{\partial x}\right) \tag{2.12}$$

with $D = \frac{c^2}{4\pi\sigma}$, where J represents the current density and σ the electrical conductivity in the plasma. To generate strong electric fields through current dissipation in the neutral sheet, the conductivity σ must become anomalously low, i.e. much lower than the classical value, which will inhibit reconnection in the first place as result of the freezing-in of magnetic field into a highly conducting fluid (e.g. Parker (1975) for a review). The presence of large-scale turbulence in the pre- and post-shock magnetised plasma may feed microturbulence into the plasma via a Kolmogorov cascade process (e.g. Yepez et al. (2009)), which will result in a dramatic decrease in the conductivity of the plasma ($\sigma \rightarrow 0$). This results in the generation of very strong electric fields which can accelerate charged particles to very high energies in the vicinity of strong shocks.

2.1.2.2 Double layers in field-aligned currents

The shear of magnetic fields as a result of strong shocks and turbulence may result in the generation of field-aligned (Birkland-Dessler) currents ($J_{\|}$) along flux tubes. Microturbulence may result in these currents to reach critical values

$$J_{\mathrm{c}} \approx \mathrm{e}\, n_{\mathrm{e}}\, C_{\mathrm{s}}, \tag{2.13}$$

where n_{e} and C_{s} represent the electron density and the speed of sound respectively. This will result in the generation of an instability in the current, especially in highly collisionless plasmas resulting in the generation of large field-aligned potential drops $\phi_{\|}$ on double layers.

It can be shown that the value of the potential drop (e.g. Haerendel (1994)) is of the order

$$\phi_{\|} = \frac{B^2 V_{\mathrm{A}}}{8\pi e n_{\mathrm{e}} C_{\mathrm{s}}} \tag{2.14}$$

which can reach significant values in regions of strong B-field and anomalous low electron density.

For strong collisionless shocks in a collisionless plasma, i.e. $\beta = nkT/\frac{B^2}{8\pi} \ll 1$, the Alfvén

speed $V_A \rightarrow C$, which implies that

$$\phi_{\parallel} \approx 3 \times 10^6 \left(\frac{B}{1\,\mathrm{G}}\right)^3 \left(\frac{n_e}{10^{-6}\,\mathrm{cm}^{-3}}\right)^{-\frac{3}{2}} \left(\frac{T_{\mathrm{eff}}}{10^4\,\mathrm{K}}\right)^{-\frac{1}{2}} \text{[Volts]}, \tag{2.15}$$

can be achieved instantaneously.

For both these processes, if the induced field exceeds a certain critical value (i.e. the so-called Dreicer field), the electrons will accelerate freely in the plasma. The Dreicer field (e.g. Dreicer (1959), Benz and Courvoisier (1994)) is given by

$$E_D \propto \left(\frac{n_e}{T_{\mathrm{eff}}}\right), \tag{2.16}$$

which shows that collisionless plasmas, i.e. $\beta \ll 1$, the critical field may be low enough that the bulk of the electron population will be accelerated instantaneously, resulting in a so-called runaway process where a large population of mildly to relativistic electrons can be injected into strong shocks, where they can be accelerated futher to very high energies.

2.2 Relativistic effects in blazars

The plasma within the jets of radio-loud AGNs is believed to move at relativistic speeds (Rees 1978), transporting energy from the vicinity of the supermassive black hole to the distant lobes. This, however, has strong implications for an observer who views the jet at relatively small angles, as is believed to be the case in BL Lacs and quasars.

Let us assume that a source emits isotropically in its rest frame (S'). Then, in the observer's frame (S), where the source moves at highly relativistic ($\beta = \frac{v}{c} \sim 1$) speed, relativistic beaming, Doppler blue shifting, and superluminal motion are manifestations of relativistic effects that severely influence the observed emission in the observer's frame of reference. A brief discussion of these effects will be presented, and is based upon discussions presented in Longair (1992), Longair (1994) and Rybicki and Lightman (2004).

2.2.1 Relativistic beaming

The beaming of emission in the direction of motion is a phenomenon following from Einstein's theory of Special Relativity (SR). It can be shown, using the Lorentz transformation, that the

observed velocity of a particle, which can be a photon, in the laboratory frame is

$$\begin{aligned} u_x &= \frac{u'_x + V}{1 + \frac{u'_x V}{c^2}}, \\ u_y &= \frac{u'_y}{\gamma(1 + \frac{u'_x V}{c^2})}, \\ u_z &= \frac{u'_z}{\gamma(1 + \frac{u'_x V}{c^2})}. \end{aligned} \tag{2.17}$$

where (u'_x, u'_y, u'_z) and (u_x, u_y, u_z) are the components of the particle's velocity in the moving (S′) and stationary (S) reference frames respectively. Here V and γ represent the velocity and Lorentz factor of the moving reference frame (S′) relative to the laboratory frame (S). These equations can be generalised into perpendicular and parallel components

$$\begin{aligned} u_\perp &= \frac{u'_\perp}{\gamma(1 + \frac{u'_\parallel V}{c^2})}, \\ u_\parallel &= \frac{u'_\parallel + V}{1 + \frac{u'_\parallel V}{c^2}}, \end{aligned} \tag{2.18}$$

resulting in the aberration formula

$$\begin{aligned} \tan\theta &= \frac{u_\perp}{u_\parallel} \\ &= \frac{1}{\gamma}\left(\frac{u'_\perp}{u'_\parallel + V}\right), \end{aligned} \tag{2.19}$$

which in the case of a photon, reduces to

$$\tan\theta = \frac{1}{\gamma}\left(\frac{\sin\theta'}{\cos\theta' + \frac{V}{c}}\right). \tag{2.20}$$

Further, since $\tan\theta' = \frac{\sin\theta'}{\cos\theta'}$, we can generate a second expression, i.e.

$$\cos\theta = \frac{\cos\theta' + \frac{V}{c}}{(1 + \frac{V}{c}\cos\theta')}, \tag{2.21}$$

where in both cases θ' represents the direction of propagation of the emitted photon in (S′) relative to the direction of motion (S). One can see that for $\theta' = \frac{\pi}{2}$, $\tan\theta = \frac{c}{\gamma V}$ and $\cos\theta = \frac{V}{c}$,

resulting in

$$\sin\theta \approx \frac{1}{\gamma}, \tag{2.22}$$

where γ represents the Lorentz factor of (S′) relative to (S). Thus the radiation emitted within $\frac{\pi}{2} < \theta' < \frac{\pi}{2}$ is beamed into the direction $-\frac{1}{\gamma} < \theta < \frac{1}{\gamma}$.

This beaming of radiation as a result of relativistic motion is evident from Figure 2.2, showing the emitted power of a charged particle moving with velocity V.

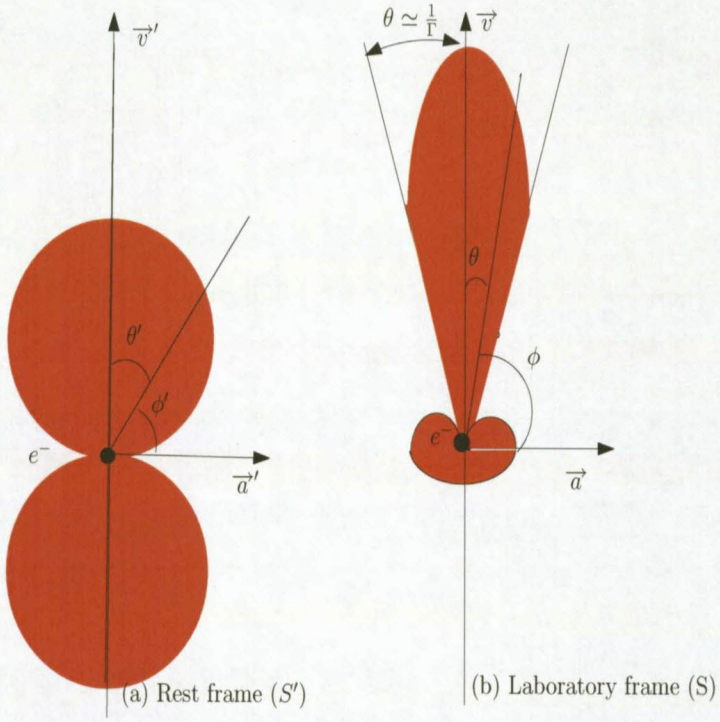

Figure 2.2: This figure (adopted from Longair (1994; p. 237)) illustrates the beaming effect for a relativistic electron emitting synchrotron radiation. Left (a): In its rest frame (S'), an electron moving in a magnetic field emits into two lobes with power proportional to $\sin^2\phi' = \cos^2\theta'$, where θ' is the angle between the emission direction and the velocity vector and ϕ' is the angle between the emission direction and the acceleration vector. Right (b): In the laboratory frame (S), the main emission power is beamed into a cone of opening angle θ, given by $\sin\theta \simeq \theta = \frac{1}{\gamma}$, in the direction of the electron's velocity, where γ is the Lorentz factor.

It can be seen that in the observer's reference frame the emission is highly beamed into a narrow cone with $\theta \approx \frac{1}{\gamma}$ for $\gamma \gg 1$.

Relativistic beaming will therefore result in a significant amplification of the observed intensity of a source in the observer's reference frame, which can lead to overestimating the luminosity of relativistic sources.

Observations confirm the blazar properties based on jets orientation and fluxes beaming, in the following way:

- Blazars (BL Lacs and FSRQs) show a core-dominated radio morphology; their continuum emission is mostly nonthermal and extends from radio to X-ray and in some cases up to γ-ray frequencies; their emission is strongly ($> 3\%$, Visvanathan and Wills (1998)) polarized at most wavelengths (a property related directly to the nature of synchrotron emission) and they exhibit rapid variability (on timescales down to days – hours). In addition, these sources often show apparent superluminal motion (this is explained in the next paragraph). This is what was expected. In fact, strongly beamed sources are expected to have multi-wavelength properties dominated by Doppler-boosted jet emission.

- Optical spectroscopic observations indicate that in BL Lacs there are weak or absent emission lines (one of their defining criteria). On the other hand, quasars have (by definition they are at cosmological distances) strong narrow emission lines, as expected. In fact, due to the fact that the flux is beamed along the direction of the motion and the jet is oriented to the line of the sight of the observer, the emission, which could come from the disc and from other regions surrounding the black hole, is swamped.

2.2.2 Doppler Blue Shift

The Lorentz transformation of the four-momentum of a photon, emitted in the moving reference frame, to the laboratory reference frame can be represented as

$$\begin{pmatrix} \frac{h\nu}{c} \\ \frac{h\nu}{c}\cos\theta \\ \frac{h\nu}{c}\sin\theta \\ 0 \end{pmatrix} = \begin{pmatrix} \gamma & \frac{\gamma v}{c} & 0 & 0 \\ \frac{\gamma v}{c} & \gamma & 0 & 0 \\ 0 & 0 & 1 & 0 \\ 0 & 0 & 0 & 1 \end{pmatrix} \begin{pmatrix} \frac{h\nu'}{c} \\ \frac{h\nu'}{c}\cos\theta' \\ \frac{h\nu'}{c}\sin\theta' \\ 0 \end{pmatrix}, \tag{2.23}$$

where γ represents the Lorentz factor of (S′) relative to (S) and when ν' and ν represent the frequency of the photon in (S′) and (S) respectively. The zeroth component of this leads to

$$\begin{aligned} \frac{h\nu}{c} &= \frac{h\nu'}{c}\gamma(1+\tfrac{v}{c}\cos\theta') \\ \rightarrow \quad \nu &= h\nu'\gamma(1+\tfrac{v}{c}\cos\theta'). \end{aligned} \tag{2.24}$$

It can readily be shown, using the inverse Lorentz transformations for velocities, that

$$\cos\theta' = \frac{\cos\theta - \frac{V}{c}}{1 - \frac{V}{c}\cos\theta} \tag{2.25}$$

which, if substituted back, results in

$$\begin{aligned}
\nu &= \gamma\left[1+\tfrac{V}{c}\left(\frac{\cos\theta-\frac{V}{c}}{1-\frac{V}{c}\cos\theta}\right)\right]\nu' \\
&= \gamma\left[\frac{1-\frac{V}{c}\cos\theta}{1-\frac{V}{c}\cos\theta}+\frac{\frac{V}{c}\cos\theta}{1-\frac{V}{c}\cos\theta}-\frac{(\frac{V}{c})^2}{1-\frac{V}{c}\cos\theta}\right]\nu' \\
&= \gamma\left[\frac{1-\frac{V^2}{c^2}}{1-\frac{V}{c}\cos\theta}\right]\nu' \\
&\quad \left(\text{since } \gamma=\frac{1}{\sqrt{1-\frac{V^2}{c^2}}},\ \text{then } 1-\frac{V^2}{c^2}=\frac{1}{\gamma^2}\right) \\
&= \frac{1}{\gamma(1-\frac{V}{c}\cos\theta)}\nu'.
\end{aligned} \tag{2.26}$$

This can be written in more compact form

$$\nu = \delta\nu', \tag{2.27}$$

where

$$\delta = \frac{1}{\gamma(1-\frac{V}{c}\cos\theta)} \tag{2.28}$$

is the Doppler factor.

A consequence of this equation for motion of the source towards the observer ($\theta = 0°$) or away from the observer ($\theta = 180°$) is[1]

$$\begin{aligned}
\nu &= \left(\frac{1+\frac{V}{c}}{1-\frac{V}{c}}\right)^{\frac{1}{2}}\nu' \text{ for } \theta = 0° \\
&\quad \text{and} \\
\nu &= \left(\frac{1-\frac{V}{c}}{1+\frac{V}{c}}\right)^{\frac{1}{2}}\nu' \text{ for } \theta = 180°,
\end{aligned} \tag{2.29}$$

leading to blueshifted ($\theta = 0°$) and redshifted ($\theta = 180°$) emission respectively. Changing to the terminology of observed $\nu_{\rm obs}$ and emitted $\nu_{\rm em}$ frequencies (i.e. ν and ν'),

$$\begin{aligned}
\tfrac{\nu_{\rm obs}}{\nu_{\rm em}} &= \left(\frac{1+\frac{V}{c}}{1-\frac{V}{c}}\right)^{\frac{1}{2}} \text{ for } \theta = 0° \\
&\quad \text{and} \\
\tfrac{\nu_{\rm obs}}{\nu_{\rm em}} &= \left(\frac{1-\frac{V}{c}}{1+\frac{V}{c}}\right)^{\frac{1}{2}} \text{ for } \theta = 180°.
\end{aligned} \tag{2.30}$$

[1]According to the Equation 2.25, $\theta = 0°$ in (S) corresponds to $\theta' = 180°$ in (S'), i.e. the photon is pointing towards the observer and $\theta = 180°$ in (S) corresponds to $\theta' = 0°$ in (S'), i.e. the photon is moving away from the observer.

In the limit of $\frac{V}{c} \ll 1$ one shows that

$$\frac{\nu_{\rm em}}{\nu_{\rm obs}} - 1 = \mp\frac{V}{\rm c}, \tag{2.31}$$

where the (-) sign corresponds to $\theta = 0$ (or $\theta' = 180°$) and the (+) sign corresponding to $\theta = 180°$ (or $\theta' = 0°$). This is now the time to introduce the Doppler redshift $Z_{\rm Dop}$ as a quantity defined by

$$Z_{Dop} = \frac{\nu_{\rm emit}}{\nu_{\rm obs}} - 1 = \mp\frac{V}{c}. \tag{2.32}$$

It can be seen that $Z_{\rm Dop}$ is positive when the $\nu_{\rm em} > \nu_{\rm obs}$ or $\lambda_{\rm em} < \lambda_{\rm obs}$, that is for photons moving away from the observer (i.e. redshifted), and is negative when $\nu_{\rm em} < \nu_{obs}$ or $\lambda_{\rm em} > \nu_{\rm obs}$, when photons are moving towards the observer (i.e. blueshifted).

2.2.3 Apparent transverse velocities (superluminal motion)

This phenomenon involves the observed projected velocity of a moving source in the sky, which can lead to the bizarre effect of superluminal motion if the velocity of the source is relativistic (Rees 1966).

Consider a source (see Figure 2.3) which moves from P_1 to P_2 in a time Δt, as is measured in the observer's reference frame.

The time difference between the time of reception of the photons emitted at P_1 and P_2 is

$$\Delta t_{\rm rec} = (1 - \frac{V}{c}\cos\theta)\Delta t. \tag{2.33}$$

The apparent distance moved by the emitting object is

$$l_\perp = V\Delta t \sin\theta, \tag{2.34}$$

which translates to an apparent velocity of

$$\begin{aligned} V_{\rm app} &= \frac{l_\perp}{\Delta t_{\rm rec}} \\ &= \frac{V\sin\theta}{1-\frac{V}{c}\cos\theta}. \end{aligned} \tag{2.35}$$

This can be written as

$$\beta_{\rm app} = \frac{V_{\rm app}}{c} = \frac{\beta\sin\theta}{1-\beta\cos\theta}. \tag{2.36}$$

For angles close to the line of sight, the effect of this equation can be dramatic. This can be illustrated in the following: The effect of the angle θ between source and observer can be

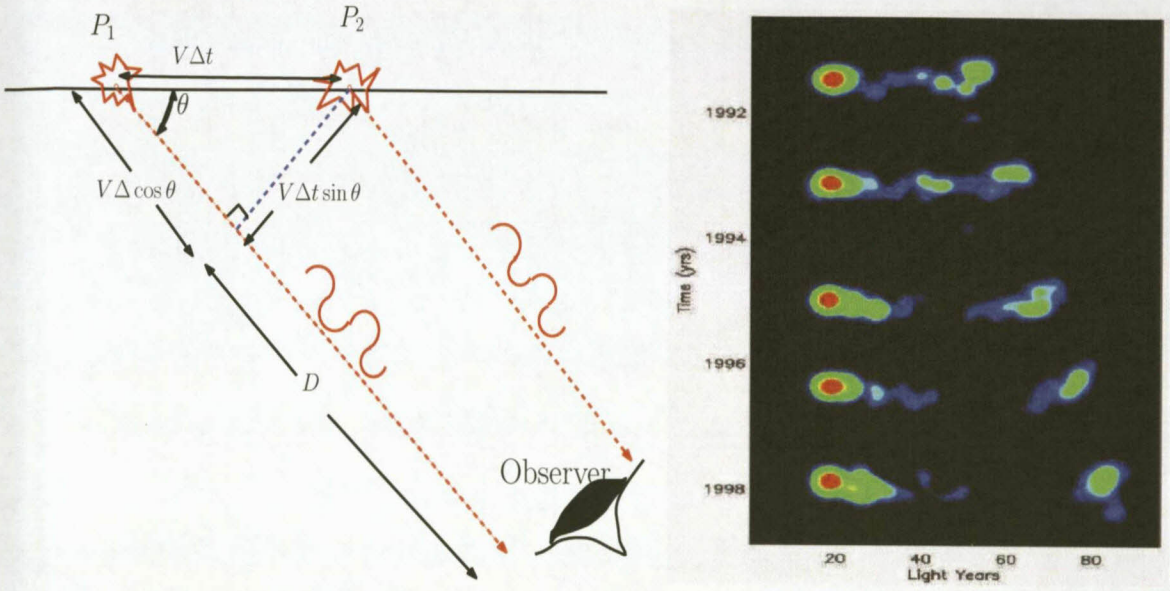

(a) (b)

Figure 2.3: (a) A schematic diagram illustrating the superluminal motion of a jet's ejected plasma from a cosmological distant object. (b) Superluminal motion in the FSRQ 3C 279. The stationary core is the bright red spot to the left of each image. The observed location of the rightmost blue-green blob moved about 25 light years from 1991 to 1998, hence the changes appear to an observer to be faster than the speed of light i.e. $V_{\rm app} \simeq 3.57$. The blue-green blob is part of a jet pointing within 2 degrees to our line of sight, and moving at a true speed of 0.997 times the speed of light. Courtesy of the *National Radio Astronomy Observatory (NRAO)* of the National Science Foundation (NSF) operated under cooperative agreement by Associated Universities, Inc (AUI).

illustrated by taking the derivative

$$\frac{\partial\beta_{\rm app}}{\partial\theta} = \frac{\beta\cos\theta - \beta^2}{(1-\beta\cos\theta)^2}. \tag{2.37}$$

The maximum of $\beta_{\rm app}$ of this source is obtained for

$$\frac{\partial\beta_{\rm app}}{\partial\theta} = 0, \tag{2.38}$$

which implies that

$$\beta\cos\theta - \beta^2 = 0 \tag{2.39}$$

for $\beta = \cos\theta$. This gives

$$\begin{aligned} \beta_{\rm app} &= \frac{\beta\sin\theta}{1-\beta\cos\theta} \\ &= \gamma\beta. \end{aligned} \tag{2.40}$$

It is evident from this equation that when $\gamma \gg 1$, then $\beta \approx 1$ and the apparent velocity of

the source

$$\beta_{\rm app} = \frac{V_{\rm app}}{\rm c} \gg 1, \tag{2.41}$$

i.e. $V_{\rm app}$ appears to be much larger than the speed of light. The effect is actually seen in AGNs.

2.3 Cosmic expansion

The development of spectroscopy led to the surprising discovery that the universe is in a state of dynamic expansion. A systematic spectroscopic survey of the "spiral nebulae", i.e. galaxies outside the Milky Way, showed that spectral lines are systematically shifted towards the red end of the spectrum. The Doppler redshift, defined as

$$Z_{\rm Dop} = \frac{\nu_{\rm em} - \nu_{\rm obs}}{\nu_{\rm obs}} = \frac{\nu_{\rm em}}{\nu_{\rm obs}} - 1, \tag{2.42}$$

was found to be directly proportional to the distance of these galaxies as was determined using distance indicators like Cepheid variable stars. Astronomers had known that the spectra of most spiral galaxies tend to be redshifted, based on the observation of Vesto Slipher at the Lowell Observatory in 1912.

The Doppler effect relates the redshift directly to the recession velocity of an emitting source i.e. it has been shown earlier (Equation 2.30) that

$$\frac{\nu_{\rm obs}}{\nu_{\rm em}} = \left(\frac{1 - \frac{V}{c}}{1 + \frac{V}{c}}\right)^{\frac{1}{2}}. \tag{2.43}$$

This results in $\nu_{\rm obs} < \nu_{\rm em}$, or alternatively $\lambda_{\rm obs} > \lambda_{\rm em}$.

Using this relation, it can be seen that in the limit $\frac{V}{c} < 1$, using $Z_{\rm Dop} = \frac{\nu_{\rm em}}{\nu_{\rm obs}} - 1$ that (in the limit $\frac{V}{c}$ to first order) the following is obtained

$$Z_{\rm Dop} = \frac{V_{\rm rec}}{c}, \tag{2.44}$$

showing that the redshift relates to the recession velocity[2] of a source away from the observer.

The wavelength of emission in an expanding Universe will be proportional to the scale length R. If the wavelength at the time of emission is λ, when the scale length is R, then it will be λ_0 when the scale factor has changed to R_0, i.e.

$$\frac{\lambda_0}{\lambda} = \frac{R_0}{R}. \tag{2.45}$$

[2]The recession velocity of the spiral galaxies can be explained in terms of an expanding Universe

The cosmological redshift is then defined as

$$\begin{aligned} Z_{\rm cosm} &= \left(\frac{\lambda_0-\lambda}{\lambda}\right) \\ &= \frac{R_0}{R} - 1, \end{aligned} \tag{2.46}$$

which is

$$\rightarrow \frac{R_0}{R} = 1 + Z_{\rm cosm}. \tag{2.47}$$

The cosmological redshift expresses the change of the scale factor since the light has been emitted. It can be assumed that

$$\begin{aligned} \frac{V_{\rm exp}}{c} &= Z_{\rm Dop} \\ &= Z_{\rm cosm}. \end{aligned} \tag{2.48}$$

By measuring the redshifts of distant galaxies, using distance indicators like Cepheid variables, Edwin Hubble plotted a velocity versus distance graph of the nearest galaxies, revealing the well known relationship established by Hubble in 1929 (e.g. Hubble (1929)),

$$V_{\rm exp} = H_0 d, \tag{2.49}$$

where H_0 represents the Hubble constant. Therefore, one can measure a galaxy's speed from its redshift and using Hubble's law to determine its distance. The Hubble constant H_0 ranges between 68–74 km/s/Mpc based on the most recent estimates (Altavilla et al. 2004). The cosmological redshift relates directly to the expansion velocity, i.e.

$$\begin{aligned} Z_{\rm cosm} &= \frac{R_0 - R}{R} \\ &= \frac{(\frac{\Delta R}{\Delta t})\Delta t}{R} \\ &= \frac{V_{\rm exp}\Delta t}{R}, \end{aligned} \tag{2.50}$$

where R represents the scale factor of the Universe when the light was emitted. For small redshifts the scale length is proportional to the light travel time

$$R \approx c\Delta t \tag{2.51}$$

and

$$Z_{\rm cosm} = \frac{V_{\rm exp}}{\rm c}, \tag{2.52}$$

resulting in

$$V_{\rm exp} = Z_{\rm cosm}{\rm c}. \tag{2.53}$$

2.4 Definitions and Lorentz invariants

The principle of relativity states that the equations, describing the laws of Physics, have the same form in all inertial frames of reference, i.e. Physics laws are said to be Lorentz invariant.

Moreover, some physical quantities remain unchanged by a Lorentz transformation, i.e. are independent of the inertial frame. Such quantities are also said to be Lorentz invariants. Any scalar, and in general the norm of any four-vector, are examples of common Lorentz invariants. Lorentz invariants are important in Physics as they help to establish how other physical quantities are transformed between different frames of reference. In this section, a brief discussion of some useful Lorentz invariants, relevant to this study, will be presented.

2.4.1 Power radiated, $P = \frac{dE}{dt}$

In this study we will focus on calculating the power [J s^{-1}] radiated by a source that is the energy it emits per unit time, i.e.

$$P = \frac{dE}{dt}. \tag{2.54}$$

Let $P' = \frac{dE'}{dt'}$ and $P = \frac{dE}{dt}$ be the power measured in the rest frame of the source and in the observer's frame respectively. The transformation relation of the power from the rest frame of the source to the observer frame (or vice versa), depends on how the quantities dt and dE are themselves transformed into dt' and dE' respectively.

The time interval dt is obtained from the Lorentz transformation between the rest frame and the lab frame of the displacement element $(cdt, d\overrightarrow{r})$

$$dt = \gamma(dt' + \beta\frac{dx'}{c}) = \gamma dt',$$

since in the rest frame $dx' = 0$. dE is the zeroth component of the four-vector of momentum element $(\frac{dE}{c}, \overrightarrow{dP})$ and transforms from the rest frame and the lab frame as

$$dE = \gamma(dE' + \beta c\, dp'_x) = \gamma dE'(1 + \beta\cos\theta').$$

Averaging over solid angle there is:

$$\begin{aligned}\langle dE\rangle &= \gamma\langle dE'\rangle\frac{\int_0^\pi(1+\beta\cos\theta')2\pi\sin\theta' d\theta'}{4\pi} \\ &= \gamma\langle dE'\rangle.\end{aligned}$$

Thus,

$$\frac{dE}{dt} = \frac{\gamma dE'}{\gamma dt'} = \frac{dE'}{dt'},$$

i.e. $\frac{dE}{dt}$ = Lorentz invariant.

2.4.2 Particles' distribution function, $f(\bar{x}, \bar{p})$

The particles' distribution function $f(\bar{x}, \bar{p})$, is the number of particles with position and momentum vectors $(\bar{x} + d\bar{x}, \bar{p} + d\bar{p})$ at time (t) per unit volume in phase space.

Alternatively, $f(\bar{x}, \bar{p}) d^3x d^3p$ = Number of photons within a spatial volume element d^3x and within a momentum volume element d^3p.

Consider a group of particles that occupy a slight spread in position and in momentum at a particular time. In a frame (K′) comoving with the particles, they occupy a spatial volume element $d^3x' = dx'dy'dz'$ and a momentum volume element $d^3p' = dp'_x dp'_y dp'_z$, but no spread in energy, i.e. $dW' = dP'_0 = 0$. The group thus occupies an element of phase space $dV'_{xp} = d^3p' d^3x'$. In the observer's frame moving with the velocity parameter β with respect to the (K′) frame along the X-axis, the spatial volume element occupied by particles is d^3x, as measured by (K). Since perpendicular distances are unaffected, $dy = dy'$ and $dz = dz'$, but there is a length contraction in the X- direction, i.e. $dx = \frac{1}{\gamma} dx'$ leading to

$$d^3x = \gamma^{-1} d^3x'. \tag{2.55}$$

For the momentum volume element measured by the observer d^3p, the components of the momentum transform as components of a four-vector, yielding

$$\begin{aligned} dp_y &= dp'_y \\ dp_z &= dp'_z \\ dp_x &= \gamma(dp'_x + \beta\, dp'_0). \end{aligned} \tag{2.56}$$

Since the particles have the same energy in the comoving frame, i.e. $dp'_0 = 0 \rightarrow dp_x = \gamma dp'_x$, the following is obtained

$$d^3p = \gamma d^3p' \tag{2.57}$$

and

$$dV_{\mathrm{px}} = d^3p d^3x = d^3p' d^3x' = dV'_{\mathrm{px}}, \tag{2.58}$$

i.e. the phase-space volume element is a Lorentz invariant.

It follows that the phase-space density (distribution function)

$$f = \frac{dN}{dV_{\mathrm{px}}} = \text{Lorentz invariant} \tag{2.59}$$

since the number of particles within the phase element, dN, is a countable quantity and therefore itself invariant.

2.4.3 Transformation relation of the intensity

For a source radiating energy, it is often necessary to know the energy flowing from it through a given surface dA at an angle θ with respect to the normal of the surface in a given solid angle. Consider the elementary surface dA' which is normal to the ray, and is the projection of dA (see Figure 2.4).

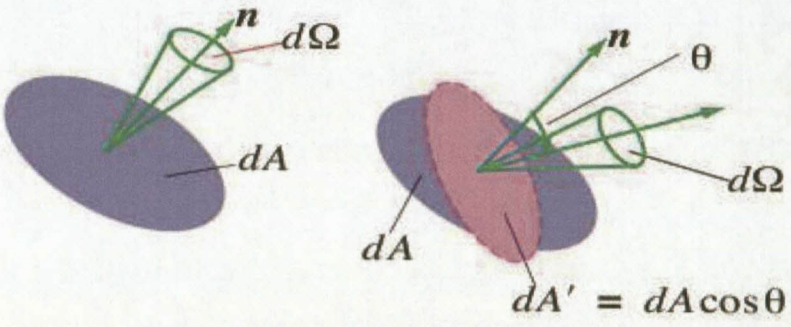

Figure 2.4: Intensity passing through a surface.

The electromagnetic energy passing through the surface dA at an angle θ to surface is given by

$$dE_\nu = I_\nu(\theta, \phi) \cos\theta d\nu dA dt d\Omega, \tag{2.60}$$

where $I_\nu(\theta, \phi)$ is the spectral intensity.

The spectral intensity I_ν [J s^{-1} m^{-2} sr^{-1}] will be defined as the energy emitted per unit time per unit frequency from a unit projected surface area into a unit solid angle.

From the definition of the distribution function, it is evident that the energy density of photons within d^3p is equal to

$$h\nu f d^3p = h\nu f p^2 dp d\Omega, \tag{2.61}$$

since $d^3p = p^2 dp d\Omega$ in spherical coordinates. The alternative expression for this involves the energy density per unit frequency per unit solid angle, $u_\nu(\Omega)$, which is

$$u_\nu(\Omega) = \frac{I_\nu}{c}. \tag{2.62}$$

Hence, the energy density within $d\nu$ and within solid angle $d\Omega$ is $u_\nu d\nu d\Omega = \frac{I_\nu}{c} d\nu d\Omega$. Therefore,

$$\begin{aligned} h\nu f p^2 dp d\Omega &= h\nu f \left(\tfrac{h\nu}{c}\right)^2 d\left(\tfrac{h\nu}{c}\right) d\Omega \\ &= \tfrac{I_\nu}{c} d\nu d\Omega, \end{aligned} \tag{2.63}$$

which implies

$$f = \frac{c^2 I_\nu}{h^4 \nu^3}. \tag{2.64}$$

Since f is a Lorentz invariant, then

$$\frac{I_\nu}{\nu^3} = \text{Lorentz invariant.} \tag{2.65}$$

Thus, the transformation relation of the spectral intensity can be deduced using the invariance principle, i.e.

$$\frac{I_\nu}{\nu^3} = \frac{I'_{\nu'}}{\nu'^3} \quad \Rightarrow I_\nu = I'_{\nu'}\left(\frac{\nu}{\nu'}\right)^3.$$

Using Equation 2.27 it can be expressed as

$$I_\nu = \delta^3 I'_{\nu'}, \tag{2.66}$$

with δ presented by Equation 2.28. For an integrated intensity, there is

$$\begin{aligned} I = \int I_\nu d\nu &= \int \delta^3 I'_{\nu'} d\nu \\ &= \delta^4 \int I'_{\nu'} d\nu' \\ &= \delta^4 I', \end{aligned} \tag{2.67}$$

i.e.

$$I = \delta^4 I'. \tag{2.68}$$

2.4.4 Transformation relation of the absorption coefficient

Light is absorbed when it is crossing a medium (even within the emitting region, i.e. self-absorption). The absorption coefficient, α_ν, is a quantity that characterises how easily a material or medium can be penetrated by a beam of light. A large absorption coefficient means that the beam is quickly "attenuated" (weakened) as it passes through the medium, and a small attenuation coefficient means that the medium is relatively transparent to the beam. Often absorption is presented in the following form:

$$\frac{dI_\nu}{ds} = -\alpha_\nu I_\nu. \tag{2.69}$$

Putting emission and absorption into the one equation, there is

$$\frac{dI_\nu}{ds} = j_\nu - \alpha_\nu I_\nu, \tag{2.70}$$

which is called the radiative transfer equation. This equation is fundamental in radiative processes as its solution points to a way of estimating the output intensity from an emitting region or source. Equation 2.70 can be rewritten as

$$\frac{dI_\nu}{\alpha_\nu ds} = \frac{j_\nu}{\alpha_\nu} - I_\nu \tag{2.71}$$

or

$$\frac{dI_\nu}{d\tau_\nu} = S_\nu - I_\nu, \tag{2.72}$$

where $d\tau_\nu = \alpha_\nu ds$ is the differential optical depth and $S_\nu = \frac{j_\nu}{\alpha_\nu}$ is called the "source function"[3].

Having determined the Lorentz transformation properties of the specific intensity, the transformation properties of the source function can be determined. In fact, since the source function occurs in the above-mentioned transfer equation under the difference $S_\nu - I_\nu$, i.e. $\frac{dI_\nu}{d\tau} = S_\nu - I_\nu$, it is clear that S_ν must have the same transformation properties as I_ν, namely,

$$\frac{S_\nu}{\nu^3} = \text{Lorentz invariant.} \tag{2.73}$$

To find the transformation of absorption coefficient, material in frame (K) streaming with velocity v between two planes parallel to the x-axis is imagined. Let (K′) be the rest frame of the material. The optical depth τ along the ray must be an invariant, since $e^{-\tau}$ gives the fraction of photons passing through the material, and this involves simple counting. From the formal definition of the optical depth,

$$\tau = \frac{l\alpha_\nu}{\sin\theta} = \frac{l}{\nu \sin\theta}\nu\alpha_\nu = \text{Lorentz invariant.} \tag{2.74}$$

The transformation of $\sin\theta$ can be found by noting that $\nu \sin\theta$ is simply proportional to the y-component of the photon four-momentum k_y. But both k_y and l are the same in both frames, being perpendicular to the motion (see Figure 2.5). Therefore,

$$\nu\alpha_\nu = \text{Lorentz invariant} \tag{2.75}$$

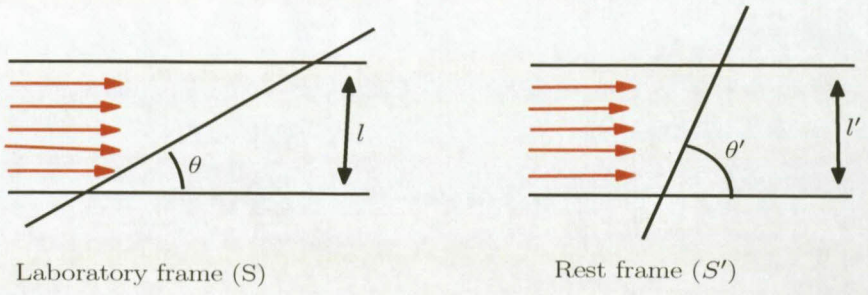

Figure 2.5: Transformation of a moving and absorbing medium.

[3]Note that the emissivity can include scattering of photons from other directions into the direction being considered.

2.4.5 Transformation relation of the emissivity

The emissivity (or emission coefficient) is a characteristic of spontaneous emission within a limited volume. Various emission processes along a ray contribute to the specific intensity. The emissivity, in principle, is angle dependent, e.g. synchrotron emission depends upon the angle between the emission direction and the magnetic field. The emissivity j_ν [J s^{-1} m^{-3} Hz^{-1} sr^{-1}] is defined by energy radiated from a volume dV in time dt in a freqency interval $d\nu$ into solid angle $d\Omega$ i.e.

$$j_\nu = \frac{dE_\nu}{dV dt d\nu d\Omega}, \tag{2.76}$$

If the emissivity is isotropic, then

$$j_\nu = \frac{1}{4\pi} P_\nu \tag{2.77}$$

where P_ν is the radiated power per unit volume. The emission may be considered to be isotropic if:

- the emission mechanism is independent of direction.
- the emission is considered as the random superposition of a number of anisotropic emitters, e.g. synchrotron emission from a tangled magnetic field.

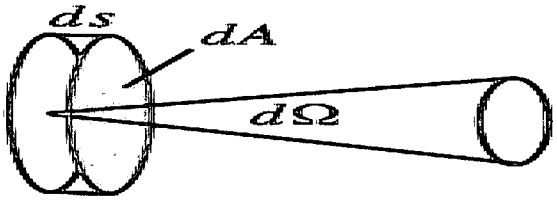

Figure 2.6: Volume element $dV = dAds$.

The energy added to the beam from emission within a volume element $dV = dAds$ is given by:

$$dE_\nu = j_\nu dV d\Omega dt d\nu = j_\nu dA ds d\Omega dt d\nu. \tag{2.78}$$

This energy is radiated into the solid angle $d\Omega$ emerging from dA and can be rewritten in terms of intensity as $dE_\nu = dI_\nu dA d\Omega dt d\nu = j_\nu dA ds d\Omega dt d\nu$. The change in specific intensity is then given by:

$$\rightarrow \frac{dI}{ds} = j_\nu. \tag{2.79}$$

Combining Equations 2.73 and 2.75 we get $\frac{S_\nu}{\nu^3} \times \nu\alpha_\nu =$ Lorentz invariant. Since the emission coefficient is defined as $j_\nu = \alpha_\nu S_\nu$, a Lorentz invariant directly related to it is

$$\frac{j_\nu}{\nu^2} = \text{Lorentz invariant}. \tag{2.80}$$

Thus a transformation relation of the emission coefficient can be written

$$\begin{aligned} j_\nu &= \left(\frac{\nu}{\nu'}\right)^2 j'_{\nu'} \\ &= \delta^2 j'_{\nu'}. \end{aligned} \tag{2.81}$$

2.4.6 Transformation relation of the flux density

The spectral flux density ($F_\nu\,[J\ s^{-1}\ Hz^{-1}\ m^{-2}]$) from a source is the power received by a detector per unit projected area and per unit frequency.

The spectral flux density from an arbitrary source is given by

$$F_\nu = \frac{1}{D^2}\int_V \delta^2 j'_{\nu'} dV = \delta^2 \frac{1}{D^2}\int_V j'_{\nu'} dV, \tag{2.82}$$

where D is the distance between source and observer and V the volume of the source. The apparent volume of the source is related to the volume in the rest frame, by

$$\Delta x'\Delta y'\Delta z' = \delta\Delta x\Delta y\Delta z \Rightarrow dV' = \delta dV, \tag{2.83}$$

in the limit[4] of $\delta \sim \gamma$.

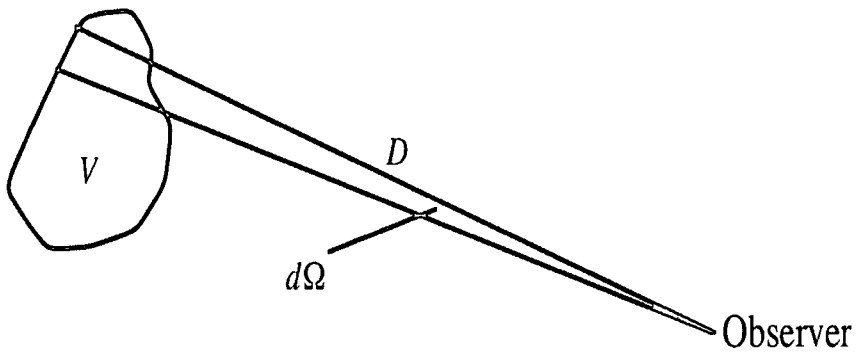

Figure 2.7: Flux from a source.

[4]From Equation 2.68 (i.e. $I \sim \delta^4 I'$), it can be established that the maximum of the observed intensity is reached for $\delta = \frac{1}{\gamma(1-\frac{v}{c}\cos\theta)}$ maximum, and this is achieved when $\theta \sim 0$ and $\beta \sim 1$ where θ is the angle between the observer and the direction of motion of the source. If $\theta \to 0$ then $\cos\theta \sim 1 - \frac{\theta^2}{2} \Leftrightarrow 1 - \cos\theta = \frac{\theta^2}{2}$. Since $\delta = \frac{1}{\gamma(1-\cos\theta)}$, we have $\delta = \frac{1}{\gamma\frac{\theta^2}{2}}$. Using Equation 2.22 i.e. $\sin\theta = \frac{1}{\gamma} \sim \theta$ (for $\gamma \gg 1$), we obtain $\delta = \frac{1}{\gamma\frac{1}{2\gamma^2}} \Rightarrow \delta = 2\gamma$.

However, in the limit of $\cos\theta = \frac{v}{c}$, $\delta = \gamma$. In fact, the Lorentz factor is defined as $\gamma = \frac{1}{\sqrt{1-\frac{v^2}{c^2}}}$. Therefore, if $\cos\theta \simeq \frac{v}{c}$, then $\delta = \dfrac{1}{\frac{1}{\sqrt{1-\frac{v^2}{c^2}}}(1-\frac{v^2}{c^2})} = \gamma$. This condition was earlier established (Equation 2.38) to explain the maximum of of apparent speed in the section of superluminal motion. It is also compatible with relativistic motions viewed at small angles.

This is the result of a factor of δ expansion in the direction of motion and no expansion in the directions perpendicular to the motion. Hence the flux density is given in terms of the rest frame parameters by:

$$F_\nu = \delta^2 \frac{1}{D^2} \int_V j'_{\nu'} dV = \delta^3 \frac{1}{D^2} \int_V j'_{\nu'} dV'.$$

For a power-law emissivity (e.g. synchrotron radiation),

$$j'_{\nu'} \sim (\nu')^{-\alpha} \text{ (and } j'_\nu \sim (\nu)^{-\alpha} \text{ likewise)}, \tag{2.84}$$

with $\nu = \delta\nu'$. This leads to

$$j'_{\nu'} = \left(\frac{\nu'}{\nu}\right)^{-\alpha} j'_\nu = \delta^\alpha j'_\nu \tag{2.85}$$

Therefore (Blandford and Konigl 1979, Georganopoulos et al. 2001)

$$\begin{aligned} F_\nu &= \delta^{3+\alpha} \tfrac{1}{D^2} \textstyle\int_V j'_\nu dV' \\ &= \delta^{3+\alpha} F'_{\nu'}. \end{aligned} \tag{2.86}$$

This gives a factor of $\delta^{3+\alpha}$ increase of flux density radiation over and above what would be measured in the rest frame at the same frequency, as much as $F_\nu = \delta^{3+\alpha} F'_{\nu'}(\nu)$, where $F_\nu(\nu)$ and $F'_{\nu'}(\nu)$ are respectively the fluxes in the observer's frame and in the rest frame. The effect of beaming is maximized for viewing angles $\theta \simeq 0°$, in which case $\delta \simeq \gamma$. This result indicates that the bulk motion of the blobs responsible for the jet emission is also relativistic.

2.5 Nonthermal radiation in blazars

The dominant radiation from blazars is of nonthermal origin, i.e. not reconcilable with "black body radiation". The multi-wavelength emission in blazars can be described satisfactorily in terms of a synchrotron self-Compton process, which justifies a brief but relevant discussion of both these processes separately. This discussion will be concluded with a brief summary of the SSC process and its implications.

2.5.1 Synchrotron radiation

2.5.1.1 Definition

The fundamental role that synchrotron radiation plays in astrophysical environments justifies a detailed discussion. Synchrotron radiation is a continuum electromagnetic radiation emitted by relativistic particles (essentially electrons in astrophysical environments) gyrating around magnetic field lines.

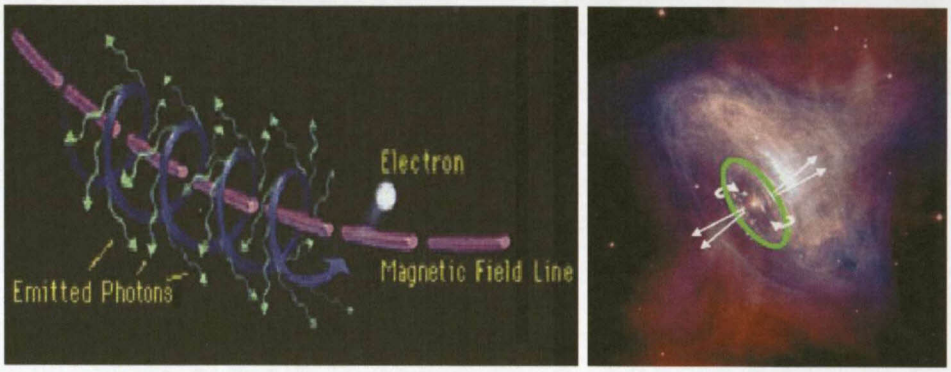

(a) (b)

Figure 2.8: (a) Graphical illustration of the synchrotron emission. Adopted from `http://imagine.gsfc.nasa.gov/docs/science/how_l2/xray_generation_el.html`. (b) X-ray image of the Crab Nebula taken by Chandra X-ray satellite. Magnetised field lines (shown by green ring) are frozen-in the magnetised plasma torus around the crab pulsar (white dot at the center). High energy electrons trapped in the plasma torus are likely to move along the circular arrows. Straight arrows indicate the rotation axis along which the pulsar wind is expected to flow. Image adopted from `http://kipac-prod.stanford.edu/pogolite/collab/CrabPulsarNebula.png`.

The force felt by a charged particle in a magnetic field is perpendicular to the direction of the field $\overrightarrow{B}$ and to the direction of the particle's velocity $\overrightarrow{v}$ (i.e. Lorentz force $\overrightarrow{f_{\rm L}} = e(\overrightarrow{v} \times \overrightarrow{B})$. The net effect of this is to cause the particle to spiral around the field. Since circular motion represents acceleration (i.e. a change in velocity), the electrons radiate photons of a characteristic energy, corresponding to the radius of the circle. For non-relativistic motion, the radiation spectrum is simple and is called "cyclotron radiation". The frequency of radiation is simply the gyration frequency, which is given in terms of the magnetic field as

$$\nu_{\rm g} = \frac{{\rm e}B}{2\pi m_{\rm e}{\rm c}} = 2.8\left(\frac{B}{1\,{\rm G}}\right)\,[{\rm MHz}], \tag{2.87}$$

where B is the field strength, e is the electric charge, m_e is the particle (electron) mass, and c is the speed of light. The situation becomes more complicated when the particle energy is relativistic (i.e. its speed approaches the speed of light). This is more common in astrophysical objects. In this case, the radiation is compressed into a small range of angles around the instantaneous velocity vector of the particle. This was explained in detail in Section 2.2.1 as relativistic beaming. Synchrotron spectra typically have a power law shape, i.e. the flux proportional to photon energy to some power, particularly when the particle distribution is also a power law. This mechanism explains the nonthermal optical and X-ray continuum emission from AGNs (Longair 1994), particularly quasars and blazars.

2.5.1.2 Synchrotron spectral emissivity

The spectral emissivity (energy emitted per unit time, per unit frequency interval and per unit of solid angle [J s^{-1} Hz^{-1} sr^{-1}], $j(\nu)$, of a single electron by synchrotron radiation is given by (Longair 1994; p. 246).

$$j(\nu) = \frac{\sqrt{3}}{8\pi^2}\frac{e^3 B \sin\theta}{\epsilon_0 cm_e} F(\frac{\nu}{\nu_c}), \tag{2.88}$$

where

$$F(x) = x\int_x^\infty K_{\frac{5}{3}}(z)dz \quad \text{with } x = \frac{\nu}{\nu_c} \tag{2.89}$$

where ν_c is the critical frequency (see details in the next section) and $K_{\frac{5}{3}}$ is the Modified Bessel function of order $\frac{5}{3}$ (Maslanka 2001). At low and high frequencies $F(x)$ is approximated by (Longair 1994; p. 248)

$$F(x) \simeq \begin{cases} \frac{4\pi}{\sqrt{3}\Gamma(\frac{1}{3})2^{\frac{1}{3}}}x^{\frac{1}{3}}, & x \ll 1, \text{ (low frequencies)} \\ \sqrt{\frac{\pi}{2}}x^{\frac{1}{2}}e^{-x}, & x \gg 1 \text{ (high frequencies)}, \end{cases} \tag{2.90}$$

where $\Gamma(z) = \int_0^\infty t^{z-1}e^{-t}\,dt$. Figure 2.9 shows the plot of the $F(x)$ using the data tabulated in Longair (1994; p248).

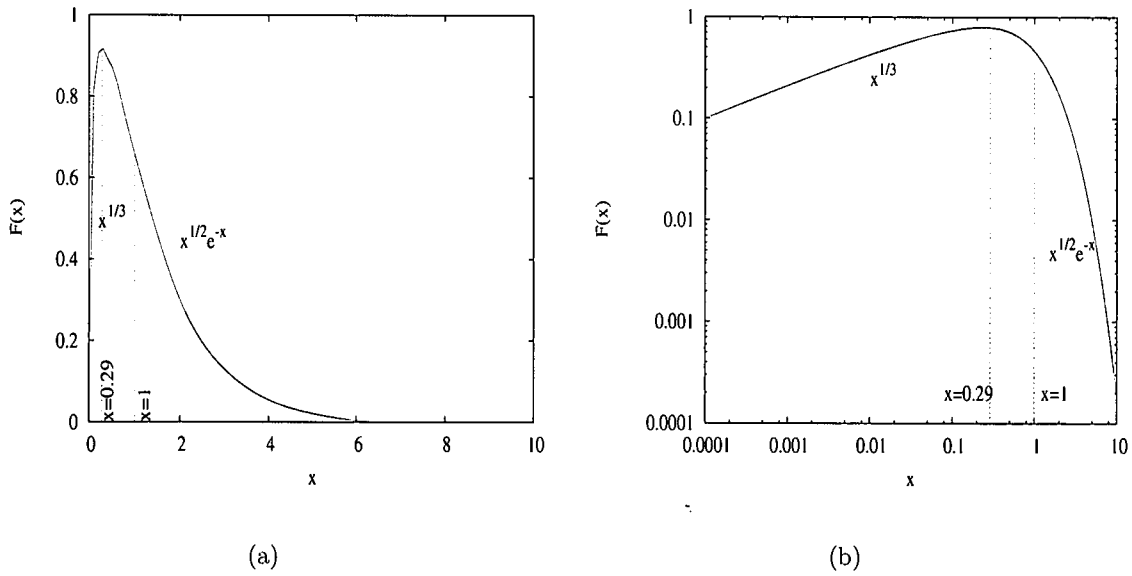

(a) (b)

Figure 2.9: Intensity of spectrum of the synchrotron radiation of a single electron (optically thin). (a) Axes in linear scale (b) Axes in logarithmic scale. The function is plotted as function of $x = \frac{\nu}{\nu_c}$. The critical frequency corresponds to $x = 1$ i.e. $\nu = \nu_c$. The peak occurs at $x = 0.29$ i.e. $\nu_{peak} = 0.29\nu_c$.

Consider the case where the electron energy distribution is a power-law, i.e.

$$dN(E) = \kappa E^{-p} dE, \tag{2.91}$$

where $dN(E)$ is the number of electrons per unit volume in the energy interval from E to $E+dE$, p is the electron spectral index and κ is the normalisation constant. Then it can be shown that the emissivity of the distribution is also a power-law[5]

$$J(\nu)[\mathrm{W\,m^{-3}\,sr^{-1}\,Hz^{-1}}] \propto B^{\frac{p+1}{2}}\nu^{\frac{-(p-1)}{2}}, \tag{2.92}$$

which depends on the spectral index (p) of the electron spectrum.

2.5.1.3 Synchrotron critical frequency

The spectrum of the synchrotron emission presents a peak of maximum synchrotron power output but vanishes at higher frequencies (Figure 2.9). There is characteristic frequency, the critical frequency ν_c, a frequency near which the synchrotron spectrum reaches the maximum and after which the spectrum decreases dramatically, given by

$$\nu_\mathrm{c} = \frac{3}{2}\gamma^2\nu_\mathrm{g}\sin\theta, \tag{2.93}$$

where θ is the pitch angle, i.e. angle between the magnetic field $\overrightarrow{B}$, and the velocity vector $\overrightarrow{v}$. Typical values of the critical frequency of synchrotron emission in blazar jets are

$$\nu_\mathrm{c} = 4.2\times10^{14}\left(\frac{\gamma}{10^4}\right)^2\left(\frac{B}{1\,\mathrm{G}}\right)\sin\theta\ \ [\mathrm{Hz}] \tag{2.94}$$

or

$$\nu_\mathrm{c} = 1.6\times10^{13}\left(\frac{E}{1\,\mathrm{GeV}}\right)^2\left(\frac{B}{1\,\mathrm{G}}\right)\sin\theta\ \ [\mathrm{Hz}], \tag{2.95}$$

where $E = \gamma \mathrm{m_e}c^2$ is the total electron energy[6].

Ghisellini et al. (1996), Tavecchio et al. (1998; 1999) show that in the observer's frame, the frequency of the peak of the synchrotron SED is given by

$$\nu_\mathrm{sync,peak} = \frac{4}{3}\nu_\mathrm{g}\gamma_\mathrm{b}^2\frac{\delta}{1+z} \tag{2.96}$$

where δ is the Doppler factor and γ_b is the Lorentz factor at the break (assuming the spectrum is modelled by a broken power-law, which is often the case for most blazars, e.g. Katarzyński et al. (2001)), and z is the cosmological redshift of the source. That is

$$\nu_\mathrm{sync,peak} = 3.7\times10^6{\gamma_\mathrm{b}}^2\left(\frac{B}{1\,\mathrm{G}}\right)\frac{\delta}{1+z} \tag{2.97}$$

[5] Note the use of the capital letter to differentiate the electron emissivity j(ν) and the emissivity of a distribution of electrons $J(\nu) = \int_0^\infty j(\nu)N(E)d(E)$ (Longair 1994)

[6] $\mathrm{m_e}c^2 = 0.511$ MeV and $E = 1$ GeV corresponds to a Lorentz factor of $\gamma \simeq 2\times10^3$

2.5.1.4 Power radiated in synchrotron radiation

The power radiated by a single electron can be obtained by integrating the emissivity over the whole spectrum interval, resulting in

$$\begin{aligned} -\tfrac{dE}{dt} &= \int_0^\infty j(\nu)d\nu \\ &= \tfrac{\sqrt{3}}{8\pi^2}\tfrac{e^3 B\sin\theta}{\epsilon_0 c m_e}\nu_c \int_0^\infty F(\tfrac{\nu}{\nu_c})d(\tfrac{\nu}{\nu_c}) \\ &= \gamma^2\beta^2\sigma_T c u_{mag}\sin^2\theta\left(\tfrac{9\sqrt{3}}{4\pi}\right)\int_0^\infty F(x)dx \text{ [Watt]}, \end{aligned} \tag{2.98}$$

where γ is the Lorentz factor, $\beta = \frac{v}{c}$, $\sigma_T = \frac{e^4}{6\pi\epsilon_0^2 m_e^2 c^4} = 6.6\times10^{-29}\,m^2$ is the Thomson scattering cross-section, $u_{mag} = \frac{B^2}{2\mu_0}$ is the magnetic energy density and θ the pitch angle.

The integral in the right-hand side of Equation 2.98 equals

$$\frac{9\sqrt{3}}{4\pi}\int_0^\infty F(x)dx = \frac{9\sqrt{3}}{4\pi}\Gamma(\frac{7}{3})\Gamma(\frac{2}{3}) = 2. \tag{2.99}$$

Thus[7], the total synchrotron power (energy per unit time) radiated by a relativistic electron is

$$-(\frac{dE}{dt}) = 2\gamma^2\,\beta^2\,\sigma_T\,c\,u_{mag}\,\sin^2\theta. \tag{2.100}$$

For an isotropic distribution of pitch angles, the average energy loss rate is then

$$< -(\tfrac{dE}{dt}) > \;=\; \tfrac{4}{3}c\sigma_T\beta^2\gamma^2 u_{mag}, \tag{2.101}$$

i.e. numerically,

$$< -(\tfrac{dE}{dt}) > \;=\; 1.058\times10^{-14}\left(\frac{B}{1\,G}\right)^2\left(\frac{\gamma}{10^4}\right)^2\beta^2 \text{ [Watt]}. \tag{2.102}$$

By using $B = \frac{\gamma m_e v}{re}$ where r is the gyro-radius and $\sigma_T = \frac{e^4}{6\pi\epsilon_0^2 m_e^2 c^4}$ is the Thomson cross-section, the above Equation (2.101) can be rewritten as

$$< -\frac{dE}{dt} >= 4\times10^9 c\,e^2\beta^4\left(\frac{E}{m_e c^2}\right)^4\frac{1}{r^2}, \tag{2.103}$$

i.e. numerically,

$$< -\frac{dE}{dt} >= 3.17\times10^{-14}\beta^4\left(\frac{m_e}{m}\right)^4\left(\frac{E}{1\,GeV}\right)^4\left(\frac{1}{[\frac{r}{1\,km}]^2}\right) \text{ [Watt]}. \tag{2.104}$$

Equations 2.102 and 2.104 can be interpreted as follows:

[7]The expression of the synchrotron power can also simply be obtained by using the basic principle of radiation in electrodynamics based on the Larmor Formula. Further details can be found in Longair (1994; p. 231).

- The energy loss is proportional to $\frac{1}{m^4}$ suggesting that low-mass particles, such as electrons and positrons, emit synchrotron radiation much more efficiently. An electron with a mass m_e almost 2000 times smaller than the proton radiates 16×10^{12} times more than a proton with the same energy. In astrophysical environments, synchrotron emission from protons will be neglected. This justifies the use of electrons (instead of any charge particle) in the equations describing the phenomenon.

- As the synchrotron radiation results from the interaction between particles and magnetic field, it is clear that a higher electron energy, E_e, or a stronger magnetic field, B, increases the generated photon energy production rate (Equation 2.101).

- The energy loss is inversely proportional to the gyro-radius squared, suggesting that the particles gyrating close to the magnetic field lines radiate more energy than the particles gyrating far from the magnetic field lines.

- The energy loss is proportional to the fourth power of the particle energy suggesting that energetic particles radiate faster than low-energy particles, explaining the cut-off of the synchrotron spectrum at high energy.

2.5.1.5 Synchrotron flux density

Equation 2.92 shows that for a power-law electron energy distribution, the spectral emissivity is also a power-law of the frequency. That is the same case as for the absorption coefficient[8] (Longair 1994; p. 262):

$$\alpha_\nu[\mathrm{m}^{-1}] \propto B^{\frac{p+2}{2}} \nu^{-\frac{(p+4)}{2}}. \tag{2.105}$$

The radiative transfer equation is written as

$$\frac{dI_\nu}{dx} = -\alpha_\nu I_\nu + j_\nu, \tag{2.106}$$

where dx is the element of length and I_ν [J s^{-1} m^{-2} sr^{-1} Hz^{-1}] is the intensity of the source. By dividing the two sides by α_ν, it follows that

$$\begin{aligned} &\Rightarrow \ \frac{dI_\nu}{\alpha_\nu dx} = -I_\nu + \frac{j_\nu}{\alpha_\nu} \\ &\Rightarrow \ \frac{dI_\nu}{d\tau_\nu} = -I_\nu + s_\nu \quad \text{where } d\tau_\nu = \alpha_\nu dx \text{ is the optical depth element} \\ &\Rightarrow \ \frac{dI_\nu}{d\tau_\nu} + I_\nu = s_\nu. \end{aligned} \tag{2.107}$$

This equation is solved by multiplying the integrating factor e^{τ_ν} on both sides. The solution is written

$$I_\nu = I_\nu(0)e^{-\tau_\nu} + \int_0^{\tau_\nu} e^{-(\tau_\nu - \tau'_\nu)} s_\nu(\tau'_\nu) d\tau'_\nu. \tag{2.108}$$

[8] A measure of the attenuation caused by absorption of energy that results from its passage through a medium; expressed in units of reciprocal distance.

The first term on the right-hand side ($I_\nu(0)e^{-\tau_\nu}$) describes the background radiation (from outside the emitting blobs) attenuated by absorption within the medium. The second term on the right-hand side ($\int_0^{\tau_\nu} e^{-(\tau_\nu-\tau'_\nu)}s_\nu(\tau'_\nu)d\tau'_\nu$) describes the spontaneous contribution of the medium to the emergent brightness. Note that the emission from the medium is also absorbed by the medium as it attempts to escape from it.

Assuming the source function is independent of the optical depth, Equation 2.107 becomes

$$\begin{aligned} I_\nu &= s_\nu e^{-(\tau_\nu-\tau'_\nu)}]_0^{\tau_\nu} \\ \Rightarrow I_\nu &= s_\nu[1-e^{-\tau_\nu}]. \end{aligned} \tag{2.109}$$

From Equation 2.109, the following results can be obtained

- For the optically thick case ($\tau_\nu \gg 1 \Rightarrow e^{-\tau_\nu} \ll 1$),

$$I_\nu \simeq s_\nu \propto \nu^{\frac{5}{2}}. \tag{2.110}$$

- For the optically thin case ($\tau_\nu \ll 1 \Rightarrow 1-e^{-\tau_\nu} \simeq \tau_\nu$),

$$I_\nu \simeq \tau_\nu s_\nu \propto j_\nu \propto \nu^{\frac{-(p-1)}{2}}. \tag{2.111}$$

The flux density can be deduced from the intensity using the following relation

$$F_\nu = \int_\Omega I_\nu d\Omega. \tag{2.112}$$

If the electron distribution is a power-law, then the flux is also a power-law

$$F_\nu \propto \begin{cases} \nu^{\frac{5}{2}} & \text{for optically thick} \\ \nu^{-\alpha} & \text{for optically thin,} \end{cases} \tag{2.113}$$

where the spectral index $\alpha = \frac{p-1}{2}$, with p representing the electron spectral index. That is, in the observer's frame (Equation 2.86 corrected for cosmic expansion),

$$F_{\nu_{\rm obs}} \propto \begin{cases} \delta^{3-\frac{5}{2}}(1+z)\nu^{\frac{5}{2}} & \text{for optically thick} \\ \delta^{3+\alpha}(1+z)\nu^{-\alpha} & \text{for optically thin.} \end{cases} \tag{2.114}$$

Figure 2.10 summarises the spectral regimes in synchrotron spectrum.

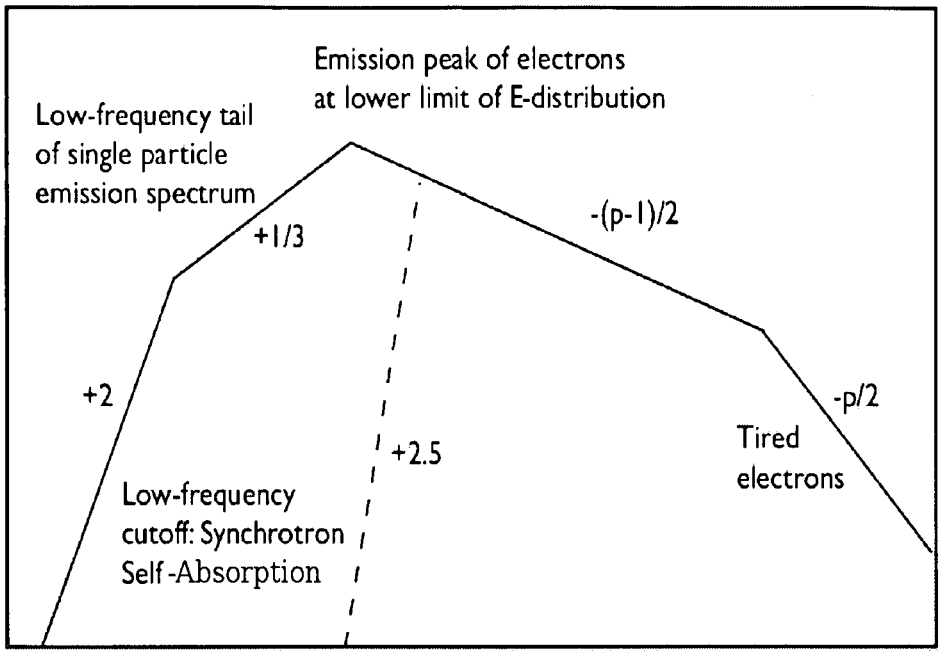

Figure 2.10: Spectral regimes in synchrotron spectrum.

Equation 2.114 already shows the importance of the electron spectral index in modelling the optically thin component of the synchrotron spectrum. In fact, the spectral shape of the synchrotron spectrum is determined by the shape of the electron energy spectrum rather than by the shape of the emission spectrum of a single particle, as it was described in Section 2.5.1.2. In the optically thick regime, photons created by synchrotron emission are self-absorbed up to a frequency where the plasma becomes optically thin. The frequency of the turnover, ν_t, depends on the plasma parameters. This thesis will mostly be concerned with synchrotron radiation from optically thin emission from blazar jets for which ν_t is expected in IR to X-rays. Synchrotron radiation from a population of electrons is commonly used to explain observed radio and X-ray spectra in blazars. Even though it is possible to produce gamma-rays through synchrotron radiation it is less favourable in blazars because of the large magnetic field strength (typical neutron star magnetospheres) required. The synchrotron peak frequency of typical very high energy HBLs ranges between 10^{17} Hz and 10^{19} Hz. Figure 2.11 shows that with the blazar magnetic field ranging from about 1μ G, to about 1 G, the peak frequency of the synchrotron emission responsible for the inverse Compton emission peaking at around 1 TeV is less 10^{17} Hz.

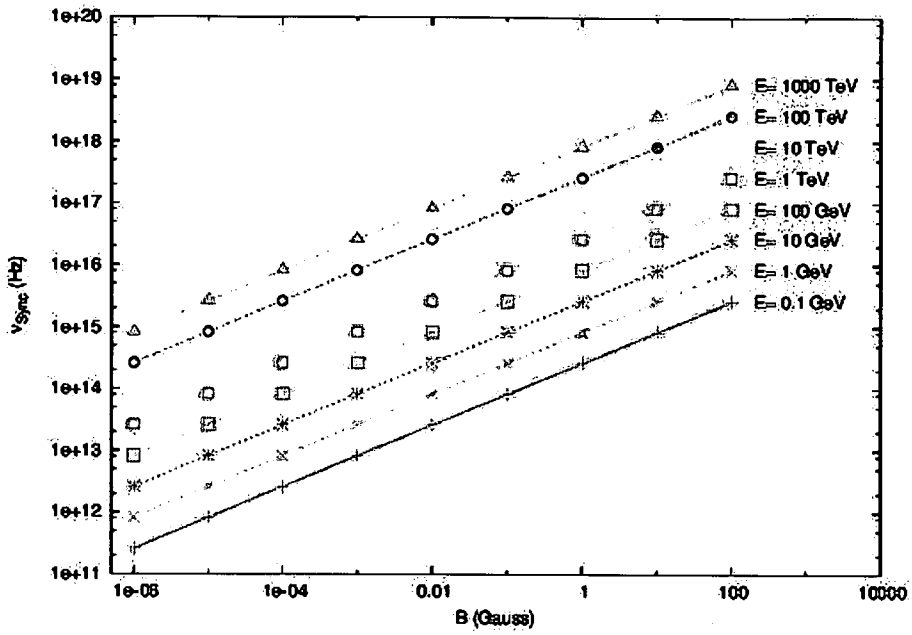

Figure 2.11: Synchrotron peak frequency as a function of magnetic field for different expected peak of the inverse Compton γ-ray photon energies.

2.5.2 Synchrotron electron cooling

The question here is to estimate the time that an electron spends in orbit before a half of its kinetic energy is radiated. In The rate of energy loss by an electron through synchrotron process (i.e. Equation 2.100 with $u_{\rm mag} = \frac{B^2}{2\mu_0}$), is

$$\frac{dE}{dt} = -c\sigma_T \frac{B^2}{\mu_0} \sin^2\theta\gamma^2. \tag{2.115}$$

Since $E = \gamma m_e c^2$, the rate of change of Lorentz factor is

$$\frac{d\gamma}{dt} = \frac{1}{m_e c^2}\frac{dE}{dt} = -\left(\frac{\sigma_T}{m_e c}\right)\left(\frac{B^2}{\mu_0}\right)\gamma^2 \sin^2\theta. \tag{2.116}$$

This equation can be put in the form

$$-\frac{1}{\gamma^2}\frac{d\gamma}{dt} = \left(\frac{\sigma_T}{m_e c}\right)\left(\frac{B^2}{\mu_0}\right)\sin^2\theta. \tag{2.117}$$

Let γ_0 be the value of γ at $t = 0$, assuming that B and θ remain constant during the time t, then

$$\frac{\gamma}{\gamma_0} = \frac{1}{1 + \left[\gamma_0\left(\frac{\sigma_T}{m_e c}\right)\left(\frac{B^2}{\mu_0}\right)\sin^2\theta\right]t} \tag{2.118}$$

The synchrotron cooling time ($t_{\rm sync}$) is the time before an electron spending a half of its total energy, i.e. $\gamma = \frac{1}{2}\gamma_0$. It can be shown that

$$t_{\rm sync} = \left(\frac{m_{\rm e}c}{\sigma_{\rm T}}\right)\left(\frac{B^2\sin^2\theta}{\mu_0}\right)^{-1}\gamma_0^{-1} \tag{2.119}$$

Equation 2.119 shows that

- $t_{\rm sync}$ decreases with increasing γ_0 - higher energy electrons cool faster.
- $t_{\rm sync}$ decreases with increasing magnetic field.

Typical values in the blazar jets can be $B \sim 0.2$ G (Stecker et al. 1996), $\gamma_0 = 10^4$. Numerical values of other parameters in the above equation are $m_{\rm e} = 9.1 \times 10^{-31}$ kg, $c = 3 \times 10^8$ m/s, $\sigma_{\rm T} = 6.65 \times 10^{-29}$ m^{-2} and $\mu_0 = 4\pi \times 10^{-7}$ S.I. units. Thus,

$$t_{\rm sync} = 1.3 \times 10^6\left(\frac{B}{0.2\,{\rm G}}\right)^{-1}\left(\frac{\gamma_0}{10^4}\right)^{-1}(\sin^2\theta)^{-1}[{\rm s}]. \tag{2.120}$$

This may be the timescale associated with variability in blazar jets, unless continuous injection and acceleration replenishes the electron population. Estimates of the ages of elliptical galaxies, which are believed to be the host of blazars, exceed 10^9 years (Chiosi et al. 1994) suggesting a strong need to continuously re-energise particles in the blazar jets. This introduces the need for particle acceleration as discussed in Section 2.1.

2.5.3 Inverse Compton scattering

2.5.3.1 Definition

The inverse Compton scattering process is one of the most important processes in high-energy astrophysics. In this process high-energy electrons scatter low-energy photons to high energy. In this case, the photons gain and the electrons lose energy (Figure 2.12).

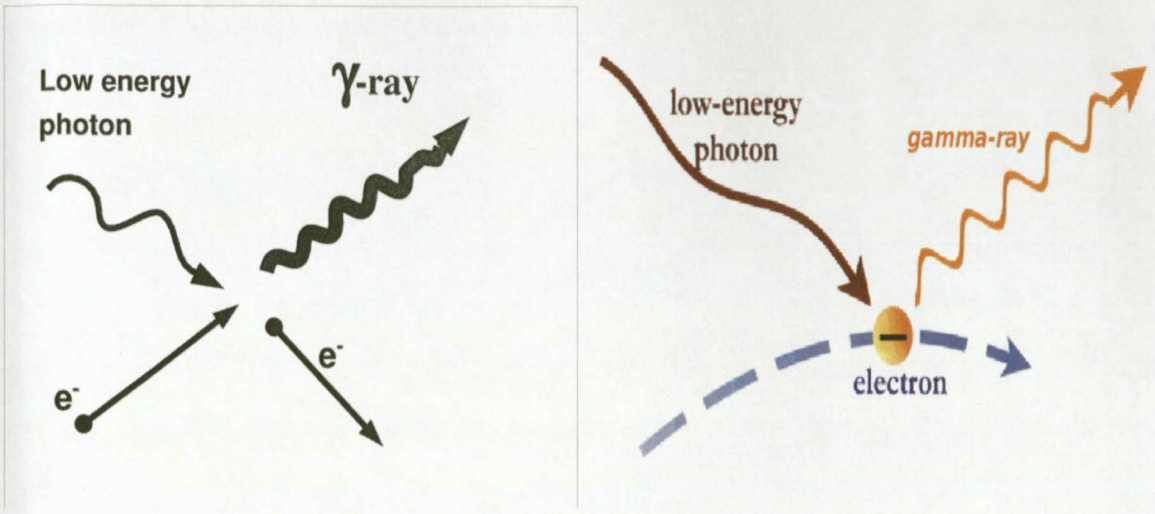

Figure 2.12: Inverse Compton scattering.

This is in contrast to Compton scattering where electrons are upscattered by high energy photons, resulting in photons losing energy.

2.5.3.2 Power radiated in inverse Compton scattering

Consider the collision between a photon and a relativistic electron in the laboratory frame of reference (S) and in the rest frame of the electron (S′) (Figure 2.13).

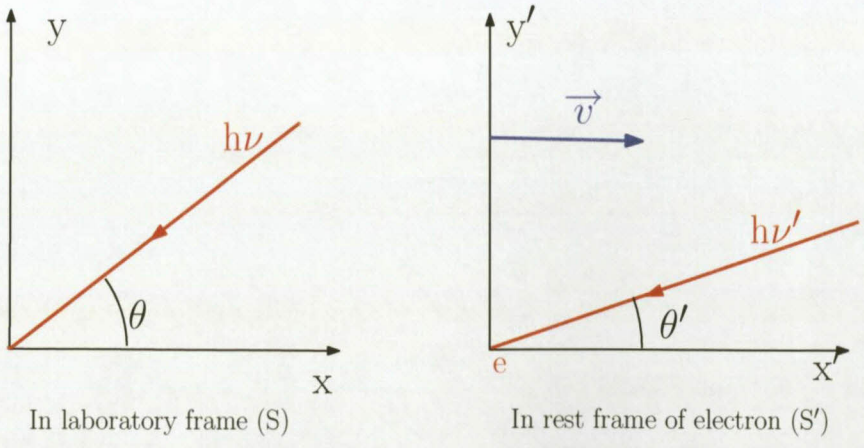

Figure 2.13: The geometry of inverse Compton scattering in the laboratory frame of reference (S) and in the electron rest frame (S′).

The most effective energy transfer in the inverse Compton scattering occurs in the limit

(Thomson scattering condition e.g Longair 1994; p. 99)

$$\frac{h\nu'}{m_e c^2} = \frac{\gamma h\nu}{m_e c^2} \ll 1, \tag{2.121}$$

where the primed and unprimed quantities are measured in the frame (S′) and (S) respectively.

If the energy of the photon is $h\nu$ and the angle of incidence θ in (S), its energy in the frame (S′) is (e.g. Equation 2.27)

$$\epsilon' = \epsilon\,\gamma(1 - \frac{v}{c}\cos\theta). \tag{2.122}$$

In the Thomson scattering regime, i.e. $h\nu' \ll m_e c^2$, the energy loss rate of the electron in (S′) is just the rate at which the energy is reradiated by the electron, i.e.

$$-(\frac{dE}{dt})' = \sigma_T c u'_{\rm rad}, \tag{2.123}$$

with $\sigma_{\rm T}$ the Thomson scattering cross section representing the probability of the scattering and

$$u'_{\rm rad} = \int \epsilon' f'(\epsilon') d\epsilon' \tag{2.124}$$

is the energy density of radiation in the rest frame of the electron, where ϵ' and $f'(\epsilon')d\epsilon'$ are the energy and the number density of incident photons in (S') (e.g. Rybicki and Lightman (2004)).

The function f, which is a Lorentz invariant, i.e. $f'(\epsilon') = f(\epsilon)$, was introduced in Section 2.4.2 representing the particle's density in phase space, given by

$$f(p) = \frac{dN(p)}{d^3x d^3p}. \tag{2.125}$$

Since the energy is related to the momentum by $\epsilon = \dfrac{p^2}{2m}$, then the above function can be expressed in terms of energy ϵ, i.e.

$$f(\epsilon) = \frac{dN(\epsilon)}{d^3x d\epsilon} = \frac{dn(\epsilon)}{d\epsilon}. \tag{2.126}$$

It has been shown earlier that $\dfrac{dE'}{dt'}$ is invariant, i.e. $\dfrac{dE'}{dt'} = \dfrac{dE}{dt}$. Therefore, the emitted power measured in the laboratory frame (S) is

$$\frac{dE}{dt} = c\sigma_{\rm T} \int \epsilon' f'(\epsilon') d\epsilon', \tag{2.127}$$

which can be rewritten as

$$\frac{dE}{dt} = c\sigma_{\rm T} \int \epsilon'^2 f(\epsilon') \frac{d\epsilon'}{\epsilon'}. \tag{2.128}$$

However, $f(\epsilon)\frac{d\epsilon}{\epsilon}$ is invariant. It was mentioned earlier, f is a Lorentz invariant, i.e. $f(\epsilon) = f'(\epsilon')$. Since $\epsilon = \gamma\epsilon'$ and $d\epsilon = \gamma d\epsilon'$, it follows that

$$\begin{aligned} f(\epsilon)\frac{d\epsilon}{\epsilon} &= f'(\epsilon')\frac{\gamma d\epsilon'}{\gamma\epsilon'} \\ &= f'(\epsilon')\frac{d\epsilon'}{\epsilon'}. \end{aligned} \tag{2.129}$$

Substituting Equation 2.129 into Equation 2.128, then

$$\frac{dE}{dt} = c\sigma_{\rm T}\int \epsilon'^2 f(\epsilon)\tfrac{d\epsilon}{\epsilon}. \tag{2.130}$$

Now since $\epsilon' = \epsilon\gamma(1-\beta\cos\theta)$, Equation 2.130 becomes

$$\frac{dE}{dt} = c\sigma_{\rm T}\int \gamma^2\,(1-\beta\cos\theta)^2\epsilon\, f(\epsilon)d\epsilon, \tag{2.131}$$

which depends only on quantities in the frame (S).

This power radiated is associated with the photons incident at an angle θ in the same frame (S) and consequently arrive within solid angle $2\pi\sin\theta d\theta$. Assuming that the radiation field in (S) is isotropic, the average power emitted by the electron in (S′) is obtained by averaging over solid angle in (S), i.e.

$$\tfrac{dE}{dt} = c\sigma_{\rm T}\gamma^2\langle(1-\beta\cos\theta)^2\rangle\int \epsilon f(\epsilon)d\epsilon. \tag{2.132}$$

where $\langle(1-\beta\cos\theta)^2\rangle = \dfrac{\int_0^\pi[1-\frac{v}{c}\cos\theta]^2 2\pi\sin\theta d\theta}{4\pi} = 1+\frac{1}{3}\beta^2$. It can be shown that $\gamma^2(1+\frac{1}{3}\beta^2) = \frac{4}{3}(\gamma^2-\frac{1}{4})$. Thus Equation 2.132 becomes

$$\frac{dE}{dt} = \frac{4}{3}c\,\sigma_{\rm T}\,u_{\rm rad}(\gamma^2-\frac{1}{4}), \tag{2.133}$$

with $u_{\rm rad} = \int \epsilon f(\epsilon)d\epsilon$.

This equation gives the energy gained by the photon field due to the scattering of low-energy photons. We therefore have to substract the energy of these photons to find the total energy gain to the photon field in (S). The rate at which energy is removed from the low-energy photon field is just $\sigma_{\rm T}\,c\,u_{\rm rad}$ and therefore, substracting, then

$$\begin{aligned} \frac{dE}{dt} &= \tfrac{4}{3}\sigma_T\,c\,u_{\rm rad}\,(\gamma^2-\tfrac{1}{4}) - \sigma_{\rm T}\,c\,u_{\rm rad} \\ &= \tfrac{4}{3}\sigma_{\rm T}\,c\,u_{\rm rad}\,(\gamma^2-1). \end{aligned} \tag{2.134}$$

The identity $\gamma^2 - 1 = \left(\frac{v}{c}\right)^2\gamma^2$ is now used to get the final form of the energy loss rate:

$$\frac{dE}{dt} = \frac{4}{3}\sigma_T \, c \, u_{\rm rad} \left(\frac{v}{c}\right)^2\gamma^2. \tag{2.135}$$

The number of photons scattered per unit time is just

$$\frac{\sigma_{\rm T} \, c \, u_{\rm rad}}{h\nu_0}, \tag{2.136}$$

and hence the average energy of the scattered photons is just

$$h\nu \simeq \frac{4}{3}\gamma^2 h\nu_0. \tag{2.137}$$

The factor γ^2 is interpreted as a result of the gain factor due to the transformation from one frame to another frame during the steps followed to compute the power. In fact, the photon energy is boosted by a factor of γ during transformation to the rest frame, i.e. $h\nu' = \gamma h\nu(1 - \beta\cos\theta)$ and again it is boosted further by the same factor γ when transforming the energy of the scattered photon back to the lab frame.

A correction factor for the cosmological expansion gives

$$\nu_{\rm IC} \simeq \frac{4}{3}\gamma^2\nu_0\frac{1}{1+z}. \tag{2.138}$$

This result makes the inverse Compton scattering process an important radiative mechanism in high energy γ-ray astrophysics. In fact, in AGNs, electrons are accelerated relativistically in an electromagnetic field such that the Lorentz factor reaches $10^3 - 10^4$. In these conditions, low-energy optical/UV photons are up-scattered to MeV – GeV γ-rays.

Equation 2.135 is similar to Equation 2.101 already obtained for the synchrotron power. This similarity is explained by considering the fact that both synchrotron radiation and inverse Compton radiation originate from the acceleration of the electron by an electric field. In fact, for synchrotron radiation, the electric field is due to the motion of electrons through the magnetic field, whereas for inverse Compton scattering the electric field comes from electromagnetic waves (photons) incident on the electron. Therefore

$$\frac{< -\frac{dE}{dt} >_{\rm IC}}{< -\frac{dE}{dt} >_{\rm sync}} = \frac{\frac{4}{3}\sigma_{\rm T}c\gamma^2\beta^2 u_{\rm rad}}{\frac{4}{3}\sigma_{\rm T}c\gamma^2\beta^2 u_{\rm B}} = \frac{u_{\rm rad}}{u_{\rm B}}. \tag{2.139}$$

The radiation losses due to synchrotron radiation and inverse Compton radiation are in the same ratio as the magnetic energy density and photon energy density, as long as the Thomson approximation ($\gamma h\nu \ll m_e c^2$) in the electron rest frame remains valid. This underlines the importance of the inverse Compton scattering for the electrons.

For $\gamma h\nu \gg m_e c^2$, most of the electron energy is transferred into scattered radiation with

$$E_\gamma \approx \gamma m_e c^2. \tag{2.140}$$

In this case[9], the Thompson cross-section in Equation 2.135 is replaced by the Klein-Nishina cross-section, given by

$$\sigma_{KN} = \frac{3}{8}\sigma_T \frac{1}{x}(\ln 2x + \frac{1}{2}), \tag{2.141}$$

where $x = \frac{h\nu}{m_e c^2}$, in which case the highest photon energies attainable are limited by the energy of the electrons. Several sources of seed photons may contribute significantly to the observed X-ray and gamma-ray flux produced by the inverse Compton scenario. Among the possible sources are synchrotron photons produced locally inside the jet and external photons, i.e. produced outside. The inverse Compton scattering of these types of seed photons leads to the synchrotron self-Compton (SSC) emission and to the external Compton emission (EC) respectively. These two components are described in the next subsections.

2.5.3.3 Synchrotron self-Compton (SSC)

When a photon produced in the jet by electrons through synchrotron radiation acts as a seed photon for the inverse Compton scattering, the process is called synchrotron self-Compton scattering (SSC). Equations governing the physics of the phenomena are the same as in the above paragraph 2.5.3.1. In the Thomson limit of SSC emission, the emitted frequency ν_{SSC} is related to the frequency of the incident synchrotron photon ν_{sync} by

$$\nu_{SSC} = \frac{4}{3}\nu_{sync}\gamma^2. \tag{2.142}$$

In the observer's reference frame

$$\nu_{SSC-peak} \simeq \frac{4}{3}\gamma_b^2 \nu_{sync-peak}, \tag{2.143}$$

where $\nu_{sync-peak}$ is the synchrotron peak frequency, defined in Equation 2.96. Therefore, if the frequencies of the two peaks $\nu_{sync-peak}$ and $\nu_{SSC-peak}$ are determined from observations, the energy of the electrons contributing most to the power output can be evaluated by

$$\gamma_b = \left(\frac{3}{4}\frac{\nu_{SSC-peak}}{\nu_{sync-peak}}\right)^{\frac{1}{2}}. \tag{2.144}$$

[9]The same applies when $\gamma h\nu \approx m_e c^2$. In this case $x = \frac{\gamma h\nu}{m_e c^2}$.

Using the relation (2.97), it follows that

$$B\delta \simeq (1+z)\frac{{\nu_{\rm sync-peak}}^2}{2.8\times 10^6 \nu_{\rm SSC,peak}}. \tag{2.145}$$

The last relation shows that for fixed $\nu_{\rm sync-peak}$ and $\nu_{\rm SSC,peak}$ B and δ are inversely proportional. Assuming a typical $\delta = 10$, one can estimate B by

$$B \simeq \frac{1}{28}\left(\frac{\nu_{\rm sync-peak}}{10^{14}\,{\rm Hz}}\right)^2\left(\frac{\nu_{\rm SSC-peak}}{10^{22}\,{\rm Hz}}\right)^{-1}\,[{\rm G}] \tag{2.146}$$

Due to the fact that the population of electrons which gives rise to synchrotron radiation is the same as that interacting with the emitted synchrotron radiation through inverse Compton scattering, i.e. the synchrotron self-Compton is the inverse Compton scattering of the synchrotron radiation, the full spectral energy distribution (SED) will therefore feature two distinct peaks (Figure 2.14), both very similar-one for synchrotron (Radio-UV or in some cases up to X-ray band) and another for the inverse Compton scattering (in γ-ray band). The SSC model successfully fits most of the observed spectral energy distributions of blazars, particularly the BL Lacs objects.

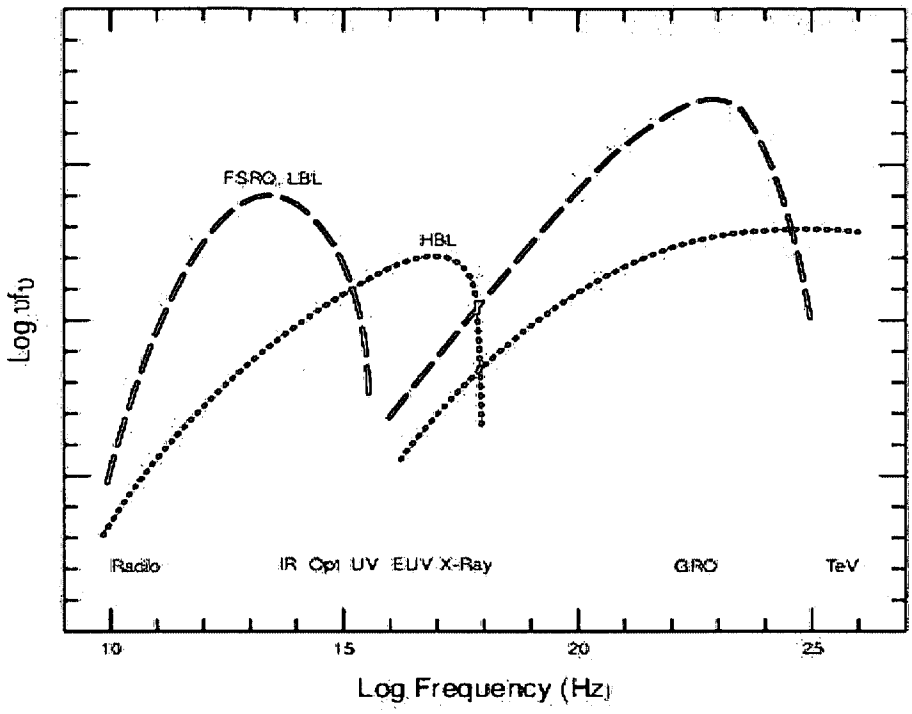

Figure 2.14: Spectral Energy Distribution of synchrotron-Compton blazars (adopted from Urry (1998)). Both in HBL and in FSRQs-LBLs, the Spectral Energy Distributions are double peaked. The first peak (located in IR-Opt for FSRQs-LBLs and in X-rays in HBLs) is the signature of the synchrotron emission from electrons in magnetic field while the second peak located in γ-ray band is interpreted as the signature on the inverse Compton process between synchrotron produced photons and electrons in the jet.

2.5.3.4 External Compton scattering (EC)

Apart from the case of synchrotron self-Compton emission from incident photons originating from the jet, several external low-energy photons can interact with relativistic particles of the jet by the inverse-Compton mechanism, a process referred to as External Compton scattering (EC). In blazars, low-energy seed photons can be (e.g. Figure 2.15):

- photons coming directly from the disk such as X-ray photons coming from the corona (Dermer et al. 1992),
- photons coming indirectly from the disk, i.e. disk photons which have been reprocessed in clouds producing the broad emission lines, and disk photons which have been absorbed and thereafter thermally re-radiated by dust. Both types of photons are
  - Optical-UV photons from recombination in the Broad Line Region excited by the disk radiation (Sikora et al. 1994a),

– IR photons coming from dust heated by the core of the AGN. In fact, the dust in the inner portions of the torus facing the central continuum source is heated to a temperature $T \simeq 1000$ K and emits infrared radiation roughly as a blackbody (Sokolov and Marscher 2005).

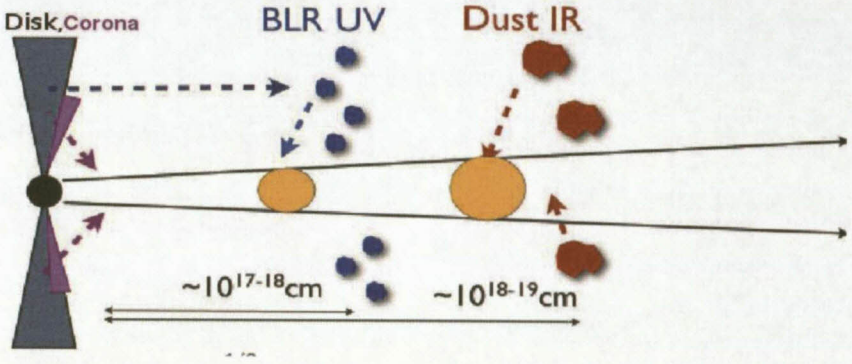

Figure 2.15: Origin of external Compton photons.

Depending on the origin of the external photons, the external Compton radiation is sudivided into two types:

- the External Comptonisation of direct Disk radiation (ECD) and,
- the External Comptonisation of radiation from Clouds (ECC) including the thermal re-radiation by hot dust.

Figure 2.16 illustrates all the different radiation components including ECD and ECC contributing to the jet radiation in the so-called leptonic model, i.e. involving the electrons (leptons) as opposed to hadronic models, i.e. involving the proton-proton (hadrons) interactions as well as their different relative contribution to the SED.

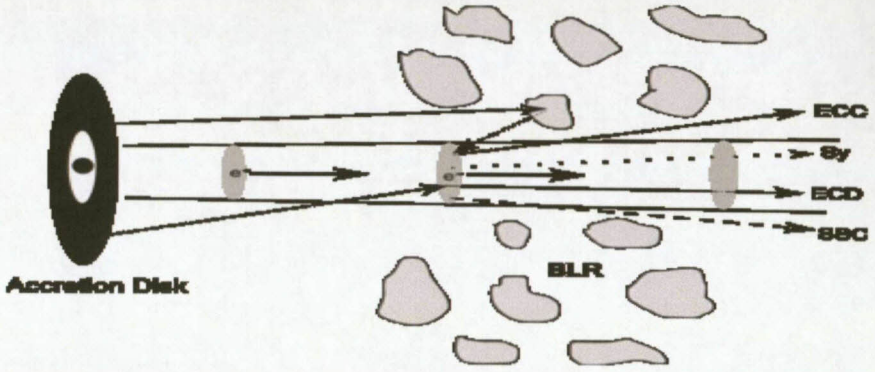

(a)

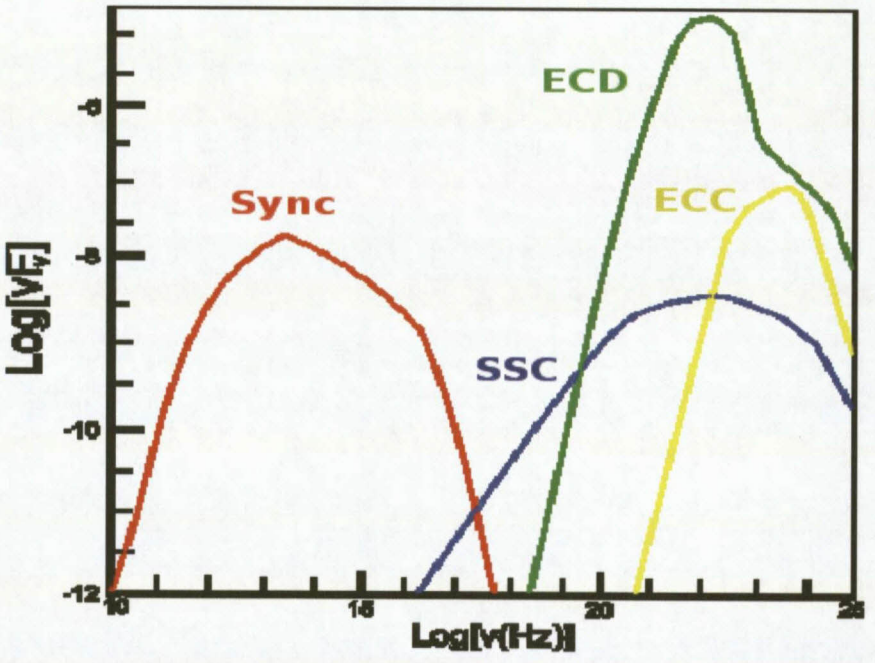

(b)

Figure 2.16: (a) Leptonic jet model geometry for blazar emission. Electrons are accelerated to relativistic speeds in the jet and emit photons through a variety of high-energy radiative processes, including synchrotron and inverse Compton emission, which involve photon and gas fields surrounding the accretion disk. Adopted from (Böttcher 2002). (b) Blazar spectral energy distribution (SED) of the leptonic jet model. Four different components are represented: Synchrotron emission (Sy) in red, synchrotron self-Compton (SSC) emission in blue, External Comptonisation of Direct disk radiation (ECD) in green, and External Comptonisation of radiation from the clouds (ECC) in yellow. Adopted from `http://large.stanford.edu/courses/2008/ph204/eclov1/`.

Depending on the details of geometry and kinematics in FSRQs jets, the radiation from the inverse Compton interaction will be dominated by either the SCC (formed by the direct

radiation field from the central jet flow) or the external Compton radiation (ECD and ECC), since the Broad Line Region is assumed to be bright, while in BL Lacs it is believed that the SSC is strongly beamed so that it swamps the disk radiation leading to the faint BLR region (see illustration in Figure 2.17).

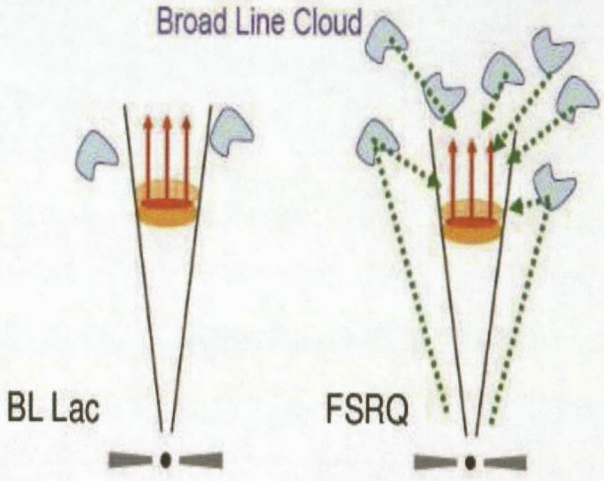

Figure 2.17: Graphical illustration of different contributions of radiation in blazars. In BL Lacs the accretion disc and the Broad Line Region are faint. The high energy γ-ray photons are produced via the synchrotron self-Compton process. In FSRQs, the accretion disc is bright and a fraction of its photons are scattered off the BLR into the jet. Both the synchrotron self-Compton and the External Compton contribute to the production of the high energy γ-ray photons.

Consider an isotropic distribution of ambient photons of frequency ν_0. These photons will be boosted in the blob frame to

$$\nu_0{}' = \delta' \nu_0, \tag{2.147}$$

where δ' is the Lorentz factor related to the motion of the blob frame with respect to the external plasma frame (where the photon is coming from). The scattering of the above-mentionned photons, by relativistic electrons in the jet of energy γ_b will produce γ-rays at the observed frequency

$$\nu_{\rm EC} = \frac{4}{3}{\gamma_{\rm b}}^2 \delta' \nu_0 \frac{\delta}{1+z}. \tag{2.148}$$

It can be shown that Equations 2.148 and 2.96 lead to the the ratio

$$\frac{\nu_{\rm EC-peak}}{\nu_{\rm sync-peak}} = \frac{\delta' \nu_0}{2.8\, B}, \tag{2.149}$$

which in this case yields (Ghisellini et al. 1996)

$$B = 3.6 \times 10^8 \delta' \left(\frac{\nu_{\rm sync-peak}}{\nu_{\rm EC-peak}}\right)\left(\frac{\nu_0}{10^{15}}\right)[\rm G]. \tag{2.150}$$

Since $\nu_0\delta'\delta$ is different from $\nu_{\rm sync,peak}$ (usually larger than $\nu_{\rm sync}$, and typical values for ν_0 are 10^{15} Hz, since the external radiation in FSRQs is dominated by the UV radiation of the accretion disk, and 10 for δ' and δ), the two scenarios (SSC and EC) imply different values of γ and B. That is for the same observed spectrum, an interpretation of the gamma-ray peak with an SSC model yields a higher electron energy and lower magnetic field than for the EC model. The differences disappear when $\nu_{\rm sync,peak} \simeq \nu_0\delta'\delta$, that is for $\nu_{\rm sync,peak} \simeq 10^{17}$ Hz.

The electron energy loss rate due to the external Comptonisation is given by (e.g. Sikora et al. (1997))

$$\frac{dE}{dt} \simeq \frac{16}{9}\sigma_{\rm T}\gamma^2\delta'^2 u_{\rm D}, \tag{2.151}$$

where δ' is the bulk Lorentz factor, γ is the random electron Lorentz factor and $u_{\rm D} = \frac{\zeta L_{UV}}{4\pi r^2 c}$ is the energy density of an external diffuse radiation field, where $L_{\rm UV}$ is the luminosity of the central source which in FSQRs, and in quasars in general, is dominated by Ultra-Violet (UV) radiation of an accretion disk, and ζ is the fraction of UV radiation, which at a given distance r contributes to the diffuse (isotropized by reprocessing and rescattering) radiation field. For FSRQs the fraction ζ is expected to be $\sim$ 0.01–0.1.

The discussion presented in this section was aimed at introducing the reader to some of the most basic aspects of radiation applicable to these sources. This will also aid in providing a theoretical framework to evaluate some of the model calculations that will be introduced in later chapters.

Chapter 3

Unidentified *EGRET* Blazar Candidates

EGRET detected 271 gamma-ray sources emitting high-energy γ-ray photons above 100 MeV. From the first sample of 101 *EGRET* sources initially identified, 92% of them belong to the class of blazars[1]. Efforts to identify more *EGRET* sources continued and up to now about 131 remain unidentified, i.e. not associated with any known sources in other wavelengths. Based on similarities with blazar properties, a sample of 13 high latitude extragalactic radio sources has been selected in the unidentified *EGRET* error boxes for further characterisation. In this section, a brief overview of the *Compton Gamma-Ray Observatory* with emphasis on the *EGRET* telescope and its detector is given. The selection criteria employed to isolate possible blazars from the Unidentified *EGRET* sources for further study are briefly discussed and finally gamma-ray and radio properties of the selected sources are presented.

3.1 A brief summary of the *EGRET* γ-ray telescope

3.1.1 The *Compton Gamma-Ray Observatory* (*CGRO*)

NASA's *CGRO* satellite was launched on 5 April 1991. After almost 10 years of service, it was de-orbited and it re-entered the Earth atmosphere on 4 June 2000. *CGRO* incorporated the following four different instruments designed to be sensitive to gamma-rays from 20 keV to about 30 GeV:

- the *Burst And Transient Source Experiment (BATSE)*: 20 keV–1 GeV),
- the *Oriented Scintillation Spectrometer Experiment (OSSE)*: 50 keV–10 MeV),
- the *Imaging Compton Telescope (COMPTEL)*: 1–30 MeV) and
- the *Energetic Gamma-Ray Experiment Telescope EGRET*: 20 MeV–30 GeV).

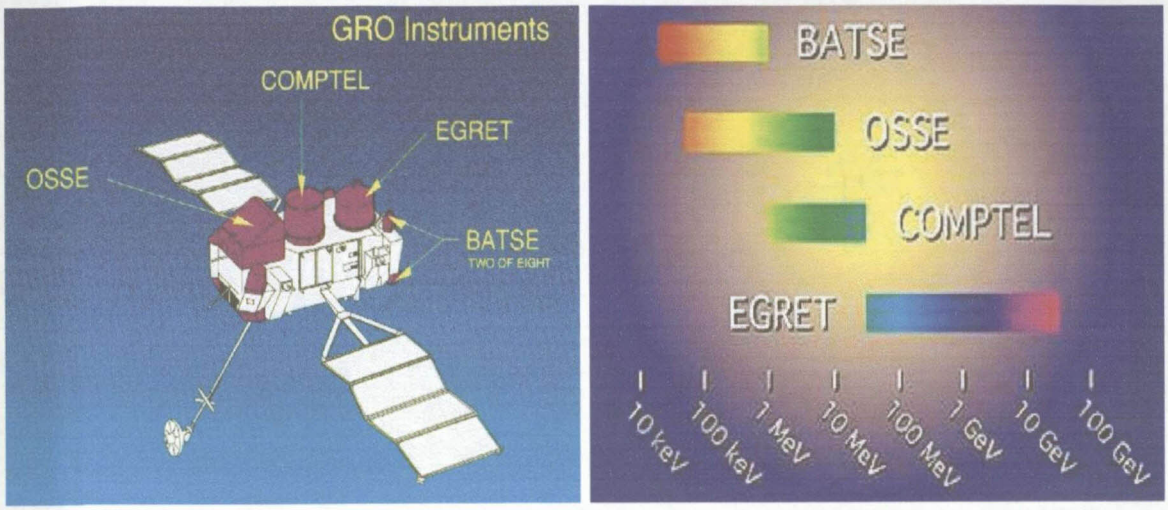

(a) (b)

Figure 3.1: (a) Four instruments on board the *Compton Gamma-Ray Observatory*. *BATSE*: The *Burst And Transient Source Experiment*, *OSSE*: The *O*riented Scintillation Spectrometer Experiment, *COMPTEL*: The *Imaging Compton Telescope* and *EGRET*: The *Energetic Gamma-Ray Experiment Telescope*. Image adopted from `http://www.am.ub.es/~josep/science/english/egret/index.html`. (b) Graphical illustration of the energy range of the instruments. *BATSE*: 20 keV–1 GeV, *OSSE*: 50 keV–10 MeV, *COMPTEL*: 1–30 MeV and *EGRET*: 20 MeV–30 GeV. Image adopted from `http://ces.iisc.ernet.in/hpg/envis/Remote/section205.htm`.

With an energy range from 20 MeV to about 30 GeV, *EGRET* was the more important of the four instruments in terms of the detection of high-energy gamma-rays. In this study the focus was primarily on the *EGRET* instrument and the high-energy γ-ray sources that it detected. More information on other instruments can be found on the official *CGRO* website: `http://heasarc.gsfc.nasa.gov/docs/cgro`.

[1]Radio-loud AGNs with jets pointing almost directly at the earth.

3.1.2 The *EGRET* detector

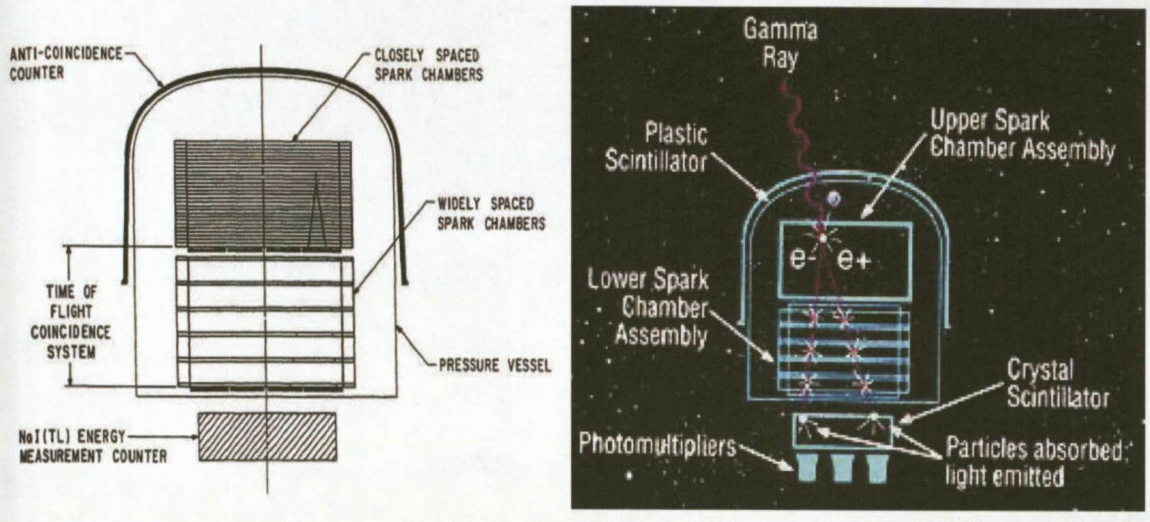

(a) (b)

Figure 3.2: (*a*) Graphical illustration of main parts of the detector. Two sparks chambers and a calorimeter all together surrounded by an anti-coincidence detector protecting the system from the cosmic ray background events, constitute the main elements of the detector. (*b*) Gamma-ray photon path in the *EGRET* detector (Thompson et al. 1993). A γ-ray photon which enters the top of the telescope is converted into an electron-positron pair in one of the thin plates between the spark chambers[1] in the upper spark chamber assembly. The pair is detected by the directional time-of-flight coincidence system as a downward moving particle. If there is no signal in the large anti-coincidence[2] scintillator[3] surrounding the upper portion of the telescope, the track imaging system is triggered, providing a digital picture of the gamma-ray event. This is done in the lower spark chamber assembly which is between the two time-of-flight scintillator planes. It allows the electron trajectories to be followed, and provides further information on the division of energy between the particles, permitting seeing the separation of the two particles for very high energy gamma rays, and shows the entry points of the pair into the Sodium Iodide doped with Thallium NaI(Tl) (in order to increase the energy resolution in scintillation) detector where the energy of the γ-ray is determined.

[1] Spark-chamber detectors consists of metal plates placed in a sealed box filled with a gas such as helium, neon or a mixture of the two. As a charged particle travels through the detector, it will ionize the gas between the plates. A trigger system is used to apply high voltage to the plates to create an electric field immediately after the particle goes through the chamber, producing sparks on its exact trajectory.

[2] Anti coincidence is a method used to suppress unwanted, "cosmic -ray background" events in detectors operating in gamma-ray energy range above 100 keV. The anti-coincidence detector is a plastic scintillator in which incoming cosmic ray charged particles interact with atoms in the detector leading to exciting electrons to higher energy levels giving rise to scintillation light. A gamma-ray photon passes through the shield since it is not charged.

[3] Material which exhibits the property of luminescence when excited by ionizing radiation. When a particle passes through the material it collides with atomic electrons, exciting them to higher energy levels. After a very short period of time the electrons fall back to their natural levels, causing emission of light.

Figures 3.3(a) and 3.3(b) show that high-energy γ-rays with energy $E_\gamma \geq 10$ MeV interact with matter mainly by electron-positron pair production. γ-ray detectors utilise this effect. An incoming γ-ray is converted, inside the detector, into an electron-positron pair by collision with atoms in a caesium-iodide crystal and the energy loss rate $\frac{dE}{dt}$ is measured in the scintillation counters in the calorimeter where the electron and positron pair is brought to rest.

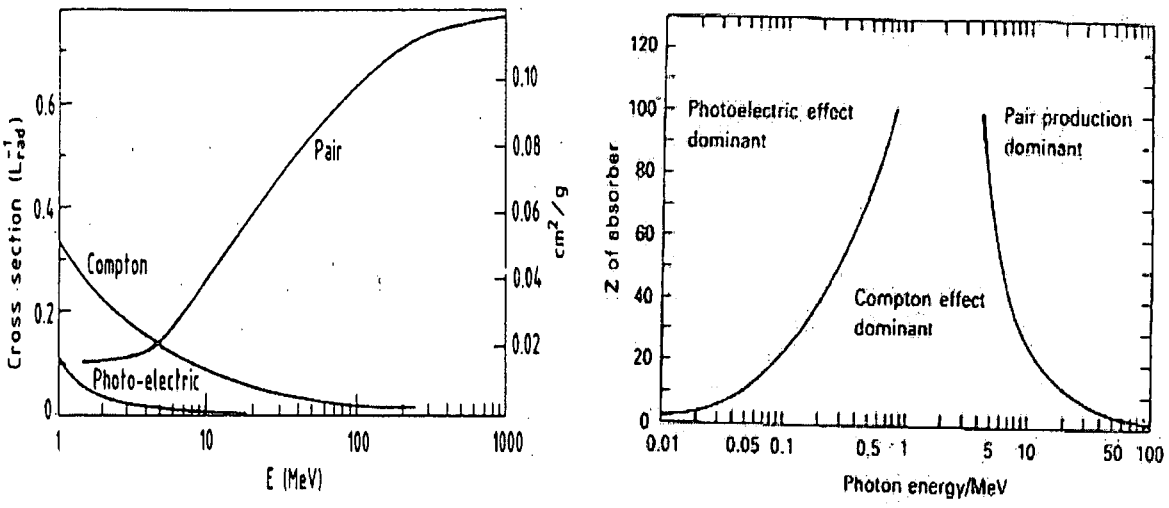

Figure 3.3: (*a*) Photon cross-section σ in lead as a function of photon energy. The intensity of photons can be expressed as $I = I_0 e^{-\sigma x}$, where x is the path length in radiation lengths. It can be seen that pair production process dominates other processes at energies above 10 MeV. Adopted from Review of Particle Properties, April 1980 edition. (*b*) The relative importance of different forms of energy loss mechanisms for gamma-rays as function of photon energy and the atomic number of material. Adopted from Longair (1992) p. 199.

The direction of incident gamma-rays could be determined using high-voltage spark chambers through the tracks produced as the γ-ray pair produce and initiate electromagnetic showers[4], causing sparks in the chambers. The gamma-ray energy would then be measured by the amount of energy deposited in the calorimeter, consisting of 36 NaI(TI) crystal blocks optically coupled into an eight radiation length thick monolithic 76 cm $\times$ 76 cm calorimeter, located below the spark chambers. The calorimeter was read out with photomultiplier tubes. A one-piece plastic scintillator covered the spark chambers and the calorimeter, which is the anti-coincidence detector. The instrument was 225 cm tall, 165 cm in overall diameter and weighed 1830 kg.

[4]An electromagnetic shower begins when a high-energy electron, positron or photon enters a material. At high energies (above a few MeV) photons interact with matter primarily via pair production, that is they convert into an electron-positron pair, interacting with an atomic nucleus or electron in order to conserve momentum. High-energy electrons and positrons primarily emit photons, a process called bremsstrahlung. These two processes continue in turn, until the remaining particles have lower energy. Electrons and photons then lose energy via scattering until they are absorbed by atoms.

3.1.3 The *EGRET*'s performance

The *EGRET* γ-ray telescope provided the highest energy γ-ray window on board the *Compton Gamma-Ray Observatory*. The main scientific objectives of *EGRET* were to survey the high-energy gamma-ray sky and to study point sources emitting high-energy gamma-rays. It surpassed its predecessors the *COS-B* and the Small Astronomy Satellite-2 (SAS-2), in both energy resolution and sensitivity and the mission was a great success. With *EGRET*, the discovery of previous gamma-ray telescopes was confirmed. For the first time, a complete survey of the gamma-ray sky was made and a large number of new point sources, many of them still unidentified, were detected.

Although the instrument was designed with an energy range up to about 30 GeV, both detection efficiency and resolution were poor for energies above 10 GeV. The detection efficiency was limited not only by weak source fluxes, but also the decreasing effective area of the instrument and self-veto due to particles in the electromagnetic shower propagating backwards and hitting the anti-coincidence shield. The *EGRET* energy resolution was estimated to about 20% at 10 GeV and decreased rapidly with energy.

Note also that the long dead time, in the order of milliseconds due to the use of spark chambers in the tracker, for reading out event data when the instrument triggered, limited the use of the instrument in studies of fast transient sources.

However, major discoveries with *EGRET* include the identification of blazars as emitters of γ-rays. *EGRET* provided the first all-sky map of the diffuse gamma-ray emission in the Galaxy, showing that most of the diffuse emission comes from the so-called Galactic bulge, usually taken as the slice $|l| < 30°$, $|b| < 5°$ around the Galactic centre.

The gamma-ray spectrum measured by *EGRET* showed an apparent excess of gamma-rays above 1 GeV over what the model predicted. Several ideas, including contributions from dark matter annihilation and/or systematic errors in the data caused by an incorrect instrument response function (Stecker et al. 2008), have been forwarded as possible explanations for this excess. It is expected that the *Large Area Telescope* on board Fermi will help to understand and determine this excess. The 3rd *EGRET* catalogue contains a large number of unidentified sources. The limitations of *EGRET* instruments such as its poor angular resolution, have made it impossible to match these sources with known sources in other wavebands such as optical and X-rays. Here also the *LAT* on board the Fermi gamma-ray observatory is expected to pin down these sources and find matching counterparts.

3.1.4 Comparison between *EGRET* and *LAT*

The *Fermi Gamma-Ray Large Observatory (Fermi)*, launched on 11 June 2008, is the new generation space-based gamma-ray observatory. Its main instrument is the *Large Area Telescope (LAT)*, comparable to *EGRET* on *CGRO*, which is designed to be sensitive to gamma-rays in

the 20 MeV to 300 GeV energy window. Fermi is also equipped with a secondary instrument, the *Gamma-Ray Burst Monitor (GBM)*, for the specific purpose of monitoring gamma-ray bursts. The *GBM* is sensitive to X-rays and gamma-rays in the energy between 8 keV and 25 MeV. This combination makes Fermi a very powerful gamma-ray detector. The *GBM* will not be described further in this thesis and the reader is referred to the description given on the *Fermi-GBM* web page at `http://www.batse.msfc.nasa.gov/gbm/`.

The *LAT* instrument relies on the pair-conversion technique for the detection of the gamma-rays with energies in the MeV to several hundred GeV range. The pair-conversion technique is outlined in Figure 3.4(a).

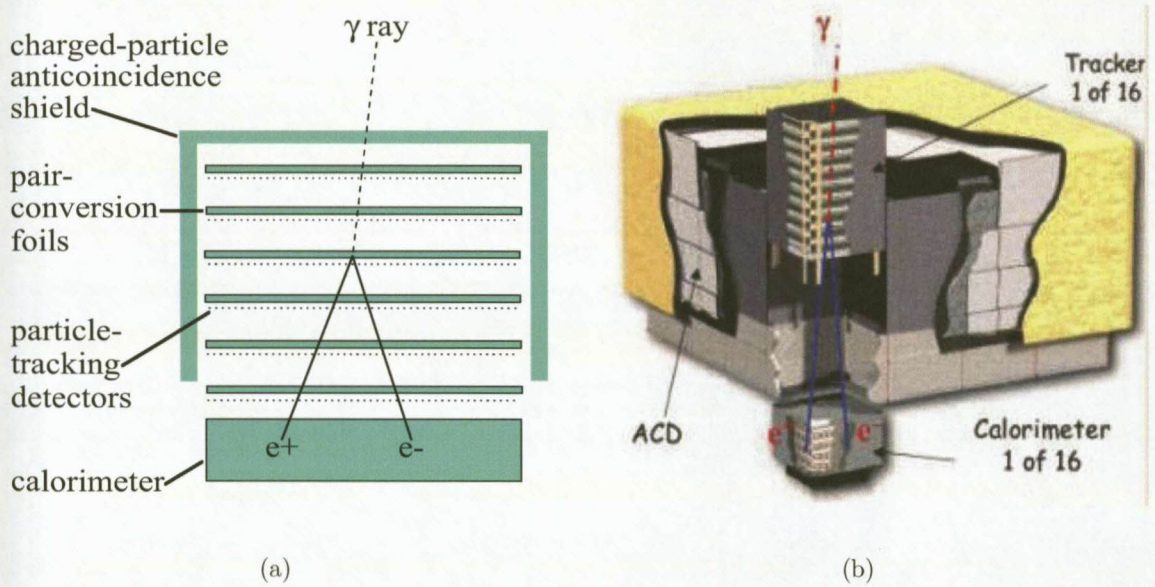

(a) (b)

Figure 3.4: (a) Graphic illustration of the pair-conversion technique used by the *LAT* for gamma-ray detection. An incoming gamma-ray interacts in one of the conversion layers and produces an electron-positron pair. The direction of the primary gamma-ray is reconstructed from the tracks of secondary charged particles in the tracker and the energy is measured by the calorimeter. The anti-coincidence shield vetoes against background charged particles (b) *LAT* elements: a tracker, a calorimeter and an anti-coincidence shield work together to measure the energies and directions of the incoming gamma-rays.

Gamma rays that strike the *LAT* first meet several layers of tungsten metal in the tracker. Tungsten's massive and highly charged atomic nuclei interact with the high-energy gamma ray in a way that creates a charged pair of particles: one electron and one positron. These particles travel in V-shaped trajectories, with the electron going one way and the positron going another, which are detected by the silicon-strip sensors positioned just below each tungsten layer.

Later, these signals are reconstructed by algorithms to obtain the direction and time of the original gamma-ray photon. After traversing through tracking layers, the particles pass into a caesium iodide imaging calorimeter and generate tiny amounts of lightflashes with brightness

proportional to the particles' energies. The anti-coincidence shield provides veto against background charged particles. The *LAT* instrument design is modular, consisting of 16 identical tower modules arranged in a 4x4 grid which are covered by a sectional anti-coincidence detector. Each detector tower consists of a silicon micro-strip tracker, a calorimeter and a data acquisition unit. A schematic view of the elements of the instrument is shown in Figure 3.4(b). A comparison between the two detectors, i.e. *EGRET* and *LAT*, is presented in Table 3.1. Of particular interest is the significant improvement in angular resolution and sensitivity of the *LAT* with respect to *EGRET*.

Parameter	*EGRET*	*Fermi-LAT*
Energy range	20 MeV–30 GeV	20 MeV–300 GeV
Energy resolution ($\frac{\Delta E_{\rm FWHM}}{E}$)		
50 MeV	14 %	12 %
100 MeV	12 %	8 %
1 GeV	9 %	4.4 %
10 GeV	12 %	6 %
100 GeV	...	18 %
Angular resolution		
(Single photon position error)		
50 MeV	5.6°	2.5°
1 GeV	1.5°	0.42°
10 GeV	0.5°	0.10°
Point Source Location	5–30 arcmin	0.1–1 arcmin
Effective area		
50 MeV	250 cm^2	4000 cm^2
1 GeV	1200 cm^2	8000 cm^2
10 GeV	700 cm^2	8000 cm^2
100 GeV	...	8000 cm^2
Field of View	$\sim$ 0.6 sr	2 sr
Point Source sensitivity		
E>100 MeV	5.4×10^{-8} ph cm^{-2} s^{-1}	1.5×10^{-9} ph cm^{-2} s^{-1}
E> 1 GeV	1.2×10^{-8} ph cm^{-2} s^{-1}	1.5×10^{-10} ph.$cm^{-2}s^{-1}$
E> 10 GeV	2.1×10^{-8} ph cm^{-2} s^{-1}	9.5×10^{-11} ph cm^{-2} s^{-1}
Dead time per event	100 ms	10 μs

Table 3.1: Performance of *EGRET* compared with *Fermi* (Mattox et al. 1996).

3.2 The *EGRET* sources

The 3rd *EGRET* Catalogue (Hartman et al. 1999) contains 271 sources detected by *EGRET* during the period from April 1991 to October 1995 (four cycles with full functionality of the detector). The first sample of 101 identified sources include a solar flare (11.06.1991), the Large Magellanic Cloud, five pulsars, 1 radio galaxy (Centaurus A), 66 blazars (BL Lac objects and

flat-spectrum radio quasars) with high confidence, and 27 lower-confidence blazar identifications. Later on Sowards-Emmerd et al. in their papers (Sowards-Emmerd et al. 2003; 2004) contributed to the identification of an additional 39 sources. In total about 131 of them remain unidentified and it is believed that possible counterparts may include pulsars and their wind nebulae, supernova remnants, massive stars, X-ray binaries, microquasars, blazars, nearby radio galaxies, luminous infrared and starburst galaxies, and galaxy clusters.

After October 1995, *EGRET* continued to observe for an additional 4.5 years despite the fact that its sensitivity was reducing because of the aging gas in the spark chamber. In this period it managed to detect an additional 30 sources (Casandjian and Grenier 2008).

Based on a new model of estimation of the galactic γ-ray background (Grenier et al. 2005), a revised catalogue for *EGRET* γ- ray sources, named the *EGRET* Revised catalogue (EGR), was recently produced (Casandjian and Grenier 2008). The new catalogue contains only 188 sources against 271 sources catalogued in the 3EG catalogue. The number of *EGRET* sources in the new catalogue has been reduced as a result of a total of 107 sources of the 3EG catalogue not confirmed in the new catalogue. Most of these unconfirmed sources are assumed to be associated with diffuse radiation from gas concentrations, particularly in regions located near the galactic plane.

However, Thompson (2008) argued that the revised diffuse galactic gamma-ray emission should not result in the exclusion of confirmed transient sources in the new catalogue, therefore questioning the validity of the revised catalogue.

Fortunately, with its improved sensitivity and better source spatial resolution compared to *EGRET*, the *Fermi Gamma-Ray Telescope* is expected to contribute significantly towards the identification of the rest of the unidentified *EGRET* sources.

A detailed study (Sowards-Emmerd et al. 2004; 2003) of the *EGRET* sources, focusing on the identification of blazars resulted in 140 *EGRET* sources being identified (Table 3.2).

	Ref: Hartman et al. 1999	Ref: Sowards-Emmered et al. 2003 and 2004	Total	%
Blazars with high confidence	66	10	76	54.3
AGNs-blazars with low confidence	27	18	45	32.1
Total blazars	*93 (92%)*	*28 (71.8%)*	*121*	*86.4*
Pulsars	5	9	14	10.0
Radio galaxy	1	2	3	2.1
Normal galaxy	1	0	1	0.7
Solar flare	1	0	1	0.7
Total	101	39	140	100

Table 3.2: Identified *EGRET* sources.

Together with 101 sources initially identified (Hartman et al. 1999) together with 39 identified later by (Sowards-Emmerd et al. 2003) & (Sowards-Emmerd et al. 2004), about 131 *EGRET* remain with no associations with known objects in other wavelengths. Of the 131, 69 are at high latitude, i.e. $|b| > 10$ deg and other 62 are confined in the galactic plane.

The large number of blazars and blazar-like objects, i.e. 121 of the 140, motivated the search for more possible blazars among the high galactic latitude unidentified sources.

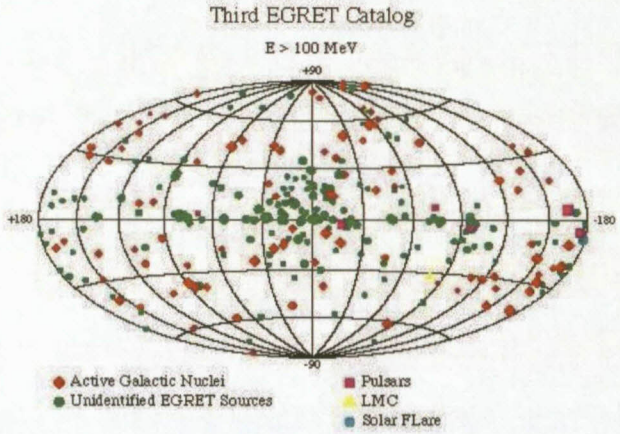

(a)

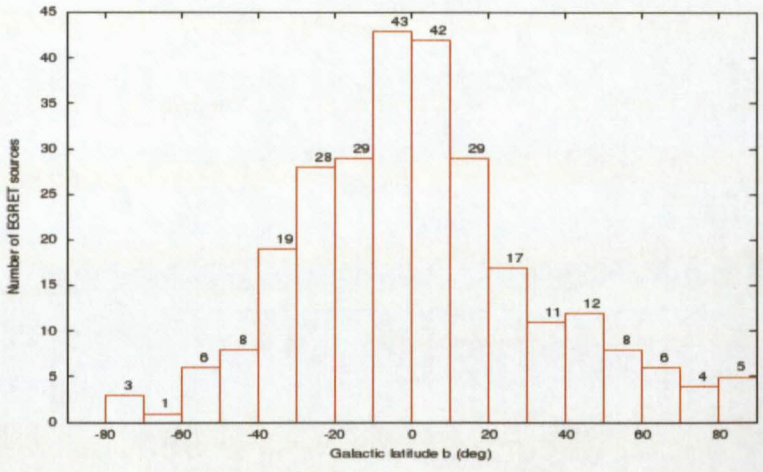

(b)

Figure 3.5: (a) The 3rd *EGRET* catalogue: The γ-ray sky map from the 3rd *EGRET* catalogue. From: `http://heasarc.gsfc.nasa.gov/docs/cgro/egret/3rd_EGRET_Cat.html`. (b) Histogram of Distribution of *EGRET* sources with respective to the galactic latitude. Noticeable is the high concentration of the gamma-ray sources in the galactic equatorial region. 140 *EGRET* sources (about 53%) are confined within $|b| < 20°$.

3.3 Selection criteria of blazar candidates among the high galactic latitude *EGRET* sources

The initial phase of this study constituted the tedious search for flat spectrum radio counterparts in the online and published catalogues inside the *EGRET* error boxes of sources that are possibly extragalactic, i.e. with $|b| > 10°$. The strategy was to select sources with $|\alpha| < 0.7$ for further multi-wavelength studies. To enable the utilization of the 26-m Hartebeesthoek radio telescope in this study, only sources with the declination range $-70° < Dec < +45°$ were considered. A further consideration was to select only those flat spectrum sources with flux density above 200 mJy at 12.4 GHz.

Each and every source in the 3^{rd} *EGRET* catalogue has been assigned a statistical error box of 95% confidence in source location ranging from 0.0 to 1.5 degrees of radius from the centre of the pointing position. A strong correlation of the γ-ray emission with the high frequency radio emission, both from the same blazar, was identified by Yang and Fan (2005). This correlation is a result of the fact that γ-rays are produced in radio jet via the synchrotron self-Compton process which increases during high states. Consequently, blazars have been found to be strong radio sources. The first step of the method is to analyse all radio sources within the error box. For this, it was found that the catalogue *SPECFIND*, which can be accessed using the online Vizier catalogue access tool, which is available at `http://vizier.u-strasbg.fr/cgi-bin/VizieR`, gives the radio spectrum of all radio sources within the *EGRET* error box for different radio surveys. Based on the general properties of blazars mentioned in Chapter 1, the following criteria have been established to select good radio counterparts of EGRET objects which will be subject to further follow-up studies:

The error box:

The counterpart has to be within the error box associated with the detection of the object by *EGRET* (Hartman et al. 1999). Table 3.3 gives all radio sources in the error boxes of the *EGRET* selected sources.

Extragalactic sources:

In order to limit any source confusion in the areas where there is a high sky density, especially near the galactic centre, only sources with ($|b| > 10°$) were selected. Also because the sample is expected to consist most likely of AGNs, selected sources here had to be confirmed in the NASA/IPAC Extragalactic Database (NED) as extragalactic.

Radio brightness:

Only sources in the error boxes which are bright enough in the radio band are of interest to this study. It was noted that sources classified in the 3^{rd} *EGRET* catalogue as blazars with high confidence, have flux densities above 100 mJy at 8.4 GHz (Sowards-Emmerd

No	Name	RA h m s	Dec d m s	Spec.ind	$S_{1.4}$ mJy	$S_{4.85}$ mJy	$S_{12.4}$ mJy
1	*3EG J0159-3603*	01 59 26	- 36 04 48	-0.58	567	276	160
		01 56 48	**- 36 16 12**	**-0.82?**	**1300**	**471**	**219?**
2	*3EG J0500+2502*	05 00 27	+24 59 29	-0.41	117	69.6	47.48
		05 02 59	**24 16 12**	**-0.53**	**5480**	**2720**	**1661**
		04 57 14	+25 45 51	-0.58	186	89.8	52.01
		04 57 06	+25 57 41	-0.88	492	164	71.51
		04 56 27	+25 37 52	-0.53	120	62.5	38
		05 02 19.7	+24 41 55	-0.87	440	149	65.75
		04 56 04	+25 18 36	-0.86	157	65	24.12
3	*3EG J0702-6212*	**06 57 02.4**	**- 61 39 26**	**-0.41**	**545**	**326**	**221**
		06 55 57	- 62 41 03	-0.97	228	68	27
4	*3EG J0706-3837*	07 08 57	- 38 33 52	-1.01	490	139	54
		07 10 43.6	**- 38 50 36**	**-0.5**	**882**	**476**	**299**
5	*3EG J0724-4713*	07 23 58	- 47 36 13	-0.81	418	152	71
		07 28 22.8	**- 47 45 14**	**-0.11**	**358**	**311**	**280**
6	*3EG J0821-5814*	**08 20 58.4**	**- 57 05 35**	**-0.64**	**1501**	**675**	**369**
7	*3EG J1300-4406*	**13 02 31**	**- 44 46 52**	**-0.85**	**1297**	**450**	**202**
8	*3EG J1659-6251*	**17 03 37**	**-62 12 38**	?	-	**587**	?
9	*3EG J1709-0828*	**17 13 06**	**- 08 17 01**	**-0.64**	**1350**	**609**	**334**
10	*3EG J1800-0146*	18 01 45	- 01 31 53	-0.88	316	106	46
		18 00 37	- 02 17 22	-0.51	92	49	30
		18 02 50.1	**- 02 07 44**	**-0.96**	**1700**	**515**	**209**
11	*3EG J1813-6419*	**18 07 54**	**- 64 13 50**	**-0.4**	**708**	**431**	**296?**
12	*3EG J1822+1641*	18 22 56	+ 16 14 01	-0.19	118	93	78
		18 22 11	**+ 16 00 12**	**-0.15**	**620**	**513**	**445**
		18 19 46	+ 17 00 34	-0.71	63	26	13
13	*3EG J1824+3441*	18 24 09	+ 34 53 15	-1.08	108	28	10
		18 24 27	+ 35 02 31	-0.62	52	24	13
		18 26 50	+ 34 49 52	-0.52	118	62	38
		18 22 16	+ 34 28 46	-1.1	55	14	5
		18 27 00	**+ 34 31 05**	**-0.07**	**481**	**440**	**411**
		18 23 46	+ 34 09 18	-0.9	603	198	85
		18 22 37	+ 35 07 16	-0.97	507	152	61
		18 26 42	+ 34 00 45	-0.46	34	19	12
		18 28 16.8	35 01 44.4	-0.49	70	57	35

Table 3.3: All prominent radio sources in the selected *EGRET* unidentified sources. In bold are the most likely radio counterparts of the *EGRET* sources. (*) The highlighted candidate was later found to be a Seyfert galaxy (reference this thesis) therefore, it is suggested to also study the other candidate in the same error box.

et al. 2003) & (Sowards-Emmerd et al. 2004), while all selected sources for this study have flux densities above 200 mJy at 12.4 GHz, in order to select the strongest radio candidates.

Spectral index:

EGRET-observed sources classified as blazars with high and low confidence show spectral indices $|\alpha| < 0.7$, for radio fluxes between 1.4 and 8.4 GHz, assuming a power-law $S_\nu \sim \nu^\alpha$ (Sowards-Emmerd et al. 2003) & (Sowards-Emmerd et al. 2004). This includes all FSRQs (with $|\alpha| < 0.5$) and BL lacs and excludes normal radio-quiet galaxies dominated by the emission from radio lobes. In our sample more attention was given to objects which have $|\alpha| < 0.7$ between 1.4 and 4.85 GHz (which is harder).

Variability:

In addition to the above conditions, any indication of the possible variability influences positively the selection of the candidate. The variability can be an indication that the emission is coming from the inner part (near the core) of the jet.

Based upon the criteria mentioned above a selection of 13 blazar-like candidates (see Table 3.4) was made among the high latitude unidentified sources. The positions of these sources have been plotted on a galactic diagram (Figure 3.6) and their finding charts are illutrated in Appendix A.

No	*EGRET* name	Counterpart	RA	Dec	b	α	$S_{1.4}$	$S_{4.85}$	$S_{12.4}$	V_{index}	Class	z
			h m s	d m s	(o)		(mJy)	(mJy)	(mJy)			
	(1)	(2)	(3)	(4)	(5)	(6)	(7)	(8)	(9)	(10)	(11)	(12)
1	*3EG J0159-3603*	*J0156-3616*	01 56 47	-36 16 14	-73.04	-0.82	1300	471	219			
2	*3EG J0500+2502*	*J0502+2516*	05 02 59	+25 16 24	-14.28	-0.51	5770	2720	1541		FSRQ	0.277
3	*3EG J0702-6212*	*J0657-6139*	06 57 02	-61 39 26	-22.56	-0.41	545	326	221	1.06		
4	*3EG J0706-3837*	*J0710-3850*	07 10 43	-38 50 36	-13.76	-0.5	882	476	299			
5	*3EG J0724-4713*	*J0728-4745*	07 28 22	-47 45 14	-14.38	-0.11	358	311	280		FSRQ	2.28
6	*3EG J0821-5814*	*J0820-5705*	08 20 58	-57 05 35	-12.04	-0.64	1501	675	369	2.02		
7	*3EG J1300-4406*	*J1302-4446*	13 02 31	-44 46 52	18.74	-0.85	1297	450	202	1.05		
8	*3EG J1659-6251*	*J1703-6212*	17 03 37	-62 12 38	-12.47	-0.13	-	587	513			
9	*3EG J1709-0828*	*J1713-0817*	17 13 06	-08 17 01	18.25	-0.64	1350	609	334			
10	*3EG J1800-0146*	*J1802-0207*	18 02 50	-02 07 44	10.39	-0.96	1730	1000	240			
11	*3EG J1813-6419*	*J1807-6413*	18 07 54	-64 13 50	-20.32		-	171	-		FSRQ	1.02
12	*3EG J1822+1641*	*J1822+1600*	18 22 11	+16 00 12	13.84	-0.15	620	513	445	2.26		
13	*3EG J1824+3441*	*J1827+3431*	18 27 00	+34 31 05	20.14	-0.07	481	440	411		FSRQ	1.81

(1): *EGRET* Name (from 3rd *EGRET* catalogue; (Hartman et al. 1999)).

(2): Possible radio counterpart selected among the radio sources in the error box of the unidentified *EGRET* source (e.g. Table 3.3).

(3) and (4): Right Ascension and Declination of the Counterpart.

(5): Galactic latitude given by *EGRET*.

(6): The radio spectral index ($S_\nu \propto \nu^\alpha$) (calculated between 1.4 GHz and 4.85 GHz).

(7), (8) and (9): The 1.4, 4.85 and 12.4 GHz flux densities (e.g. VizieR online catalogue Ochsenbein et al. (2000)).

(10): Gamma-ray variability index (Mc Laughlin et al. 1996).

(11): Existing classification.

(12): Redshift (*J0502+2516*: $z = 0.28$, e.g. Hewitt and Burbidge 1991 and Laing et al. 1983, *J0728-4745*: $z = 2.28$, e.g. Véron-Cetty and Véron 2006, *J1807-6413*: $z = 1.02$, e.g. Healey et al. 2008a and *J1827+3431*: $z = 1.81$, e.g.Véron-Cetty and Véron 2001 and Zhang et al. 1998).
Selection criteria: $|b| > 10°, S_{12.4} < 200\,\mathrm{mJy}, |\alpha| < 1, V_{\mathrm{index}} > 1$.

Table 3.4: Radio properties of 13 possible blazar candidates selected among the unidentified *EGRET* objects.

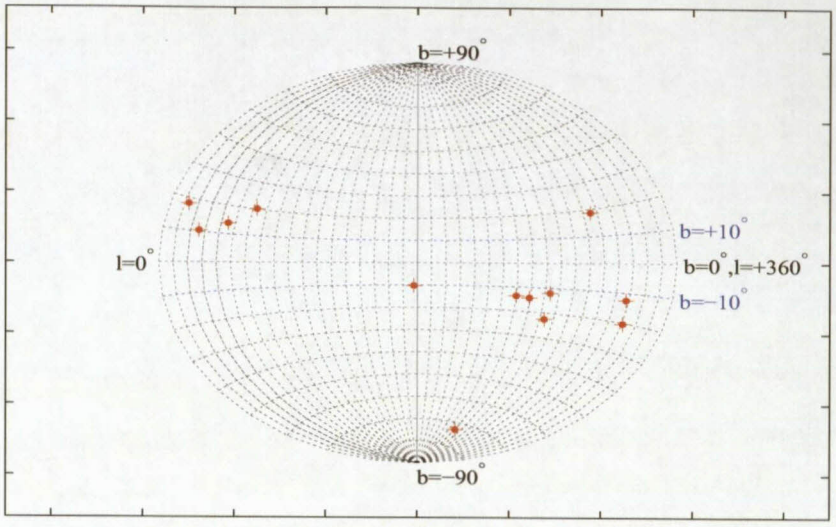

Figure 3.6: Position of the selected sources on the galactic sky map. All are outside the Galactic Plane.

The identification of radio counterparts constitutes the first step in the long run towards the complete identification of the gamma-ray sources and has two significant interpretations:

1. the radio source position is known to be accurate for the source localisation, i.e. the radio position is the one recommended for use in the further search for counterparts in other wavelengths,

2. the radio emission, of synchrotron origin, is the intrinsic characteristic of blazars as radio-loud AGNs oriented at small angles relative to the line of sight.

The typical blazar spectra shown in Section 2.5.3.4 of Chapter 2 cover a broad band of photon energies from Radio to high energy γ-rays. Therefore, in order to get the whole picture of the true γ-ray source, information in all wavelengths need to be collected. In the next Chapter, the results of a multi-wavelength observation campaign of the selected sources aiming mainly at building the Spectral Energy Distribution (SED) of the selected radio counterparts will be reported.

Chapter 4

Multi-wavelength Observations and Data Analysis

The purpose of this study is the search for possible blazar-like candidates in the error boxes of some of the high latitude unidentified *EGRET* sources. It has been mentioned that preference will be given to those sources which contain flat spectrum extra-galactic radio sources in the error boxes. Based upon this criterion a sample of 13 sources has been selected (see list in Table 3.4) for further multi-wavelength scrutiny. In this Chapter, a detailed discussion of the observational multi-wavelength properties of these sources will be presented.

In fact, blazars are identified by their Spectral Energy Distribution (SED) (see Figures 2.14 and 2.16(b)). Therefore, since the MeV–GeV part of the spectrum of the selected unidentified *EGRET* sources can partly be generated from the *EGRET* data, multi-wavelength archive data and observations of counterparts can be used to construct the rest of the SED. This will finally be compared with typical blazars dominated by the SSC emission with a possible contribution of the radiation from the external Comptonisation as mentioned in Section 2.5.3.4 of Chapter 2.

It is believed that radio-optical observations could possibly reveal the non-thermal synchrotron signature of the SED while a signature of self- or external Compton component could be identified from higher energy data. Optical observations over a sufficiently long base line could possibly identify typical blazar-like variability. Spectroscopic observations could constrain the redshifts of these objects in order to confirm their extragalactic location as well as to investigate the presence of ambient clouds which could contribute to the external Comptonisation by reprocessing the radiation from the disk. These observations are supplemented by data in online catalogues, particularly in the wavelength bands which are accessible only to space-based telescopes.

4.1 Multi-wavelength observations of the selected sources

The observational information that was obtained of the selected sources, both by using different observing facilities and by searching in online catalogues, is listed in Table 4.1.

The observed radio data were obtained using the 26-m *HartRAO* radio telescope in 5 frequency bands, i.e. 1.6 GHz/18 cm, 2.3 GHz/13 cm, 5 GHz/6 cm, 8.5 GHz/3.5 cm, 12.2 GHz/2.5 cm and 22 GHz/1.3 cm. This was supplemented with data obtained in online radio catalogues, e.g. the SPECFIND Catalogue of radio continuum spectra (Vollmer et al. 2005), the 1.4 GHz *NRAO VLA Sky Survey (NVSS)* (Condon et al. 1998) and the Parkes Radio Sources catalogue (PKS) (Wright and Otrupcek 1996).

The Near Infrared data have been obtained from the *Two Micron All Sky Survey catalogue (2MASS)* catalogue (Skrutskie et al. 2006). The catalogue gives the magnitudes in the J, H and K bands corresponding to the central wavelengths 1.235 μm (2.425×10^{14} Hz), 1.662 μm (1.805×10^{14} Hz) and 2.159 μm (1.389×10^{14} Hz).

The observed optical magnitudes in U, B, V, R and I bands were obtained using the *South African Astronomical Observatory (SAAO)* telescopes such as the 1.0-m, the 1.9-m telescopes, and the *Southern African Large Telescope (SALT)*. Together with the near infrared, the magnitudes are converted into fluxes using the online converter at `http://www.stecf.org/observing/tools/nicmos/nicmos_units_p.php` or at `http://www.astro.soton.ac.uk/~rih/applets/MagCalc.html`.

An important aspect of this study is to confirm the extragalactic nature of the sources that have been selected in the error boxes by determining their redshift. Due to the unavailability of the Robert Stobie Spectrograph (RSS)) on *SALT* for this initial phase of this study the first spectroscopic observations were made using the the *Goodman Spectrograph* at the *Southern Observatory for Astrophysical Research (SOAR)* at Cerro Pachón in Chile.

X-ray data of the selected sources were obtained from the *ROSAT* (0–2 keV), *XMM-Newton* (0.2–12 keV) and the *EINSTEIN* archives using the VizieR catalogue access tool which is found at `http://vizier.u-strasbg.fr/cgi-bin/VizieR`.

The γ-ray data were obtained from the *EGRET* (30 MeV–20 GeV) and the *Fermi-LAT* (100 MeV–300 GeV) archives. An overview of the multi-wavelength coverage of each particular source has been presented in Table 4.1. More detailed discussions related to the observations and data analyses are presented in the following sections.

	Band/Instrument													
	Radio		IRAS	NIR	Optical (Photometry)				Opt (Spec.)	X-ray			γ-ray	
Source	*HartRAO*	Online	*IRAS*	*2MASS*	1.0-m	1.9-m	*SALT*	Online	*SOAR*	*ROSAT*	*XMM*	*EINSTEIN*	*EGRET*	*Fermi-LAT*
	1.6–24	0.74–12.4	12–100	*J*, *H*, *K*	*U*, *B*, *V*, *R* and *I*				*V*	0–2	0.2–12	0.2 –20	0.03–20	0.1–300
	(GHz)	(GHz)	μm							(keV)	(keV)	(keV)	(GeV)	(GeV)
3EG J0159-3603	x	x						x					x	
3EG J0500+2502	x	x		x				x				x	x	
3EG J0702-6212	x	x			x	x	x	x					x	
3EG J0706-3837	x	x		x	x	x	x	x	x	x			x	
3EG J0724-4713	x	x						x					x	x
3EG J0821-5814	x	x		x	x	x	x	x	x	x	x		x	
3EG J1300-4406	x	x						x					x	x
3EG J1659-6251	x	x	x	x				x					x	x
3EG J1709-0828	x	x						x					x	x
3EG J1800-0146	x	x		x				x		x			x	
3EG J1813-6419	x	x		x				x					x	
3EG J1822+1641	x	x		x				x					x	
3EG J1824+3441	x	x		x				x		x			x	

Table 4.1: Available multi-wavelength data for each target. The 26-m *HartRAO* radio telescope provided radio flux measurments in 5 frequency bands, i.e. 1.6 GHz/18 cm, 2.3 GHz/13 cm, 5 GHz/6 cm, 8.5 GHz/3.5 cm, 12.2 GHz/2.5 cm and 22 GHz/1.3 cm, other data are found in Online catalogues (Cat). The Infrared data (12, 25, 60, 100 μm) were obtained from the Infrared Astronomical Satellite *(IRAS)* (Online Vizier catalogue) whereas the Near Infrared data (J H K) were obtained from the *Two Micron All Sky Survey catalogue (2MASS)* (Skrutskie et al. 2006). The observed optical magnitudes in U, B, V, R and I bands were obtained using the *SAAO* 1.0-m, the 1.9-m telescopes as well as the *Southern African Large Telescope (SALT)*. Online optical data have been found in the Hipparcos and Tycho catalogues (ESA, 1997), the *Naval Observed Merged Astrometric Dataset (NOMAD)* catalogue (Zacharias et al. 2005) and the *United States Naval Observatory (USNO)* catalogue (Monet et al. 2003)). Together with the near infrared, the magnitudes were converted to fluxes using the online converter at `http://www.stecf.org/observing/tools/nicmos/nicmos\_units\_p.php` or at `http://www.astro.soton.ac.uk/~rih/applets/MagCalc.html`. Spectroscopic obervations have been made using the Goodman Spectrograph at the *Southern Observatory for Astrophysical Research (SOAR)* at Cerro Pachón in Chile. The three X-ray satellites, i.e. the *Roentgen Satellite (ROSAT)* (0–2 keV), 1 count=6×10^{-12} erg.cm^{-2}), the *European Space Agency (ESA)*'s *X-ray Multi-Mirror Mission (XMM-Newton)* (0.2–12 keV) and the *Second High Energy Astrophysical Observatory (HEAO-2)* (0.15–20 keV), named *EINSTEIN* after launch, provided the X-ray fluxes for some selected sources. Finally, the gamma-ray data were obtained from *EGRET* (30 MeV–20 GeV) and the *Fermi-LAT* (100 MeV–300 GeV).

4.2 Radio observations

4.2.1 The 26-m *HartRAO* telescope

The Hartebeesthoek Radio Astronomical Observatory (HartRAO) is located northwest of Johannesburg, just within the provincial boundary of Gauteng, at latitude -25° 53' 14.4", longitude 27° 41' 05.2" East and at an elevation of 1415.821 m, in South Africa. It operates a radio telescope with a diameter of 26 m, the only major[1] radio telescope in South Africa, equipped with radio receivers operating in microwave bands centered on wavelengths at 18 cm, 13 cm, 6 cm, 5 cm, 4.5 cm, 3.5 cm and 2.5 cm. The characteristics of the output of the receivers are summarised in Table 4.2. For maximum sensitivity, receivers are cooled down to 16 K (-257° Celcius). The absolute northern declination pointing limit is +45°.

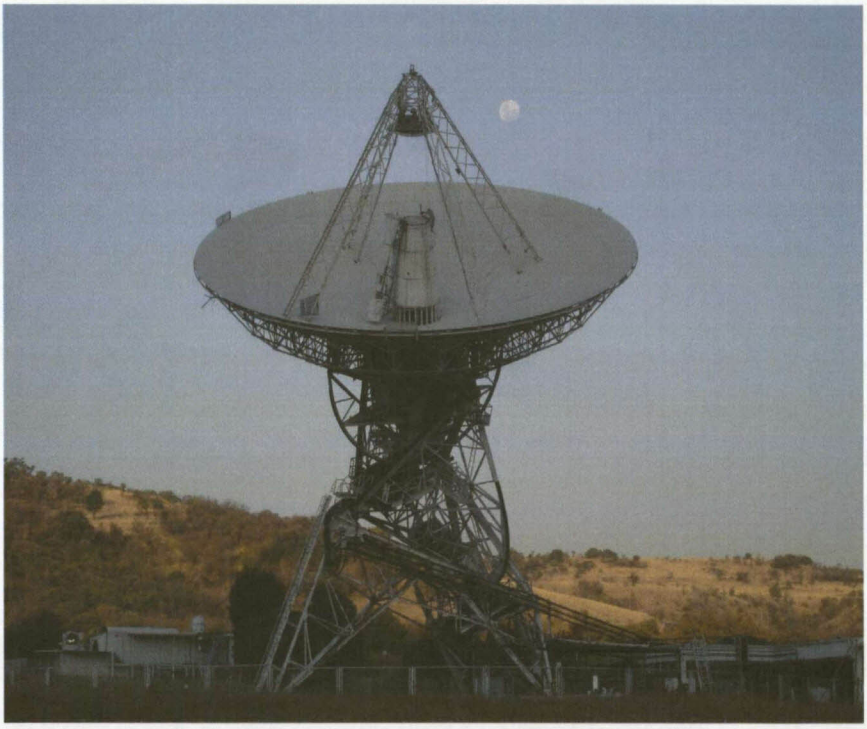

Figure 4.1: The 26-m *HartRAO* radio telescope. Image adopted from `http://www.hartrao.ac.za/gallery/`.

[1]South Africa has been shortlisted together with Australia to host the *Square Kilometre Array (SKA)*, the most powerful radio telescope ever. South Africa is building an *SKA* technology pathfinder telescope, the *Karoo Array Telescope (KAT)*). At the time of writing this thesis the first phase of a seven-dish prototype interferometer array (named *KAT-7*) is almost complete.

Band	18 cm	13 cm	6 cm	4.5 cm	3.5 cm	2.5 cm	1.3 cm
Polarization (L& R)CP [a]	L & R	L & R	L & R	L & R	L & R	L & R	L & R
Standard frequency (MHz)	1666	2280	5000	6670	8580	12180	23000
Lower frequency limit (MHz)	1608	2210	4650	6008	8180	12048	22000
Upper frequency limit (MHz)	1727	2450	5200	6682	8980	12216	24000
Receiver bandwidth (MHz)	120	240	400	660	800	168	2000
Beamwidth: FWHM (degrees)	0.49	0.33	0.16	0.11	0.09	0.06	0.03
Beamwidth: between first nulls (degrees)	1.19	0.8	0.36	0.32	0.23	0.16	0.07
T_{syst} Minimum at Zenith (K) [b]	39	44	50	57	60	95	220
PSS per polarization (Jy/K/Pol) [c]	5.1	4.8	5.8	5.1	5.7	5.8	6
SEFD per polarization (Jy/Pol)[d]	200	210	290	290	340	670	1500

[a] LCP = Left Circular Polarisation, RCP = Right Circular Polarisation

[b] T_{syst} = Temperature System

[c] PSS = Point Source Sensitivity

[d] SEFD = System Equivalent Flux Density

Table 4.2: Microwave receivers at the 26-m *HartRAO* radio telescope. Adopted from `http://www.hartrao.ac.za/factsfile.html`.

4.2.2 Calibration

The sensitivity of a radio telescope, i.e. the ability to measure weak radio fluxes, depends on the surface area and efficiency of the antenna and on the sensitivity of the radio receiver used to amplify and detect the radio signals from noise. The calibration is the process of measuring the Point Source Sensitivity (PSS) of a telescope. The PSS is defined[2] as a measure of the number of Janskys of flux density required to produce one Kelvin of antenna temperature in each polarisation. The PSS (in each polarisation) is easily determined experimentally from the antenna temperatures measured for standard sources (calibrators) of known flux density using the relation

$$PSS_{LCP/RCP}(\nu) = \frac{\frac{S(\nu)}{2}}{K_s T_{A_{LCP/RCP}}} [Jy/K/pol], \tag{4.1}$$

where $S(\nu)$ is the flux density and $T_{A_{LCP/RCP}}$ is the antenna temperature (in left or right circular polarisation) and K_s is the size correction factor given by (e.g. Baars (1973))

$$K_s = 1 + (\frac{\theta_S}{\theta_A})^2 \text{ or } K_s = \frac{x^2}{1 - e^{-x^2}} \tag{4.2}$$

for the Gaussian and disc-like brightness distributions respectively, where θ_S is the beamwidth, θ_A is the scan width and $x = \frac{R}{0.6\theta_A}$ with R the radius of the disc. For sources that are very small compared to the beam size, $K_s \simeq 1$. The factor 2 in Equation 4.2 means that half of the

[2]This definition is commonly used for small antennas like the one at Hartebeeshoek. Otherwise, the correct definition is the reverse i.e. the PSS is a measure of a number of Kelvins of antenna temperature per polarisation obtained per Jansky of source flux density

flux density is received in each polarisation. Theoretically, the values for the two polarisations should be the same but in practice there is always a small difference between them, and data from each polarisation should be corrected using the appropriate value to that polarisation.

The standard sources used as calibrators were *3C123*, *3C218* (also known as *Hydra A*), *3C353* and *Jupiter*.

To be selected as radio standard, an object must

- be a non-variable source,
- be small in angular size and,
- show a flux density which is high enough and frequency dependent. The flux density is related empirically to the frequency by

$$\log_{10} S(\nu) = a + b \times \log_{10}(\nu) + c \times (\log_{10}(\nu))^2, \tag{4.3}$$

where ν is the frequency given in MHz and a, b and c are coefficients fixed for each calibrator (Ott et al. 1994).

Specifically for observations at *HartRAO*, the pointing limit of the 26-m dish requires the standards to have a declination less than 45°. Finally the standard must appear in the same part of the sky as the object to be observed during the observing period. Table 4.3 shows the characteristics of the sources used as standards or calibrators.

Source	Size	Coefficients			Flux density (in Jy)					
		a	b	c	1.6 GHz	2.3 GHz	4.8 GHz	8.5 GHz	12.2 GHz	22.4 GHz
3C123	$23'' \times 5''$	2.525	0.246	-0.164	42.1	31.68	16.25	9.17	6.24	2.88
3C218 Hydra A	$47'' \times 15''$	4.729	-1.025	0.229	37.87	26.92	13.55	7.98	5.72	3.08
3C353	$210'' \times 60''$	3.148	-0.157	-0.091	51.25	38.96	21.65	13.32	9.67	5.16
Jupiter[a]	$40.73''$ [b]	-	-	-			1.47	4.32	8.47	-

[a]For *Jupiter*, the flux density for calibration is estimated using $S = \frac{2\times10^{26} k T_B \Omega_S}{\lambda^2}$ [Jy], where T_B and Ω_S are the brightness temperature and the solid angle subtended by the planet respectively. The brightness temperature of the planet is related to the antenna temperature by $T_B = \frac{\Omega_A}{\Omega_S} T_A$ where T_A and Ω_A are the Antenna temperature and the beam solid angle respectively. The values of the flux density of Jupiter at 6 cm (4.8 GHz), 3.5 cm (8.5 GHz) and 2.5 cm (12.2 GHz), which are used in this table, were adopted from Carr 2005.

[b]Angular diameter (on 5 April 2007). From `http://www.calsky.com.cgi/Planets/6/4?`

Table 4.3: Calibrator's flux density dependence on frequency.

Figure 4.2 shows the raw data of the on-source (centered in the antenna beam) scans, in left and right circular polarisations of the standards.

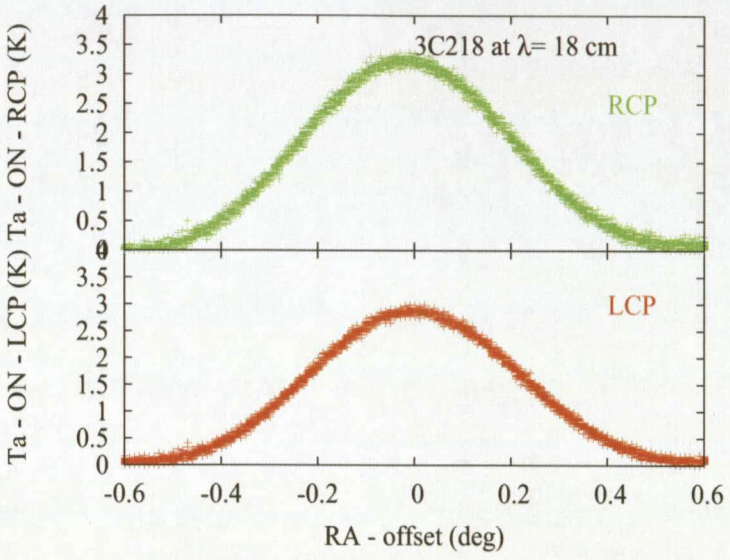

(a) *3C218 at λ =18 cm*

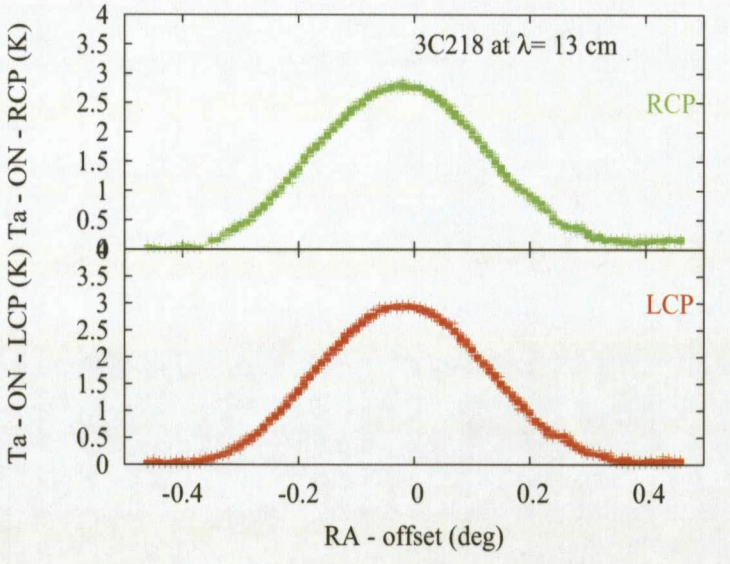

(b) *3C218 at λ = 13 cm*

Figure 4.2: Calibration.

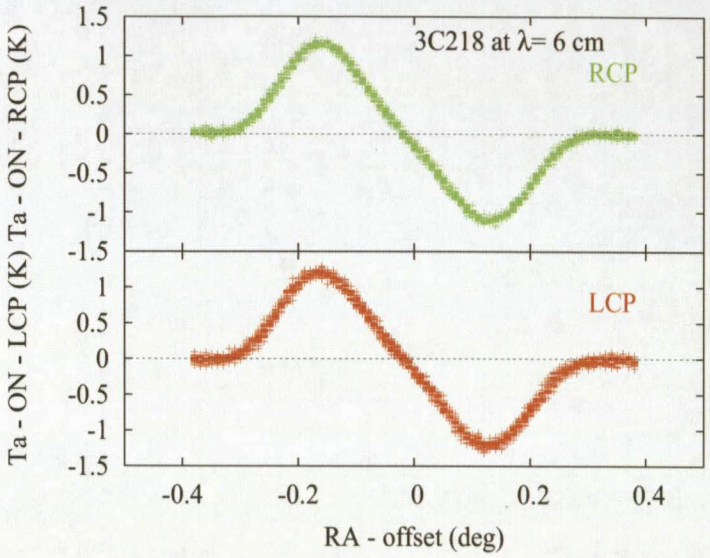

(c) *3C218 at* $\lambda = 6$ *cm*

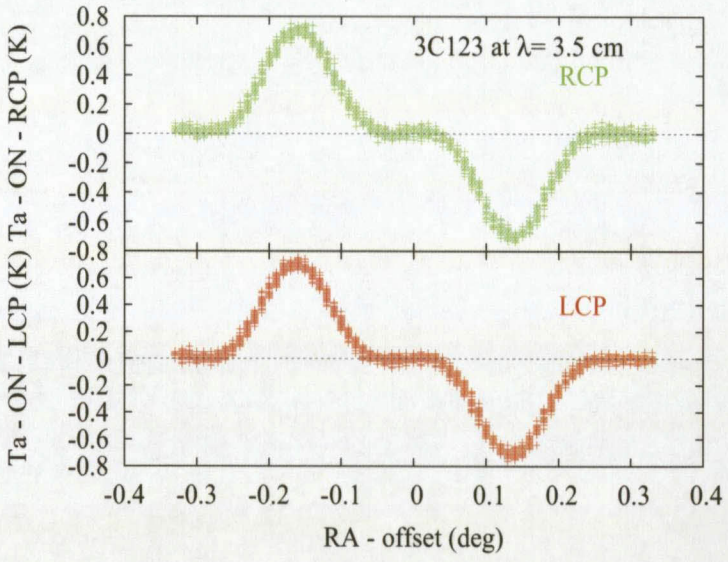

(d) *3C123 at* $\lambda = 3.5$ *cm*

Figure 4.2: Calibration (continued).

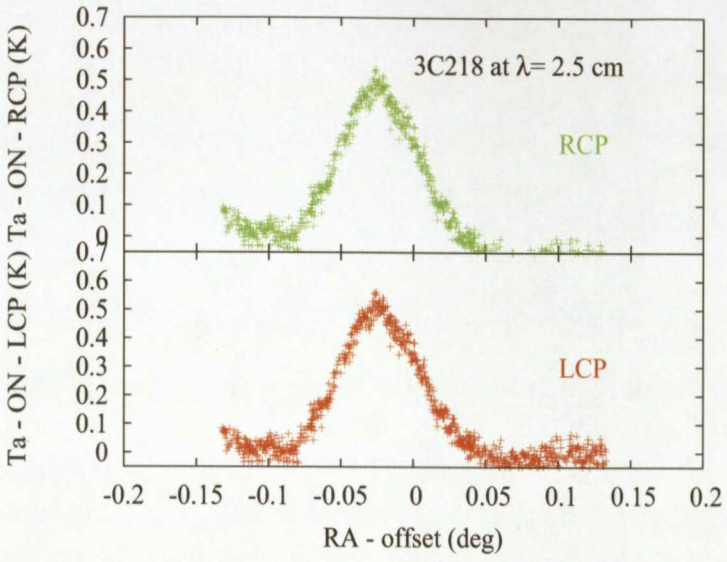

(e) *3C218 at λ = 2.5 cm*

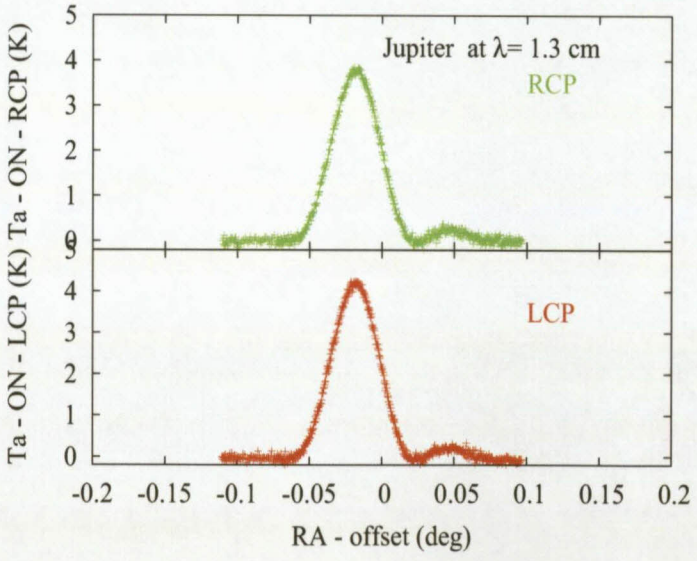

(f) *Jupiter at λ = 1.3 cm*

Figure 4.2: Calibration (continued).

A close look (e.g. by comparing the scales on the Y-axis) at the subfigures of *3C218* at $\lambda = 18$ cm, 13 cm, 6 cm and 2.5 cm, indicates that the radio continuum flux density (which is

proportional to the antenna temperature) of radio galaxies generally falls steeply with increasing frequency. The big error bars at high frequencies (small wavelengths) are due to the atmospheric water vapour problem which increases with increasing frequency. This indicates that generally the higher the frequency, the greater the difficulty in getting good flux measurements on radio galaxies.

The different shapes of the source signals show how the real sources will be represented as they cross the antenna beam for different wavelengths (or frequencies). The double-parabola shape seen in the 6 cm and 3.5 cm receivers is due to dual-feed systems permitting Dicke-switched[3] radiometry, i.e. signals from the source are received by two parallel feeds (A and B). The total signal is obtained by subtracting the two components (A-B) as illustrated in Figure 4.3.

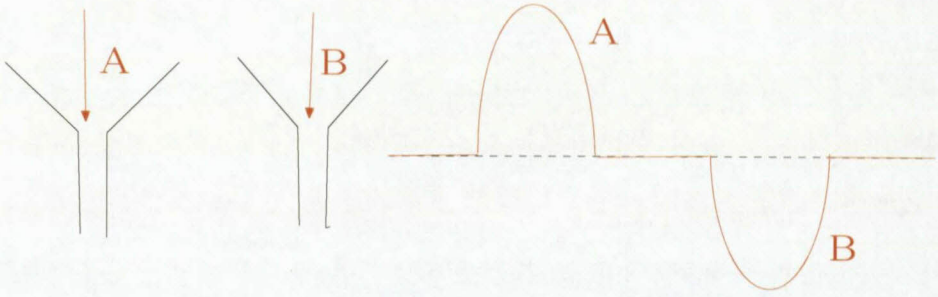

Figure 4.3: Two feeds in the 6 and 3.5 cm receivers.

Table 4.4 displays the central frequency and the wavelength of the observational band, the point source sensitivity of the telescope in each polarisation (Left Circular Polarisation and Right Circular Polarisation) for the sources used as calibrators.

4.2.3 Data

Subscans were examined and those affected by interference, bad weather or instrumental problems were removed. Polynomials of the second order were fitted to individual scans e.g Figure 4.4. The peak value of the fitted parabola corresponded to the antenna temperature which was corrected by multiplying it with the pointing correction. The antenna temperature (T_A) relates to

[3]The Dicke-switch technique works by rapidly switching the input of the radio telescope receiver between the antenna and a resistor. Gain variations in the receiver can have their effects neutralized by measuring not the signal from the antenna, but the difference in signals between the antenna signal and the noise input of the resistor. This difference signal is obtained by the use of a synchronous detector circuit (Adopted from `http://www.radiosky.com/dicke.html`)

Frequency	Wavelength	Calibrator	Beam	LCP		RCP	
				PSS Jy/K/pol	A_p eff	PSS Jy/K/pol	A_p eff
1.6 GHz	18 cm	3C353		6.550	0.400	5.800	0.452
		Hydra A		6.424	0.511	5.676	0.602
		average		6.487	0.456	5.738	0.527
2.3 GHz	13 cm	*3C123*		5.400	0.482	5.439	0.482
		Hydra A		5.627	0.465	5.039	0.520
		average		5.514	0.474	5.239	0.501
5 GHz	6 cm	*3C123*	A	5.794	0.452	5.940	0.441
		3C123	B	5.901	0.444	6.187	0.418
		Hydra A	A	5.584	0.469	5.940	0.441
		Hydra A	B	5.780	0.453	6.117	0.428
		average	A	5.689	0.461	5.940	0.441
			B	5.841	0.449	6.152	0.423
8.5 GHz	3.5 cm	*3C123*	A	5.969	0.439	5.894	0.440
		3C123	B	6.101	0.429	6.201	0.422
		Hydra A	A	6.307	0.415	6.421	0.408
		Hydra A	B	6.182	0.424	6.266	0.418
		average	A	6.138	0.427	6.158	0.424
			B	6.142	0.427	6.234	0.420
12 GHz	2.5 cm	*3C123*		5.925	0.442	5.710	0.459
		Hydra A		5.537	0.473	5.720	0.590
		average		5.731	0.458	5.715	0.525
24.04 GHz	1.3 cm	*Jupiter*		5.362	0.489	5.952	0.440
				5.477	0.478	5.972	0.439
		average		5.420	0.483	5.962	0.439

Table 4.4: Measured point source sensitivity (PSS) for calibration. LCP: Left circular polarisation, RCP: Right Circular polarisation, PSS: Point Source Sensitivity, A_p eff: Aperture efficiency.

the flux density by[4]

$$T_{A_{LCP/RCP}} = \frac{S_\lambda}{2K_s PSS_{LCP/RCP}} \tag{4.4}$$

obtained from Equation 4.1 where K_s and PSS are the size correction factor and the Point Source Sensitivity. The total flux is obtained by summing the fluxes in the two polarisation modes i.e. Left Circular Polarisation (LCP) and Right Circular Polarisation (RCP). The data reduction was done using "lines"[5].

[4]The expression of the flux density at radio frequencies, $S_\lambda = \frac{2k\int_{\Omega_s} T_B(\Omega)d\Omega}{\lambda^2}$ with T_B the brightness temperature defined by the blackbody radiation expression $I_\nu = \frac{2h}{c^2}\frac{\nu^3}{(e^{\frac{h\nu}{kT_B}}-1)}$ and Ω_s the solid angle subtended by the source, is obtained by combining the Rayleigh-Jeans approximation, i.e. at low frequencies $\frac{h\nu}{kT} \ll 1$, $I(\nu) = \frac{2kT\nu^2}{c^2}$ and the equation $S_\nu = \int_\Omega I_\nu d\Omega$.

[5]"lines" is a software developed by M. Gaylard to reduce and analyse spectra from the 26-m Hartebeesthoek radio telescope.

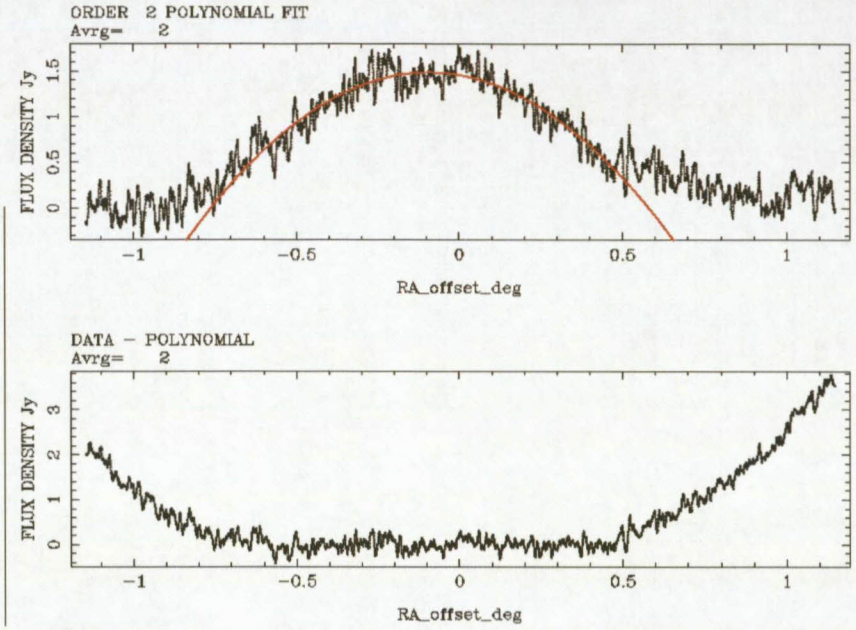

(a) Polynomial fit of order two of the drift scan of *PKS J0820-5705 (3EG J0821-5814)* at λ =18 cm (LCP+RCP, day=237, flux density=1.48±0.13 Jy)

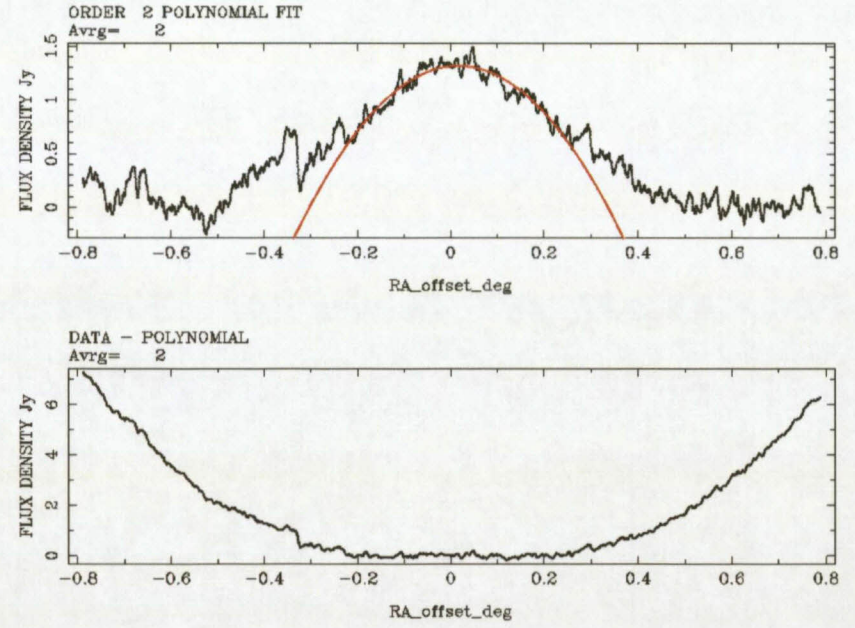

(b) Polynomial fit of order two of the drift scan of *PKS J0820-5705 (3EG J0821-5814)* at λ = 13 cm (LCP+RCP, day=267, flux density= 1.31±0.06 Jy)

Figure 4.4: Radio data reduction.

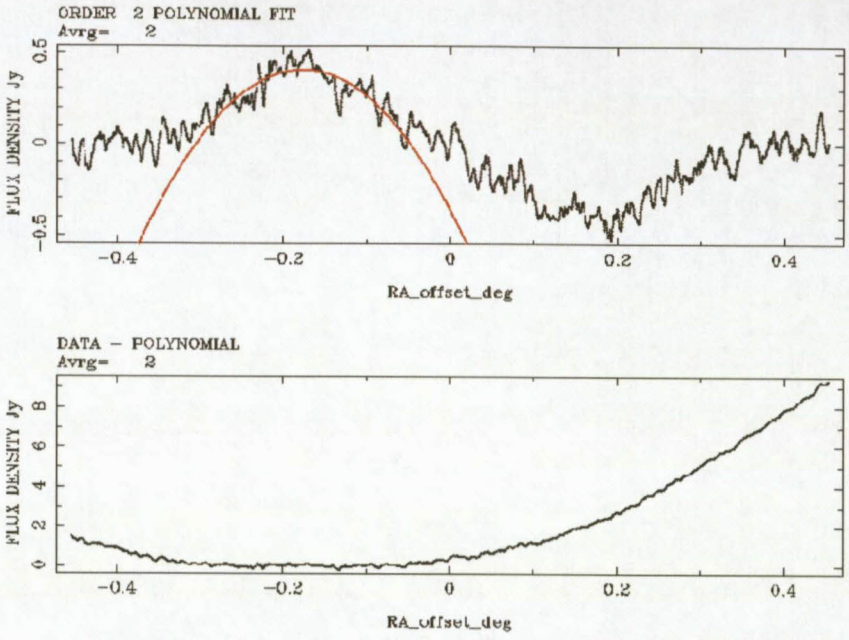

(d) Polynomial fit of order two of the sum of the drift scans (LCP+RCP) of *PKS J0820-5705 (3EG J0821-5814)* at $\lambda = 6$ cm in A- feed (day= 248, flux density=0.64±0.07 Jy)

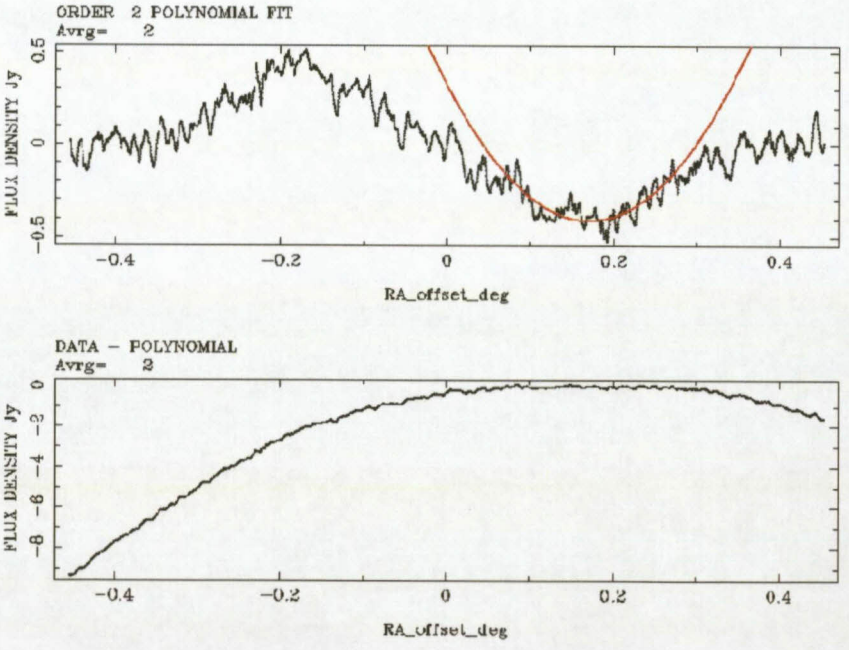

(e) Polynomial fit of order two of the sum of the drift scans (LCP+RCP) of *PKS J0820-5705 (3EG J0821-5814)* at $\lambda = 6$ cm in B- feed (day=248, flux density= (-)0.65±0.05 Jy)

Figure 4.4: Radio data reduction (continued). The average flux in A and B feeds is 0.64± 0.06 Jy ($= \frac{(A-B)}{2}$).

Table 4.5 gives the radio flux densities in six spectral bands (1.6 GHz (18 cm), 2.3 GHz (13 cm), 5 GHz (6 cm), 8.5 GHz (3.5 cm), 12.2 GHz (2.5 cm), 22 GHz (1.3 cm)) using the 26-m *HartRAO* telescope during the periods of April and October 2007.

1.6 GHz / 18 cm		2.3 GHz / 13 cm		5 GHz / 6 cm		8.4 GHz / 3.5 cm		12 GHz / 2.5 cm		24 GHz / 1.3 cm	
date (day)	Flux (jy)	date (day)	Flux (jy)	date (day)	Flux (jy)	date (day)	Flux (jy)	date (day)	Flux (jy)	date (day)	Flux (jy)
3EG J0159-3603											
236.85	1.34 ± 0.17	250	0.78 ± 0.03	236.07	0.38 ± 0.05	264.97	0.23 ± 0.01	263.99	0.23 ± 0.05		
		266.95	1.11 ± 0.07	248.04	0.4 ± 0.06	272.98	0.13 ± 0.03	268.98	0.43↓		
				265.99	0.41 ± 0.06						
				273.97	0.39 ± 0.06						
3EG J0500+2502											
		250.19	0.4 ↓	248.13	0.1↓			263.13	0.10↓		
		267.05	0.3 ↓								
3EG J0702-6212											
96.66	1.07 ± 0.17	95.56	1.22 ± 0.2	94.64	0.3 ± 0.07	94.67	0.2 ± 0.02	96.6	0.13 ± 0		
236.42	1.31 ± 0.1			97.61	0.34 ± 0.09	264.14	0.21 ± 0.02				
237.05	1.46 ± 0.11			105.66	0.38 ± 0.07						
				236.26	0.26 ± 0.06						
				248.23	0.31 ± 0.06						
				266.18	0.41 ± 0.07						
				274.16	0.25 ± 0.07						
3EG J0706-3837											
		267.14	0.73 ± 0.02	97.64	0.33 ± 0.09	94.67	0.39 ± 0.02			94.64	0.21↓
				104.65	0.35 ± 0.06	264.14	0.57 ± 0.01	96.6	0.22 ± 0.01		
				105.65	0.49 ± 0.05	273.13	0.59 ± 0.06	100.75	0.47 ± 0.02		
				248.27	0.53 ± 0.06			101.67	0.68↓		
				266.21	0.51 ± 0.05			263.22	0.34 ± 0.01		
				274.19	0.52 ± 0.06			264.22	0.25 ± 0.02		
3EG J0724-4713											
236.44	1.11 ± 0.13	95.6	0.61 ± 0.07	97.64	0.54 ± 0.08	94.68	0.49 ± 0.01	96.6	0.22 ± 0.01		
237.07	0.9 ± 0.14	96.59	0.52 ± 0.09	104.66	0.3 ± 0.07	263.31	0.46 ± 0.02	235.32	0.34 ± 0.05		
		236.31	0.46 ± 0.06	105.66	0.5 ± 0.07	264.16	0.45 ± 0.01				
		236.38	0.91 ± 0.09	235.31	0.48 ± 0.05	273.15	0.42 ± 0.03				
		237.24	0.9 ± 0.09	236.3	0.5 ± 0.06						
		250.23	0.66 ± 0.05	248.28	0.44 ± 0.07						
				265.25	0.5 ± 0.06						
				266.22	0.47 ± 0.06						
				274.2	0.47 ± 0.07						
3EG J0821-5814											
93.73	1.35 ± 0.14	96.61	1.3 ± 0.06	94.66	0.64 ± 0.08	94.69	0.52 ± 0.01	96.64	0.62↓	97.03	0.41↓
236.44	1.07 ± 0.12	236.39	1.3 ± 0.13	97.66	0.52 ± 0.07	263.31	0.4 ± 0.02	100.76	0.68↓		
237.11	1.48 ± 0.13	267.19	1.31 ± 0.06	104.7	0.65 ± 0.07	264.2	0.39 ± 0.01	105.7	0.54↓		
				105.7	0.65 ± 0.14	272.33	0.42 ± 0.02	235.35	0.73↓		
				235.35	0.68 ± 0.07			264.27	0.4 ± 0.03		
				248.31	0.64 ± 0.06						
				265.27	0.49 ± 0.06						
				266.26	0.55 ± 0.08						

Continued on the next page

Table 4.5: Radio flux density measurements for all selected counterparts, using the 26-m dish at *HartRAO*. Days correspond to day number of the 2007 observing year. A down arrow (↓) represents a flux upper limit.

1.6 GHz / 18 cm		2.3 GHz / 13 cm		5 GHz / 6 cm		8.4 GHz / 3.5 cm		12 GHz /2.5 cm		24 GHz / 1.3 cm	
date (day)	Flux (jy)	date (day)	Flux (jy)	date (day)	Flux (jy)	date (day)	Flux (jy)	date (day)	Flux (jy)	date (day)	Flux (jy)
3EG J1300-4406											
93.95	0.99 ± 0.09	95.82	0.82 ± 0.14	94.86	0.48 ± 0.03	94.86	0.27 ± 0.02	105.9	$0.34^{\downarrow}$		
236.45	0.81 ± 0.05	250.47	0.81 ± 0.08	97.87	0.5 ± 0.02	263.52	0.26 ± 0.03				
237.32	0.98 ± 0.15			104.91	0.58 ± 0.02	264.41	0.26 ± 0.02				
				105.9	0.46 ± 0.02						
				235.54	0.53 ± 0.01						
				247.51	0.54 ± 0.01						
				265.45	0.54 ± 0.01						
				273.44	0.55 ± 0.02						
3EG J1659-6251											
236.49	1.36 ± 0.14	236.66	$0.71^{\downarrow}$ ±	235.69	0.84 ± 0.02	264.71	0.79 ± 0.02				
				247.66	0.77 ± 0.01						
				265.62	0.88 ± 0.02						
3EG J1709-0828											
94.12	1.15 ± 0.1	96	0.87 ± 0.03	95.03	0.56 ± 0.02	95.04	0.41 ± 0.01	234.73	$0.55^{\downarrow}$		
236.5	1.27 ± 0.28	97	0.79 ± 0.09	105.07	0.59 ± 0.02	263.69	0.42 ± 0.01	263.6	$0.55^{\downarrow}$		
				106.06	0.56 ± 0.02						
				235.69	0.57 ± 0.03						
				247.68	0.64 ± 0.03						
				265.62	0.58 ± 0.03						
3EG J1800-0146											
94.17	1.09 ± 0.1			95.08	0.53 ± 0.02	95.12	0.21 ± 0.02				
236.54	0.87 ± 0.15			98.2	0.52 ± 0.03	263.7	0.31 ± 0.01				
				105.09	0.54 ± 0.02						
				106.06	0.53 ± 0.01						
				235.72	0.56 ± 0.01						
				247.68	0.55 ± 0.02						
				265.64	0.55 ± 0.02						
3EG J1813-6419											
94.18	1 ± 0.13	96.16	0.45 ± 0.09	95.11	0.2 ± 0.03	263.7	0.22 ± 0.01				
236.55	1.15 ± 0.11	236.69	0.63 ± 0.17	98.2	0.35 ± 0.02						
				105.11	0.29 ± 0.03						
				106.08	0.28 ± 0.02						
				235.73	0.35 ± 0.01						
				247.69	0.44 ± 0.02						
				265.67	0.49 ± 0.02						
3EG J1822+1641											
94.19	0.62 ± 0.1	96.13	0.55 ± 0.05	95.12	0.37 ± 0.02	95.13	0.36 ± 0.02				
		236.69	0.71 ± 0.16	98.21	0.38 ± 0.02	263.71	0.39 ± 0.01				
				105.12	0.53 ± 0.01						
				106.11	0.47 ± 0.02						
				235.74	0.48 ± 0.02						
				247.71	0.44 ± 0.02						
3EG J1824+3441											
94.2	0.51 ± 0.09	96.13	$0.55^{\downarrow}$ ± 0.03	95.12	0.31 ± 0.03	263.71	0.22 ± 0.01				
236.61	0.49 ± 0.07	97.13	0.60↓ ± 0.02	98.21	0.36 ± 0.02						
				106.14	0.34 ± 0.02						
				235.77	0.28 ± 0.02						
				265.68	0.29 ± 0.04						

Table 4.5: Radio flux density measurements for all selected counterparts, using the 26-m dish at *HartRAO*. Days correspond to day number of the 2007 observing year. A down arrow (↓) represents a flux upper limit (continued).

A close look at the data, particularly at 5 GHz where there are more than 4 measurements on average in each source, could not reveal any clear radio variability of the objects. However, more data are recommended for a such study. The radio variability, if confirmed, can be an indication that the radio emission (dominated mostly by the synchrotron emission) is coming from a region close to the AGN core.

4.3 Optical observations

In the initial phase of this study, optical photometric follow-up observations could be made for only three of the selected sources, i.e. *3EG J0702-6212*, *3EG J0706-3837* and *3EG J0821-5814*, while spectroscopic observations could be made for *3EG J0706-3837* and *3EG J0821-5814*. The photometric observations, aiming at determining possible variability of those sources, were made with *SALT*[6], the 1.9-m and 1.0-m telescopes during observing campaigns in 2008 and 2009 (first quarter). The spectroscopic observations were made during one night in February 2009. A more detailed discussion will be presented later.

4.3.1 *SALT* observations

The *Southern African Large Telescope (SALT)* is an 11-m telescope located close to the town of Sutherland in the semi-desert region of the Karoo, in the North Western Cape province in South Africa at latitude: -32 d 22 min 46 s , longitude: 20 d 48 min 38.5 s East and at an elevation of 1798 m. It is operated by the *South African Astronomical Observatory (SAAO)*, the national optical observatory of South Africa. *SALT* is the largest optical telescope in the southern hemisphere. It enables imaging, spectroscopic, and polarimetric analysis of the radiation from astronomical objects.

The *SALT* primary mirror is an array of 91 identical mirrors producing a hexagonal shape of 11 x 9.8 meters in size. To compensate for the spherical primary mirror, the telescope has a four-mirror Spherical Aberration Corrector (SAC) that provides a corrected, flat focal plane with a field of view of 8 arcminutes at prime focus. During an observation, the mirror remains at a fixed altitude and azimuth and the image of an astronomical target produced by the telescope is tracked by the "payload", which resides at the position of the prime focus and includes the spherical aberration corrector (SAC) and prime focus instrumentation (see Figure 4.5). This results in a limited observing window (called the window of visibility) per target. Therefore,

[6] *SALT: Southern African Large Telescop* is an 11-m optical telescope operated by the *South African Astronomical Observatory* under a consortium consisting of the National Research Foundation of South Africa, Nicholas Copernicus Astronomical Center of the Polish Academy of Sciences, Hobby Eberly Telescope Founding Institutions, Rutgers University, Georg-August-Universität Göttingen, University of Wisconsin - Madison, Carnegie Mellon University, University of Canterbury, United Kingdom *SALT* Consortium, University of North Carolina - Chapel Hill, Dartmouth College, American Museum of Natural History and the Inter-University Centre for Astronomy and Astrophysics and India.

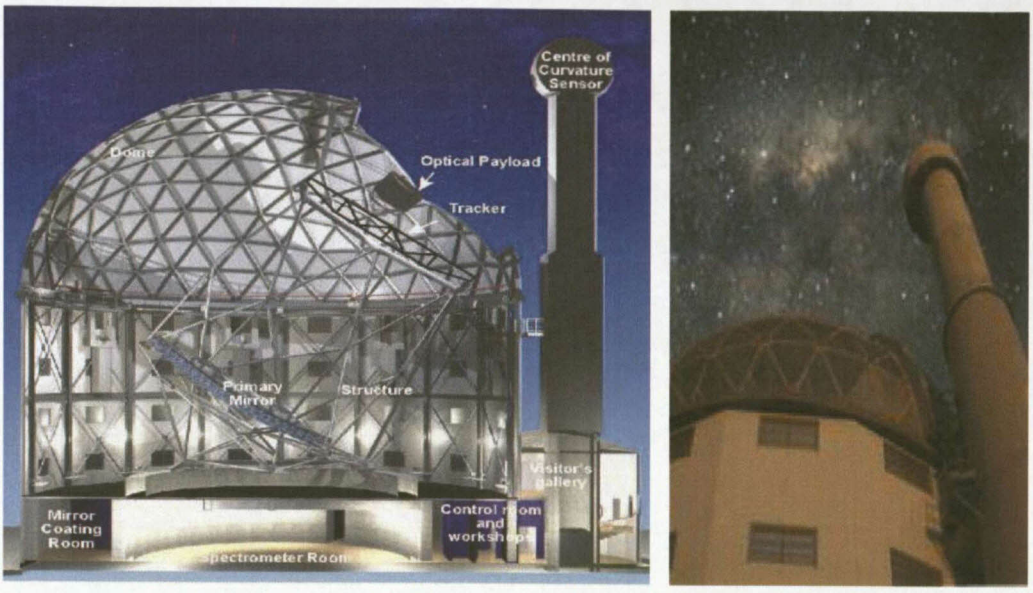

(a) (b)

Figure 4.5: (a) Structure of the *SALT* telescope. (b) *SALT* external view.

objects are not always accessible to *SALT*, even though they may be above the horizon. However, the times an object can be observed during the course of a year are almost identical to those of traditional telescopes. *SALT* has a fixed zenith angle of 37 degrees, but because of the full range of azimuths and the celestial rotation, *SALT* has access to $\sim$ 70% of the sky available at the Sutherland site.

The instruments at *SALT* include the *SALT Imaging Camera (SALTICAM)*, the Robert Stobie Spectrograph (RSS), a multi-purpose long slit and multi-object imaging spectrograph, a spectro polarimeter and a fiber-fed *High Resolution Spectrograph (HRS)*. This study has made use of *SALTICAM* and a proposal for *RSS* observations was submitted in February 2010. The next two paragraphs briefly describe these instruments.

SALTICAM was installed in early 2005 and has been operational since then despite many observing interruptions due for image quality improvement, while the *RSS* was installed on 11 October 2005, but was later removed due to technical problems encountered. At the time of writing this thesis, preparations were underway to put the spectrograph back on the telescope and that any time soon the commissioning phase could start. *SALTICAM* is a prime-focus camera that images the entire science and guider fields of view (i.e. $\sim$ 10 x 10 arcmin) onto a 4K x 4K Charge Coupled Device (CCD) detector. The CCD detector is a mosaic of two 2K$\times$ 4K pixel CCD chips of 15 μm pixel size and 30.7 x 61.5 mm^2 imaging area per chip. Observations can be made from 320 nm to 900 nm in mainly 5 filters, namely U, B, V, R and I.

The *Robert Stobie Spectrograph (RSS)*, formerly known as the *Prime Focus Imaging Spectrograph (PFIS)*, is named in honor of the late Director of the *South African Astronomical Observatory*,

Dr Robert (Bob) Stewart Stobie (1941-2002). This is an efficient low to medium resolution imaging spectrograph operating from about 320 nm to 900 nm. There is an upgrade path for a Near-IR arm (to 1.7 microns) using a dichroic beam splitter. Efficient and tunable Volume Phase Holographic (VHP) gratings provide resolutions of up to $R \sim 6000$ with 1 arcsec slits and $R \sim 10{,}000$ with 0.6 arcsec slits. For more details on other *SALT* instruments the reader is referred to the *SALT* official website `http://www.salt.ac.za/`.

The reduced number of observed targets is explained by the fact that during the course of this study, the observing time requested at *SALT* was initially constrained not only by the availability of the targets in the sky but also by the target "window of visibility" at *SALT*. Further complications arose for a long term engineering programme which was given priority to characterise, diagnose and fix a serious image quality problems, i.e. aberrations resulting in the field image degradation, noticed in the *SALT* optics since the first phase of telescope operation. This problem persisted resulting in the continuation of the observational programme using the smaller 1.0-m and 1.9-m telescopes.

The time-series imaging of the targets was performed using the *SALT* imaging camera (*SALTICAM*) on the nights of February 14 and 15, 2008, April 25, 26 and 28, 2008, May 7, 2008 and June 01, 2008. Exposure times ranged between 20, 10, 15, 40 and 100 s respectively for the filters *I*, *R*, *V*, *B* and *U*. The data were taken in full-frame mode, binned 4x4, and the instrument cycled through the filters in the sequence *UBVRIRVBU*. Figure 4.5 shows CCD images (8 arcmin × 8 arcmin) of *PKS J0820-5705*, *PKS J0710-3850* and *PKS J0657-6139*, counterparts of *3EG J0821-5814*, 3EG J0706-3827 and *3EG J0702-6212* respectively, using *SALTICAM*. The images were taken with the *I* filter with 20 s exposure time and 4×4 binning during the nights 07/08 May 2008 (seeing=1.4″), 15/16 February 2008 (seeing=1.5″) and 26/27 April 2008 respectively.

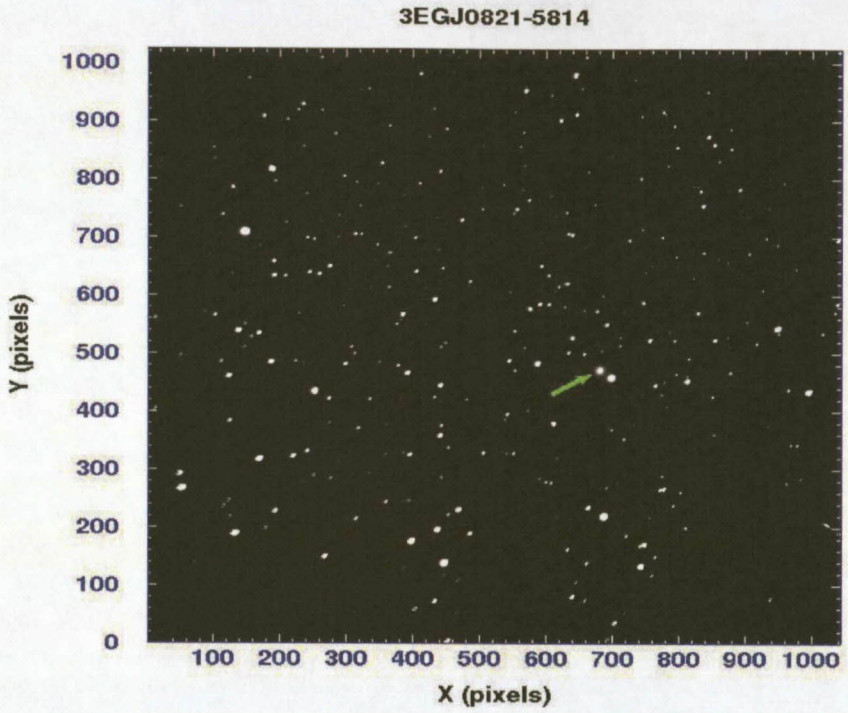

(a) *PKS J0820-5705 (3EG J0821-5814)*

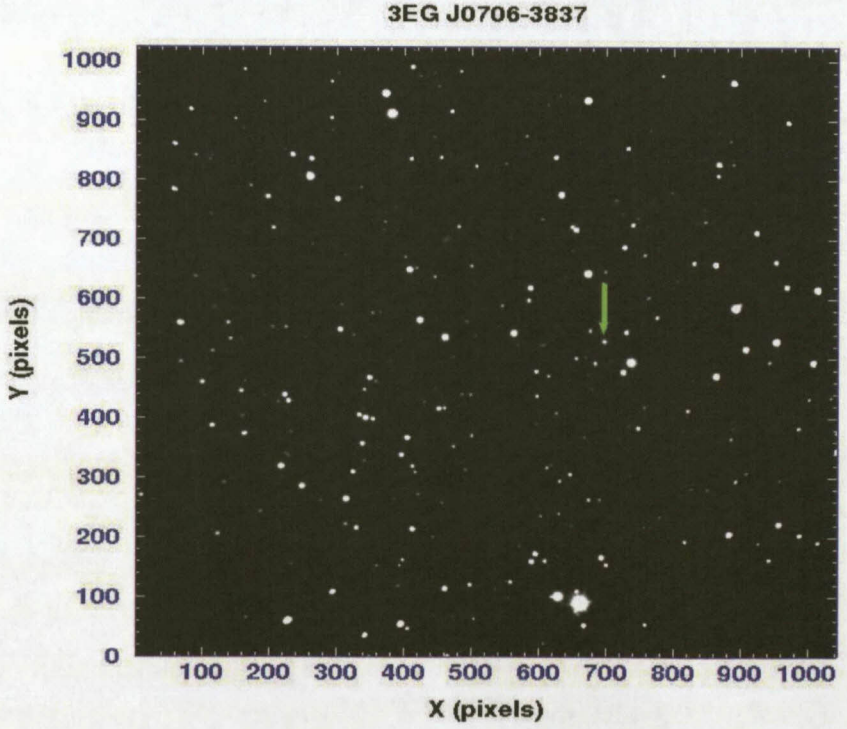

(b) *PMN J0710-3850 (3EG J0706-3837)*

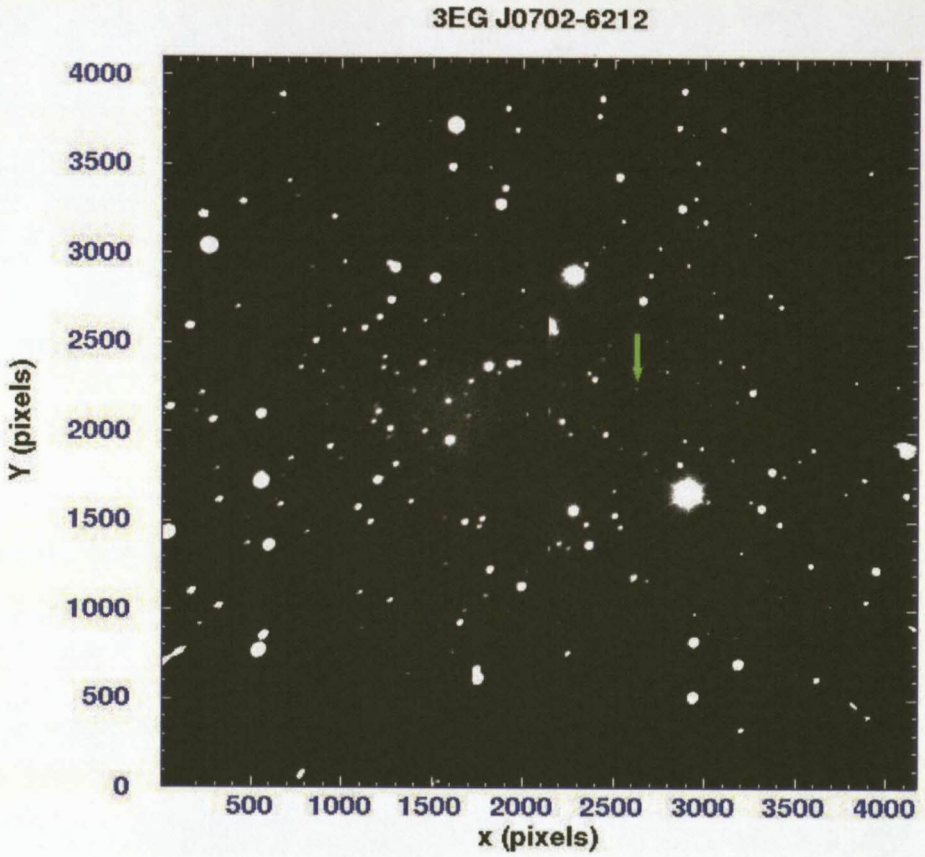

(e) *PKS J0657-6139* (*3EG J0702-6212*)

Figure 4.5: CCD images (8 arcmin × 8 arcmin) taken by SALTICAM at the *Southern African Large Telescope* (*SALT*). (a) Image of *PKS J0820-5705* (*3EG J0821-5814*) field obtained using the *I* filter for 20 s exposure time and 4×4 binning during the night of 07/08 May 2008 (seeing = 1.4″). (b) Image of *PMN J0710-3850* (*3EG J0706-3837*) field obtained using the *I* filter with 20 s exposure time and 4×4 binning during the night of 15/16 February 2008 (seeing = 1.5″). (c) Image of *PKS J0657-6139* (*3EG J0702-6212*) field obtained using the *I* filter for 20 s exposure time and 4×4 binning during the nights 26 April 2008. It was reported by the seeing was good at the time of observation.

A list of exposure times per filter is presented in Table 4.6 and an observational log is presented in Table 4.7. The total observing time is ∼ 7h 44 min.

EGRET source name	*3EG J0702-6212*		*3EG J0706-3837*		*3EG J0821-5814*	
Counterpart	*PKS J0657-6139*		*PMN J0710-3850*		*PKS J0820-5705*	
RA (h m s)	06 57 02		07 10 43		08 20 58	
Dec (d m s)	-61 39 26		-38 50 36		-57 05 35	
Filter array	Filter	Exposure time per frame	Filter	Exposure time per frame	Filter	Exposure time per frame
	U	100 s	U	100 s	U	100 s
	B	40 s	B	40 s	B	40 s
	V	15 s	V	15 s	V	15 s
	R	10 s	R	10 s	R	10 s
	I	20 s	I	20 s	I	20 s
	R	10 s	R	10 s	R	10 s
	V	15 s	V	15 s	V	15 s
	B	40 s	B	40 s	B	40 s
	U	100 s	U	100 s	U	100 s
Total time (excluding dead time)		350 s		350 s		350 s
Number of iterations		12		6		9
Total time for observations.		6455 s		3228 s		4841 s
Source availability on the 1st March 2008		8750 s		3998 s		6458 s

Table 4.6: *SALT* observing payload configuration.

Target	Date of observation	Number of sequences *UBVRIRVBU*	Total number of fits files	Observation time	Binning
3EG J0702-6212	14/02/2008	4	36	38min	4x4
	26/04/2008	5	48	57.1min	4x4
	27/04/2008	6.8	60	65.1min	4x4
3EG J0706-3837	15/02/2008	2	17	10.7 min	4x4
3EG J0821-5814	14/02/2008	5	45	56 min	4x4
	28/04/2008	7	61	1 h 15 min	4x4
	07/05/2008	7.8	79	1 h 23 min	4x4
	01/06/2008	6.1	47	1 h 20 min	4x4

Table 4.7: Targets' observing time on *SALT*.

Basic processing of the data, like gain correction and bias subtraction, was done in the instrument's pipeline. The counts of the objects and of their reference stars in the same frame were extracted using the command *imexamine* of IRAF. Magnitudes were calculated using a comparison star in the nearby region, which was observed in the same period using the UCT CCD at the 1.9-m *SAAO* telescope. Results are summarised in Table 4.8.

Source	Filter	Observed magnitude per night and per filter					Mag. in literature
3EG J0702-6212		14.02.2008	26.04.2008	27.04.2008		Average obs. mag.	Catalogued mag. (*)
	U	21.07 ±0.19				21.07 ±0.19	
	B	20.11 ±0.06	20.04 ±0.14	20.21 ±0.1		20.12 ±0.1	20.75
	V	21.16 ±0.04	21.07 ±0.09	21.17 ± 0.1		21.13 ±0.08	
	R	19.67 ±0.09	19.5 ±0.05	19.55± 0.1		19.57±0.08	19.93
	I	19.76 ±0.09	19.72± 0.06	19.79 ±0.11		19.76± 0.09	
3EG J0706-3837		15.02.2009				Average obs. mag.	
	U	17.04± 0.14				17.04 ±0.14	
	B	16.77± 0.29				16.77± 0.29	16.96
	V	16.68± 0.31				16.68± 0.32	16.58
	R	16.48± 0.29				16.48 ±0.29	
	I	15.32±0.35				15.32± 0.35	
3EG J0821-5814		14.02.2008	28.04.2008	07.05.2008	01.06.2008	Average obs. mag.	
	U	19.54± 0.02	19.47 ±0.17	19.26±0.08	19.26 ±0.37	19.38± 0.18	
	B	17.6 ±0.05	17.38 ±0.08	17.36 ±0.07	17.13 ±0.07	17.37± 0.07	
	V	16.98 ±0.03	16.79 ±0.08	16.78 ±0.07	16.61± 0.17	16.79±0.08	
	R	16.69±0.26	16.31 ±0.28	16.4 ±0.07	16.19± 0.09	16.4 ±0.18	16.16
	I	15.39 ±0.02	15.18 ±0.02	15.17 ±0.02	14.95 ±0.01	15.17±0.0175	

Table 4.8: Targets' magnitudes per filter and per observing night obtained from *SALT*. (*) Targets' Magnitudes from the *NOMAD* catalogue (Zacharias et al. 2005) which can be accessed via the online VizieR catalogue access tool at `http://vizier.u-strasbg.fr/cgi-bin/VizieR`.

4.3.2 1.9-m *SAAO* telescope observations

Suplementary optical photometric observations were performed using the *SAAO* 1.9-m telescope (see Figure 4.3.2) utilising the 1k × 1k STE-4 CCD camera with a 5 × 5 arcmin field.

Figure 4.6: 1.9-m *SAAO* telescope.

The characteristics of STE-4 are given in Table 4.12.

Parameter	STE-4
Number of Pixels	1024 x 1024
Pixel size	24 microns
Scale (1.9-m)	0.14 arcsec/pix
Field of view (1.9-m)	146 x 146 arcsec squared
Read Noise	6.5 electrons
Scale Factor	2.8 electrons/ADU (*)
Linear Count Limit	65535 ADU
Readout Time	43 sec
U zero point (1ADU/sec)	19.2
B	22
V	22.35
I	21.8

(*) ADU: Analog to Digital Units

Table 4.9: Characteristics of STE-4 *SAAO* CCD camera.

Table 4.10 displays the observing log for 5 observing nights from 2009, January 9/10 to January 13/14 with the 1.9-m *SAAO* telescope. Figure 4.7 shows a sample of two STE-4 CCD frames of the objects taken during this observing period.

Day	Night	Flats	Standard	*3EG J0706-3837*	*3EG J0821-5814*
Friday	9-10	Uflats	No Science data, Guiding problem		
Saturday	10-11	No data, pointing problem			
Sunday	11-12		UBVRI	BVRI(1X1) and U (2X2)	UBVRI
Monday	12-13	All flats	UBVRI	BVRI	BVRI
Tuesday	13-14		UBVRI		

Table 4.10: Observing log for the 1.9-m *SAAO* telescope observations.

With the STE-4, frames were binned 2×2. The basic reductions (bias-subtraction, dark-correction, flat-fielding) were carried out using the standard IRAF routines of duphot and diffphot packages of the telescope (1.9-m) pipeline (e.g. O'Donoghue et al. 1999) performing magnitude measurements using both techniques: aperture photometry[7] and PSF photometry[8]. Final magnitudes, airmass-corrected, are presented in Table 4.11.

The Aperture Photometry (APP) magnitudes seem to be here more reliable than the ones obtained using PSF photometry. In fact, compared with the magnitudes obtained from SALT

[7]In aperture photometry, one aperture (usually circular) enclosing the source is defined, and another (usually a ring outside the first) that contains only the sky background. The mean counts per pixel from the sky aperture is obtained, then subtracted from each pixel in the source aperture, and finaly the remaining counts are summed to find the total in the stellar image.

[8]In Point Spread Function (PSF) photometry, photons are estimated using a 3-D gaussian function (the PSF) fitted to the stars in the field.

and others found in literature (e.g. Table 4.8) for the observed objects, the APP magnitudes are more close than the PSF magnitudes.

The differences between PSF magnitudes and APP magnitudes may be related to the settings of the parameters (here we used the default) of the PSF function which may need to be adjusted when the seeing is varying whereas for the APP photometry the annuli are reevaluated for each observation. For the rest of the thesis, it is the APP magnitudes which were considered for further analysis of the data.

Filter	Night	Julian date	Exposure time (s)	Seeing	Aperture (pixels)	mag_{PSF}	mag_{APP}	Error
3EG J0706-3837								
V	12/13 Jan 2009	2454844.39	45	3.54	15	18.13	17.64	0.03
R	12/13 Jan 2009	2454844.4	14	2.7	15	17.71	17.09	0.03
I	12/13 Jan 2009	2454844.4	18	2.51	15	16.92	16.25	0.02
3EG J0821-5814								
V	11/12 Jan 2009	2454843.56	45	2.28	20	17.98	16.48	0.01
	12/13 Jan 2009	2454844.52	45	3.19	20	17.82	16.35	0.01
R	11/12 Jan 2009	2454843.56	14	2.16	20	18.25	16.35	0.01
I	11/12 Jan 2009	2454843.56	18	2.02	20	17.09	15.67	0.01
	12/13 Jan 2009	2454844.52	18	3.07	20	17.03	15.36	0.01

Table 4.11: Measurements of optical magnitudes for the two sources, *3EG J0821-5814* and *3EG J0706-3837* with 1.9-m telescope. mag_{PSF} = Point Spread Function magnitude and mag_{APP}= Aperture Photometry magnitude.

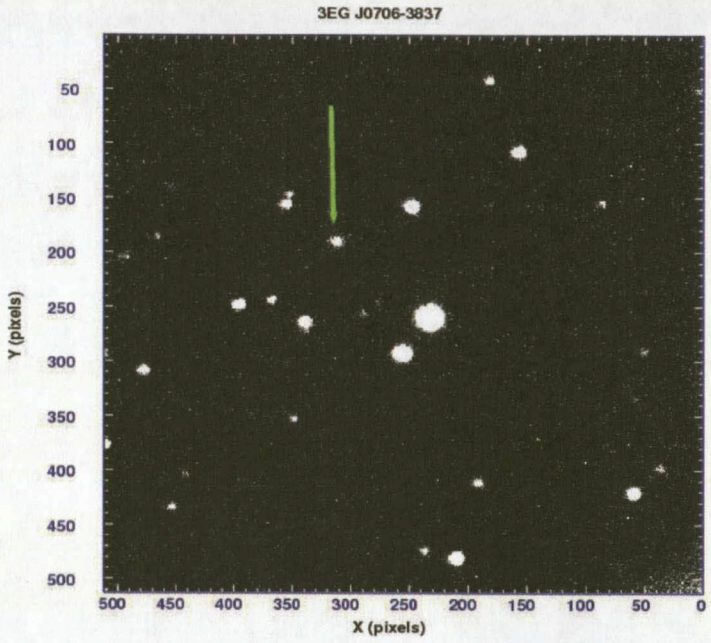

(a) *3EG J0706-3837*

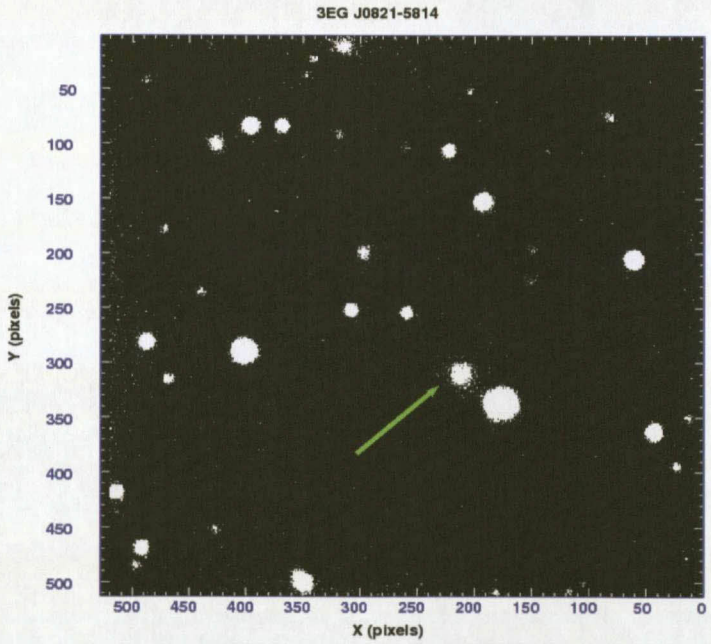

(b) *3EG J0821-5814*

Figure 4.7: (a) Image of 3EG J0706-3837 (RA: 07:10:43, Dec: -38:50:36) obtained from the 1.9-m telescope using the STE-4 CCD camera (V-filter, exposure time: 45 s, Date of observation: 12 January 2009 at 21:39:48 (UTC)).
(b) Image of 3EG J0821-5814 (RA: 08:20:58, Dec: -57:05:35) obtained from the 1.9-m SAAO telescope using the STE-4 CCD camera (R-filter, exposure time: 14 s; Date of observation: 13 January 2009 at 00:30;37 (UTC)).

4.3.3 1.0-m *SAAO* telescope observations

The *SAAO* 1.0-m telescope (see Figure 4.8) was used with the STE-3 CCD camera of 512 x 512 pixels size.

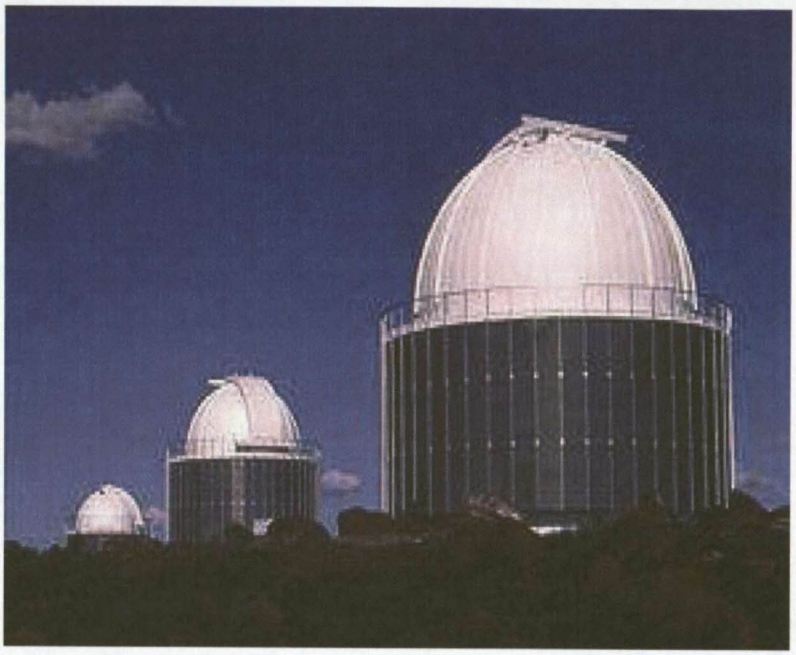

Figure 4.8: 1.0-m *SAAO* telescope (first from right).

The characteristics of STE-3 are given in Table 4.12.

Parameter	STE-3
Number of Pixels	512 x 512
Pixel size	24 microns
Scale (1.0-m)	0.31 arcsec/pix
Scale (1.9-m)	0.14 arcsec/pix
Field of view (1.0-m)	158 x 158 arcsecs squared
Field of view (1.9-m)	73 x 73 arcsec squared
Read Noise	6.5 electrons
Scale Factor	2.8 electrons/ADU
Linear Count Limit	65535 ADU
Readout Time	10 sec
U zero point (1ADU/sec)	19.2
B	22
V	22.35
I	21.8

Table 4.12: Characteristics of the STE -3 *SAAO* CCD camera.

Table 4.13 displays the observing log for 7 observing nights from 2009, January 14/15 to

January 20/21. Figure 4.9 shows a sample of two STE-3 CCD frames of the objects taken during this observing period.

Day	Night	Flats	Standard	*3EG J0706-3837*	*3EG J0821-5814*
Wednesday	14/15				BVRI
Thursday	15/16	All flats (morning)		No science data, Focus problem	
Friday	16-17			U, BVRI	
Saturday	17/18	UBVRI	UBVRI		U,BVRI
Sunday	18/19				UBVRI
Monday	19/20	UBVRI	UBVRI	B	
Tuesday	20/21				B

Table 4.13: Observing log for the 1.0-m *SAAO* telescope.

The STE-3 CCD was used without prebinning. The basic reductions (bias-subtraction, dark-correction, flat-fielding) were carried out using the standard IRAF routines of duphot, diffphot packages of the telescope (1.0-m) pipeline performing magnitude measurements using both techniques: aperture photometry and PSF photometry. Final magnitudes, airmass-corrected, are presented in Table 4.14. As stated previously in the case of the 1.9-m, the PSF magnitudes seem to be more reliable than the ones obtained using aperture photometry particularly in crowded field (e.g. 3EG J0821-5814 which is close to a bright star) where apertures can be contaminated by nearby bright star counts.

Filter	Night	Julian date	Exposure time (s)	Seeing	Aperture (pixels)	mag_{PSF}	mag_{APP}	Error
3EG J0706-3837								
B	19/20 Jan 2009	2454851.41	560	3.4	20	18.81	18.7	0.02
	16/17 Jan 2009	2454848.38	560	2.4	25	19.43	18.89	0.02
V	16/17 Jan 2009	2454848.39	180	2.47	25	18.17	17.79	0.01
R	19/20 Jan 2009	2454848.39	56	2.26	20	17.54	17.04	0.02
I	16/17 Jan 2009	2454848.39	72	2.34	25	15.87	15.4	0.02
3EG J0821-5814								
B	20/21 Jan 2009	2454852.43	560	2.61	20	19.02	17.76	0.01
	17/18 Jan 2009	2454849.39	560	2.75	25	19.22	17.82	0.01
V	17/18 Jan 2009	2454849.39	180	2.79	25	17.88	16.44	0.01
R	17/18 Jan 2009	2454849.39	56	2.79	25	17.46	16.1	0.01

Table 4.14: Measurements of optical magnitudes for the two sources, *3EG J0821-5814* and *3EG J0706-3837* with the 1.0-m telescope. mag_{PSF} = Point Spread Function magnitude and mag_{APP} = Aperture Photometry magnitude.

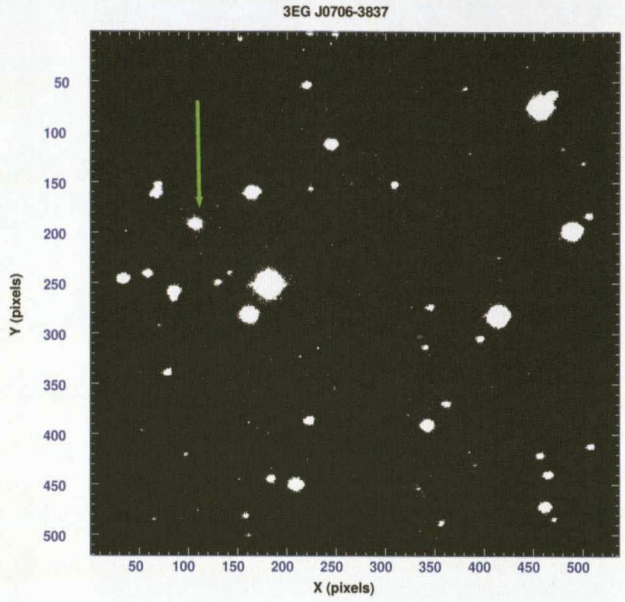

(a) *3EG J0706-3837*

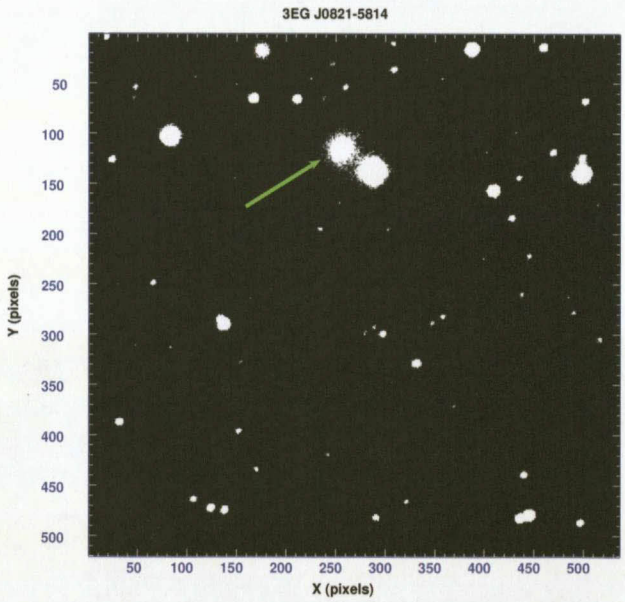

(b) *3EG J0821-5814*

Figure 4.9: (a) Image of 3EG J0706-3837 (RA: 07:10:43, Dec: -38:50:36) obtained from the 1.0-m telescope using the STE-3 CCD camera (V-filter, exposure time: 180 s, Date of observation: 16 January 2009 at 21:27:10 (UTC)). (b) Image of 3EG J0821-5814 (RA: 08:20:58, Dec: -57:05:35) obtained from the 1.0-m SAAO telescope using the STE-3 CCD camera (I-filter, exposure time: 72 s; Date of observation: 17 January 2009 at 23:02:47 (UTC)).

4.3.4 Optical light curves

Typical blazars show a variability on time scales from hours to months. Variability can be periodic or irregular. It can be also intra-day/night (few minutes to hours within a day), short-term (days to months) and long-term variability (months to years). The intra-day/night variability is believed to be related to relativistic shocks propagating down a jet and interacting with irregularities in the flow. The shortest intra-day/night variability time scale can be used to estimate an upper limit of the mass of the black hole using Equation 5.16a and Equation 5.19. The short-term variability is believed to be related to flares of hot spots on the surface of the accretion disk while the long-term variability, which can only be obtained by analysing long-time data base, is related to outbursts.

Differential photometry was performed on *3EG J0706-3837* and *3EG J0821-5814* data obtained using small telescopes i.e. 1.0-m and 1.9-m *SAAO* telescopes, with the aim of detecting possible intra-night variability in these objects.

Differential magnitudes of the targets (relative to a set of comparison stars (named star 1, 2, 3 and 4) in the same image) were measured for all images taken throughout an observing night and compiled into the light curves. Figures 4.10 and Figure 4.11 show the optical light curves of *3EG J0821-5814* and *3EG J0706-3837* respectively, in different filters. Magnitudes are obtained using the APP photometry.

Optical light curves of *3EG J0821-5814*

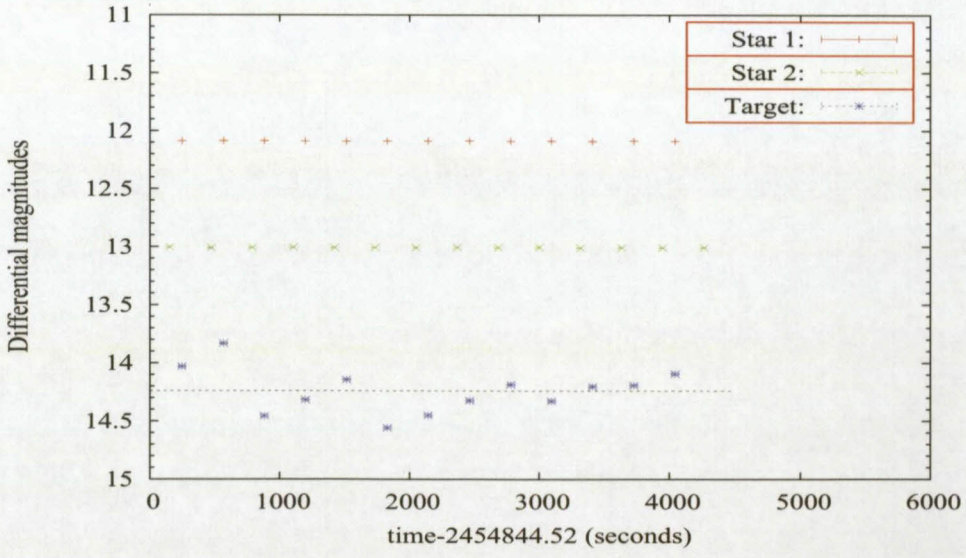

(a) Light curve of *3EG J0821-5814* in I Filter (12/01/2009)

Figure 4.10: Optical light curves of *3EG J0821-5814*.

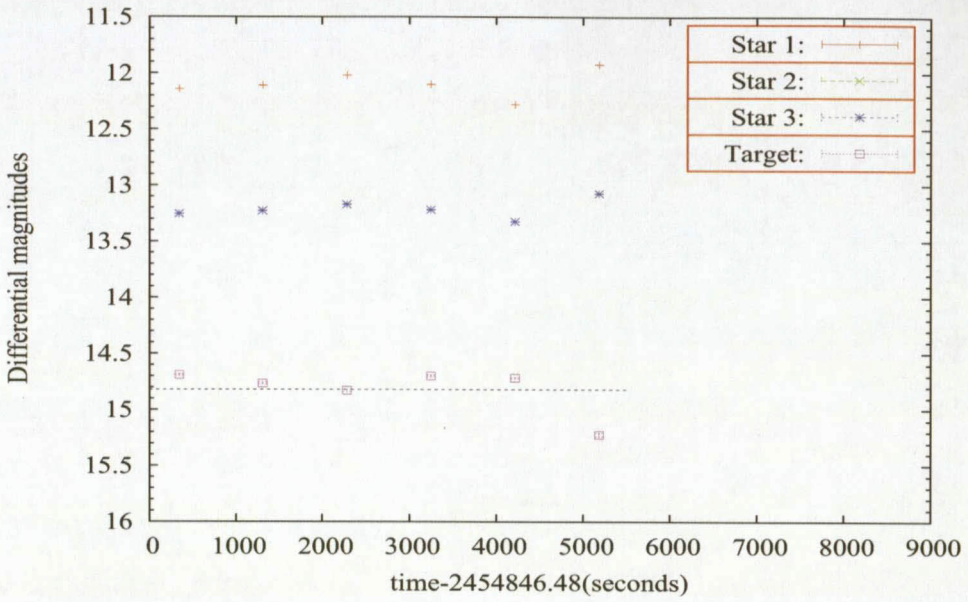

(b) Light curve of *3EG J0821-5814* in R Filter (14/01/2009)

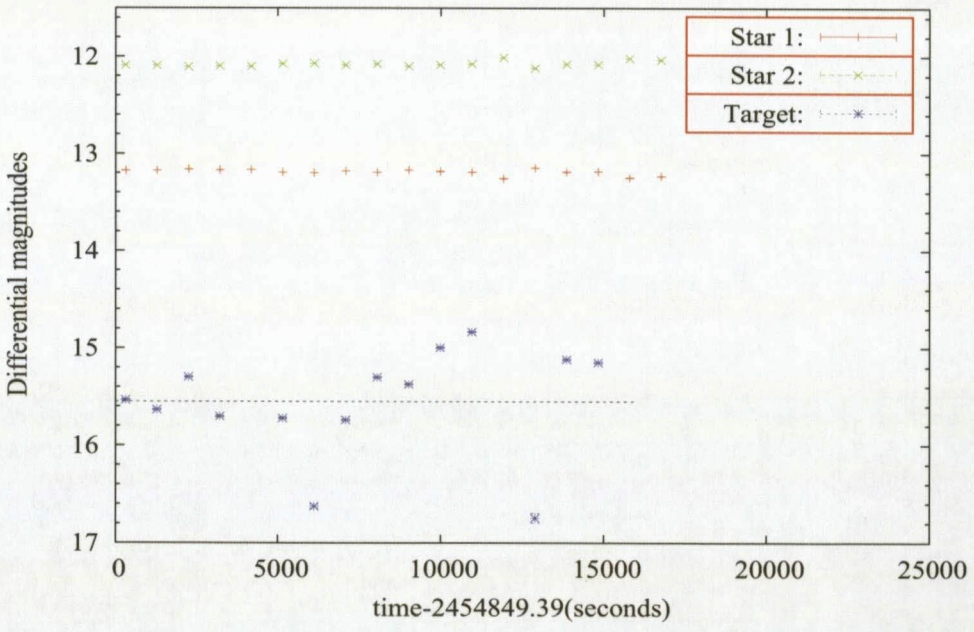

(c) Light curve of *3EG J0821-5814* in R Filter (17/01/2009)

Figure 4.10: Optical light curves of *3EG J0821-5814* (continued).

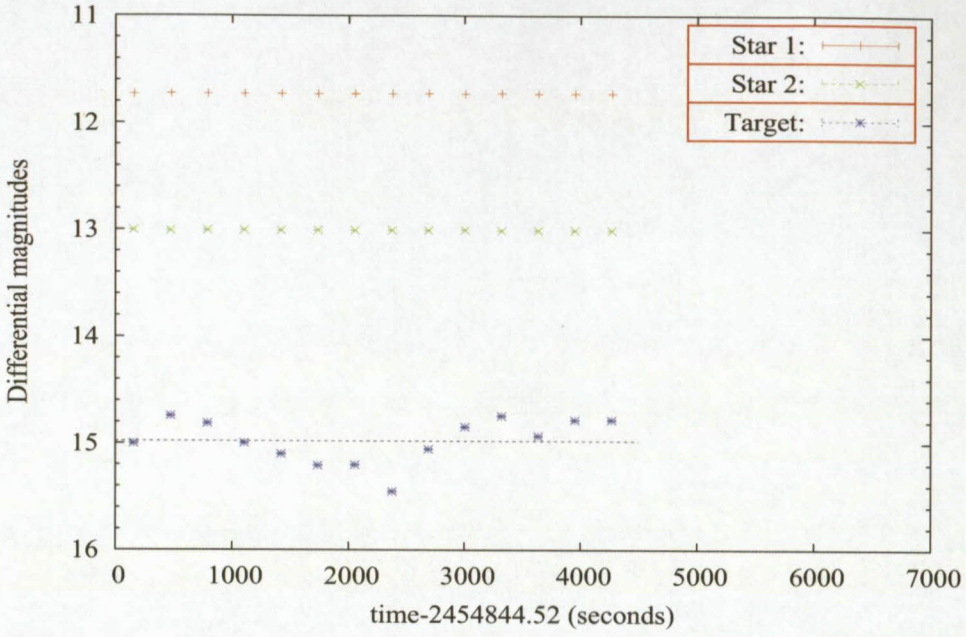

(d) Light curve of *3EG J0821-5814* in V Filter (12/01/2009)

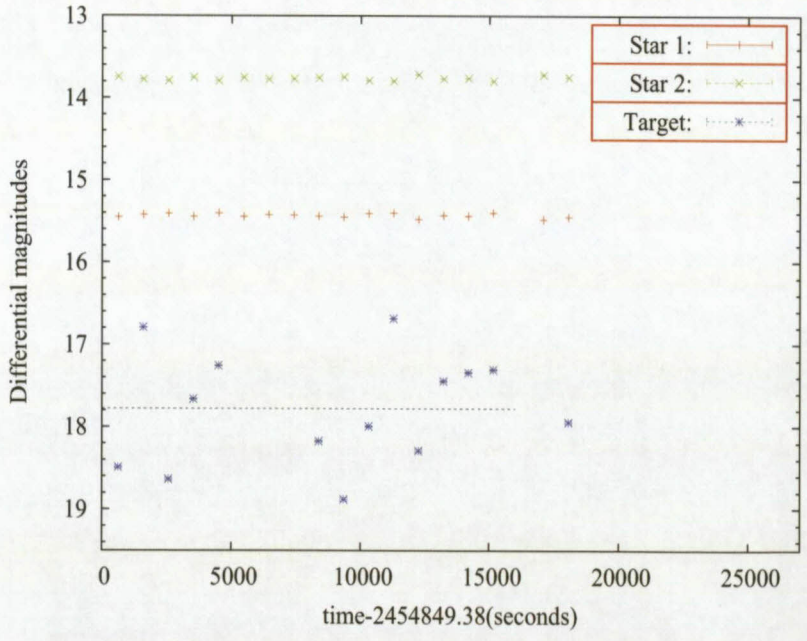

(e) Light curve of *3EG J0821-5814* in B Filter (17/01/2009)

Figure 4.10: Optical light curves of *3EG J0821-5814* (continued).

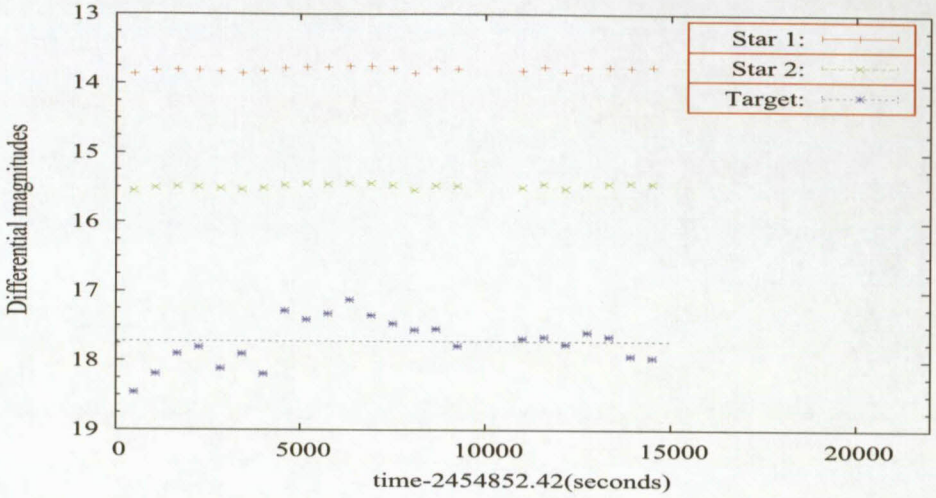

(f) Light curve of *3EG J0821-5814* in B Filter (20/01/2009)

Figure 4.10: Optical light curves of *3EG J0821-5814* (continued).

Optical light curves of *3EG J0706-3837*

Figures below show the optical light curves of *3EG J0706-3837* in different filters. Magnitudes are PSF differential magnitudes obtained using the 1.0-m and the 1.9-m telescopes.

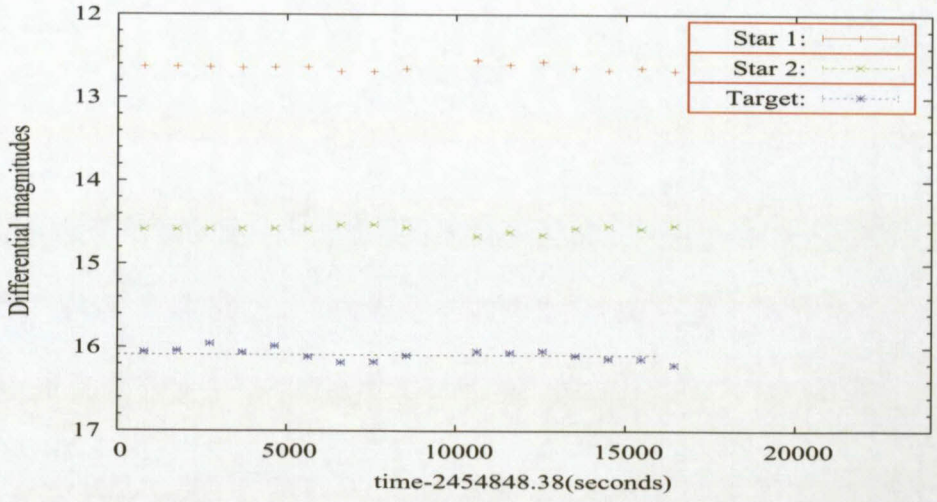

(a) Light curves of *3EG J0706-3837* in I Filter (16/01/2009)

Figure 4.11: Optical light curves of *3EG J0706-3837*.

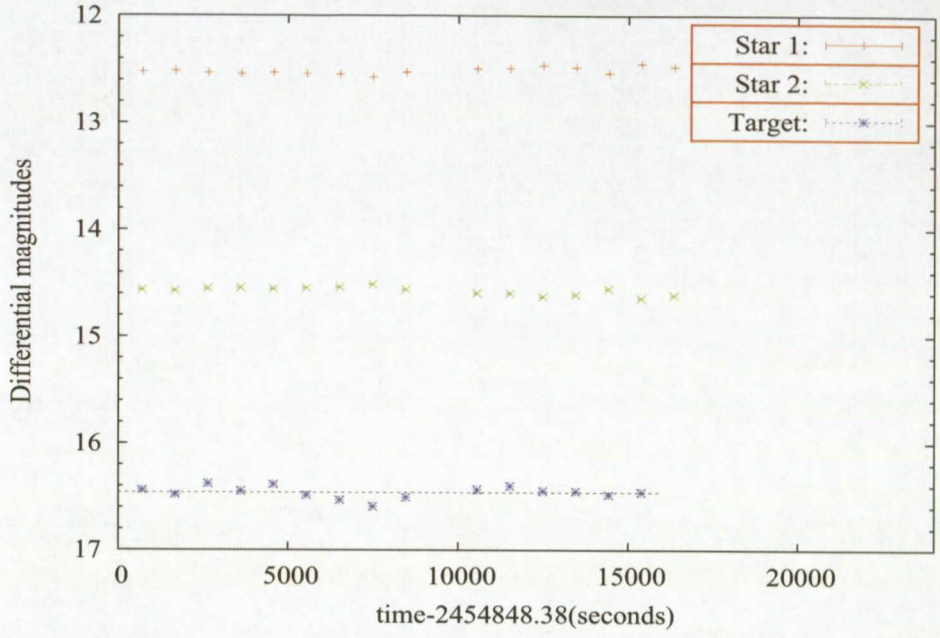

(b) Light curves of *3EG J0706-3837* in R Filter (16/01/2009)

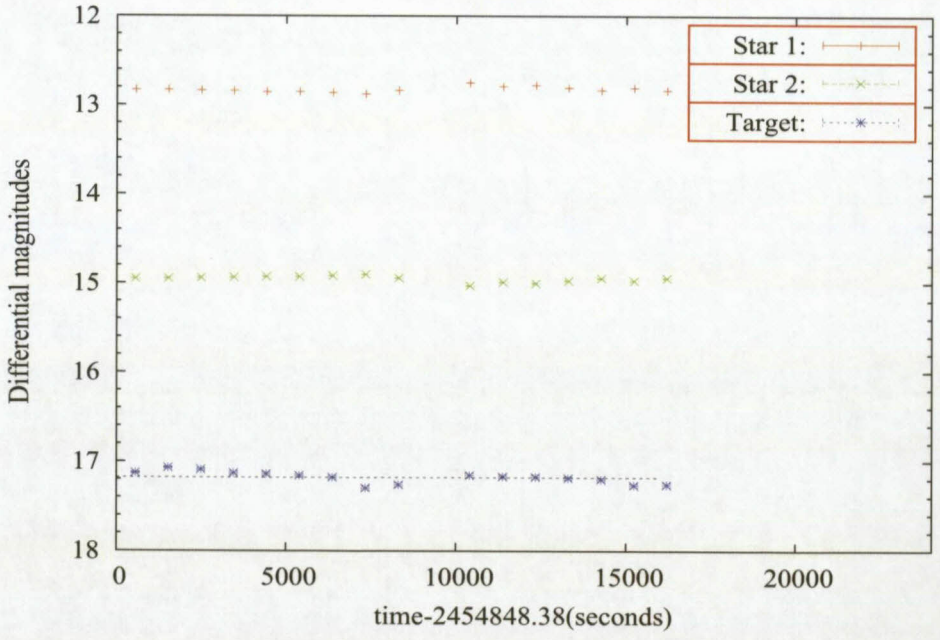

(c) Light curves of *3EG J0706-3837* in V Filter (16/01/2009)

Figure 4.11: Optical light curves of *3EG J0706-3837* (continued).

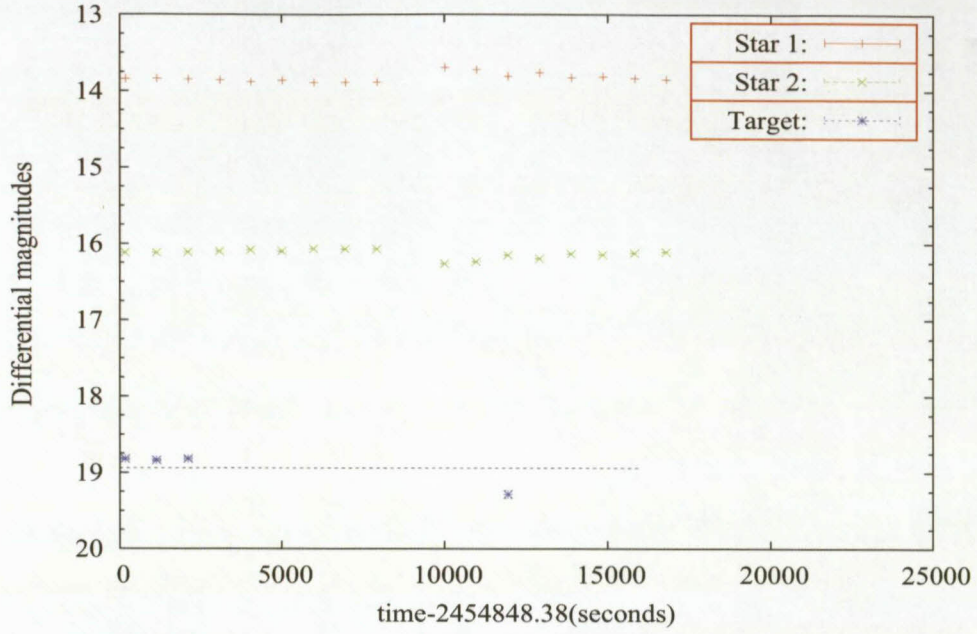

(d) Light curves of *3EG J0706-3837* in B Filter (16/01/2009)

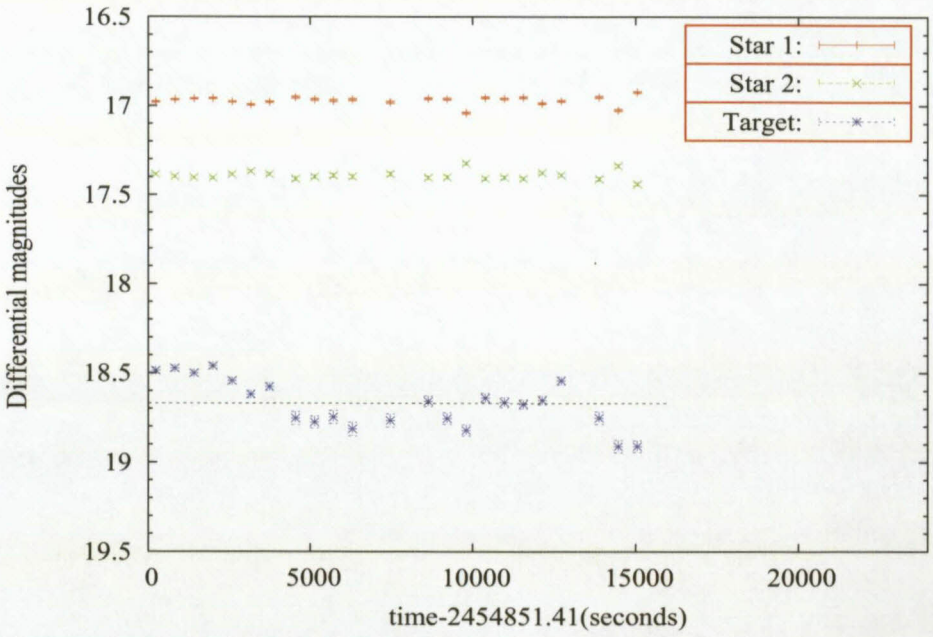

(e) Light curves of *3EG J0706-3837* in B Filter (19/01/2009)

Figure 4.11: Optical light curves of *3EG J0706-3837* (continued).

The light curves shown above seem to suggest variability of the program objects selected. However, atmospheric conditions during most of these nights were not favorable for photometry,

and follow-up observations need to be scheduled to quantify the nature of the possible variability.

4.3.5 Spectroscopic observations

4.3.5.1 Goodman spectrograph observing conditions.

The *Southern Observatory for Astrophysical Research (SOAR)* telescope (Figure 4.12) is a modern 4.1-m aperture optical & near-IR telescope located on Cerro Pachón, Chile at an elevation of 2738 metres. It was commissioned in 2003 and is operated by the *Cerro Tololo Inter-American Observatory (CTIO)* (part of the *National Optical Astronomy Observatory (NOAO)*). The telescope attains median image quality of 0.7 arcsec at 0.5 μm wavelength. Multiple instruments are available on standby. This study made use of the UV–optical 16-million pixel Goodman Spectrograph.

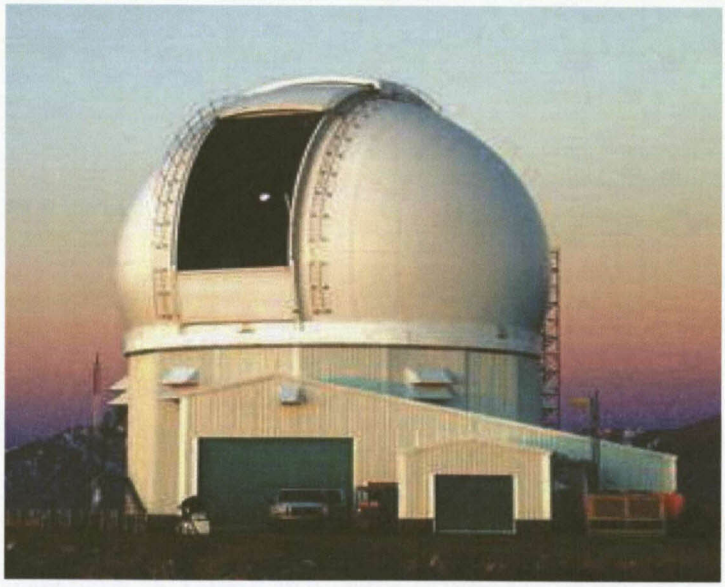

Figure 4.12: The 4.1-m *SOAR* telescope at Cerro Pachón in Chile.

Only two objects, *3EG J0821-5814* and *3EG J0706-3837*, were submitted due to the fact that they were only accessible in the southern hemisphere sky during the 2009A proposal season (running from February 2009 up to July 2009).

Observations of *3EG J0821-5814* and *3EG J0706-3837* with the *SOAR/Goodman* spectrograph were made during the night of 16/17 February 2009, in good observing conditions with seeing of 0.61 and airmass of 1.13. The *Goodman* spectrograph is equipped with a 4K×4K CCD[9] with a field of view of 3.0×5.0 arcminutes. The spatial size of a CCD pixel is 15 μm, while its angular size is 0.15 arcseconds. The low-resolution (resolving power R=1380) mode with the 300 lines/mm Volume Holographic Phase (VHP) grating covering the wavelengths from 3600 Å

[9]The useful format used is 4K×2K with a 2×2 binning.

to 9150 Å and a spectral resolution of 1.3 Å/pixel was used. Due to the fact that these objects are quite faint, a slightly larger slit of 1.68" was used. Each object was exposed for a period of 30 minutes. For flux calibration the standard star *LTT7379* was used. During the period of observation the exposures of bias, flats and comparison lamp (HgAr) for the wavelength calibration were obtained. The spectra were extracted and calibrated using the standard methods of the Image Reduction and Analysis Facility (IRAF). The process includes bias subtraction, correction for the pixel sensitivity variations, localisation, optimal extraction and rebinning to linear wavelength scale. The spectra, flux-calibrated, are plotted on Figure 4.13 and Figure 4.14.

4.3.5.2 Spectral lines analysis and redshifts

4.3.5.2.1 Spectral lines and redshift of *3EG J0821-5814*

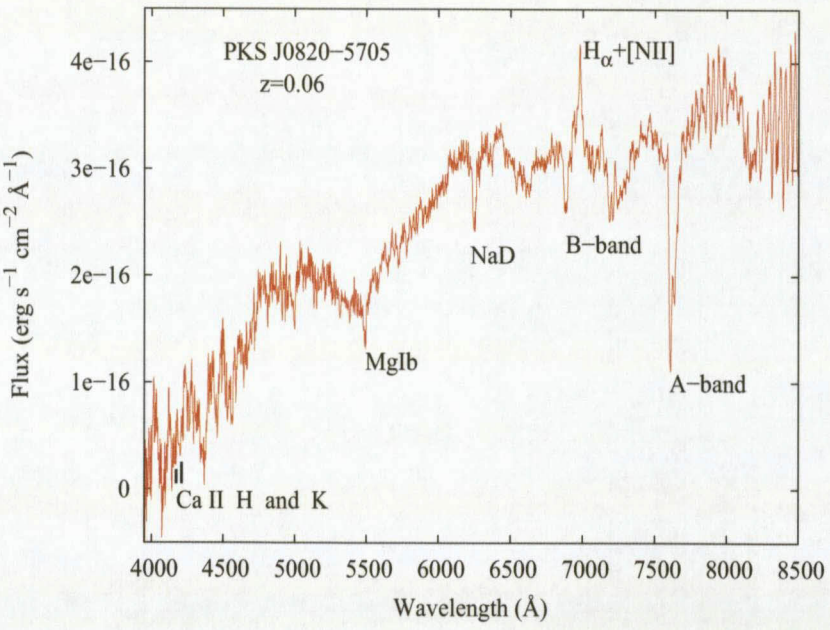

Figure 4.13: Spectral lines of *3EG J0821-5814*.

The redshift of $z = 0.06 \pm 0.01$ was determined using the shift of spectral lines in *3EG J0821-5814* (see Table 4.15).

Line	$\lambda_{\rm rest}$ (Å)	$\lambda_{\rm obs}$ (Å)	$z = \frac{\lambda_{\rm obs}}{\lambda_{\rm rest}} - 1$
Ca II	3933.66	4171.2	0.0604
	3968.47	4201.17	0.0586
MgIb	5183	5493.97	0.0600
	5172	5485.15	0.0605
Na D	5896	6253.28	0.0606
	5890	6247.71	0.0607
Hα	6562.8	6977.27	0.0632
			$z = 0.06 \pm 0.01$

Table 4.15: Measuring the redshift of *3EG J0821-5814*

The spectrum of *3EG J0821-5814* features some absorption lines at redshift z=0.06 (corresponding to a recession velocity of 18 000 km/s), e.g. Ca II K & H $\lambda\lambda$ 3933, 3968 Å, MgI b $\lambda\lambda\lambda\lambda$ 5169, 5167, 5183, 5172 Å, Na D $\lambda\lambda$5890, 5896 Å, Hβ λ 4861 Å, and only one emission line Hα + [N II] $\lambda\lambda\lambda$ 6562, 6548, 6583 Å. An instrumental fringing at the wavelengths $\lambda \geq 7600$ Å was noted. The telluric lines resulting from the earth's atmosphere absorption (essentially by Oxygen), consequently not redshifted, can also be identified, e.g. *A*-band $\lambda\lambda$ 7594-7621 Å and *B*-band $\lambda\lambda$ 6867-6884 Å. The emission line fluxes and widths were measured using the command SPLOT in IRAF (Table 4.16).

Absorption line	Line center (Å)	Flux (erg s^{-1} cm^{-2} Å^{-1})	Continuum (erg s^{-1} cm^{-2} Å^{-1})	Equivalent width (Å)
MgI b	5485.709	1.641×10^{-16}	6.64×10^{-16}	4.036
Na D	6247.768	2.893×10^{-16}	1.41×10^{-15}	4.887

Table 4.16: Line widths in *3EG J0821-5814*.

4.3.5.2.2 Spectral lines and redshift of *3EG J0706-3837*.

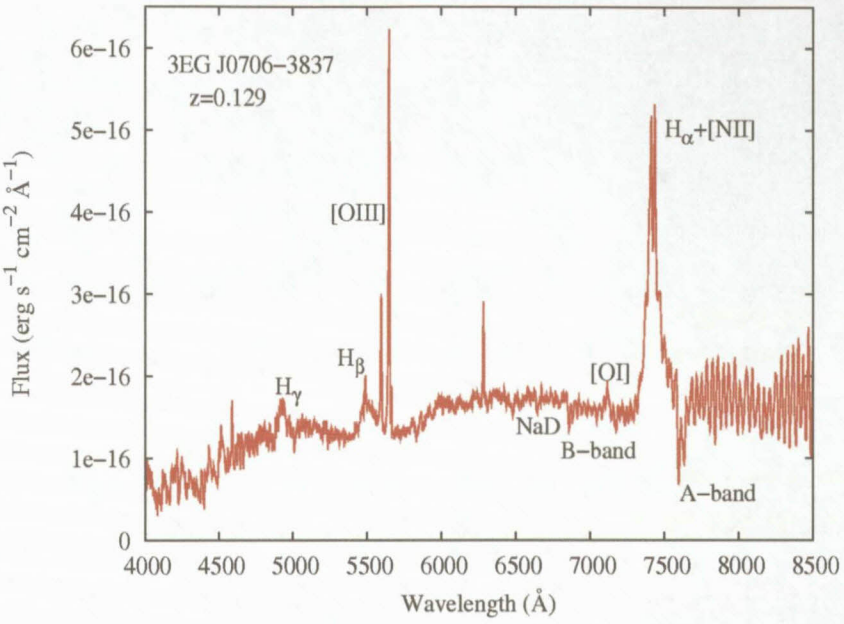

Figure 4.14: Spectral lines of *3EG J0706-3837*.

The redshift of $z = 0.129 \pm 0.001$ was determined using the shift of spectral lines in *3EG J0706-3837* (see Table 4.17).

Line	$\lambda_{\rm rest}$ (Å)	$\lambda_{\rm obs}$ (Å)	$z = \frac{\lambda_{\rm obs}}{\lambda_{\rm rest}} - 1$
Na D	5890	6647.8	0.1287
Hγ	4340.46	4917	0.1328
Hβ	4861.32	5489.12	0.1291
O III	4958.91	5595.74	0.1284
O III	5006.84	5649.21	0.1283
O I	6300.3	7116.37	0.1295
Hα	6562.8	7412.68	0.1295
N II	6583.39	7436.81	0.1296
			$z = 0.129 \pm 0.001$

Table 4.17: Measuring the redshift of *3EG J0706-3837*

The spectrum of *3EG J0706-3837* features strong and broad emission lines from the BLR such as Hα (λ 6563 Å) blended with [N II] (λ 6583 Å) at redshift $z = 0.129 \pm 0.001$, indicating a recession velocity of 38400±300 km/s. The spectrum also shows emission lines coming from

the NLR region such as [O III] lines ($\lambda\lambda$ 4959 Å, 5007 Å), Hβ (λ 4861 Å), Hγ (λ 4340 Å), and [O I] (λ 6300 Å) at the same redshift $z = 0.129$. Table 4.18 gives the widths of these highly broadened lines. The presence of Hα of velocity above 1000 km s^{-1} and forbidden lines ([O III] and [O I]) of an average velocity of about 500 km s^{1} suggests that the source is a Seyfert I galaxy (e.g. Khachikian and Weedman 1974, Osterbrock and Veilleux 1986, Osterbrock 1987).

The absorption lines Na D ($\lambda\lambda$ 5890 Å, 5896 Å respectively $3s\,^2\mathrm{S}-3p\,^2\mathrm{P}$ (yellow), $3p\,^2\mathrm{P}-3d\,^2\mathrm{D}$ (near red)) can also be identified. These lines usually indicate a strong intrinsic absorption within the galaxy.

The emission line fluxes and widths were measured using the command SPLOT in IRAF (Table 4.18).

Line	Center (Å)	Continuum erg s^{-1} cm^{-2} Å^{-1}	Flux erg s^{-1} cm^{-2} Å^{-1}	Equivalent width (Å)	FWHM (Å)	Velocity (km/s)
Hα	7409	1.784×10^{-16}	7.702×10^{-15}	43.18	58.06	2350.92
[N II]	7434	1.788×10^{-16}	1.329×10^{-14}	74.34	88.33	3564.57
[O I]	7115.75	1.512×10^{-16}	3.309×10^{-16}	2.19	9.92	418.4
[O III]	5648.5	1.396×10^{-16}	4.419×10^{-15}	31.66	8.95	475.35
[O III]	5595.25	1.312×10^{-16}	1.495×10^{-15}	11.4	9.08	487
Hβ	5486.97	1.488×10^{-16}	4.874×10^{-16}	3.28	11.52	629.86

Table 4.18: Line widths in *3EG J0706-3837*.

4.3.5.2.3 Measurement of the K_{4000} depression

H & K lines are two absorption lines of singly ionised calcium Ca II in the intergalactic gas located between the source and the observer. Ca II lines in quasars and AGNs can also come from the interstellar medium (ISM) or from late type stars located in halos of the host galaxies.

The question of the location of the absorbing material due to the fact these absorption lines appear sometimes shifted has been a big debate in literature (e.g. Boksenberg et al. (1980), Boksenberg and Sargent (1978)). In principle, these lines are supposed to be at rest wavelength position on the spectrum. If they appear shifted, the absorbing regions may be intrinsic to the objects, having been somehow ejected at observed velocities, or they may be cosmologically distributed, in direct association with close galaxies or as intergalactic clouds (Boksenberg et al. 1980).

The Ca H & K lines featured in *3EG J0821-5814*, i.e. H (λ_{rest}= 3933.66 Å, λ_{emit}= 4171.93 Å) and K (λ_{rest}= 3968.47 Å, λ_{emit}= 4208.85 Å), present the same redshift ($z \sim 0.06$) as the object suggesting the absorption material is possibly located in an extended halo[10] of the galaxy.

Ca II lines occur in the near-ultraviolet at wavelengths of H: 3969 Å and K: 3934 Å and result

[10]cloud of stars that expand out of the plane of galaxy

from the electronic transition from H: $4s\ ^2S_{\frac{1}{2}}$–$4p\ ^2P_{\frac{1}{2}}$ and K: $4s\ ^2S_{\frac{1}{2}}$–$4p\ ^2P_{\frac{3}{2}}$ (Goldberg 1964). The absorption around 4000 Å results in a depression in the emission at these wavelengths. The Ca II depression at 4000 Å is calculated using the relation

$$K_{4000} = \frac{f^+ - f^-}{f^+}, \tag{4.5}$$

where f^- is the average flux between 3750 Å and 3950 Å and f^+ is the average flux between 4050 Å and 4250 Å in the rest frame (Caccianiga et al. 1999b). For sources like BL lac objects where the optical emission of the source is dominated by a strong nonthermal emission from a nucleus, K_{4000} is less than 40% (Caccianiga et al. 1999a, Galbiati et al. 2005).

The spectrum of 3EG J0821-5814 displays a depression of $K_{4000} = 8.8$ % (e.g. Table 4.19), in accordance with what is expected from blazars. Although the H & K lines are not visible in 3EG J0706-3837, a depression of $K_{4000} \sim 80$ % is estimated (via calculation of f^+ and f^- as in the previous source), which is not in accordance with what is expected from blazars.

Object	Ca Band (in Å, rest frame)	Ca Band (in Å at $z = 0.06$)	Continuum (erg s^{-1} cm^{-2} Å^{-1})	Flux (erg s^{-1} cm^{-2} Å^{-1}))	K_{4000}
3EG J0821-5814	3750-3950	3975-4187	2.356×10^{-17}	$f^- = 2.052 \times 10^{-15}$	
	4050-4250	4293-4505	6.694×10^{-17}	$f^+ = 1.870 \times 10^{-15}$	8.8%
3EG J0706-3837	3750-3950	4233-4459	6.32×10^{-17}	$f^- = 1.297 \times 10^{-15}$	
	4050-4250	4572-4798	1.099×10^{-16}	$f^+ = 2.451 \times 10^{-16}$	80.1%

Table 4.19: Ca depression near 4000 Å in *3EG J0821-5814* and in *3EG J0706-3837*.

4.4 Multi-wavelength online data

Data from own observations were supplemented by others found in online catalogues. This is useful for the Infrared, X-ray and γ-ray photon energy bands which are not accessible with the ground-based telescopes.

4.4.1 γ-ray data

The high-energy gamma-ray data were obtained from the *EGRET* (30 MeV–10 GeV) on board the *Compton Gamma-Ray Observatory* and from the *LAT* (20 MeV–300 GeV) on board the Fermi observatory formerly known as *Gamma-ray Large Area Space Telescope (GLAST)* before it was launched.

4.4.1.1 *EGRET* data

The *EGRET* telescope on board the *Compton Gamma-Ray Observatory* was described in detail in Chapter 3. As mentioned in that Chapter, the telescope detected γ-ray photons with

energy between 30 MeV and 20 GeV emitted by 271 objects. Efforts to identify the nature of the *EGRET*-detected sources have been made so far, but a number of them still remain unidentified. The main purpose of this study is to search for possible blazars among the unidentified *EGRET* population. Thirteen *EGRET* sources were selected (see Table 4.20) for further investigation. The *EGRET* γ-ray data from these objects, were collected between April 22, 1991 and October 3, 1995 (cycles 1, 2, 3, and 4 of the mission) and obtained via `ftp://legacy.gsfc.nasa.gov/compton/data/egret/`. The data (see Table 4.21) include the observed photon flux (photons cm^{-2} s^{-1} MeV^{-1}), as well the flux estimate obtained by fitting the spectra with a power-law model over the equally spaced logarithmic energy bins (where the spectral index was kept constant and equal to the value fitted over the whole range).

No	Source Name	RA	DEC	l	b	θ_{95}	F $\pm$ Δ F	$\gamma \pm \Delta\gamma$	Counts	$\sqrt{TS}$	VP	Other names	Note
	(1)	(2)	(3)	(4)	(5)	(6)	(7)	(8)	(9)	(10)	(11)	(12)	(13)
1	*3EG J0159-3603*	29.84	-36.06	248.89	-73.04	0.79	9.8 $\pm$ 2.8	2.89 $\pm$ 0.51	47	4.3	P1234	2EG J0159-3557	
2	*3EG J0500+2502*	75.07	25.49	177.18	-10.28	0.36*	11.3$\pm$ 3	2.52 $\pm$ 0.32	152	4.1	P1		em
3	*3EG J0702-6212*	105.58	-62.21	272.65	-22.56	1.04	13.5$\pm$ 3.7	2.4 $\pm$ 0.33	70	4.3	P34		em
4	*3EG J0706-3837*	106.72	-38.63	249.57	-13.76	0.9	52$\pm$ 17.8	2.3 $\pm$ 0.43	22	4.1	44		em
5	*3EG J0724-4713*	111.09	-47.23	259	-14.38	0.95	16.8$\pm$ 3.5	2.6 $\pm$ 0.36	122	5.5	P12	2EG J0720-4746 1FGL J0724.7-4714 CGRaBS J0728-4705	em
6	*3EG J0821-5814*	125.32	-58.24	273.1	-12.04	1.26	28.2$\pm$ 8.4	3.22 $\pm$ 0.79	49	4	P4		em
7	*3EG J1300-4406*	195.06	-44.1	304.6	18.74	0.84	10.6$\pm$ 2.9	3.07 $\pm$ 0.40	95	4.1	P12	*1FGL J1304.3-4352*	C
8	*3EG J1659-6251*	254.97	-62.86	327.32	-12.47	0.73*	47$\pm$ 13.1	2.54 $\pm$ 0.37	43	4.6	314	2EGS J1703-6302 *1FGL J1702.7-6217* CGRaBS J1703-6212	em
9	*3EG J1709-0828*	257.26	-8.47	12.86	18.25	1.01	12.6$\pm$ 3.2	3 $\pm$ 0.35	161	4.2	P1234	2EGS J1708-0927 *1FGL J1708.4-0755*	em
10	*3EG J1800-0146*	270.22	-1.78	25.49	10.39	0.77	26.1$\pm$ 6.1	2.79 $\pm$ 0.22	151	4.8	P34		em
11	*3EG J1813-6419*	273.34	-64.33	330.04	-20.32	0.68	14.2$\pm$ 4	2.85 $\pm$ 0.44	64	4.2	P1234	CGRaBS J1807-6413	C
12	*3EG J1822+1641*	275.57	16.7	44.84	13.84	0.77	40.6$\pm$ 11.5	3.06 $\pm$ 0.68	45	4.5	328		em
13	*3EG J1824+3441*	276.21	34.69	62.49	20.14	0.82	28.7$\pm$ 9.3	2.03 $\pm$ 0.50	30	4	20		em

Table 4.20: *EGRET* Gamma-ray parameters of selected sources. (1) *EGRET* name in the third catalogue. (2) Right Ascension in degrees. (3) Declination in degrees. (4) Galactic longitude in degrees. (5) Galactic latitude in degrees. (6) The radius in degrees of the circle containing the same solid angle as the 95% confidence contour of the confinement of the source. An asterisk means that the value was obtained by multiplying the 68% by 1.62. This was sometimes necessary for unclosed or extremely irregular 95% contours (e.g. Hartman et al. (1999)). (7) Photon Flux ($\times 10^{-8}$ photons.cm^{-2}.s^{-1}). (8) Photon spectral index, $F = F_0 E^{-\gamma}$. (9) Counts. (10) Test Statistics , $\sqrt{TS}$ is equivalent to the well-known σ. (11) Viewing period. (12) Other names in other γ-ray catalogues e.g. the *Second EGRET* catalogue (2EG) (Thompson et al. 1995), the *First Fermi Gamma-Ray Large Area Telescope Catalogue (1FGL)* (Abdo et al. 2010b), the *Candidate Gamma-Ray Blazar Survey (CRGaBS)* (Healey et al. 2008b). (13) Note: em=possibly extended source or multiple sources (based on source location maps inconsistent with single point source or poor fit to the calibrated PSF, from observation of sum of observations. C=source confusion may affect the flux, significance or position). Below-threshold may have been considered in assigning this symbol, so weak sources may be designated as confused despite no other catalogue sources nearby. Sources with no entry in this column are consistent with the *EGRET* PSF for a single source.

Source name	Channel	E_{min} MeV	E_{max} MeV	Model flux (*)	Obs flux (*)	Error (*)	χ (**)
3EG J0159-3603	1	30	50	2.55×10^{-08}			
	2	50	70	7.38×10^{-09}			
	3	70	100	2.71×10^{-09}	2.97×10^{-09}	1.63×10^{-09}	0.16
	4	100	150	9.04×10^{-10}	1.17×10^{-09}	4.89×10^{-10}	0.54
	5	150	300	1.91×10^{-10}	2.58×10^{-10}	1.11×10^{-10}	0.6
	6	300	500	3.27×10^{-11}			
	7	500	1000	5.87×10^{-12}			
	8	1000	2000	7.90×10^{-13}			
	9	2000	4000	1.06×10^{-13}			
	10	4000	10000	1.08×10^{-14}	8.88×10^{-13}	8.12×10^{-13}	1.08
3EG J0500+2502	1	30	50	1.26×10^{-08}			
	2	50	70	4.28×10^{-09}	1.04×10^{-08}	4.56×10^{-09}	1.35
	3	70	100	1.78×10^{-09}	2.25×10^{-09}	1.21×10^{-09}	0.39
	4	100	150	6.83×10^{-10}			
	5	150	300	1.74×10^{-10}	1.55×10^{-10}	9.23×10^{-11}	-0.2
	6	300	500	3.75×10^{-11}	4.47×10^{-11}	3.01×10^{-11}	0.24
	7	500	1000	8.30×10^{-12}			
	8	1000	2000	1.44×10^{-12}	1.80×10^{-12}	1.69×10^{-12}	0.21
	9	2000	4000	2.50×10^{-13}	4.01×10^{-13}	3.99×10^{-13}	0.38
	10	4000	10000	3.35×10^{-14}			
3EG J0702-6212	1	30	50	9.19×10^{-09}	6.52×10^{-08}	2.69×10^{-08}	2.08
	2	50	70	3.30×10^{-09}			
	3	70	100	1.44×10^{-09}			
	4	100	150	5.75×10^{-10}	5.28×10^{-10}	3.53×10^{-10}	-0.13
	5	150	300	1.56×10^{-10}			
	6	300	500	3.63×10^{-11}	5.45×10^{-11}	2.72×10^{-11}	0.67
	7	500	1000	8.61×10^{-12}	1.90×10^{-11}	8.06×10^{-12}	1.29
	8	1000	2000	1.63×10^{-12}			
	9	2000	4000	3.07×10^{-13}			
	10	4000	10000	4.50×10^{-14}			
3EG J0706-3837	1	30	50	8.36×10^{-09}	4.00×10^{-08}	2.86×10^{-08}	1.11
	2	50	70	3.15×10^{-09}	1.02×10^{-08}	6.44×10^{-09}	1.1
	3	70	100	1.42×10^{-09}			
	4	100	150	5.93×10^{-10}			
	5	150	300	1.69×10^{-10}			
	6	300	500	4.23×10^{-11}	8.89×10^{-11}	4.94×10^{-11}	0.94
	7	500	1000	1.07×10^{-11}	2.87×10^{-11}	1.47×10^{-11}	1.23
	8	1000	2000	2.17×10^{-12}	1.82×10^{-12}	2.41×10^{-12}	-0.15
	9	2000	4000	4.42×10^{-13}			
	10	4000	10000	7.04×10^{-14}			
3EG J0724-4713	1	30	50	1.72×10^{-08}	2.70×10^{-08}	2.32×10^{-08}	0.42
	2	50	70	5.65×10^{-09}			
	3	70	100	2.30×10^{-09}	2.47×10^{-09}	1.30×10^{-09}	0.13
	4	100	150	8.54×10^{-10}	1.08×10^{-09}	4.52×10^{-10}	0.5
	5	150	300	2.09×10^{-10}	1.53×10^{-10}	8.84×10^{-11}	-0.63
	6	300	500	4.30×10^{-11}	5.35×10^{-11}	3.13×10^{-11}	0.34
	7	500	1000	9.10×10^{-12}	1.16×10^{-11}	8.85×10^{-12}	0.28
	8	1000	2000	1.50×10^{-12}			
	9	2000	4000	2.47×10^{-13}			
	10	4000	10000	3.11×10^{-14}	3.39×10^{-13}	3.04×10^{-13}	1.01

(*): Photon cm^{-2} s^{-1} MeV^{-1} (**): $\chi = \frac{\text{Obs flux} - \text{Model flux}}{\text{Error}}$

Table 4.21: *EGRET* γ-ray data of selected sources.

Source name	Channel	E_{min} MeV	E_{max} MeV	Model flux (*)	Obs flux (*)	Error (*)	χ (**)
3EG J0821-5814	1	30	50	2.92×10^{-08}	3.52×10^{-08}	2.92×10^{-08}	0.2
	2	50	70	7.28×10^{-09}			
	3	70	100	2.39×10^{-09}	1.51×10^{-09}	1.34×10^{-09}	-0.66
	4	100	150	7.06×10^{-10}	1.26×10^{-09}	4.46×10^{-10}	1.25
	5	150	300	1.27×10^{-10}			
	6	300	500	1.76×10^{-11}			
	7	500	1000	2.63×10^{-12}			
	8	1000	2000	2.82×10^{-13}			
	9	2000	4000	3.03×10^{-14}			
	10	4000	10000	2.40×10^{-15}			
3EG J1300-4406	1	30	50	3.21×10^{-08}	5.20×10^{-08}	2.77×10^{-08}	0.72
	2	50	70	8.58×10^{-09}	8.17×10^{-09}	5.00×10^{-09}	-0.08
	3	70	100	2.97×10^{-09}	2.67×10^{-09}	1.26×10^{-09}	-0.24
	4	100	150	9.26×10^{-10}	9.83×10^{-10}	4.30×10^{-10}	0.13
	5	150	300	1.79×10^{-10}	1.48×10^{-10}	9.03×10^{-11}	-0.35
	6	300	500	2.74×10^{-11}			
	7	500	1000	4.44×10^{-12}	1.00×10^{-11}	7.56×10^{-12}	0.74
	8	1000	2000	5.29×10^{-13}	3.45×10^{-12}	2.21×10^{-12}	1.32
	9	2000	4000	6.31×10^{-14}			
	10	4000	10000	5.59×10^{-15}			
3EG J1659-6251	1	30	50	5.04×10^{-08}			
	2	50	70	1.53×10^{-08}	1.95×10^{-08}	6.88×10^{-09}	0.62
	3	70	100	5.82×10^{-09}	7.67×10^{-09}	1.84×10^{-09}	1
	4	100	150	2.02×10^{-09}	1.20×10^{-09}	6.22×10^{-10}	-1.32
	5	150	300	4.50×10^{-10}	4.61×10^{-10}	1.50×10^{-10}	0.07
	6	300	500	8.25×10^{-11}	1.52×10^{-10}	5.41×10^{-11}	1.29
	7	500	1000	1.57×10^{-11}	1.91×10^{-11}	1.32×10^{-11}	0.25
	8	1000	2000	2.28×10^{-12}			
	9	2000	4000	3.31×10^{-13}			
	10	4000	10000	3.63×10^{-14}			
3EG J1709-0828	1	30	50	3.96×10^{-08}			
	2	50	70	1.17×10^{-08}	9.54×10^{-09}	7.70×10^{-09}	-0.28
	3	70	100	4.37×10^{-09}	4.29×10^{-09}	2.15×10^{-09}	-0.04
	4	100	150	1.48×10^{-09}	2.02×10^{-09}	7.10×10^{-10}	0.75
	5	150	300	3.21×10^{-10}	3.46×10^{-10}	1.45×10^{-10}	0.18
	6	300	500	5.66×10^{-11}			
	7	500	1000	1.04×10^{-11}			
	8	1000	2000	1.45×10^{-12}			
	9	2000	4000	2.02×10^{-13}			
	10	4000	10000	2.12×10^{-14}	4.79×10^{-13}	5.48×10^{-13}	0.83

(*): Photon cm^{-2} s^{-1} MeV^{-1} (**): $\chi = \frac{\text{Obs flux} - \text{Model flux}}{\text{Error}}$

Table 4.21: *EGRET* γ-ray data of the selected sources (continued).

Source name	Channel	E_{min} MeV	E_{max} MeV	Model flux (*)	Obs flux (*)	Error (*)	χ (**)
3EG J1800-0146	1	30	50	5.04×10^{-08}			
	2	50	70	1.53×10^{-08}	1.95×10^{-08}	6.88×10^{-09}	0.62
	3	70	100	5.82×10^{-09}	7.67×10^{-09}	1.84×10^{-09}	1
	4	100	150	2.02×10^{-09}	1.20×10^{-09}	6.22×10^{-10}	-1.32
	5	150	300	4.50×10^{-10}	4.61×10^{-10}	1.50×10^{-10}	0.07
	6	300	500	8.25×10^{-11}	1.52×10^{-10}	5.41×10^{-11}	1.29
	7	500	1000	1.57×10^{-11}	1.91×10^{-11}	1.32×10^{-11}	0.25
	8	1000	2000	2.28×10^{-12}			
	9	2000	4000	3.31×10^{-13}			
	10	4000	10000	3.63×10^{-14}			
3EG J1813-6419	1	30	50	3.96×10^{-08}			
	2	50	70	1.17×10^{-08}	9.54×10^{-09}	7.70×10^{-09}	-0.28
	3	70	100	4.37×10^{-09}	4.29×10^{-09}	2.15×10^{-09}	-0.04
	4	100	150	1.48×10^{-09}	2.02×10^{-09}	7.10×10^{-10}	0.75
	5	150	300	3.21×10^{-10}	3.46×10^{-10}	1.45×10^{-10}	0.18
	6	300	500	5.66×10^{-11}			
	7	500	1000	1.04×10^{-11}			
	8	1000	2000	1.45×10^{-12}			
	9	2000	4000	2.02×10^{-13}			
	10	4000	10000	2.12×10^{-14}	4.79×10^{-13}	5.48×10^{-13}	0.83
3EG J1822+1641	1	30	50	2.92×10^{-08}	3.52×10^{-08}	2.92×10^{-08}	0.2
	2	50	70	7.28×10^{-09}			
	3	70	100	2.39×10^{-09}	1.51×10^{-09}	1.34×10^{-09}	-0.66
	4	100	150	7.06×10^{-10}	1.26×10^{-09}	4.46×10^{-10}	1.25
	5	150	300	1.27×10^{-10}			
	6	300	500	1.76×10^{-11}			
	7	500	1000	2.63×10^{-12}			
	8	1000	2000	2.82×10^{-13}			
	9	2000	4000	3.03×10^{-14}			
	10	4000	10000	2.40×10^{-15}			
3EG J1824+3441	1	30	50	2.67×10^{-09}			
	2	50	70	1.13×10^{-09}			
	3	70	100	5.58×10^{-10}			
	4	100	150	2.57×10^{-10}	4.18×10^{-10}	3.95×10^{-10}	0.41
	5	150	300	8.42×10^{-11}			
	6	300	500	2.48×10^{-11}			
	7	500	1000	7.28×10^{-12}	2.19×10^{-11}	1.07×10^{-11}	1.37
	8	1000	2000	1.78×10^{-12}	3.76×10^{-12}	2.88×10^{-12}	0.69
	9	2000	4000	4.35×10^{-13}			
	10	4000	10000	8.47×10^{-14}			

(*): Photon cm^{-2} s^{-1} MeV^{-1} (**): $\chi = \frac{\text{Obs flux} - \text{Model flux}}{\text{Error}}$

Table 4.21: *EGRET* γ-ray data of the selected sources (continued).

4.4.1.2 *Fermi-LAT* data

Details on the *Fermi-LAT* were discussed in Chapter 3 of this thesis. As mentioned in that chapter, the *F*ermi-LAT is a pair-conversion γ-ray telescope sensitive to photon energies between 20 MeV and 300 GeV. Launched on 11 June 2008, *Fermi-LAT* started to collect high energy γ-ray photons on 4 August 2008. The Fermi data are made public on a daily basis and can be accessed online at the official website of Fermi Science support center (`http://fermi.gsfc.nasa.gov/cgi-bin/ssc/LAT/LATDataQuery.cgi`). Results on the sources detected during the first 11

months of operation were released in February 2010, in the form of the First Fermi Gamma-Ray Large Area Telescope Catalogue (1FGL) (`http://fermi.gsfc.nasa.gov/ssc/data/access/lat/1yr\_catalog/`). Four sources in our sample of study were detected. These are 1FGL J0724.7-4714, *1FGL J1304.3-4352*, *1FGL J1702.7-6217* and *1FGL J1708.4-0755*, counterparts of *3EG J0724-4713*, *3EG J1300-4406* , *3EG J1659-6251* and *3EG J1709-0828* respectively.

The data analysed for these sources and in general for sources in the 1FGL catalogue were obtained during 4 August 2008 4 July 2009 (*LAT* runs 239557414 through 268411953, where the numbers refer to the Mission Elapsed Time (MET) in seconds since 00:00 UTC on 1 January 2001, at the start of the data acquisition runs). During most of this time Fermi was operating in sky-scanning survey mode (viewing direction rocking 35° north and south of the zenith on alternate orbits).

To minimize systematic errors, only photons with energies greater than 100 MeV were considered in the analysis. In order to avoid contamination from Earth limb gamma-rays, a selection on the zenith angle, < 105, was applied. This analysis was performed with the standard analysis tool, *gtlike*, part of the *Fermi-LAT* Science Tools software package (version v9r12). Photons were selected in circular Region of Interest (ROI) centred at the positions of the sources of interest. Figures 4.15,4.16,4.17 and 4.18 show the 12 degree-radius Region of Interests (ROIs) around the selected objects.

The ROI was obtained using *gtselect*, followed by *gtmktime* of the *Fermi-LAT* tools. *gtselect* is applied to a list of input files of the raw event data file and creates a new FITS file of selected rows based on specified cuts that are applied to each row of the input files. The selection involves mainly the type of *event-class* which is *diffuse* in this case, the time range (start time and end time of the target observation) and the energy range (between 100 MeV and 100 GeV). The *gtmktime* tool is used to read the spacecraft data file and, based on specified cuts, creates a set of Good Time Intervals (GTIs). These are time ranges when the data can be considered valid. Briefly, GTIs are lists of times that the *LAT* was collecting good data over the time range selected. All events outside this new set of GTI are removed from the file. The *gtmktime* tool is finally applied to event data selected using *gtselect* and by default the event data will be filtered according to the GTIs that are created. The default is to select times when the spacecraft is not in the South Atlantic Anomaly (SAA).

It can be seen that the regions display bright caps at the top (when $b < 0$) or at the bottom when ($b > 0$). These bright regions are diffuse galactic background γ-rays. Different analyses were performed by fitting the spectra with various models over the whole energy range covered by the *LAT* above 100 MeV, or with a power-law model over equally spaced logarithmic energy bins (where the spectral index was kept constant and equal to the value fitted over the whole range). Results are presented in Table 4.22. More on Fermi Science Data Analysis Tools can be found at `http://fermi.gsfc.nasa.gov/ssc/data/analysis/documentation/Cicerone/`.

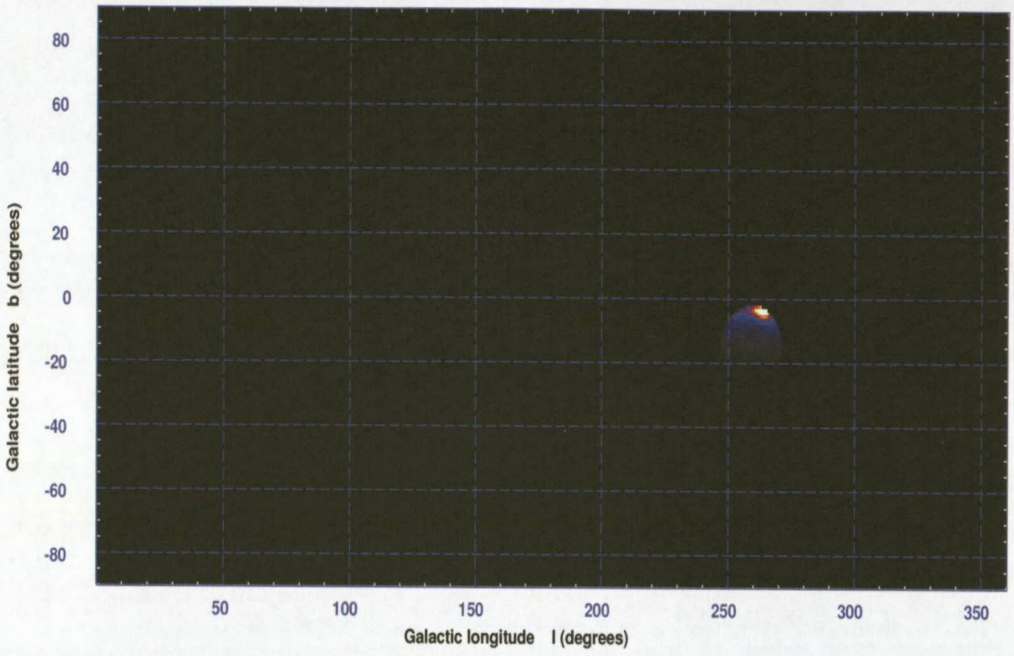

(a) *3EG J0724-4713* (b=-14.32°)

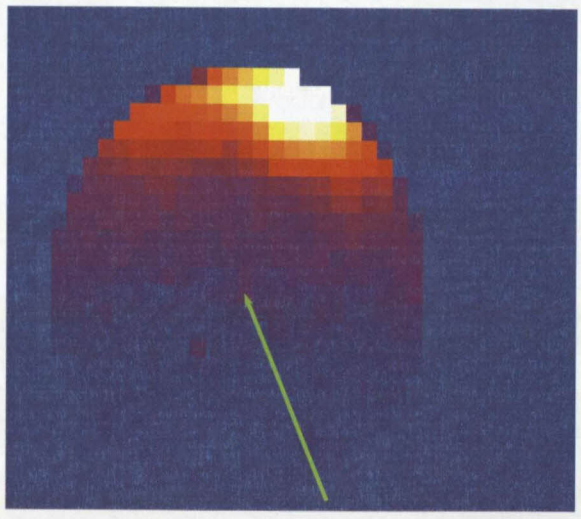

(b) *3EG J0724-4713 (zoom-in of the ROI)*

Figure 4.15: Regions of Interest (ROI) centred at *3EG J0724-4713*. It can be seen that as $b < 0°$, the γ-ray galactic diffuse emission contributes towards the North of the ROI.

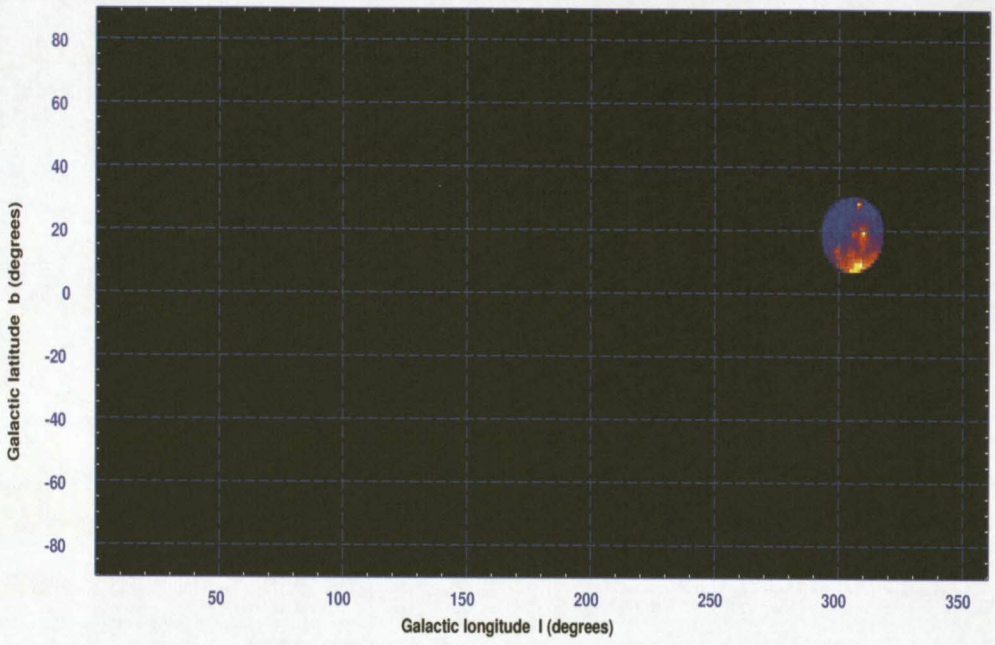

(a) *3EG J1300-4406* (b=18.94°)

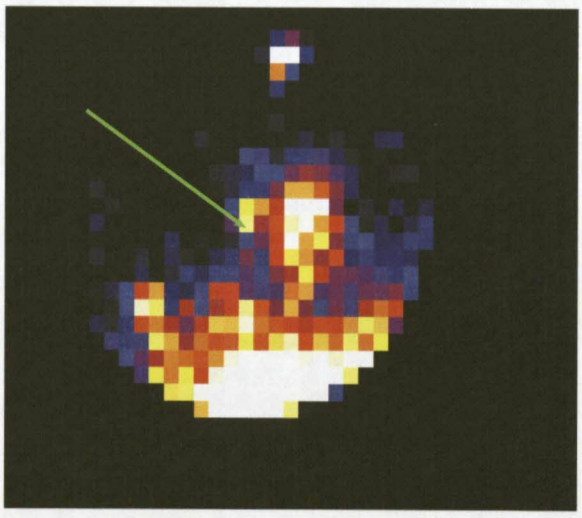

(b) *3EG J1300-4406 (zoom-in of the ROI)*

Figure 4.16: Regions of Interest (ROI) centred at *3EG J1300-4406* . It can be seen as $b > 0°$, the γ-ray galactic diffuse emission contributes towards the South of the ROI.

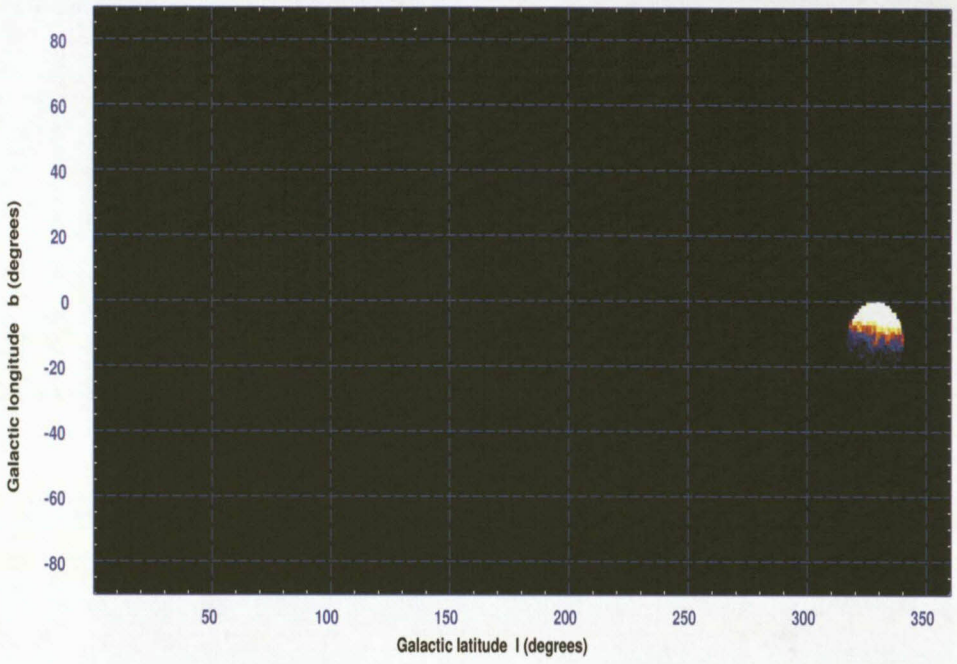

(a) *3EG J1659-6251* (b=-12.40°)

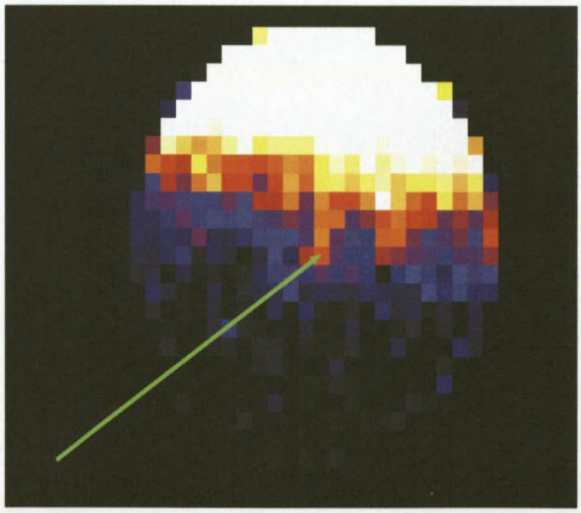

(b) *3EG J1659-625 (zoom-in of the ROI)*

Figure 4.17: Regions of Interest centred at *3EG J1659-6251*. It can be seen that for targets with $b < 0°$, the γ-ray galactic diffuse emission contributes towards the North of the ROI.

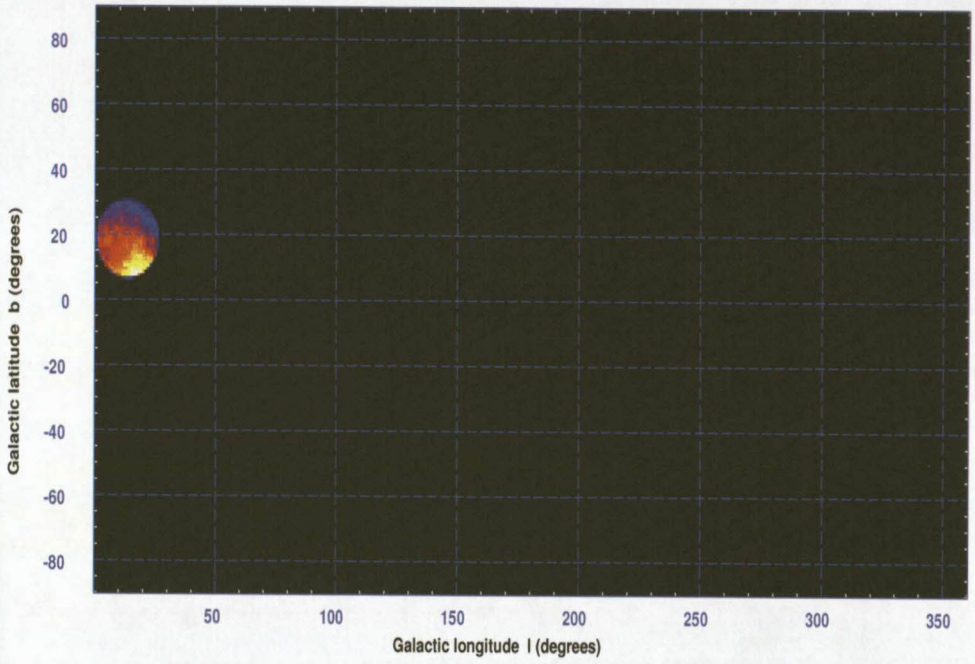

(a) *3EG J1709-0828* (b=18.7.40°)

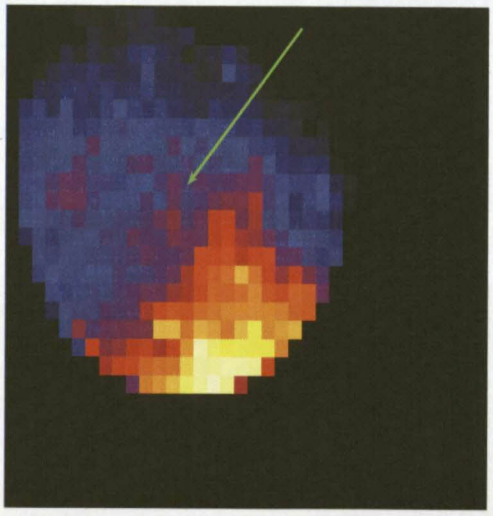

(b) *3EG J1709-0828 (zoom-in of the ROI)*

Figure 4.18: Regions of Interest centred at *3EG J1709-0828*. It can be seen that as $b > 0°$, the γ-ray galactic diffuse emission contributes towards the South of the ROI.

Parameters	Units	Sources			
3EG_Name (1)		*J0724-4714*	*J1300-4406*	*J1659-6212*	*J1709-0828*
1FGL_Name (2)		*J0724.7-4714*	*J1304.3-4352*	*J1702.7-6217*	*J1708.4-0755*
RA (3)	deg	111.00	196.09	256.00	257.00
DEC (4)	deg	-47.20	-43.87	-62.30	-7.92
l (5)	deg	259.00	305.39	328.00	13.30
b (6)	deg	-14.32	18.94	-12.40	18.67
Flux_Density (7)	($\times 10^{-12}$) photon/cm^2/MeV/s	2.16±0.45	1.43±0.15	7.08±0.11	7.66±0.11
Spectral_Index (8)		2.45±0.16	2.05±0.08	2.54±0.13	2.55±0.12
Flux1000 (9)	($\times 10^{-9}$) photon/cm^2/s	0.81±0.36	3.69±0.47	1.21±0.41	1.61±0.44
Energy_Flux (10)	($\times 10^{-11}$) erg/cm^2/s	1.10±0.38	3.45±0.62	1.75±0.48	2.37±0.45
Curvature_Index (11)		1.79	1.18	2.98	1.04
Flux100_300 (12)	($\times 10^{-9}$) photon/cm^2/s	33.33	54.70	55.08	50.70±13.70
Sqrt_TS100_300 (13)		1.20	1.09	2.30	3.76
Flux300_1000 (14)	($\times 10^{-9}$) photon/cm^2/s	5.59±1.52	7.60±1.76	6.14±1.74	7.36±2.14
$\sqrt{TS}$300_1000 (15)		3.99	4.77	3.82	3.62
Flux1000_3000 (16)	($\times 10^{-9}$) photon/cm^2/s	1.38	2.61±0.43	1.13±0.38	1.36±0.41
$\sqrt{TS}$1000_3000 (17)		3.00	9.82	3.62	4.28
Flux3000_10000 (18)	($\times 10^{-9}$) photon/cm^2/s	0.28	0.86±0.20	0.22	0.55
$\sqrt{TS}$3000_10000 (19)		1.62	9.35		3.09
Flux10000_100000 (20)	($\times 10^{-9}$) photon/cm^2/s	0.16	0.22±0.09	0.26	0.11
$\sqrt{TS}$10000_100000 (21)		2.21	7.29	2.97	
Variability_Index (22)		11.70	8.63	11.80	12.30
Flux_History (23)	($\times 10^{-8}$) photon/cm^2/s	0.80±2.05	3.70±1.27	3.55±2.58	3.10±2.98
		2.28±1.80	3.49±1.31	1.94±2.26	5.88±3.13
		3.26±2.14	3.07±1.10	5.45±2.85	13.20±3.14
		0.62±1.67	3.21±1.29	7.72±2.42	5.41±2.88
		1.92±1.62	2.17±1.05	6.94±2.98	2.02±2.52
		0.00±1.55	4.52±1.42	3.57±2.71	6.54±2.98
		5.17±2.23	6.73±1.40	1.96±2.38	6.20±2.86
		2.18±1.98	4.71±1.55	2.09±2.53	3.41±2.79
		5.64±2.00	4.15±1.31	8.50±2.41	6.51±3.17
		0.39±2.08	2.70±1.51	1.34±2.15	5.56±2.81
		5.28±1.94	3.89±1.36	7.11±2.86	0.63±2.77

Table 4.22: *Fermi-LAT* observations of 4 selected sources (Abdo et al. 2010a). (1) and (2): add 3EG and 1FGL resepectively to get the complete source names. (3) and (4): Right Ascension (J2000) and Declination (J2000). (5) and (6): Galactic Longitude and Galactic Latitude (7): Differential photon flux derived for 100 MeV–100 GeV. (8): Photon number power-law index derived from for 100 MeV–100 GeV. (9): Photon flux for 1 GeV–100 GeV obtained by summing the photon flux values in the three bands from 1 GeV to 100 GeV. (10): Energy flux from 100 MeV to 100 GeV obtained by summing the energy values in the five bands (11): Result of a χ^2 test of the photon fluxes in the five bands against the predicted fluxes in those bands as derived from the best-fit power law for 100 MeV–100 GeV. A value greater than 11.34 indicates less than 1% chance that the power-law spectrum is a good fit to the 5-band fluxes. (12 and 13, 14 and 15, 16 and 17, 18 and 19, 20 and 21): Integral photon fluxes, and the $\sqrt{TS}$ in the bands 100 to 300 MeV, 300 to 1000 MeV, 1000 to 3000 MeV, 3000 to 10000 MeV and 10000 to 10000 MeV respectively with fixed photon power-law index from the 100 MeV–100 GeV fit. (22): Result of χ^2 test of deviations of the flux in 11 time Intervals from a flat light curve over the full 11-month catalogue interval. A value greater than 23.21 indicates less than 1% chance of being a steady source. (23): Integral fluxes and uncertainties from 100 MeV to 100 GeV in each of the 11 time intervals of the 11 month.

4.4.1.3 Gamma-ray spectra of the sources

Figure 4.19 shows the gamma-ray spectra of the selected *EGRET* sources plotted using the *EGRET* data in Table 4.21 combined with the Fermi data in Table 4.22. Red dots with Y-errorbars represent *EGRET* data from 20 MeV to 10 GeV. Blue dots with Y-errorbars in four sources *3EG J0724-4713*, *3EG J1300-4406*, *3EG J1659-6251*, *3EG J1709-0828* represent *Fermi-LAT* data for these after 11 months of Fermi operation. The green straight line is the fitted power-law on the data. In the bottom panels, residuals ($\frac{\Delta F}{F}$) with respect to the fitted power-law model are represented.

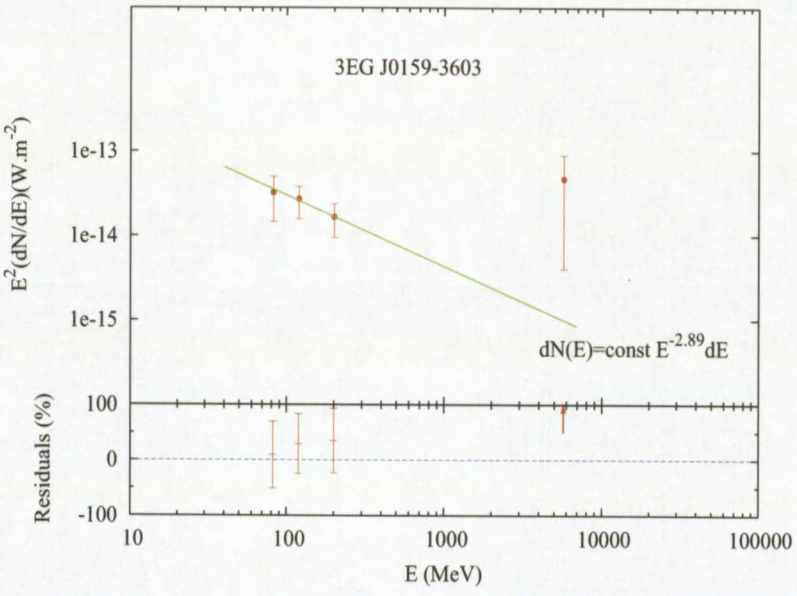

(a) *3EG J0159-3603*

Figure 4.19: Gamma-ray spectra of the selected *EGRET* sources. Red dots with Y-errorbars represent *EGRET* data from 20 MeV to 10 GeV. Blue squares with Y-errorbars in four sources *3EG J0724-4713*, *3EG J1300-4406*, *3EG J1659-6251*, *3EG J1709-0828* represent *Fermi-LAT* data for these sources after 11 months of operation. The green straight line is the fitted power-law on the data. In the bottom panels, residuals ($\frac{\Delta F}{F}$) with respect to the fitted power-law model are represented.

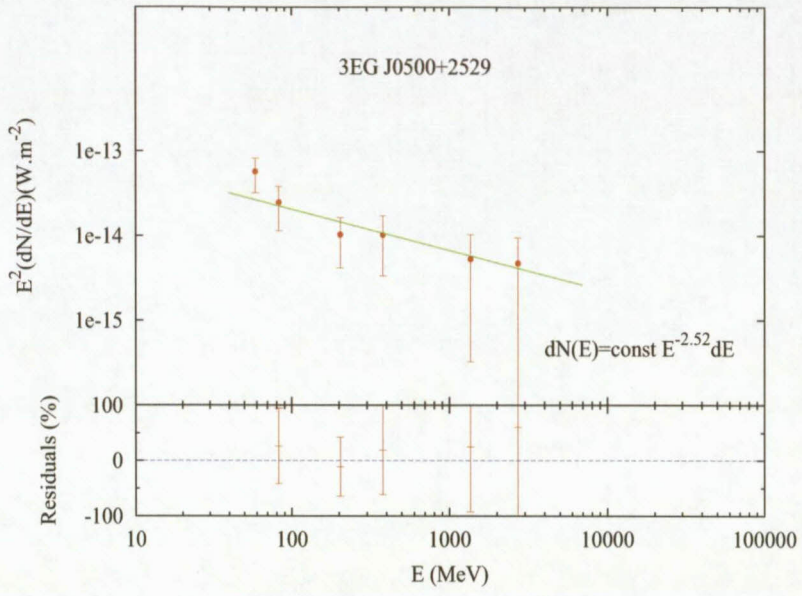

(b) *3EG J0500+2502*

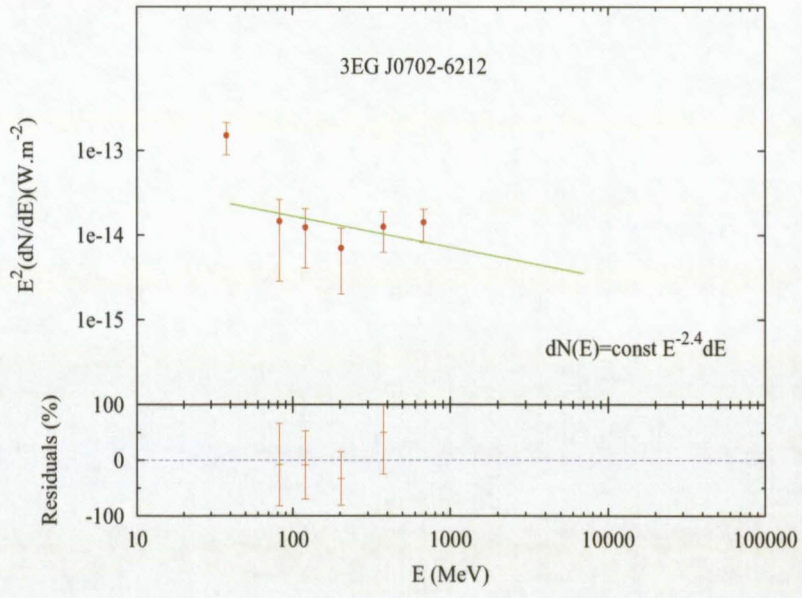

(c) *3EG J0702-6212*

Figure 4.19: Gamma-ray spectra of the selected *EGRET* sources. Red dots with Y-errorbars represent *EGRET* data from 20 MeV to 10 GeV. Blue dots with Y-errorbars in four sources *3EG J0724-4713*, *3EG J1300-4406*, *3EG J1659-6251*, *3EG J1709-0828* represent *Fermi-LAT* data for these sources after 11 months of operation. The green straight line is the fitted power-law on the data. In the bottom panels, residuals ($\frac{\Delta F}{F}$) with respect to the fitted power-law model are represented (continued).

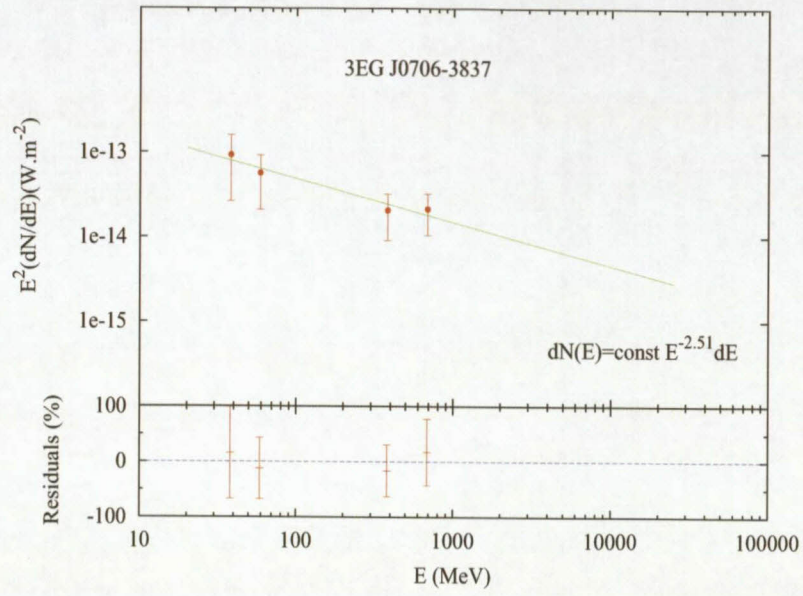

(d) *3EG J0706-3837*

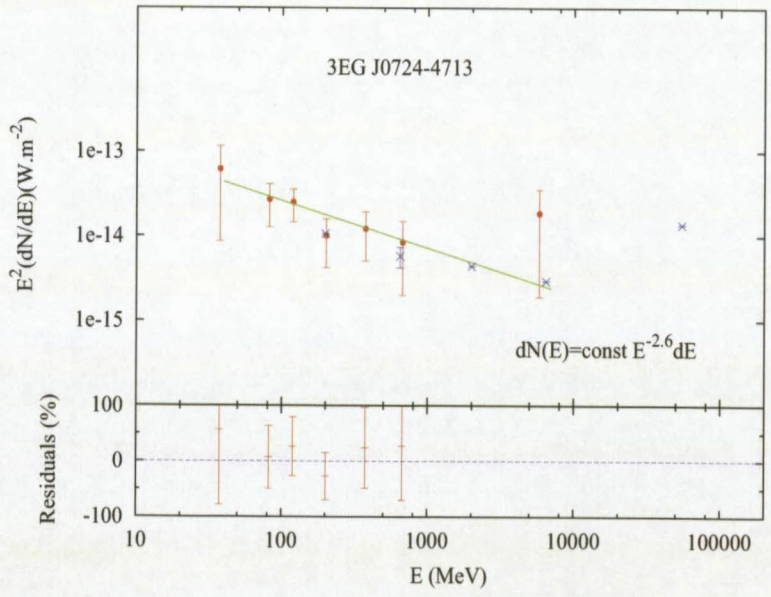

(e) *3EG J0724-4713*

Figure 4.19: Gamma-ray spectra of the selected *EGRET* sources. Red dots with Y-errorbars represent *EGRET* data from 20 MeV to 10 GeV. Blue dots with Y-errorbars in four sources *3EG J0724-4713*, *3EG J1300-4406*, *3EG J1659-6251*, *3EG J1709-0828* represent *Fermi-LAT* data for these sources after 11 months of operation. The green straight line is the fitted power-law on the data. In the bottom panels, residuals ($\frac{\Delta F}{F}$) with respect to the fitted power-law model are represented (continued).

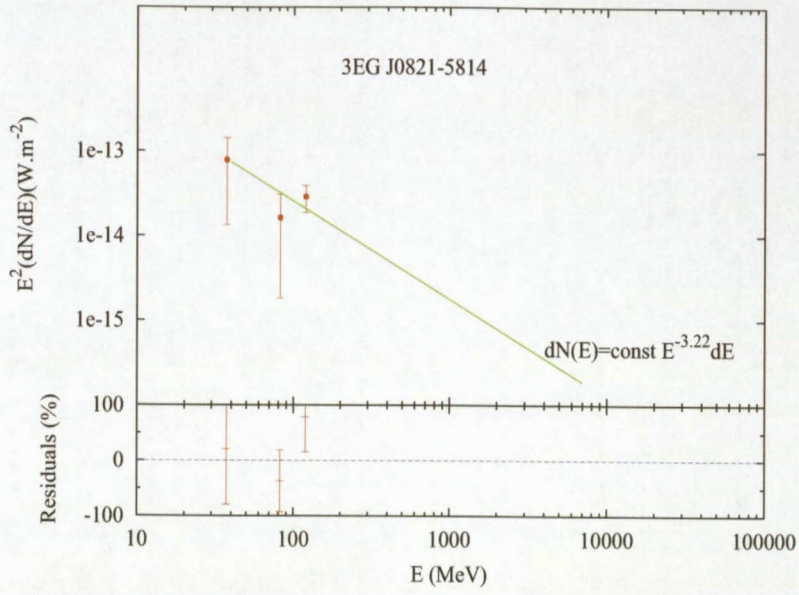

(f) *3EG J0821-5814*

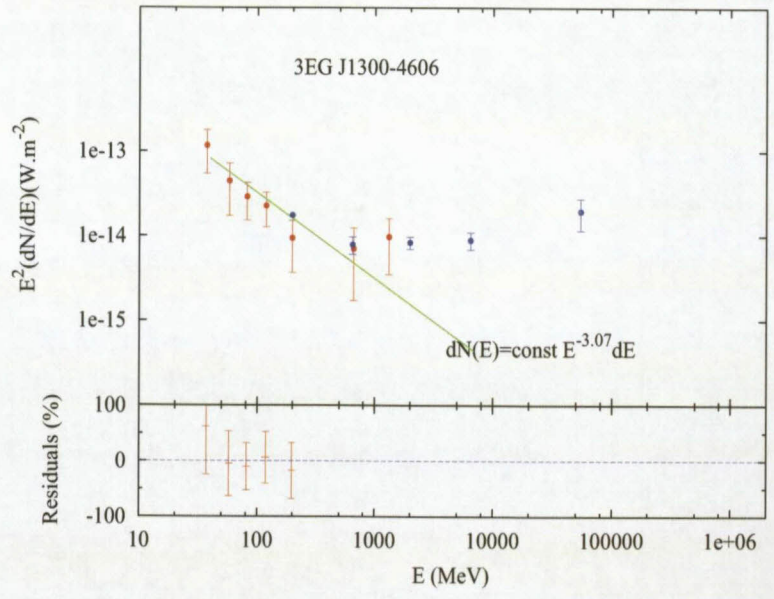

(g) *3EG J1300-4406*

Figure 4.19: Gamma-ray spectra of the selected *EGRET* sources. Red dots with Y-errorbars represent *EGRET* data from 20 MeV to 10 GeV. Blue dots with Y-errorbars in four sources *3EG J0724-4713*, *3EG J1300-4406*, *3EG J1659-6251*, *3EG J1709-0828* represent *Fermi-LAT* data for these sources after 11 months of operation. The green straight line is the fitted power-law on the data. In the bottom panels, residuals ($\frac{\Delta F}{F}$) with respect to the fitted power-law model are represented (continued).

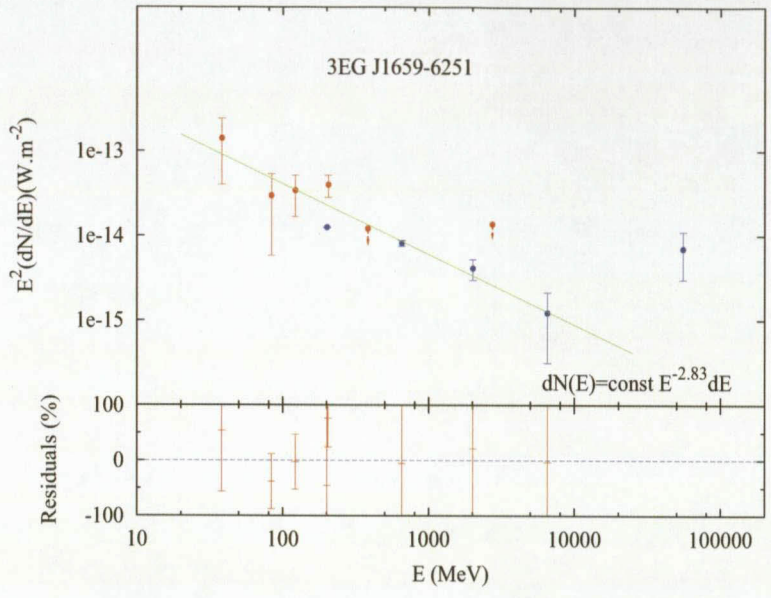

(h) *3EG J1659-6251*

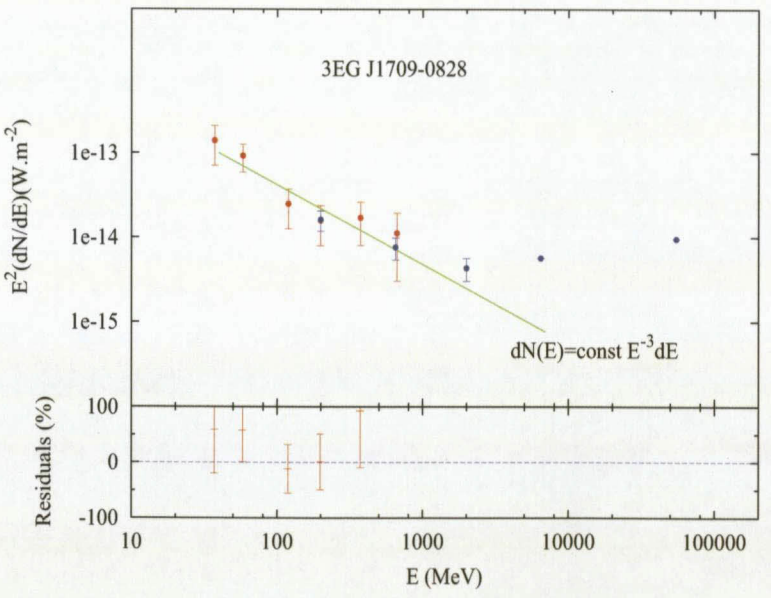

(i) *3EG J1709-0828*

Figure 4.19: Gamma-ray spectra of the selected *EGRET* sources. Red dots with Y-errorbars represent *EGRET* data from 20 MeV to 10 GeV. Blue dots with Y-errorbars in four sources *3EG J0724-4713*, *3EG J1300-4406*, *3EG J1659-6251*, *3EG J1709-0828* represent *Fermi-LAT* data for these sources after 11 months of operation. The green straight line is the fitted power-law on the data. In the bottom panels, residuals ($\frac{\Delta F}{F}$) with respect to the fitted power-law model are represented (continued).

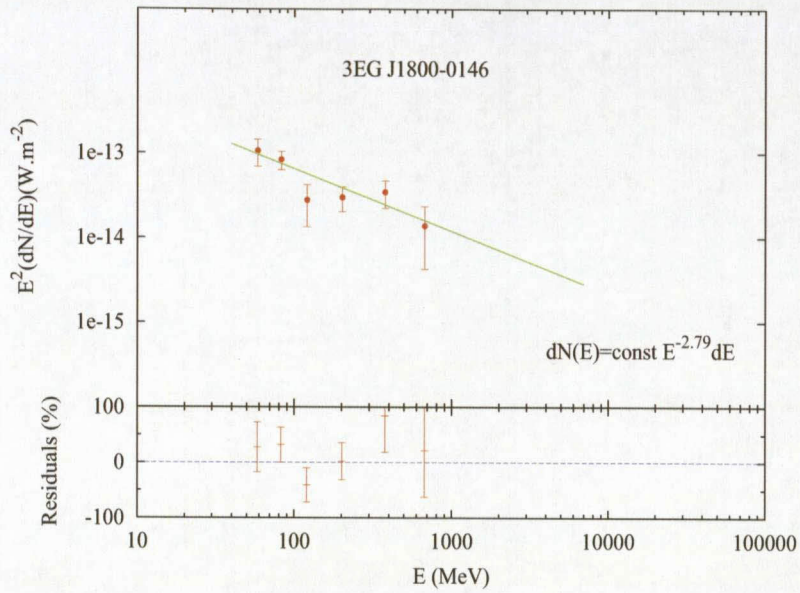

(j) *3EG J1800-0146*

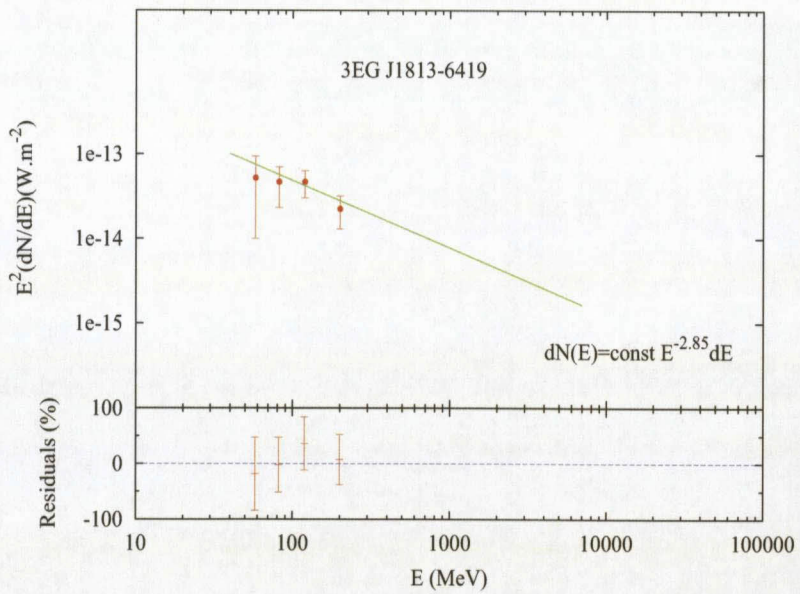

(k) 3EG J1813–6419

Figure 4.19: Gamma-ray spectra of the selected *EGRET* sources. Red dots with Y-errorbars represent *EGRET* data from 20 MeV to 10 GeV. Blue dots with Y-errorbars in four sources *3EG J0724-4713*, *3EG J1300-4406*, *3EG J1659-6251*, *3EG J1709-0828* represent *Fermi-LAT* data for these sources after 11 months of operation. The green straight line is the fitted power-law on the data. In the bottom panels, residuals ($\frac{\Delta F}{F}$) with respect to the fitted power-law model are represented (continued).

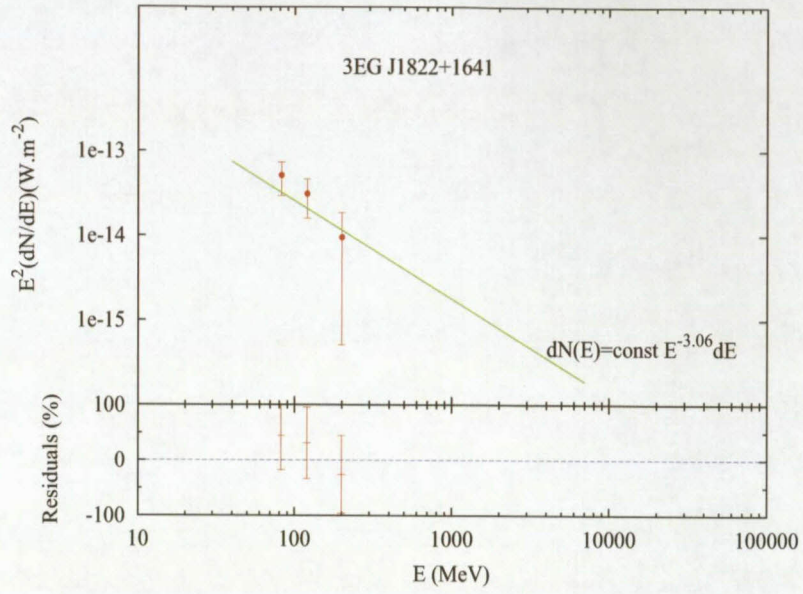

(l) *3EG J1822+1641*

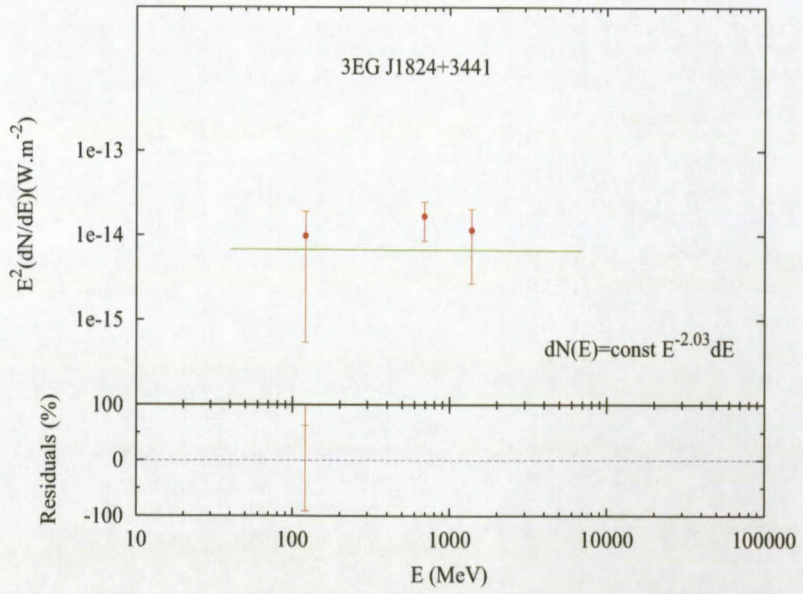

(m) *3EG J1824+3441*

Figure 4.19: Gamma-ray spectra of the selected *EGRET* sources. Red dots with Y-errorbars represent *EGRET* data from 20 MeV to 10 GeV. Blue dots with Y-errorbars in four sources *3EG J0724-4713*, *3EG J1300-4406*, *3EG J1659-6251*, *3EG J1709-0828* represent *Fermi-LAT* data for these sources after 11 months of operation. The green straight line is the fitted power-law on the data. In the bottom panels, residuals ($\frac{\Delta F}{F}$) with respect to the fitted power-law model are represented (continued).

Except for the source *3EG J0702-6212*, a single power-law model (represented by a green straight line on log-log scale) is the best fit for the data in the *EGRET* energy range. However, the energy fluxes predicted by single power-law models are below the observed data for photons with energy above 1 GeV. This was reported in (Stecker et al. 2008) as an apparent excess of gamma-rays above 1 GeV over what models predict. Several ideas, including contributions from dark matter annihilation and systematic errors in the data caused by an incorrect instrument response function have been proposed as possible explanations for this excess. Consequently all the *EGRET* fluxes above 1 GeV can be taken as upper limits.

Above 1 GeV (particularly for the sources detected by *Fermi-LAT* in its first 11 months of operation), data show a turnover with a positive slope. The turnover generally is interpreted as the transition between two different modes of emission, or emission coming from two different regions.

4.4.1.4 Blazar subclasses in the sample

The spectral index from the single power-law models over the sample of the selected sources ranges from 2.03 (*3EG J1824+3441*) to 3.2 (*3EG J0821-5814*). The recent classification based on 11 months of *Fermi LAT* data (Abdo et al. 2010a), associates different BL Lac subclasses to distinct photon index distributions (see Table 1.1). Flat spectrum radio Quasars (FSRQs), Low Synchrotron Peaked BL Lacs (LSP-BL Lacs), Intermediate Synchrotron Peaked BL Lacs (ISP-BL Lacs) and High Synchrotron Peaked BL Lacs (HSP-BL Lacs) have an average of the photon index 2.46 ± 0.18, 2.21 ± 0.16, 2.13 ± 0.17 and 1.86 ± 0.17 respectively.

Using the same classification, it appears that only one[11] source *3EG J0706-3837*, is classified as L- or ISP-BL Lacs while the rest correspond to FSRQs (Figure 4.20). It is therefore promising that the γ-ray spectral indices of the selected 13 *EGRET* sources display properties that are reconcilable with extra-galactic sources like blazars, and justify more detailed investigation.

[11]The second source, *3EG J1824+3441*, which is falling in this category was classified as a FSRQ (e.g. Véron-Cetty and Véron (2001) and Zhang et al. (1998))

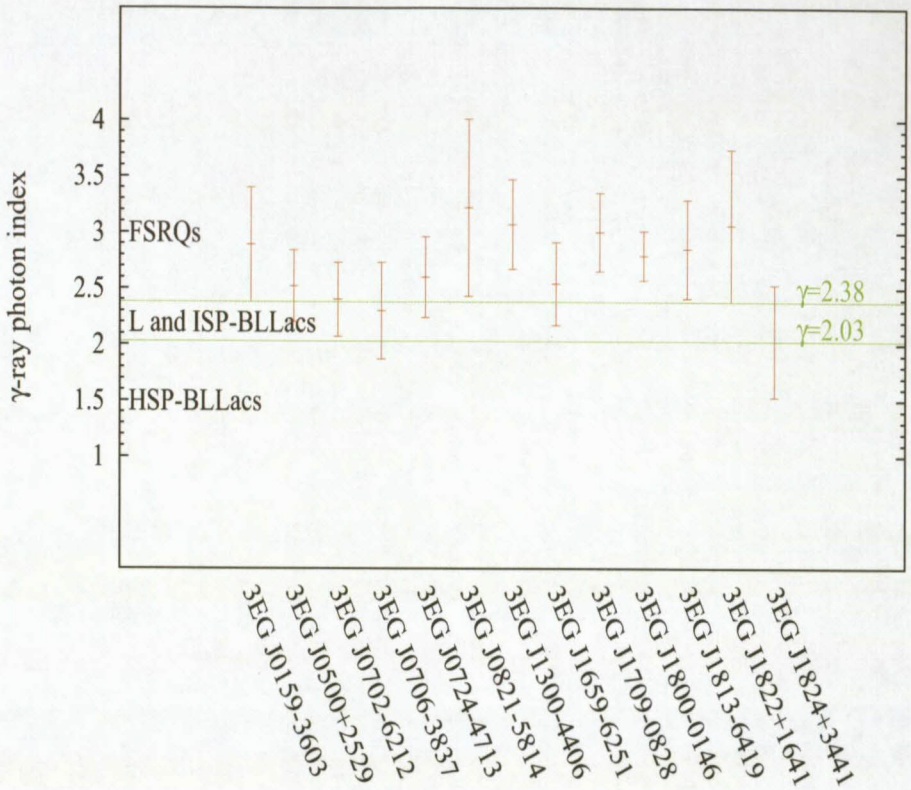

Figure 4.20: Distribution of the photon index in the sample.

4.4.1.5 γ-ray light curves

4.4.1.5.1 γ-ray light curves with *EGRET*

One means of determining source class is the study of flux variability on timescales of days and even shorter periods of time. For accretion-driven systems like AGNs, the rapid flux change and large isotropic luminosity are consistent with an assumption that the gamma-ray emission is beamed, which is one of the characterstics of blazars which are known to be highly variable (Mattox et al. 1997). However, on timescales of $\sim$ 1 day, other γ-ray sources like pulsars are believed to be stable (Ramanamurthy et al. 1995).

Although many instances of flaring active galactic nuclei have been reported, the *EGRET* database has not been systematically searched for occurrences of short-timescale ($\sim$ 1 day) variability. This is due to the fact that the *EGRET* was incapable of resolving variations on timescales shorter than $\sim$ 1 week (Mattox et al. 1997), i.e. the statistics of the data are very limiting, especially for the 1 day light curves. In fact, *EGRET* was sensitive to only the most dramatic short-term variations in flux (Mattox et al. 1997). On the other hand, much of the data is subject to large statistical uncertainties.

To justify the variability, data have to be significant enough. A minimum of 4σ over all single or combination periods is suggested (Wallace et al. 2000), which is unlikely for most of the unidentified *EGRET* faint sources, where in some single or combination viewing period the average standard deviation (σ) falls slightly below 2. However, it is possible for a source to display a short-duration significance well above that of the entire viewing period. This is almost always true for flaring sources. For most of the selected sources, the overall detection during their viewing periods falls below the minimum required to justify the presence of variability in the data, but it cannot be ruled out that they possibly have short-duration excesses above that value.

Figure 4.21 shows the light curves of the selected sources. The vertical error bars indicate the ranges of the 68% confidence flux estimates. In the lower panel of each figure, the square root of the test statistics (equivalent to the well-known σ, which indicates the level of statistical significance of the detection) is plotted.

In the *EGRET* data, results with $\sqrt{TS} = 2$ are considered to be significant. In upper panels, the average of the fluxes were plotted for the full effective *EGRET* observing period that is the sum of the 4 cycles (P1234). It appears that most of the significant measurements are above the averages. This suggests that *EGRET* was sensitive only to flare events. In fact, *EGRET* was not able to detect many high-energy gamma-ray sources, which remained quiet during its viewing period, and some were observed by the Cherenkov telescopes before Fermi came online. During 11 months of operation, Fermi has already detected 1079 (about 4 times the number detected by *EGRET*) objects emitting above 100 MeV.

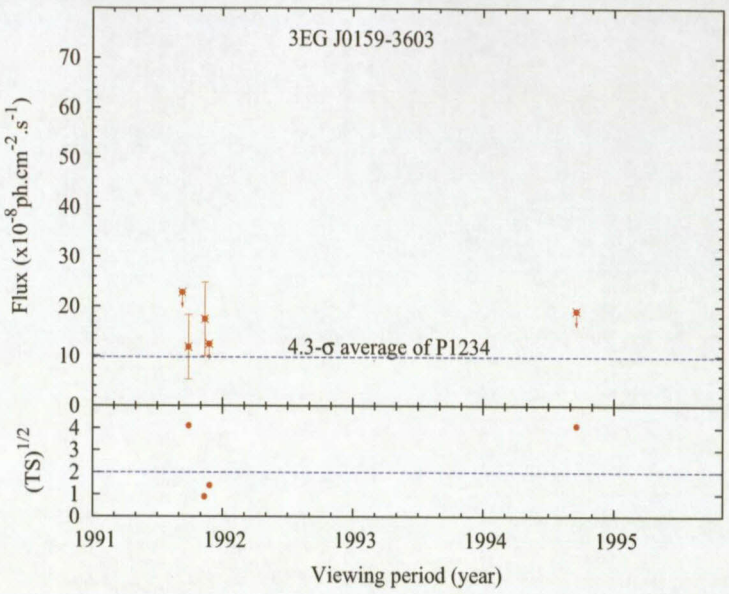

(a) *3EG J0159-3603*

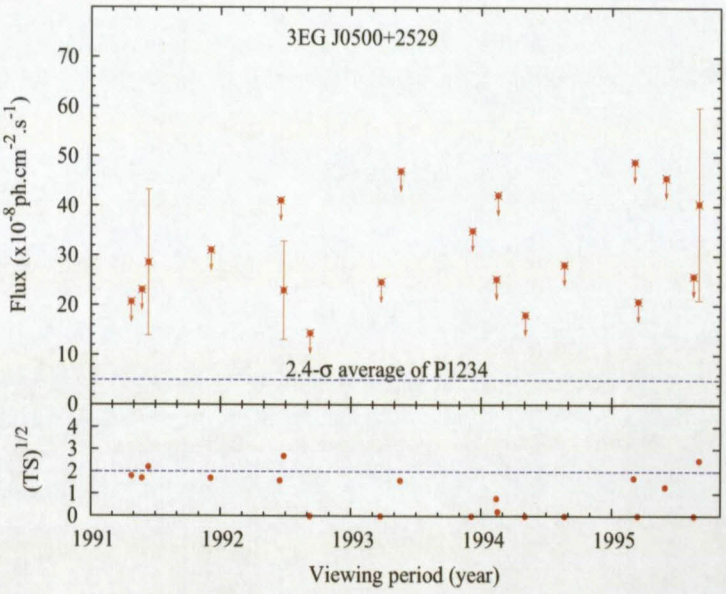

(b) *3EG J0500+2502*

Figure 4.21: γ-ray light curves of the selected sources from *EGRET* observations. For all light curves, the dashed lines indicate the average flux for the viewing period. The vertical bars indicate the range of the 68% confidence flux estimates.

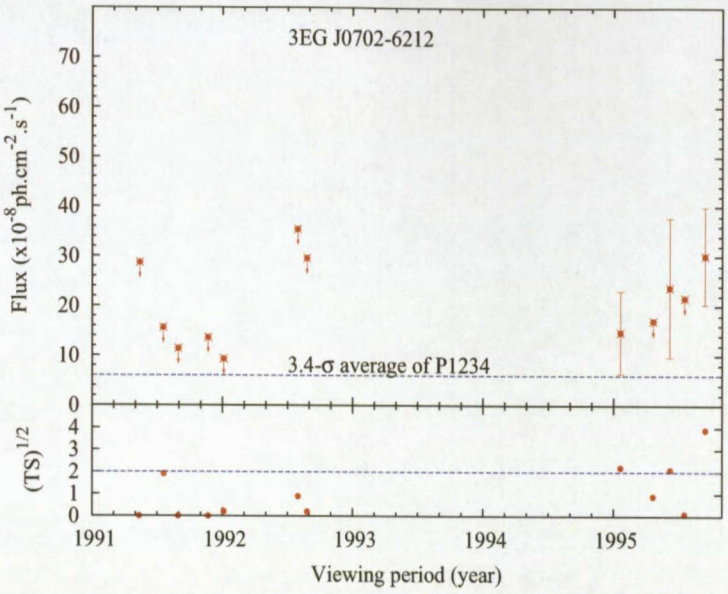

(c) *3EG J0702-6212*

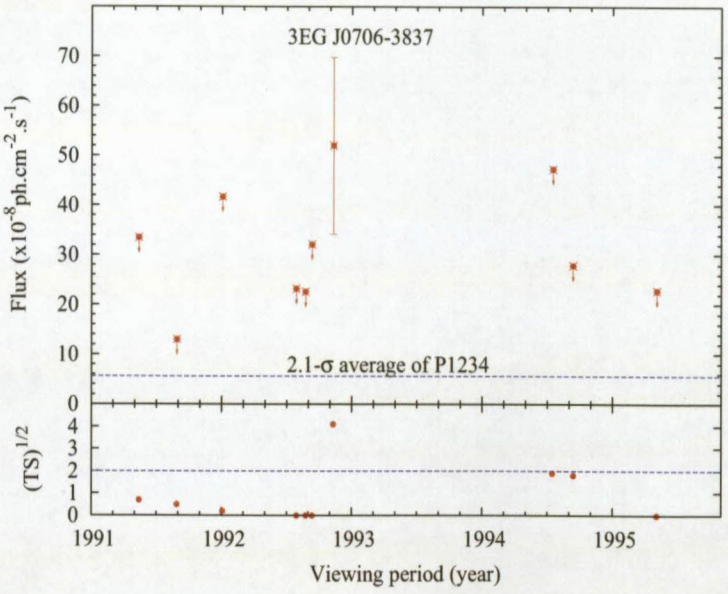

(d) *3EG J0706-3837*

Figure 4.21: γ-ray light curves of the selected sources from *EGRET* observations. For all light curves, the dashed lines indicate the average flux for the viewing period. The vertical bars indicate the range of the 68% confidence flux estimates (continued).

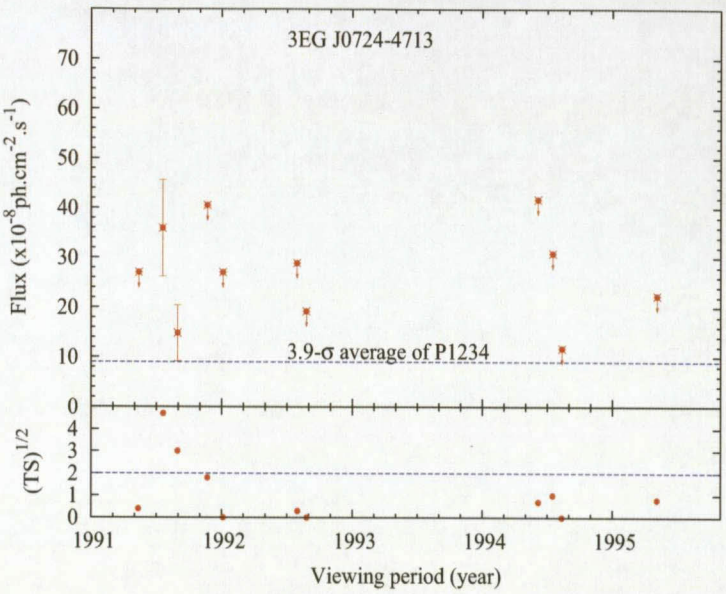

(e) *3EG J0724-4713*

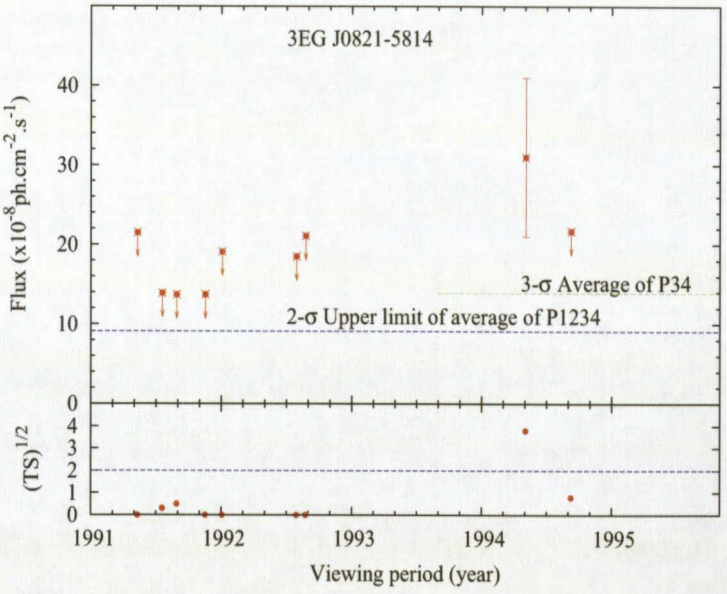

(f) *3EG J0821-5814*

Figure 4.21: γ-ray light curves of the selected sources from *EGRET* observations. For all light curves, the dashed lines indicate the average flux for the viewing period. The vertical bars indicate the range of the 68% confidence flux estimates (continued).

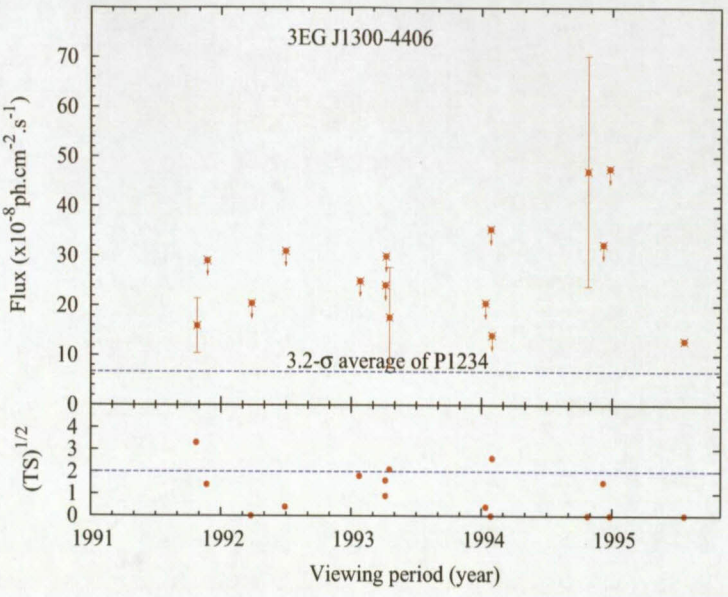

(g) *3EG J1300-4406*

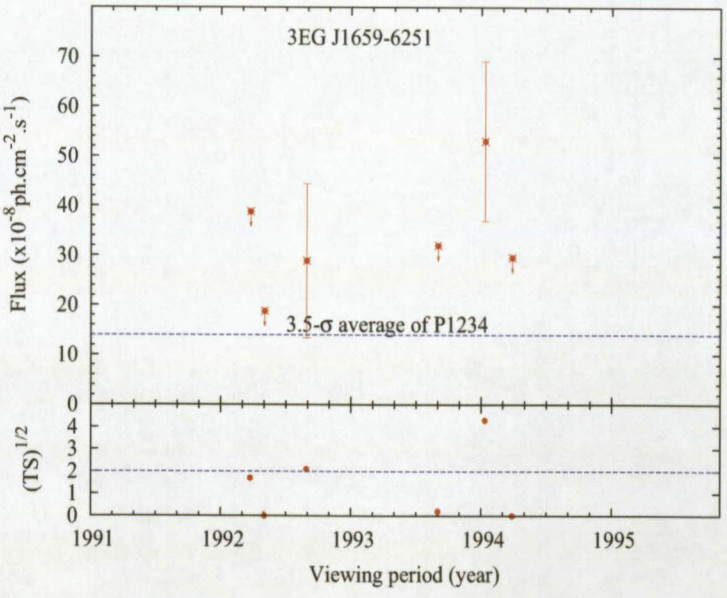

(h) *3EG J1659-6251*

Figure 4.21: γ-ray light curves of the selected sources from *EGRET* observations. For all light curves, the dashed lines indicate the average flux for the viewing period. The vertical bars indicate the range of the 68% confidence flux estimates (continued).

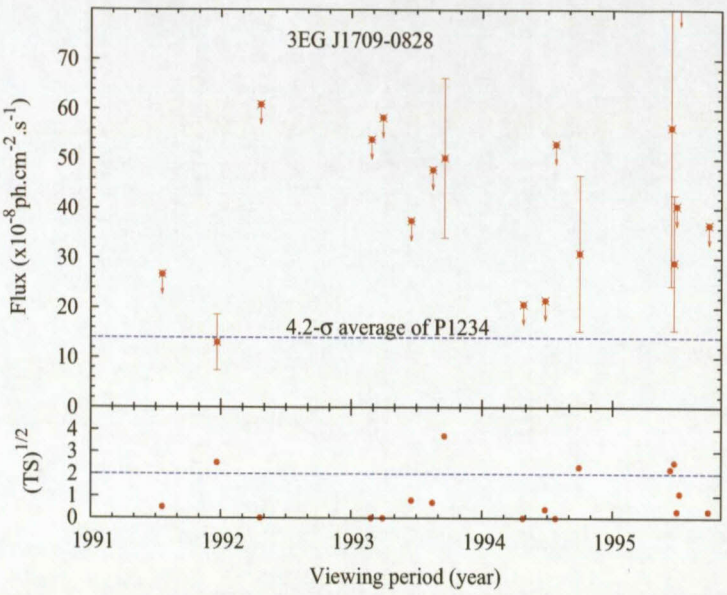

(i) *3EG J1709-0828*

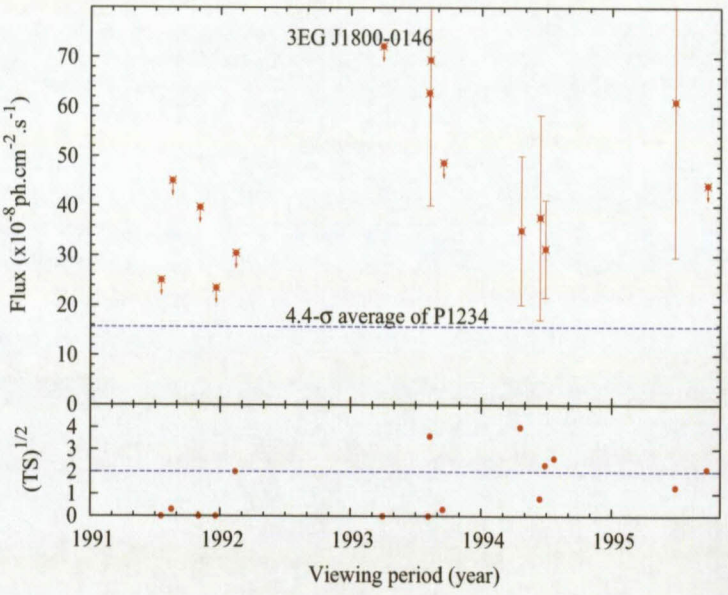

(j) *3EG J1800-0146*

Figure 4.21: γ-ray light curves of the selected sources from *EGRET* observations. For all light curves, the dashed lines indicate the average flux for the viewing period. The vertical bars indicate the range of the 68% confidence flux estimates (continued).

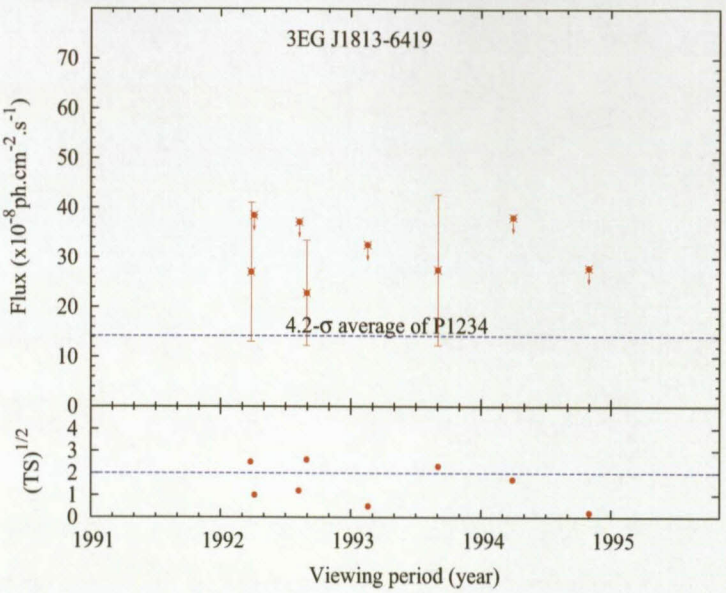

(k) *3EG J1813-6419*

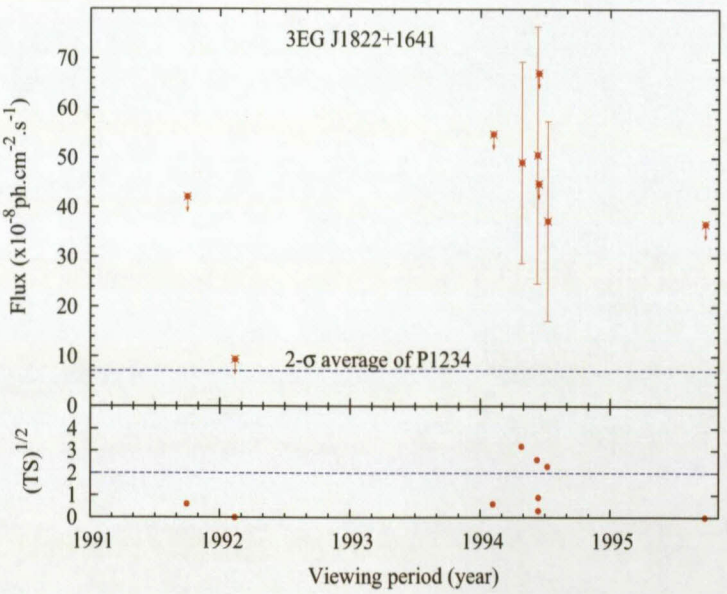

(l) *3EG J1822+1641*

Figure 4.21: γ-ray light curves of the selected sources from *EGRET* observations. For all light curves, the dashed lines indicate the average flux for the viewing period. The vertical bars indicate the range of the 68% confidence flux estimates (continued).

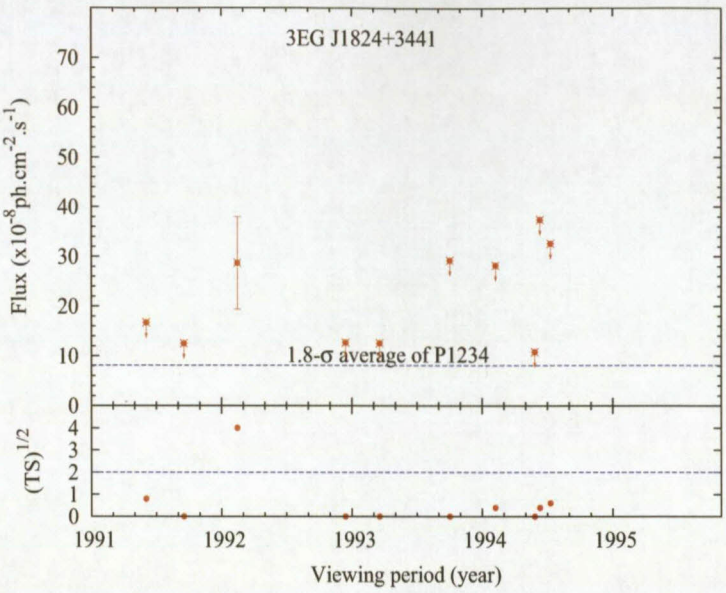

(m) *3EG J1824+3441*

Figure 4.21: γ-ray light curves of the selected sources from *EGRET* observations. For all light curves, the dashed lines indicate the average flux for the viewing period. The vertical bars indicate the range of the 68% confidence flux estimates (continued).

4.4.1.5.2 Gamma-ray light curves with *Fermi-LAT*

Variability is very common in γ-ray sources (more generally in accreting systems) as a result of a non-uniform injection rate of particles in the acceleration region. Many AGNs are seen to flare dramatically over periods of months and years. However, known pulsars are quite steady, while most of the blazars are highly variable. The study of the variability of the unidentified *EGRET* sources is therefore relevant.

Figure 4.22 presents the light curves of *3EG J0724-4713* (*1FGL J0724.4-4714*), *3EG J1300-4406* (*1FGL J1304.3-4352*), *3EG J1659-6212* (*1FGL J1702.7-6217*) and *3EG J1709-0828* (*1FGL J1708.4-0755*), plotted using the data collected from the first 11 months (between 4 August 2008 and 4 July 2009) of Fermi observations (1FGL catalogue). The fluxes have been integrated from 100 MeV to 100 GeV using power-law fits and the error bars to indicate the 1 σ statistical errors. The full 11 months' time interval is split into 11 equal intervals of about one month each (30.37 days). Apparently, none of these four sources are seen to be variable even by simply considering the level of statistical uncertainty. For quantification, the catalogue has defined a variability index as

$$V = \sum_i \frac{(F_i - F_{av})^2}{\sigma_i^2 + (f_{rel} F_i)^2}, \tag{4.6}$$

where i runs over the 11 intervals, $f_{rel} = 3\%$ is the relative systematic uncertainty applied to each flux F_i and σ_i is the statistical uncertainty in F_i. A source is interpreted to be variable if $V > 23.21$. However, it has been reported that this criterion is not sensitive to relative variations $\frac{\delta F}{F}$ smaller than 60% at $\sigma = 10$. This limit goes down to 20% as σ increases to 33. This is not an indication that fainter sources are less variable than brighter ones, but simply a failure of measuring their variability. The variability indices of these sources are, respectively, 11.70, 8.63, 11.80 and 12.30.

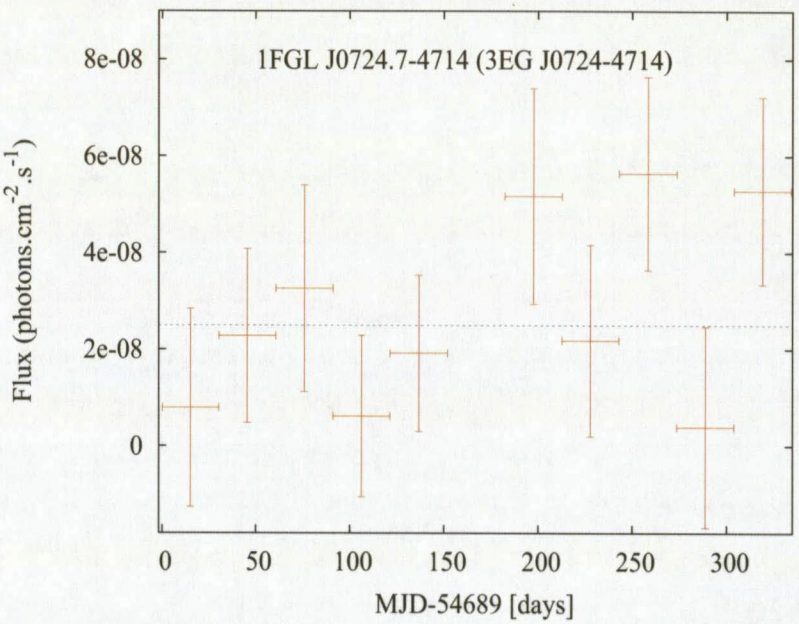

(a) *3EG J0724-4713*

Figure 4.22: Light curves of *3EG J0724-4713* (*1FGL J0724.4-4714*), *3EG J1300-4406* (*1FGL J1304.3-4352*), *3EG J1659-6251* (*1FGL J1702.7-6217*) and *3EG J1709-0828* (*1FGL J1708.4-0755*) plotted using the data of the first 11 months (between 4 August 2008 and 4 July 2009) of Fermi observations as reported in the *1FGL* catalogue. The fluxes are integrations from 100 MeV to 100 GeV using power-law fits and the error bars indicate the 1 σ statistical errors.

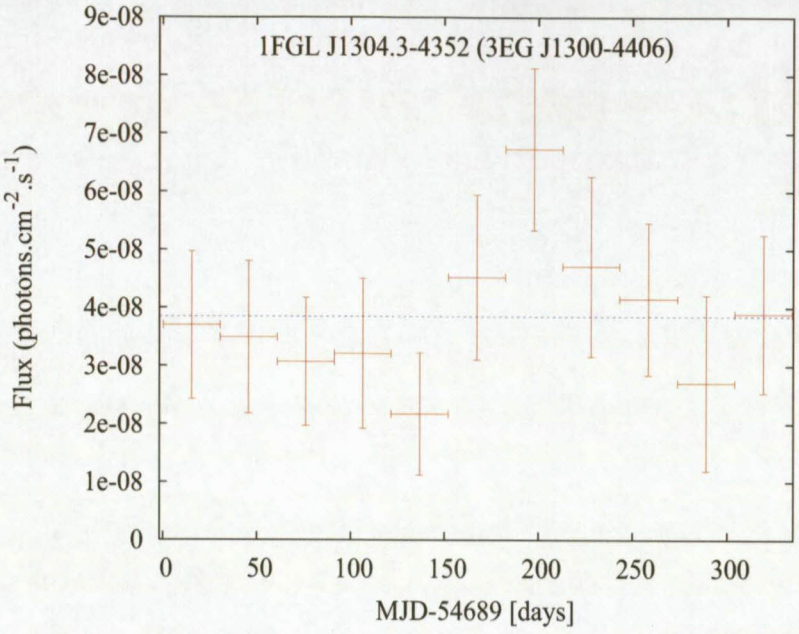

(b) *3EG J1300-4406*

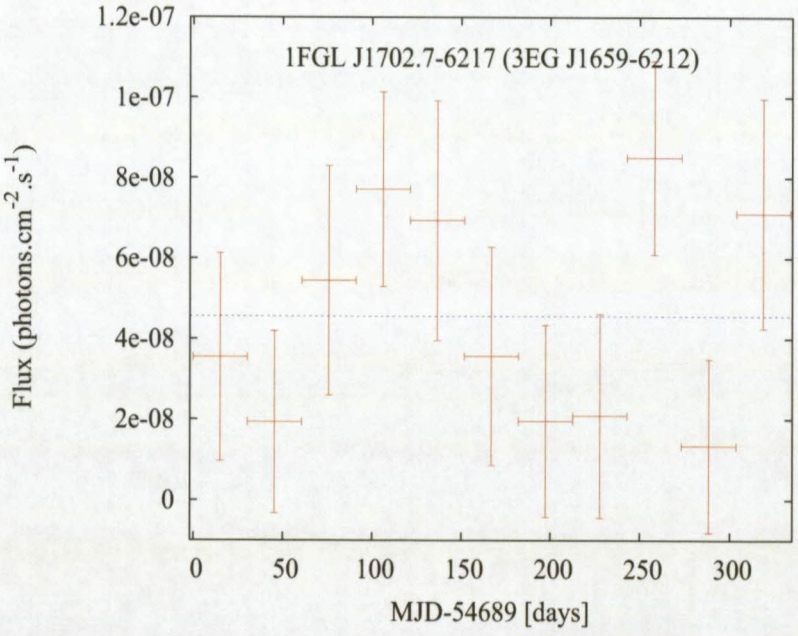

(c) *3EG J1659-6251*

Figure 4.22: Light curves of *3EG J0724-4713* (*1FGL J0724.4-4714*), *3EG J1300-4406* (*1FGL J1304.3-4352*), *3EG J1659-6251* (*1FGL J1702.7-6217*) and *3EG J1709-0828* (*1FGL J1708.4-0755*) plotted using the data of the first 11 months (between 4 August 2008 and 4 July 2009) of Fermi observations as reported in the *1FGL* catalogue. The fluxes are integrations from 100 MeV to 100 GeV using power-law fits and the error bars indicate the 1 σ statistical errors (continued).

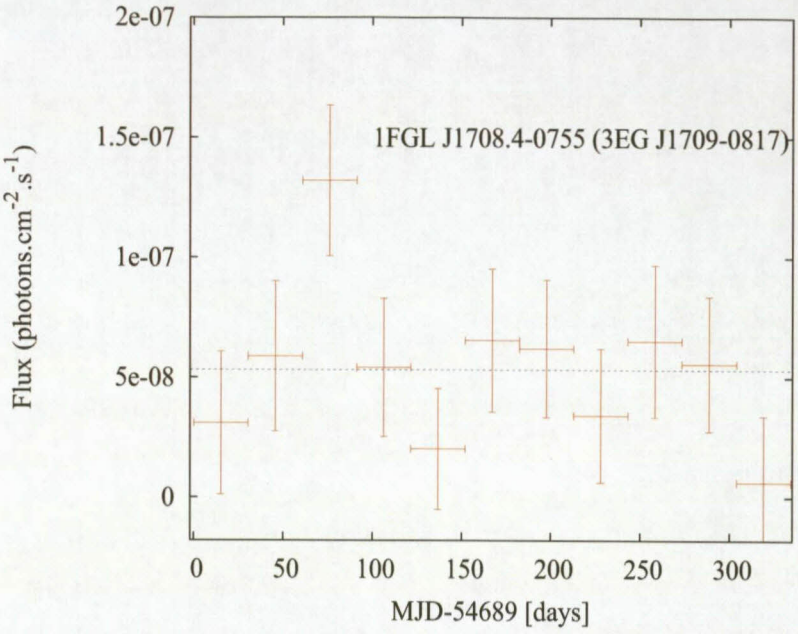

(d) *3EG J1709-0828*

Figure 4.22: Light curves of *3EG J0724-4713* (*1FGL J0724.4-4714*), *3EG J1300-4406* (*1FGL J1304.3-4352*), *3EG J1659-6251* (*1FGL J1702.7-6217*) and *3EG J1709-0828* (*1FGL J1708.4-0755*) plotted using the data of the first 11 months (between 4 August 2008 and 4 July 2009) of Fermi observations as reported in the *1FGL* catalogue. The fluxes are integrations from 100 MeV to 100 GeV using power-law fits and the error bars indicate the 1 σ statistical errors (continued).

4.4.2 X-ray data

The knowledge of the X-ray properties is of special relevance, because in this band both the synchrotron and inverse Compton processes can contribute significantly to the emission. The synchrotron emission is expected to produce a steep continuum in this band while the inverse Compton process should give rise to a flat component ($\alpha \leq 1$, rising in a νF_ν plot). Therefore the shape of the X-ray spectrum can give a valuable hint for disentangling the two components and inferring the respective peak frequencies (Fossati et al. 1998), i.e. the X-ray data help in the classification of the source.

The X-ray fluxes of some of the selected sources were obtained from the online catalogues of the three X-ray satellites i.e. the *Roentgen Satellite (ROSAT)* (0–2 keV, 1 count= 6×10^{-12} erg.cm^{-2}), the *European Space Agency (ESA)*'s *X-ray Multi-Mirror Mission (XMM-Newton)* (0.2–12 keV) and the *Second High Energy Astrophysical Observatory (HEAO-2)* (0.15–20 keV) named *Einstein* after launch. Table 4.23 gives the energy-fluxes observed for these sources.

	Source	Photon energy (keV)	Frequency (Hz)	νF_ν (W m^{-2})	Uncertainty (W m^{-2})	Reference
			ROSAT (0–2 keV)			
1	*3EG J0500+2502*	1.00	2.42×10^{17}	1.32×10^{-16}		(Rosat 2000)
2	*3EG J0706-3837*	1.00	2.42×10^{17}	2.95×10^{-16}	7.55×10^{-17}	(Voges et al. 2000)
3	*3EG J0821-5814*	1.34	3.25×10^{17}	1.24×10^{-14}	1.24×10^{-15}	(Voges et al. 1999)
4	*3EG J1824+3441*	1.00	2.42×10^{17}	8.20×10^{-17}		(Flesch and Hardcastle 2004)
			Einstein (HEAO-2) (0.15–20 keV)			
1	3EG J0500+2509	2.00	4.84×10^{17}	1.60×10^{-16}	5.03×10^{-17}	(Feigelson and Berg 1983)
			XMM-Newton (0.2–12 keV)			
1	*3EG J0821-5814*	7.01	1.70×10^{18}	3.64×10^{-15}		(Saxton et al. 2008)

Table 4.23: X-ray data of the selected sources.

4.4.3 IR data

The infrared emission in blazars is believed to be dominated by highly beamed synchrotron radiation from a relativistic jet. For most of the high-luminosity blazars (e.g. FSRQs and LBLs), the synchrotron energy output peaks in the infrared wavelengths. The synchrotron IR photons contribute to the SSC process when they are inverse Compton scattered to γ ray energies by the synchrotron emitting electrons.

Additional (thermal) infrared emission in some FSRQs may originate in a dust torus, lying at hundreds of parsecs (e.g. Haas et al. (1998) and Meisenheimer et al. (2001)) and heated by the radiation from the disk. Such infrared photons are likely to be targets for the jet's relativistic electrons in the external Compton scattering process producing high energy γ-ray emission.

The infrared spectrum resulting from the synchrotron emission is expected to be a smooth continuation of the radio spectrum (on the SED representation). Therefore, the infrared spectral shape is vital to constrain models of the broadband emission in high-energy γ-ray blazars by characterizing the physical parameters of the relativistic charged particles which do the scattering (Terebey et al. 2002).

Two important infrared surveys, the IRAS survey (Mid and Far Infrared (MIR & FIR): 12–100 μm) and the 2MASS survey (Near Infrared (NIR): 1.2–2.2 μm) have been used to search for the infrared counterparts of the selected EGRET sources. Due to their large angular resolution between 0.5 arcminute to 2 arcminutes, most of the IRAS counterpart candidates could not be reliable. In fact, the positions of the nearest IRAS sources compared to the positions of the radio counterparts could lead to an offset of several arcminutes. Most of the sources were eliminated by the fact that their fluxes don't match (smooth transition on the SED) with other data from close wavelengths particularly for the NIR and Optical. Only *IRAS 16588-6207* (e.g. Table 4.24) could fulfill this condition and therefore was selected as a counterpart of *3EG J1659-6251*.

However, 2MASS (Skrutskie et al. 2006), with much better angular resolution of 2 arcseconds, provided most of the NIR counterparts of the EGRET selected sources. The NIR fluxes in J (1.2 μm), H (1.6 μm) and K (2.2 μm) bands obtained from some of the selected sources are given in

Table 4.25.

IRAS name	RA (deg)	Dec (deg)	Flux_12μm (Jy)	Flux_25μm (Jy)	Flux_60μm (Jy)	Flux_100μm (Jy)	Search Offset (arcmin)
IRAS 16588-6207	255.87	-62.2	0.25	0.25	0.45	3.41	1.032 (17 03 37 -62 12 38)

Table 4.24: IRAS point source counterpart of 3EG J1659-6251. Source of the data: IRAS online catalogue of point sources.

No	Name Source	Near Infrared νF_ν (W m^{-2}) with *2MASS*			
		J	H	K	Reference
		1.235 μm	1.662 μm	2.159 μm	
		(2.425×10^{14} Hz)	(1.805×10^{14} Hz)	(1.389×10^{14} Hz)	
1	*3EG J0500+2502*	-	4.40×10^{-016}	1.04×10^{-015}	(Lebofsky 1981)
2	*3EG J0706-3837*	6.41×10^{-015}	4.62×10^{-015}	5.59×10^{-015}	(Skrutskie et al. 2006)
3	*3EG J0821-5814*	6.00×10^{-014}	5.73×10^{-014}	3.66×10^{-014}	(Skrutskie et al. 2006)
4	*3EG J1659-6251*	2.80×10^{-015}	5.40×10^{-015}	8.60×10^{-015}	(Skrutskie et al. 2006)
5	*3EG J1800-0146*	1.37×10^{-011}	1.70×10^{-011}	1.50×10^{-011}	(Zacharias et al. 2005)
6	*3EG J1813-6419*	6.72×10^{-016}	1.85×10^{-015}	2.69×10^{-015}	(Zacharias et al. 2005)
7	*3EG J1822+1641*	8.03×10^{-016}	1.03×10^{-015}	2.20×10^{-015}	(Zacharias et al. 2005)
8	*3EG J1824+3441*	5.94×10^{-016}	5.72×10^{-016}	1.06×10^{-015}	(Zacharias et al. 2005)

Table 4.25: Near Infrared data for the selected sources.

4.5 Spectral Energy Distributions of the selected sources

Both current theoretical models and observations suggest that the broadband spectral emission of blazars consists of two distinctive components: (a) the low-energy component which is the result of synchrotron radiation of a beam of relativistic particles and which peaks in the IR to soft X-ray region, and (b) a high-energy component, which is the result of inverse Compton scattering of the same beam of relativistic particles off ambient synchrotron-produced photons in the jet or external photons, which peaks in the MeV–GeV–TeV region.

In these models, the γ-ray spectral index should be correlated with the location of the low-energy peak, with flatter gamma-ray spectra expected for blazars with synchrotron peaks at higher photon energies and vice-versa (Maraschi and Tavecchio 2001). In the next chapter using the homogeneous model, this correlation of these two components will be examined on the sample of *EGRET*-detected sources. Figure 4.23 shows the Spectral Energy Distributions (SEDs) of all the selected sources plotted using all the data collected on the objects.

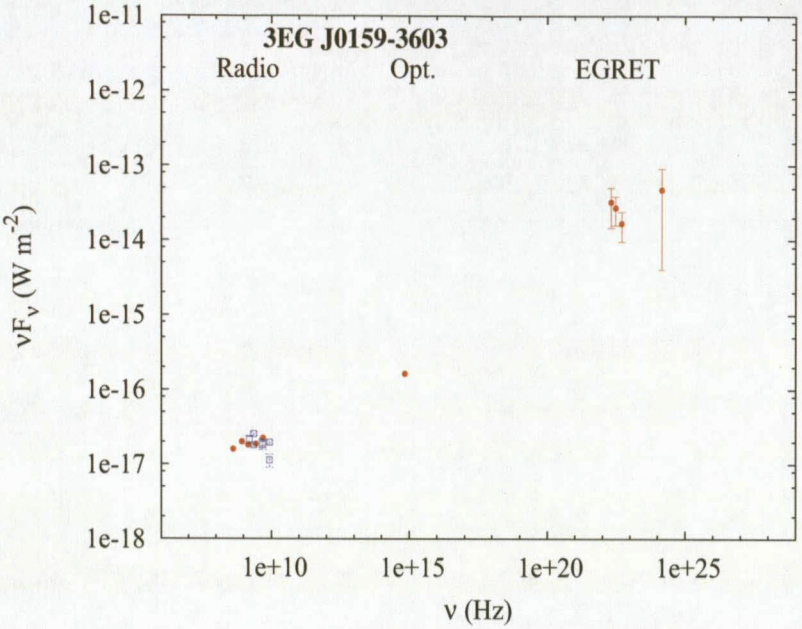

(a) *3EG J0159-3603*

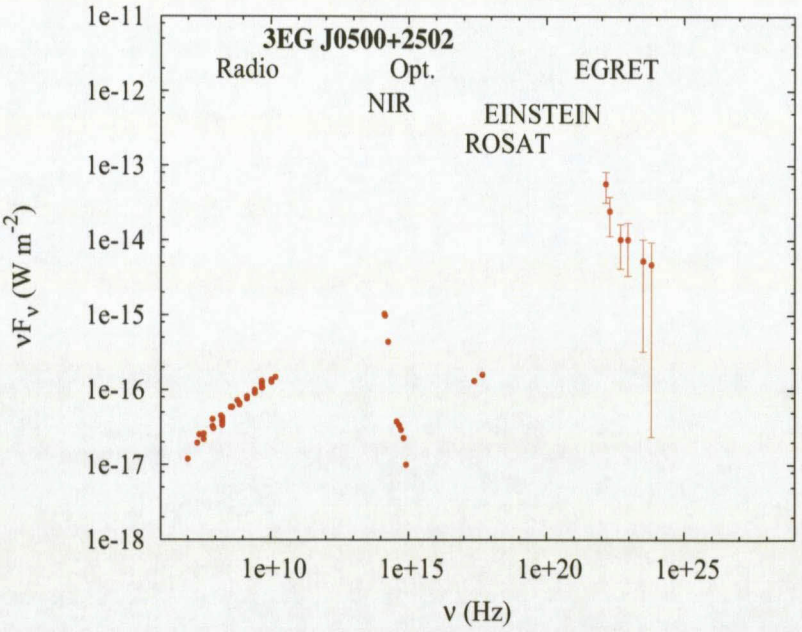

(b) *3EG J0500+2502*

Figure 4.23: Spectral Energy Distributions of the selected *EGRET* sources. Red dots represent the data collected or reduced from online catalogues and archives. Data obtained from observations using local telescopes are represented by blue squares (Radio data from the 26-m HartRAO radio telescope).

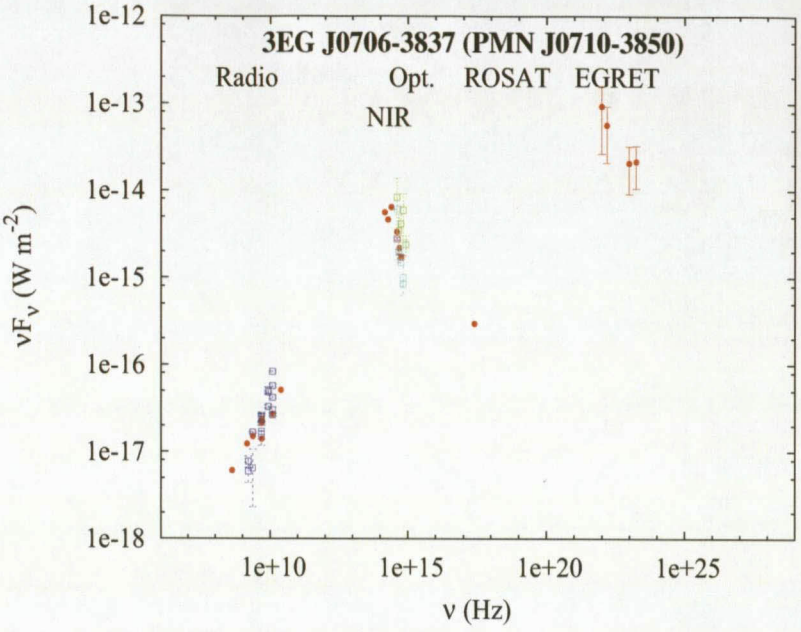

(c) *3EG J0706-3837*

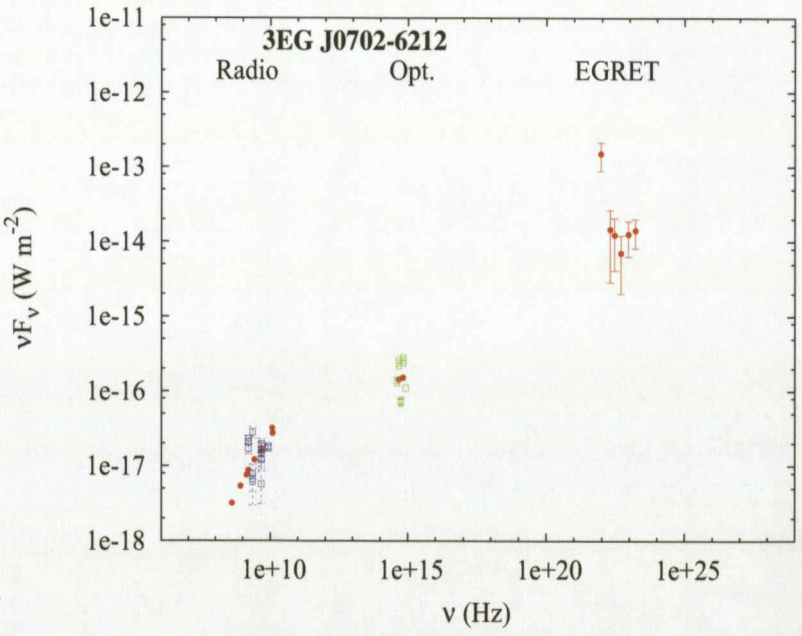

(d) *3EG J0702-6212*

Figure 4.23: Spectral Energy Distributions of the selected *EGRET* sources (continued). Red dots represent the data collected or reduced from online catalogues and archives. Data obtained from observations using local telescopes are represented by blue squares (Radio data from the 26-m HartRAO radio telescope), green squares (Optical data from SALT), purple [rose-pink] squares (Optical data from the 1.9-m SAAO telescope) and aqua [blue-green] squares (Optical data from the 1.0-m SAAO telescope).

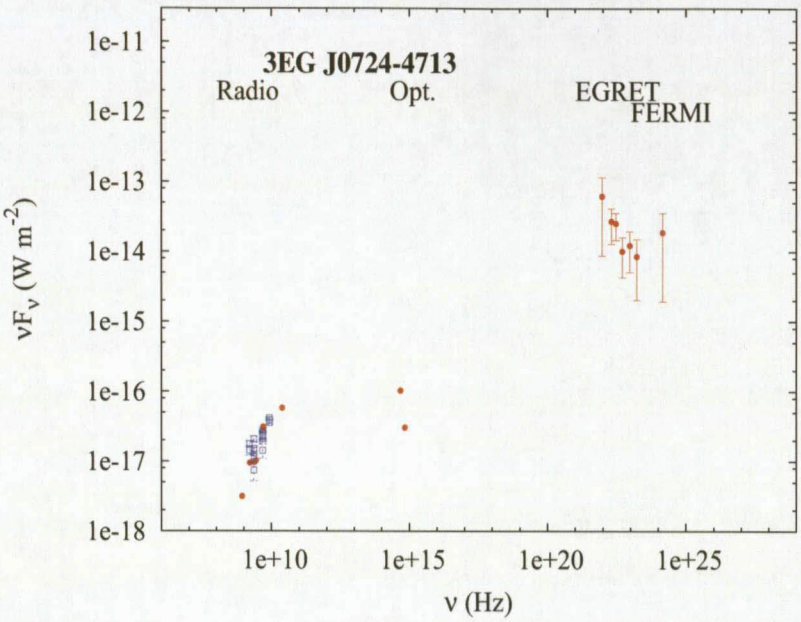

(e) *3EG J0724-4713*

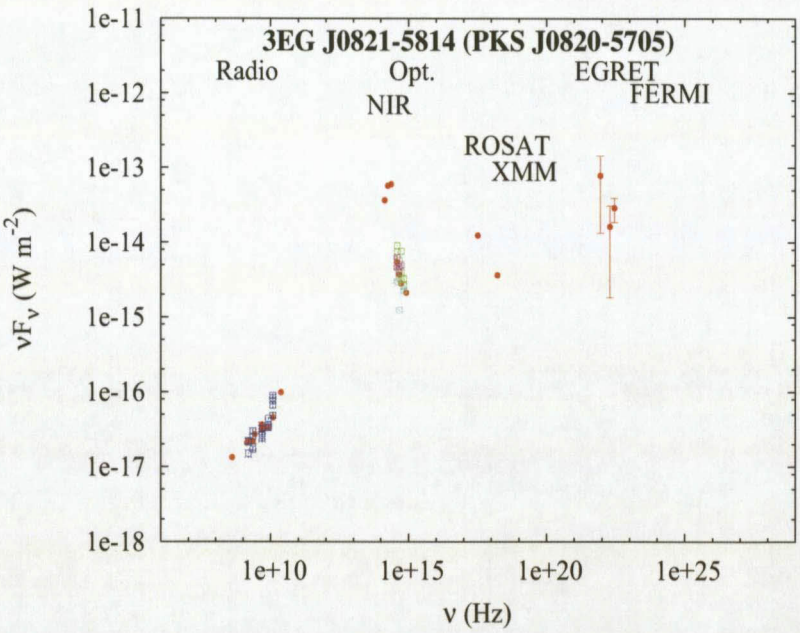

(f) *3EG J0821-5814*

Figure 4.23: Spectral Energy Distributions of the selected *EGRET* sources (continued). Red dots represent the data collected or reduced from online catalogues and archives. Data obtained from observations using local telescopes are represented by blue squares (Radio data from the 26-m HartRAO radio telescope), green squares (Optical data from SALT), purple [rose-pink] squares (Optical data from the 1.9-m SAAO telescope) and aqua [blue-green] squares (Optical data from the 1.0-m SAAO telescope).

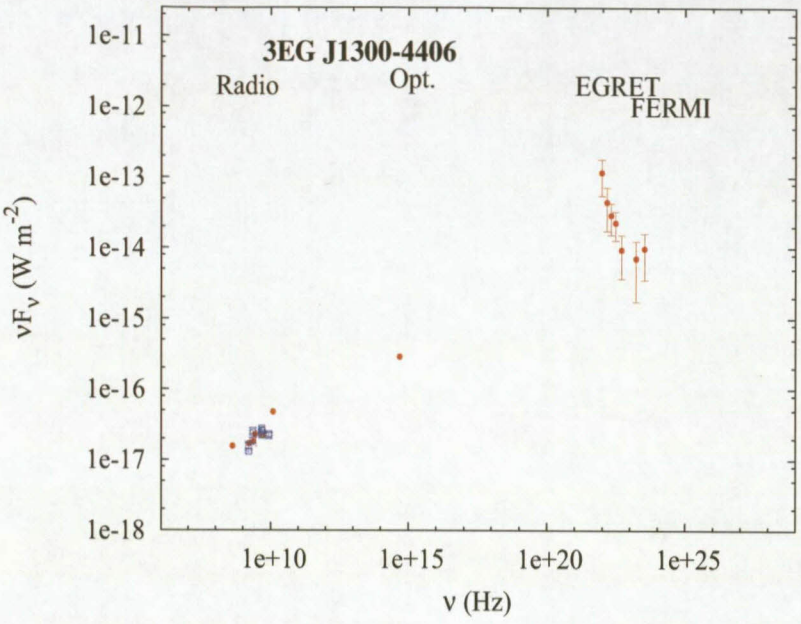

(g) *3EG J1300-4406*

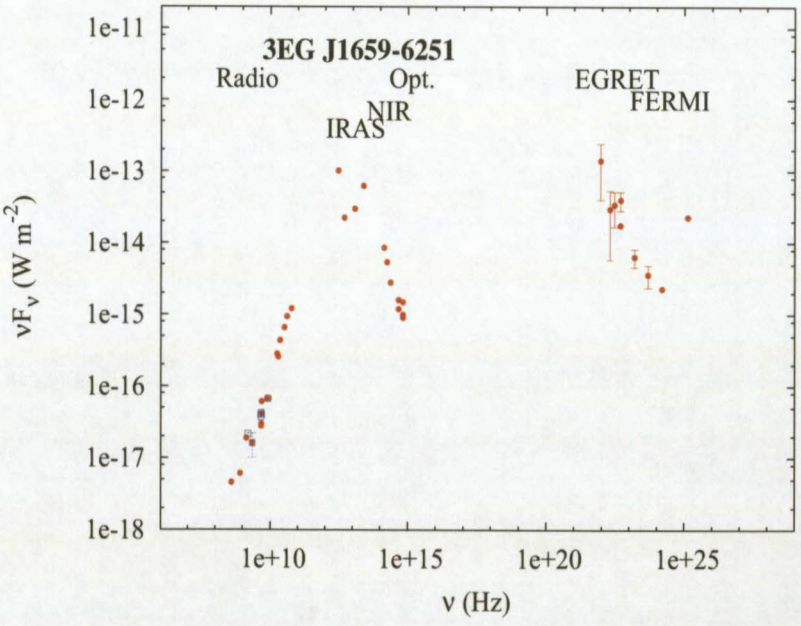

(h) *3EG J1659-6251*

Figure 4.23: Spectral Energy Distributions of the selected *EGRET* sources (continued). Red dots represent the data collected or reduced from online catalogues and archives. Data obtained from observations using local telescopes are represented by blue squares (Radio data from the 26-m HartRAO radio telescope).

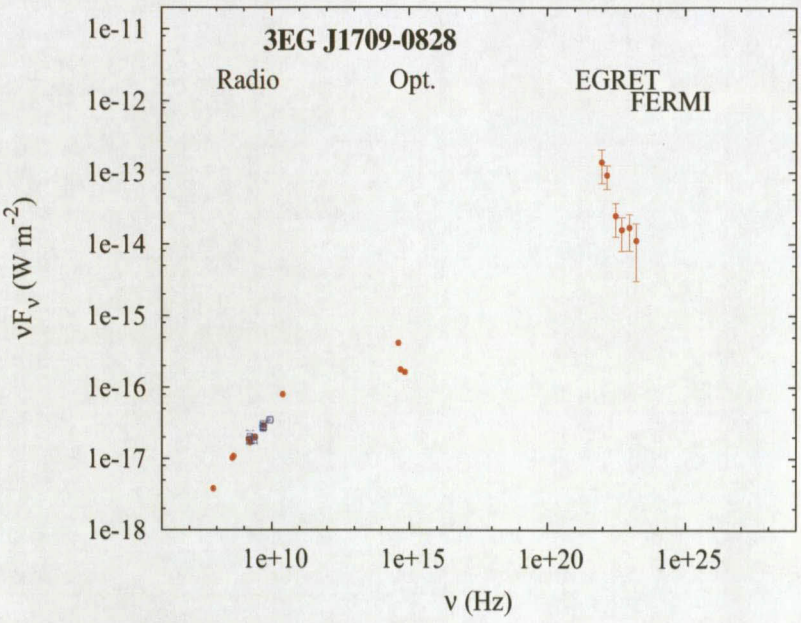

(i) *3EG J1709-0828*

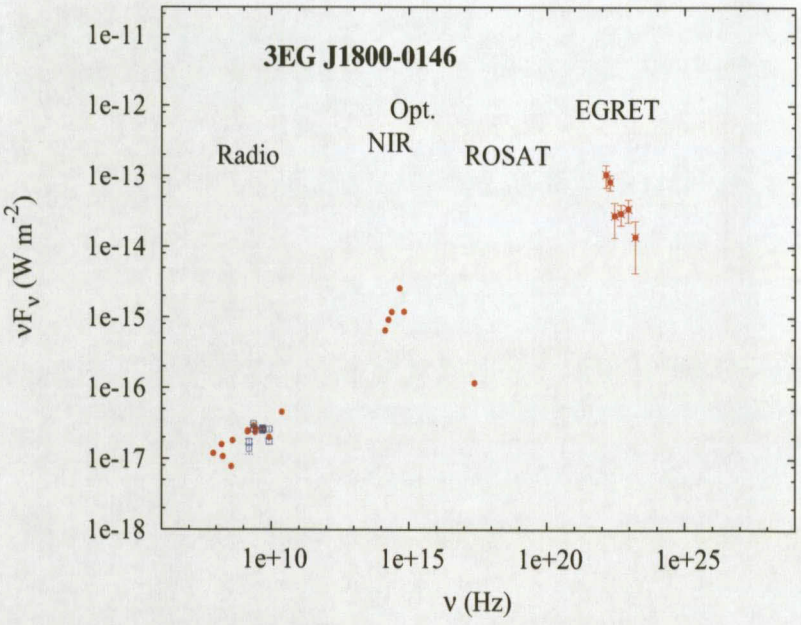

(j) *3EG J1800-0146*

Figure 4.23: Spectral Energy Distributions of the selected *EGRET* sources (continued). Red dots represent the data collected or reduced from online catalogues and archives. Data obtained from observations using local telescopes are represented by blue squares (Radio data from the 26-m HartRAO radio telescope).

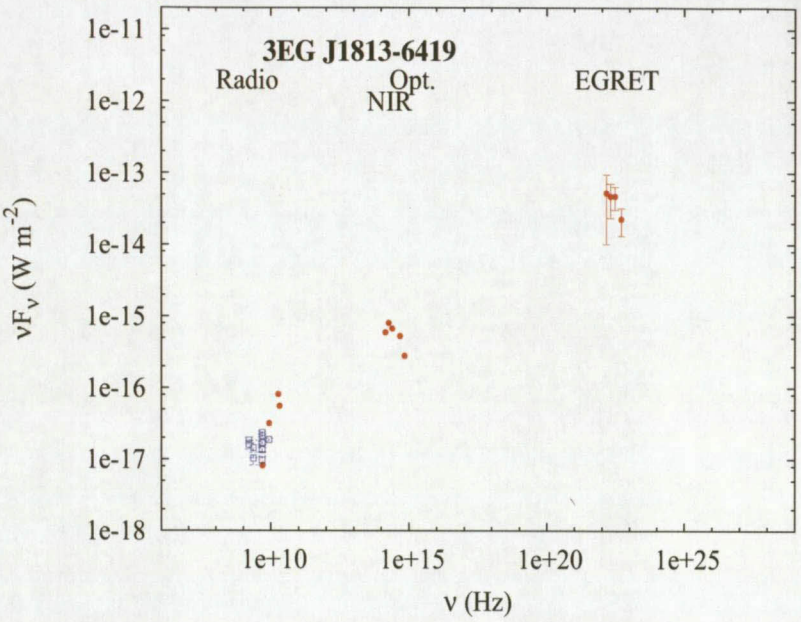

(k) *3EG J1813-6419*

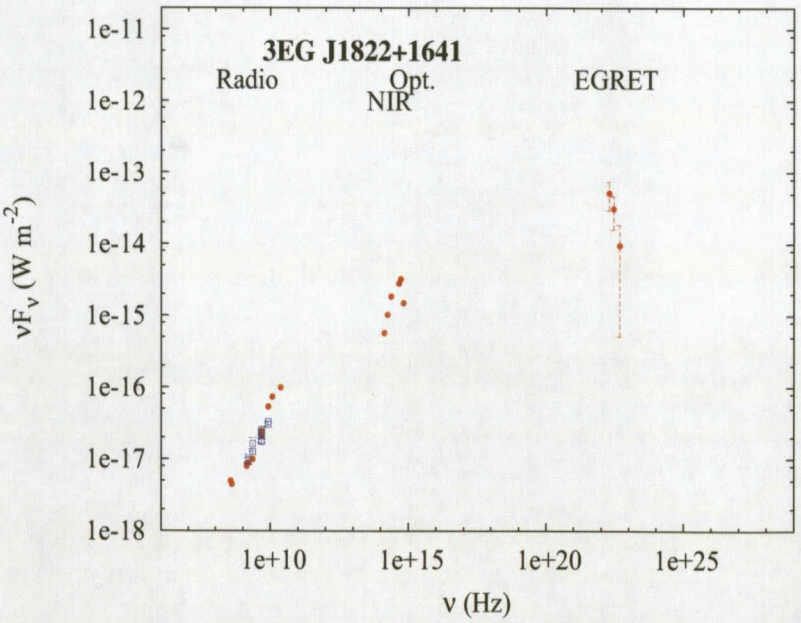

(l) *3EG J1822+1641*

Figure 4.23: Spectral Energy Distributions of the selected *EGRET* sources (continued). Red dots represent the data collected or reduced from online catalogues and archives. Data obtained from observations using local telescopes are represented by blue squares (Radio data from the 26-m HartRAO radio telescope).

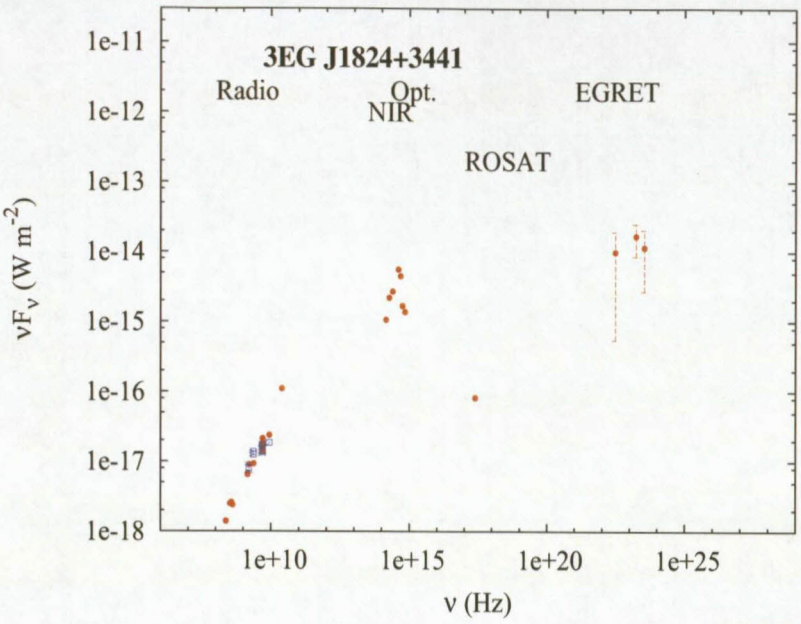

(m) *3EG J1824+3441*

Figure 4.23: Spectral Energy Distributions of the selected *EGRET* sources (continued) . Red dots represent the data collected or reduced from online catalogues and archives. Data obtained from observations using local telescopes are represented by blue squares (Radio data from the 26-m HartRAO radio telescope).

To examine the correlation between the low-energy and high-energy peaks in the SED[12] using the data is challenging as this ideally needs to match these two peaks over broad energy ranges that cover substantial segments of the spectrum. General challenges that are present in the existing data are the following:

- Due to effects of self-absorption and inhomogeneity in the outer part of the jets, radio to mm fluxes of the selected sources do not match the SED of the synchrotron self-Compton model of beamed synchrotron and inverse Compton scattering from the same population of electrons. However, this result is not surprising. In fact, by comparing with the spectra of typical blazars given in Figure 1.8, it can be seen that the low-energy radio emission is uncorrelated with the synchrotron self-Compton SED. This is particularly noticeable in 3C279 (FSRQ), BL Lacertae (LBL) and in Mrk 501 (HBL).

- The isolated thermal IR-NIR data in some sources, suggest an additional high luminous thermal dust component resulting from the heating by the accretion disk.

[12]The Spectral Energy Distribution (SED) of typical blazars (e.g. Figure 1.8) presents two peaks: the low-energy peak representing the synchrotron emission (located in IR-Optical) and the high-energy peak representing the inverse Compton scattering emission (located in the high-energy gamma-ray band).

- In Section 4.4.2 the importance of X-ray data was mentioned in helping to disentangle the synchrotron and the inverse Compton emissions on the source SEDs. Unfortunately, from the sample of this study, few sources have X-ray data and in most of the cases where the X-ray data exist, the latter were not pointed observations, but transient, presumably not allowing for an to estimation of a reliable X-ray spectral index.

However, it has been noted that the γ-ray data from *EGRET* are on the steep side of the inverse Compton scattering part. In some cases, where the γ-ray data from *Fermi-LAT* marks a turnover, a second mode of emission has been suggested which is most likely the External Compton component.

The interpretation of the observed Spectral Energy Distributions (SEDs) and the identification of the involved astrophysical interactions require not only high quality observational data, but also good knowledge of the contributing mechanisms, i.e. having accurate models describing them. The typical blazar SEDs (e.g. Figures 2.14 and 2.16(b)) were discussed in Chapter 2. It appears that in the low-energy band (from radio to UV), the blazar emission is dominated by the synchrotron emission from the interaction of particles and the jet magnetic field, while the high-energy gamma-ray band is dominated by the emission from inverse Compton scattering between particles in the jets and internal synchrotron photons (SSC) or with external Compton photons (EC). In the next chapter, detailed discussions on the synchrotron self-Compton model will be presented.

Chapter 5

Modelling the SSC Emission from Blazars

Blazars are powered by material falling into a supermassive black hole at the centre of the host galaxy. Gas, dust and plasma from nearby stars are captured and spiral into this black hole, creating a hot accretion disc and corona in the form of photons, electrons, positrons and other elementary particles.

Perpendicular to the accretion disc, a pair of relativistic jets (twin jets) carry highly energetic plasma away from the blazar.

These jets are collimated by a combination of a strong magnetic field and outflows from the accretion disc. Inside the jet[1], high-energy photons and particles interact not only with each other, but also with the strong magnetic field, releasing energy mostly through synchrotron radiation and inverse Compton scattering. This was discussed in detail in Chapter 2.

In the previous chapter, multi-wavelength observational data of the selected blazar-like sources were presented and analysed. A close analysis of their SEDs showed that the broadband multi-wavelength emission from these sources from radio to high-energy γ-rays is nonthermal in origin. It is believed that most of the VHE γ-ray emission results from the scattering between highly relativistic jet electrons and synchrotron photons in the jet, i.e. the so-called synchrotron self-Compton (SSC), although external photons may contribute as well.

The aim of this chapter is to discuss a model of synchrotron self-Compton (SSC) emission from jets and apply it to constrain both the nonthermal synchrotron and inverse Compton radiation from the selected blazar candidates.

[1]The jet can be considered as a set of blobs containing ultra-relativistic particles in a strong frozen-in magnetic field.

5.1 Spectral data and proposed model fitting

The multi-wavelength data of the selected sources were described and analysed in detail in the previous chapter. Most of their Spectral Energy Distributions (SEDs) (see Figure 4.23), commonly show three main parts:

The low-energy radio emission:

The radio data follow a simple power-law model, suggesting that the radio emission is nonthermal in origin, most likely synchrotron emission from electrons trapped in the jet magnetic field. Katarzyński et al. (2001) suggested that the radio component may originate from more extended, dilute and inhomogeneous outer parts of the jet, implying an emitting region with large jet radius and both low energy and density of particles, while Giroletti (2005) indicated that in low luminosity AGNs, the radio emission comes from less boosted regions of the jet. However, when the dissipation region is compact, synchrotron self-absorption[2] is expected to play an important role in the cooling at radio to millimetre wavelengths, resulting in a typical $S_\nu \propto \nu^{\frac{5}{2}}$ spectrum. Consequently, the radio data from farther regions of the jet are sometimes not included in the homogeneous SSC model (e.g. Figures 1.8(a) and 1.8(b), representing the SEDs of 3C279 (FSRQ) and BL Lacertae (LBL)).

Due to the fact that its contribution at high energy is very low, further modelling of this low-energy emission at high energies was not performed in this study.

The Near Infrared (NIR) and optical emission:

The observed and published optical and Near Infrared magnitudes of some selected sources show a sharp thermal peak while others show nonthermal characteristics. The Near Infrared thermal emission is interpreted as the signature of the dust, heated by the disk radiation, while the optical thermal emission is believed to be coming from the stellar emission of the host galaxy. The black body model was used to fit data in these bands.

[2] A self-absorption of photons produced by synchrotron emission occurs when the brightness temperature of the source, $T_B = \frac{\lambda^2}{2k}\frac{S_\nu}{\Omega}$, where Ω is the solid angle that the source subtends at the observer, approaches its kinetic temperature $T_e = \frac{\gamma m_e c^2}{3k}$. The self-absorption is imposed because thermodynamically the radiating electrons cannot result in a brightness greater than their kinetic temperature. Since the spectrum of the radiation is peaked at the critical frequency $\nu = \nu_c = \gamma^2 \nu_g$ i.e. $\gamma = \left(\frac{\nu}{\nu_g}\right)^{\frac{1}{2}}$ where $\gamma = \frac{E}{m_e c^2}$ and $\nu_g = \frac{eB}{2\pi m_e}$ is the non-relativistic frequency, the effective temperature of the particle becomes a function of the frequency i.e. $T_e \sim (\frac{m_e c^2}{3k})(\frac{\nu}{\nu_g})^{\frac{1}{2}}$. Therefore, for self-absorbed sources i.e. $T_B = T_e$, in the Rayleigh-Jeans limit,

$$S_\nu = \frac{2kT_B}{\lambda^2}\Omega = \frac{2m_e}{3{\nu_g}^{\frac{1}{2}}}\Omega\nu^{\frac{5}{2}} \propto \frac{\theta^2\nu^{\frac{5}{2}}}{B^{\frac{1}{2}}}, \tag{5.1}$$

where $\Omega \propto \theta^2$. This result shows that in the bands where self-absorption becomes important (e.g. radio, centimetre, millimetre wavelengths in the nuclei of active galaxies and quasars), the spectrum is in the form $S_\nu \propto \nu^{\frac{5}{2}}$ i.e. independent of the spectrum of emitting particles as long as the magnetic field is uniform.

The Near Infrared and optical nonthermal emission is believed to be the result of the synchrotron emission from relativistic electrons spiralling along the magnetic field in the inner part of the jet.

The γ-ray emission:

The SEDs of the selected sources show the high-energy gamma-rays from MeVs to GeVs with a peak in MeVs. It is believed that the high-energy gamma-ray emission is produced by the SSC process, although the EC may dominate particularly in the cases of FSRQs.

Few sources have X-ray data. The X-ray emission contributes either to the synchrotron emission or to the inverse Compton emission depending on the effectivity of the acceleration of particles in the jet. It is believed that in most of the FSRQs, the X-ray emission is part of the inverse Compton emission.

5.2 SSC model description

The key point of the SSC emission model is to find analytical solutions for the synchrotron and inverse Compton scattering radiative transfer equations as applied to homogeneous spherical sources using a minimum of geometrical and physical input parameters, which can be observed or constrained from the emitting system.

5.2.1 Basic assumptions

In the approach of the model, e.g. Katarzyński et al. (2001) and Krawczynski et al. (2004), it is assumed that

- the emitting region, a blob of plasma positioned at a certain distance in the jet, filled by relativistic electrons with the uniform density and uniform magnetic field is of spherical geometry of radius R_b.
- the electron distribution as a function of energy (or as a function of Lorentz factor) is assumed to be a broken power-law function with a sharp cut-off at high energies, i.e.

$$N_{\rm e}(\gamma) = \begin{cases} K_1 \gamma^{-p_1}, & \gamma_{\rm min} \leq \gamma \leq \gamma_{\rm b} \\ K_1 \gamma_{\rm b}^{p_2-p_1} \gamma^{-p_2}, & \gamma_{\rm b} < \gamma \leq \gamma_{\rm max}, \end{cases} \tag{5.2}$$

where $N_{\rm e}(\gamma)$ is defined such that $N_{\rm e}(\gamma)d\gamma$ is the number density of electrons with Lorentz factor[3] in the interval γ and $(\gamma + d\gamma)$, K_1 is the normalisation constant, $p_1 = 2\alpha_1 + 1$ and $p_2 = 2\alpha_2 + 1$ are the electron energy spectral indices below and above the break energy $E_b = \gamma_b mc^2$ with $\alpha_{1,2}$ the observed spectral indices and $\gamma_{\rm min}$, $\gamma_{\rm b}$, $\gamma_{\rm max}$ are the

[3]For convenience, the Lorentz factor $\gamma = \frac{E}{m_e c^2}$ is used instead of the energy, otherwise $N_{\rm e}(\gamma)d\gamma = N_{\rm e}(E)dE$.

Lorentz factor at the minimum energy, at the energy break and at the energy cut-off of the electron population respectively (see Figure 5.1). The γ_b is determined by the peak frequency of the synchrotron radiation given by Equation 2.93, i.e. $\nu_c = \frac{3}{2}\gamma^2 \nu_g \sin\theta$, where $\nu_B = 2.8 \times 10^6 B$ Hz is the cyclotron frequency of electrons in magnetic field B (expressed in Gauss) and δ is the Doppler factor.

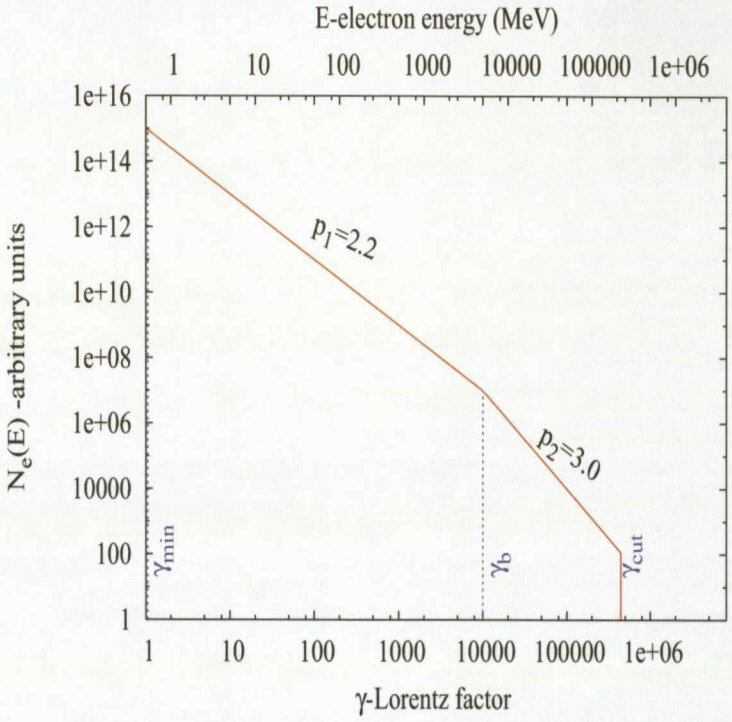

Figure 5.1: Broken power law of the electron distribution.

The two-power-law shape of the electron energy spectrum can be explained by the fact that within the shock acceleration scenario, newly accelerated electrons are continuously injected. These electrons lose energy through radiative cooling, and the instantaneous electron spectrum steepens above a critical energy E_b. All the electrons with energy greater than E_b radiate away their energy within a time shorter than the dynamical time.

The broken power-law electron energy spectrum naturally gives rise to a piece-wise power-law photon spectrum commonly observed:

$$F_\nu \propto \begin{cases} \nu^{-\alpha_1} & \text{if } \nu_m < \nu < \nu_p \\ \nu^{-\alpha_2} & \text{if } \nu > \nu_p, \end{cases} \tag{5.3}$$

where F_ν is the observed flux density (in units of mJy), ν_m and ν_p are the observed characteristic emission frequencies of the electrons with energy γ_m and γ_b , respectively, and ν_p is usually the peak frequency of the νF_ν spectrum. The low-energy power law $\nu^{-\alpha_1}$ does not extend to low

frequency indefinitely. Figure 2.10 shows that below a certain frequency $\nu_a < \nu_p$, the synchrotron self-absorption starts to play a significant role. In this case, the emitted photons are thermalised by the thermal electron population.

5.2.2 Modelling the synchrotron radiation

The synchrotron emission coefficient or synchrotron emissivity [J s^{-1} $m^{-3}Hz^{-1}$ sr^{-1}] (see Sections 2.4.4 and 2.5.1.2) of a power-law distribution of electrons, calculated in the rest frame of the emitting blob, is given by:

$$j'_{\rm s}(\nu'_{\rm s}) = \frac{1}{4\pi}\int_{\gamma_{\rm min}}^{\gamma{\rm max}} N_{\rm e}(\gamma) j'_{\rm e}(\nu'_{\rm s},\gamma){\rm d}\gamma, \tag{5.4}$$

where $\nu'_{\rm s}$ is the synchrotron peak frequency, and $j'_{\rm e}(\nu'_{\rm s},\gamma)$ is the mean emission coefficient for a single electron [J s^{-1} Hz^{-1} sr^{-1}] integrated over an isotropic distribution of pitch angles.

The synchrotron intensity [J $s^{-1}m^{-2}sr^{-1}Hz^{-1}$] in the source frame is obtained by solving the radiative transfer equation for the spherical blob geometry. In the specific case where the local synchrotron emission coefficient is assumed to be uniform the solution is given by (Equation 2.109)

$$I'_{\rm s}(\nu'_{\rm s}) = \frac{j'_{\rm s}(\nu'_{\rm s})}{k'(\nu'_{\rm s})}(1-{\rm e}^{-\tau}), \tag{5.5}$$

with $\tau = 2R_{\rm b}k'(\nu'_{\rm s})$ representing the optical depth, where $R_{\rm b}$ is the radius of the emitting region and $k'(\nu')$ is the absorption coefficient [cm^{-1}], (e.g. Rybicki and Lightman (2004), Longair (1994)) given by

$$k'(\nu'_{\rm s}) = -\frac{1}{8\pi m_{\rm e}\nu'^2_{\rm s}}\int_{\gamma_{\rm min}}^{\gamma_{cut}} \gamma^2 \frac{d}{d\gamma}\left[\frac{N_{\rm e}(\gamma)}{\gamma^2}\right] j'_{\rm e}(\nu'_{\rm s},\gamma){\rm d}\gamma. \tag{5.6}$$

The synchrotron luminosity in the source frame for spherical geometry is then simply given by

$$L'_{\rm s}(\nu'_{\rm s}) = 4\pi^2 R_{\rm b}^2 I'_{\rm s}(\nu'_{\rm s}). \tag{5.7}$$

The emitting blob at the base of the blazar jet is believed to have a bulk relativistic motion towards the observer. Using the transformation relation, from the rest frame of the source to the observer's frame, of the intensity (Equation 2.66), i.e. $I(\nu) = \delta_{\rm b}^3 I'(\nu')$, associated with the "Doppler boosting" effect, we can write the observed flux density as

$$F_{\rm s}(\nu'_{\rm s}) = \pi\frac{R_{\rm b}^2}{d_{\rm l}^2}\delta_{\rm b}^3(1+z)I'_{\rm s}(\nu'_{\rm s}), \tag{5.8}$$

where $d_{\rm l}$ is the cosmological distance of the source, z is the redshift and $\delta_{\rm b} = [\gamma_{\rm b}(1-\beta\cos\theta)]^{-1}$ is the Doppler factor, where $\gamma_{\rm b}$ is the blob Lorentz factor, θ is the angle of the blob velocity vector relative to the line of sight and $\beta = v/c$. To fully switch to the observer's frame the rest

frame frequency also has to be transformed into the observed frequency, i.e.

$$\nu_{\rm s} = \frac{\delta_{\rm b}}{1+z}\nu'_{\rm s}. \tag{5.9}$$

5.2.3 Modelling the inverse Compton radiation

The inverse Compton scattering emission coefficient is given by (e.g. Inoue and Takahara (1996))

$$j'_{\rm c}(\nu'_{\rm c}) = \frac{h}{4\pi}\epsilon'_{\rm c}q(\epsilon'_{\rm c}), \tag{5.10}$$

with $q(\epsilon'_{\rm c}) = \int {\rm d}\epsilon'_{\rm s} n(\epsilon'_{\rm s}) \int d\gamma N_{\rm e}(\gamma) C(\epsilon'_{\rm c}, \gamma, \epsilon'_{\rm s})$ representing the differential photon production rate (i.e. number of the scattered high energy photons with Lorentz factor $\epsilon'_{\rm c} = \frac{E'_{\rm c}}{m_{\rm e}c^2} = \frac{h}{m_{\rm e}c^2}\nu'_{\rm c}$), in the energy interval $(E'_{\rm c},\ E'_{\rm c} + dE'_{\rm c})$ per unit volume and per unit time).

$$C(\epsilon'_{\rm c}, \gamma, \epsilon'_{\rm s}) = \frac{2\pi r_{\rm e}^2 c}{\gamma^2 \epsilon'_{\rm s}}[2\kappa\ln(\kappa) + (1+2\kappa)(1-\kappa) + \frac{(4\epsilon'_{\rm s}\gamma\kappa)^2}{2(1+4\epsilon_{\rm s}\gamma\kappa)}(1-\kappa)]. \tag{5.11}$$

The Compton kernel is given by (Jones 1968)

$$n(\epsilon'_{\rm s}) = \frac{3}{4}\frac{4\pi}{hc\epsilon'_{\rm s}}\frac{j'_{\rm s}(\nu'_{\rm s})}{k'(\nu'_{\rm s})}\left(1 - \exp(-k'(\nu'_{\rm s})R_{\rm b})\right) \tag{5.12}$$

represents the number density of the synchrotron photons in the energy interval $(E'_{\rm s},\ E'_{\rm s} + dE'_{\rm s})$, where

$$\kappa = \frac{\epsilon'_c}{4\epsilon'_s\gamma(\gamma - \epsilon'_{\rm c})} \tag{5.13}$$

and $\epsilon'_{\rm s} = \frac{E'_{\rm s}}{m_{\rm e}c^2} = \frac{h}{m_{\rm e}c^2}\nu'_{\rm s}$ is the Lorentz factor of the synchrotron photon.

Absorption of the inverse-Compton photons by electrons can be neglected as long as frequencies of the emitted photons are high enough, but at higher energies, the inverse Compton photons may produce pairs by interacting with the synchrotron photons, leading to a decrease in the observed VHE radiation. The optical depth (Equation 5.5) associated with the pair absorption is calculated by (e.g. Coppi and Blandford (1990))

$$\tau'_{\gamma\gamma}(\epsilon'_{\rm c}) = 0.2\sigma_T\frac{1}{\epsilon'_{\rm c}}n(\frac{1}{\epsilon'_{\rm c}})R_{\rm b}. \tag{5.14}$$

Thus, Equations 5.5 and 5.8 are used to calculate the intensity and the flux density of the inverse Compton scattering emission, i.e.

$$\begin{aligned} I_{\nu'_{\rm c}} &= \frac{j_{\nu'_{\rm c}}}{\tau_{\gamma\gamma}}R_b(1 - e^{\tau_{\gamma\gamma}}) \\ F_{\rm c}(\nu'_{\rm c}) &= \pi\frac{R_{\rm b}^2}{d_{\rm l}^2}\delta_{\rm b}^3(1+z)I'_{\rm c}(\nu'_{\rm c}). \end{aligned} \tag{5.15}$$

The nonthermal optical to γ-ray emission is modeled using the homogeneous synchrotron

self-Compton model, e.g. (Katarzyński et al. 2001, Krawczynski et al. 2004)). In this thesis, only the synchrotron self-Compton model due to its broad band multi-wavelength coverage will be analysed. Detailed formulas and calculations are presented in Katarzyński et al. (2001). The source code of the model can be obtained from `http://jelley.wustl.edu/multiwave/spectrum/download.htm`. This code generates the synchrotron and the inverse Compton spectra, provided that constrained input parameters for the source are presented.

5.3 Constraints of the input model parameters

Within the SSC computation scheme, nine free independent parameters describe the high-energy part of the spectra. Four of them are related to the global properties of the emitting blob, namely

- z-the redshift
- $R_{\rm b}$ - the radius of the emitting blob,
- B - the uniform magnetic field, and
- $\delta_{\rm b}$ - the Doppler factor.

The five other parameters are related to the particle physics and describe the high-energy particle distribution, namely

- K_1 - the density factor,
- $\gamma_{\rm b}$ and $\gamma_{\rm max}$ - the Lorentz factors at the break and cut-off of the electron energy distribution, and
- p_1, p_2 the spectral indices of the electron energy distribution at low and higher energies respectively.

Depending on the quality of the available multi-wavelength data of the source, a certain number of constraints can be directly deduced. The more useful the data, the more parameters are constrainable. The data are considered good quality if they allow the accurate determination of the following observed quantities, i.e.

- the redshift z,
- the values of the break and the peak frequencies in the synchrotron spectrum $(\nu_{\rm s_b}, \nu_{\rm s_p})$, the peak frequency in the inverse-Compton spectrum $(\nu_{\rm c_p})$,
- the fluxes at these frequencies $(F_{\rm s}(\nu_{\rm s_b}), F_{\rm s}(\nu_{\rm s_p}), F_{\rm c}(\nu_{\rm c_p}))$ and
- the slopes at the low-energy and high-energy ends of the synchrotron spectrum, i.e. α_1 and α_2 respectively.

The nine parameters mentioned above are constrained, using

$$R = ct_{\rm var}\frac{\delta}{1+z}, \tag{5.16a}$$

$$\gamma_{\rm b} = \left(\frac{3}{4}\frac{\nu_{\rm c_p}}{\nu_{\rm s_p}}\right)^{\frac{1}{2}}, \tag{5.16b}$$

$$\gamma_{\rm cut} = \gamma_{\rm b}\sqrt{\frac{3.7\times10^6\nu_{\rm s_p}}{C_{\rm p}\nu_{\rm s_b}}}, \tag{5.16c}$$

$$B\delta \simeq (1+z)\frac{{\nu_{\rm s_p}}^2}{3.7\times10^6\nu_{\rm c_p}}, \tag{5.16d}$$

$$\alpha_1 = \frac{p_1-1}{2}, \tag{5.16e}$$

$$\alpha_2 = \frac{p_2-1}{2} \text{ and} \tag{5.16f}$$

$$\frac{F_{\rm c}}{F_{\rm s}} = \frac{U'_{\rm rad}}{U'_B}, \tag{5.16g}$$

where $t_{\rm var}$ is the time variability scale and $C_{\rm p}$ an empirically-estimated constant (e.g. Katarzyński et al. (2001)).

$$C_{\rm p}(p_2) \sim -3.25\times10^5 p_2^3 + 1.67\times10^6 p_2^2 - 3.62\times10^6 p_2 + 4.65\times10^6. \tag{5.17}$$

It can be seen that there are seven equations for nine parameters to constrain. Therefore, depending on the spectral data of a source, the system stays analytically unconstrained, with more than two degrees of freedom. Consequently, the solution to the problem may not be unique and in this case, a number of parameters that the data allows to contrain are set in the code, then other remaining (free parameters) are adjusted to obtain the best fit to the data.

Regarding the size of the emitting region: For confirmed variable sources, this is estimated using Equation 5.16a. It has not been possible to detect the variability in the selected sources due to the scarcity of the data collected in online catalogues and, for the sources which were observed, significant variability could not be verified as it was noticed that any fluctuation in the magnitudes could also be correlated to the fluctuation in seeing at the same time.

Instead of using the variability timescale method and assuming a compact source, the size of the emitting region was estimated by the size of the black hole, which is related to the blue absolute[4] magnitude (of the compact bulge) of the host galaxy (e.g. Kormendy and Richstone (1995)). In fact, using data of the well-known galaxies found in the above-mentioned reference, an empirical relation between the blue absolute magnitude of host galaxy and the mass of its

[4]The absolute magnitude is related to apparent magnitude by $\mathrm{M_{absolute}} - \mathrm{m_{apparent}} = -5\log_{10}(\frac{\mathrm{d_L}}{1\mathrm{pc}}) + 5$.

central black hole was established (Figure 5.2), i.e.

$$\log_{10}(\frac{M}{M_{\odot}}) = aM_{\mathrm{B}} + b, \text{ with } a = -0.524678 \pm 0.43588 \text{ and } b = -2.03273 \pm 2.015, \quad (5.18)$$

where M is the mass of the black hole, M_{B} is the blue absolute magnitude of the bulge and $M_{\odot}$ is the mass of the sun. This relation was used to estimate the masses of the black holes of the galaxies hosting the selected AGNs from our sample of study. With the mass of the black hole, the Schwarzschild radius r of a gravitating mass M was calculated using the Schwarzschild's relation, i.e.

$$r = \frac{2GM}{c^2}, \quad (5.19)$$

where $G = 6.61 \times 10^{-11}\,\mathrm{N\,m^{-2}\,kg^{-2}}$. These radii were used as initial values when running the model and then adjustments were made to find the best fit of the data. Table 5.1 gives the Schwarzschild radii and the radii obtained from the best fit of the SSC model for sources with known redshifts.

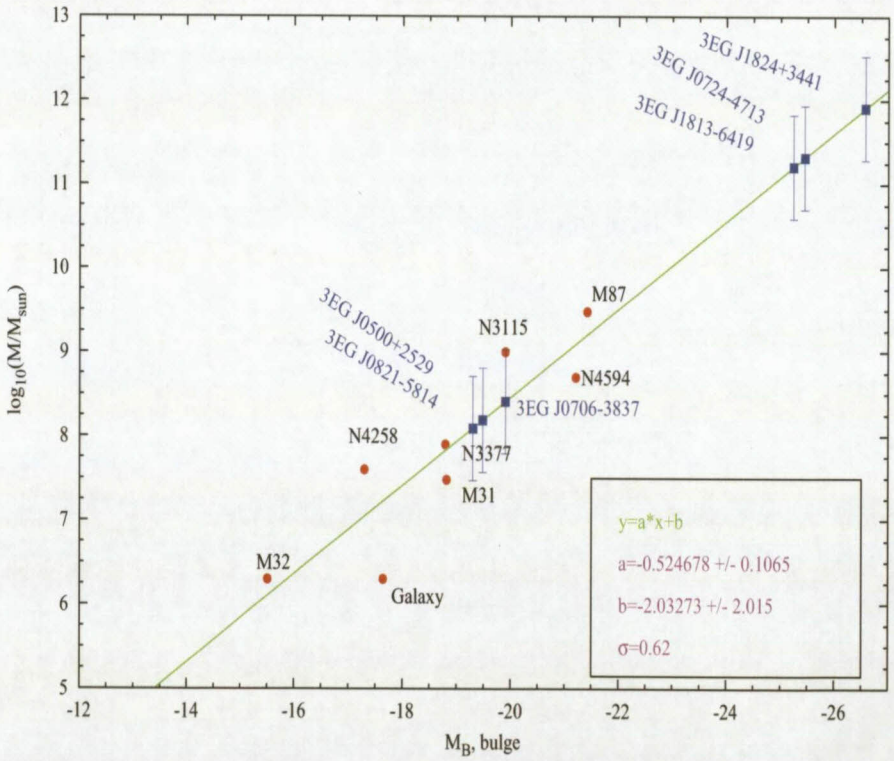

Figure 5.2: Relation between the mass of the black hole and the magnitude of the bulge. Data were obtained from (Kormendy and Richstone 1995). The error bars represent the estimated standard deviation of residuals, σ.

	Source	z (Mpc)	d (*)	m_B	M_B	$\log_{10}(\frac{M}{M_\odot})$ (m)	r (m)	r for best fit
1	*3EG J0500+2502*	0.277	1085	21	-19.48	8.19	4.57×10^{11}	1.00×10^{13}
2	*3EG J0706-3837*	0.129	523	18.72	-19.9	8.41	7.59×10^{11}	3.50×10^{13}
3	*3EG J0724-4713*	2.280	5559	20.03	-25.45	11.32	6.20×10^{14}	1.50×10^{14}
4	*3EG J0821-5814*	0.060	247	17.7	-19.3	8.09	3.68×10^{11}	1.00×10^{13}
5	*3EG J1813-6419*	1.020	3320	18.3	-25.24	11.21	4.81×10^{14}	1.00×10^{14}
6	*3EG J1824+3441*	1.810	4880	18.35	-26.57	11.91	2.40×10^{15}	1.00×10^{13}

Table 5.1: Estimates of the black hole sizes for sources with redshifts. (*) The distances (comoving radial distances due to expansion) were calculated [5] assuming the following cosmology: $H_0 = 72 \mathrm{km\,s^{-1}Mpc^{-1}}$, $\omega_M = 0.27$, $\Omega_{vac} = 0.73$.

5.4 The SSC spectral fits of the selected sources

As mentioned earlier in Section 5.1, the low-frequency radio synchrotron emission from compact sources follows the power law model of self-absorbed sources, i.e. $S_\nu \sim \nu^{\frac{5}{2}} B^{-\frac{1}{2}}$. Consequently, in low luminosity AGNs, the radio data do not follow the homogeneous SSC fitting of the SEDs due to the fact that they are believed to be generated in external regions which are less boosted (Giroletti 2005), with respect to where optical-to-γ-rays are produced (Abdo et al. 2009). This case is illustrated on the SEDs of the FSRQ 3C279 and BL Lacertae in Figures 1.8(a) and 1.8(b). This phenomenon is reflected in the selected sources. In fact, the radio data could not be connected with the IR and optical data as part of the same synchrotron emission, leaving the radio data alone unlinked to the homogeneous SSC fit.

Based on the quality of the NIR and optical data, the selected sources were subdivided into two groups:

- The first group (Group I) includes sources for which the NIR and optical data belong to the synchrotron emission and for which the redshifts of most of them have been determined. These sources are *3EG J0500+2502* (z=0.28, e.g. Hewitt and Burbidge (1991) and Laing et al. (1983)), *3EG J0706-3837* (z=1.29, reference this thesis), *3EG J0724-4713* (z=2.28, e.g. Véron-Cetty and Véron (2006)), *3EG J0821-5814* (z=0.06, reference this thesis) *3EG J1813-6419* (z=1.02, e.g. Healey et al. (2008a), *3EG J1659-6251* and *3EG J1709-0828*. The redshifts of the last two sources have not been measured yet.

- The second group (Group II) consists of sources for which the NIR and optical data correspond to the thermal emission. These sources are *3EG J0159-3603*, *3EG J0702-6212*, *3EG J1300-4406*, *3EG J1800-0146*, *3EG J1822+1641* and *3EG J1824+3441* (z=1.81, e.g. Zhang et al. (1998)).

For the first group, good optical data played an important role to identify the signature of the synchrotron emission in these sources. This implies optical data allowing the accurate calculation of the optical spectral index using a set of optical magnitudes in U, B, V, R and I optical bands. It is for this group that the homogeneous SSC model was applied due to the fact that they are the only ones which show synchrotron emission in the NIR and optical data. However, it is only in *3EG J0821-5814* that the SSC fitting incorporates the gamma-ray data (see Figure 5.3).

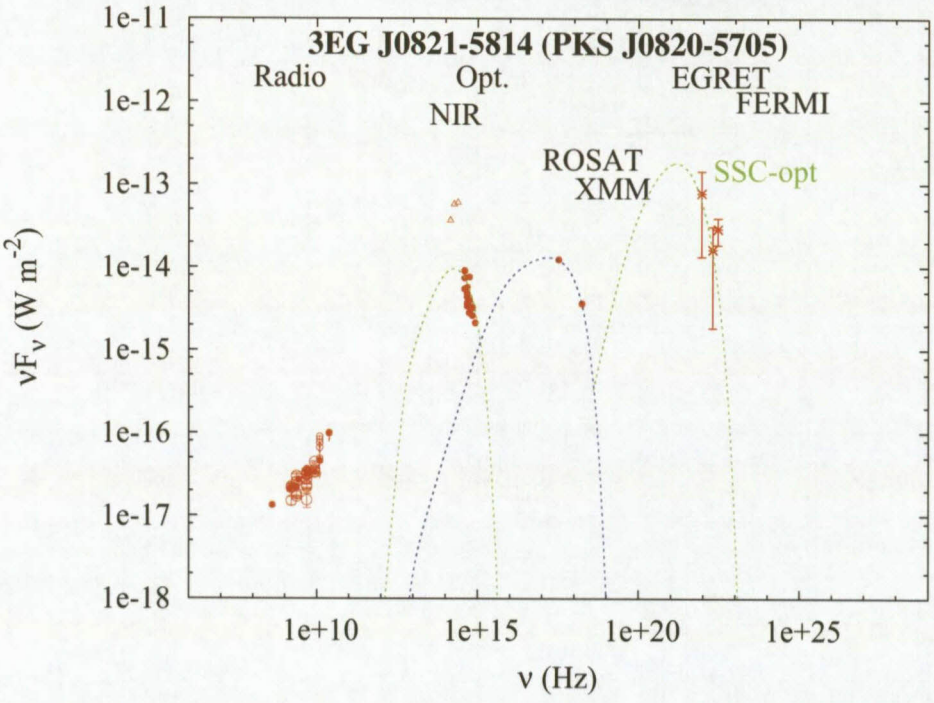

Figure 5.3: Homogeneous SSC model applied to *3EG J0821-5814*.

From the SEDs of the *3EG J0821-5814*, it can be seen that through the homogeneous SSC model, the gamma-ray data are compatible with the optical data. However, in this source the NIR to optical data and the X-ray data are not part of the same synchrotron spectrum suggesting that these emissions are produced in two different zones by two different electron populations. A multi-zone SSC modelling was suggested by Zhang (Zhang et al. 2009) for Pictor A, a nearby Fanaroff-Riley class II radio galaxy. Table 5.2 gives the constrained parameters in this source.

For other six sources of this group, the SSC model predicts the γ-ray fluxes below the observed data. The SEDs and the model parameters of these sources are shown in Figure 5.4 and Table 5.2 respectively.

For these SEDs, the External Compton (EC) model is believed to be the best model fit for the observed gamma-ray fluxes. In the next paragraph detailed discussions on this model will be given.

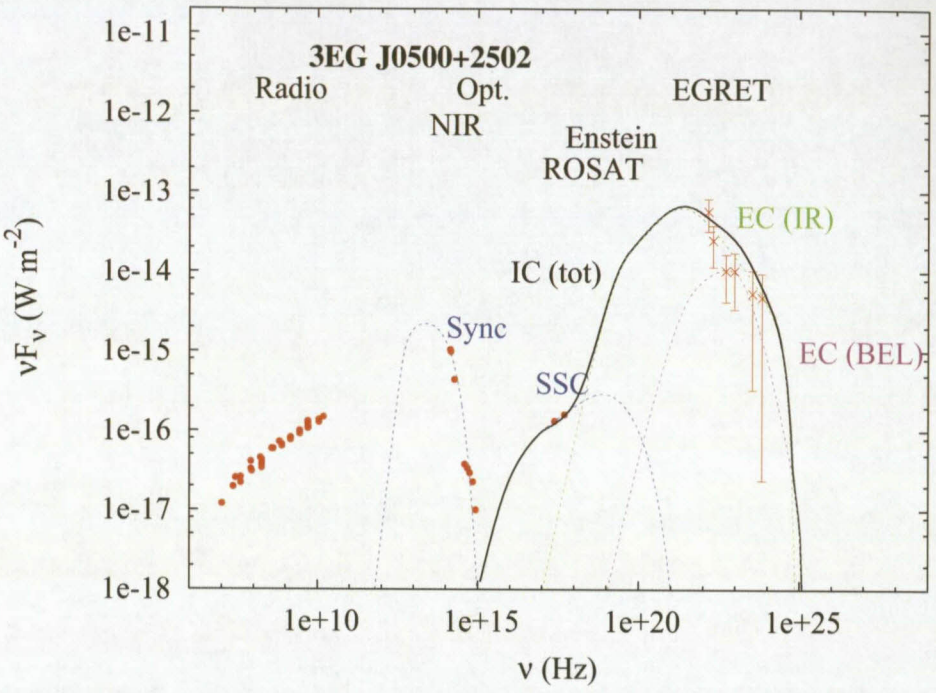

(a) *3EG J0500+2502*

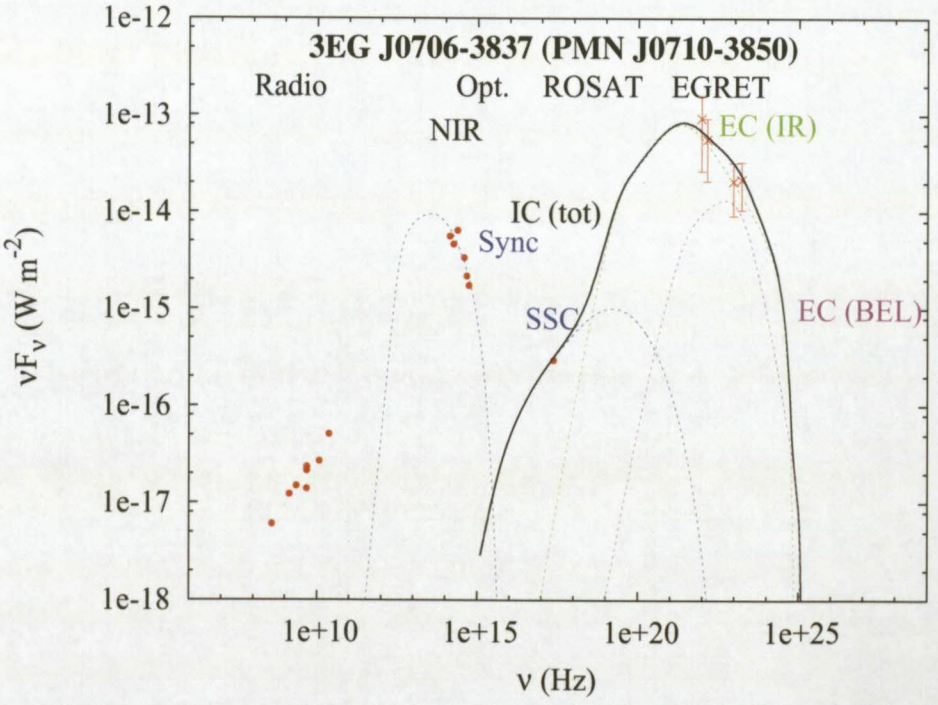

(b) *3EG J0706-3837*

Figure 5.4: Application of the SSC model (Group I).

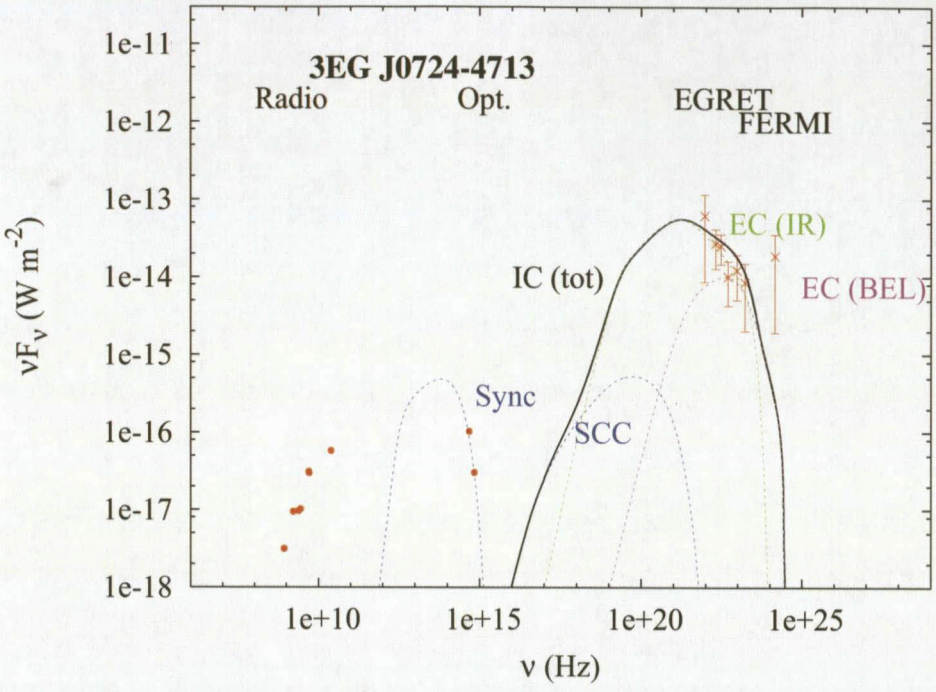

(e) *3EG J1709-0828*

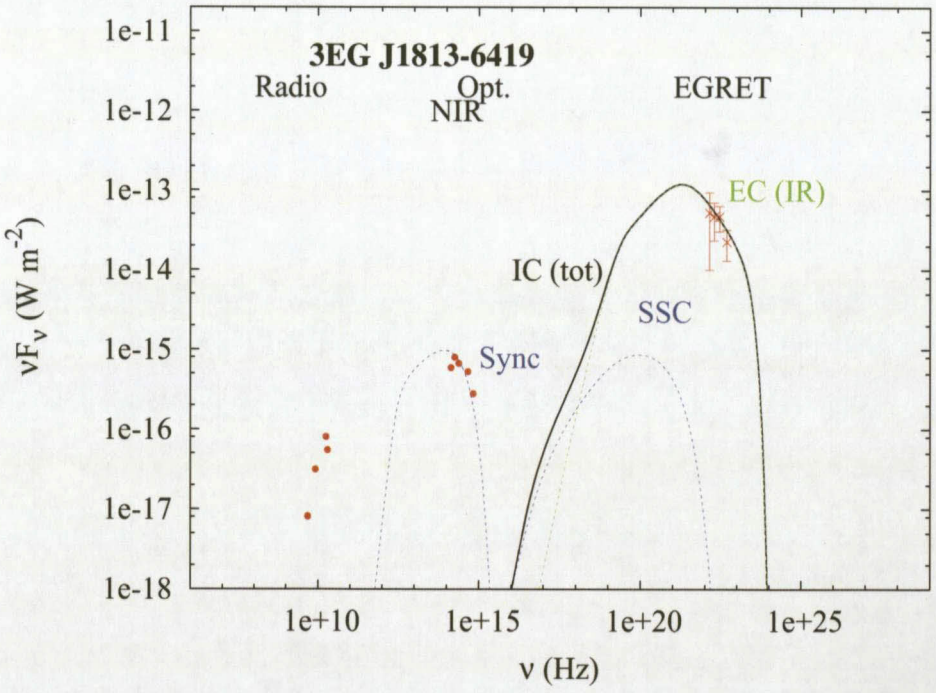

(f) *3EG J1813-6419*

Figure 5.4: Application of the SSC model (Group I) (continued).

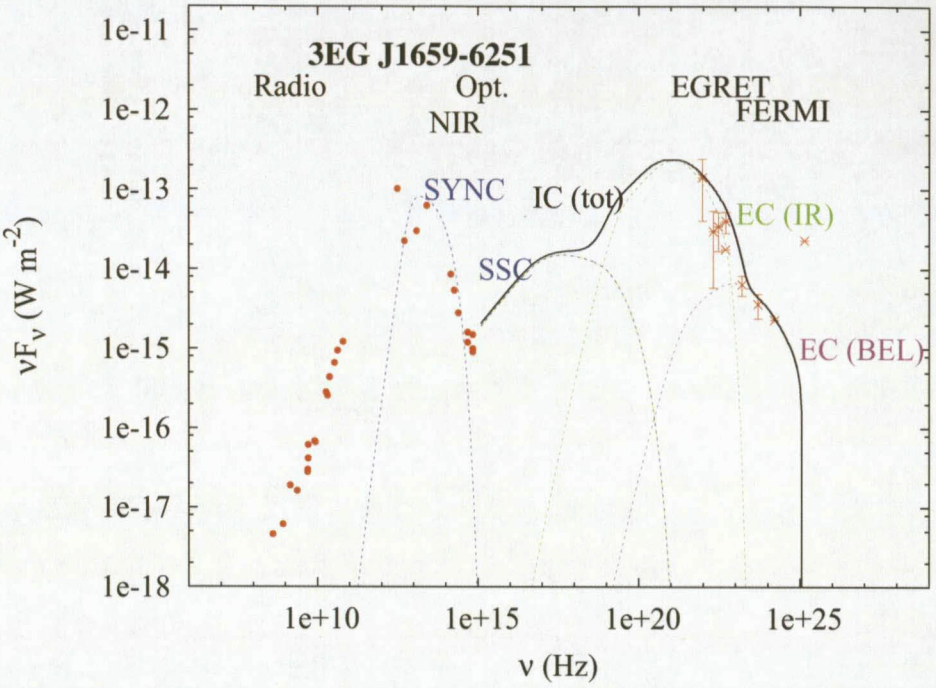

(c) *3EG J0724-4713*

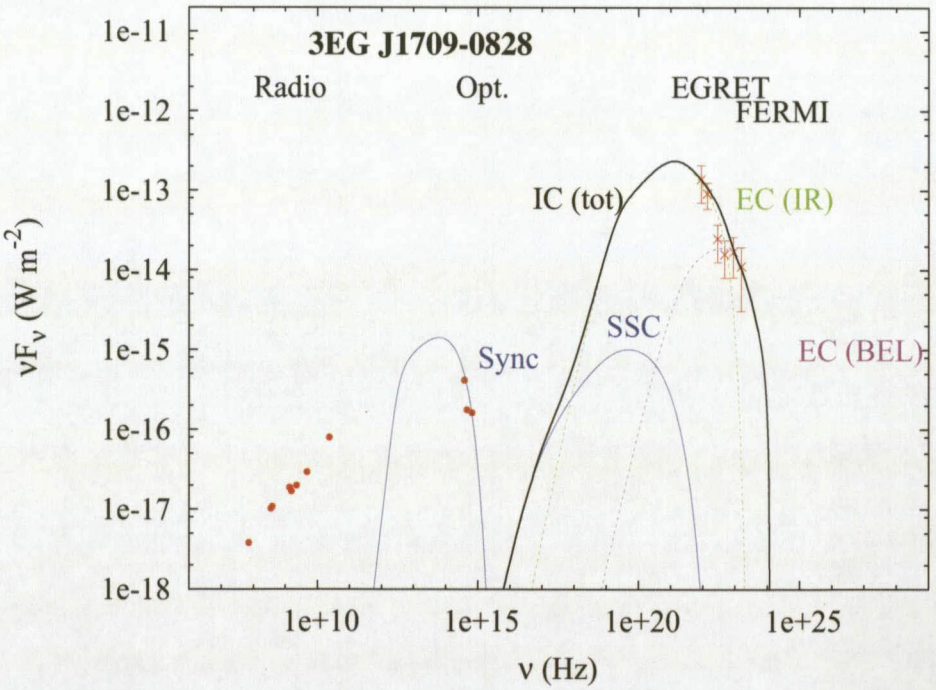

(d) *3EG J1659-6251*

Figure 5.4: Application of the SSC model (Group I) (continued). For sources with no known redshift (e.g. *3EG J1659-6251* and *3EG J1709-0828*), the energy-fluxes were estimated using z = 1.

Source		*3EG J0821-5814*		*3EG J0500+2502*	*3EG J0706-3837*	*3EG J0724-4713*	*3EG J1813-6419*	*3EG J1659-6251*	*3EG J1709-0828*
Parameter	Units	SSC (opt)	SSC (X-ray)						
z		0.06	0.06	0.28	0.13	2.28	1.02		
d_L (*)	(Mpc)	2.60×10^2	2.60×10^2	1.30×10^3	5.60×10^2	1.30×10^4	5.10×10^3		
radius	(m)	1.00×10^{13}	1.00×10^{12}	3.50×10^{13}	3.50×10^{13}	1.50×10^{14}	1.00×10^{14}	7.50×10^{14}	1.00×10^{14}
B	(T)	2.50×10^{-4}	2.50×10^{-4}	2.50×10^{-4}	2.50×10^{-4}	7.00×10^{-4}	2.50×10^{-4}	2.50×10^{-4}	2.50×10^{-4}
Lum	(eV)	6.23×10^{20}	3.81×10^{20}	1.21×10^{20}	1.74×10^{18}	5.80×10^{16}	5.99×10^{16}		
$E_{\rm min}$	$(\log_{10}(E/{\rm eV}))$	8.8	9.4	7	7	7.5	7.6	5	7.5
$E_{\rm max}$	$(\log_{10}(E/{\rm eV}))$	9.2	10.6	8.7	9	8.9	9	8.6	8.92
$E_{\rm break}$	$(\log_{10}(E/{\rm eV}))$	9.2	10	8.5	8.5	8.8	8.7	7.5	8.6
p_1		-2.2	-2.2	-2.4	-2.2	-2	-2	-2	-2
p_2		-2.8	-2.8	-4.2	-4.2	-3	-2.6	-3.2	-2.6
δ		3.8	15	11.5	12	7	7	12	8
$\nu_{\rm sync}$	(Hz)	1.80×10^{14}	1.40×10^{17}	2.30×10^{13}	3.50×10^{13}	6.1×10^{13}	8.20×10^{13}	1.60×10^{13}	6.20×10^{13}
$P_{\rm sync}$	${\rm erg.cm^{-2}.s^{-1}}$	9.60×10^{-12}	1.30×10^{-11}	2.20×10^{-12}	9.50×10^{-12}	4.80×10^{-13}	9.80×10^{-13}	8.13×10^{-11}	1.40×10^{-12}
SSA up to	(Hz)	6.90×10^{12}	1.10×10^{13}	6.20×10^{12}	4.80×10^{12}	4.30×10^{12}	3.80×10^{12}	9.85×10^{12}	4.30×10^{12}
ν_{IC}	(Hz)	1.50×10^{21}	6.90×10^{24}	7.80×10^{18}	1.60×10^{19}	5.30×10^{19}	9.10×10^{19}	4.24×10^{17}	4.80×10^{19}
$P_{\rm IC}$	$({\rm erg.cm^{-2}.s^{-1}})$	1.80×10^{-10}	7.70×10^{-11}	2.90×10^{-13}	1.00×10^{-12}	5.30×10^{-13}	8.60×10^{-13}	1.51×10^{-11}	1.00×10^{-12}
γ_{max}		3.10×10^3	7.80×10^4	9.80×10^2	2.00×10^3	1.60×10^3	2.00×10^3	7.79×10^2	1.60×10^3
$\rm KN_{sync}$	(Hz)	1.50×10^{17}	2.40×10^{16}	1.50×10^{18}	7.60×10^{17}	5.60×10^{17}	4.40×10^{17}	1.90×10^{18}	6.10×10^{17}
u_B	$({\rm erg.cm^{-3}})$	0.25	0.25	0.25	0.25	0.25	0.25	0.25	0.25
$u_{\rm sync}$	$({\rm erg.cm^{-2}.s^{-1}})$	6.39	6.21	0.04	0.03	0.38	0.31	0.35	0.24
u_p	$({\rm erg.cm^{-2}.s^{-1}})$	15	15	0.6	0.3	0.3	0.3	0.3	0.3
$t_{\rm sync}$	(s)	4.00×10^4	6.30×10^3	1.00×10^5	2.00×10^5	1.00×10^5	1.30×10^5	3.16×10^7	1.60×10^5
rate at $t_{\rm sync}$	(eV)	1.60×10^9	1.00×10^{10}	3.20×10^8	3.20×10^8	6.30×10^8	5.00×10^8	2.00×10^7	4.00×10^8

(*) Luminosity distance calculated by the model.

Table 5.2: Homogeneous SSC model parameters of the targets.

5.5 The External Compton (EC) model

In Chapter 2, Section 2.5.3.4, it has been shown that the high-energy spectrum results not only from the SSC mechanism, where seed photons of the inverse Compton scattering are produced by the synchrotron process inside the jet, but also from Comptonisation by the same population of electrons in the jet off soft photons from the accretion disk or from a fraction of the disk radiation that has been reprocessed and rescattered by the broad emission line clouds, dust and inter-cloud medium, a process referred to as external Comptonisation.

In order for the inverse Compton scattering off external radiation to dominate over the SSC emission, the energy density of the external radiation, as measured in the frame co-moving with the jet, must exceed the energy density of synchrotron radiation produced in the jet. This can be achieved at long distances from the central engine, where the local magnetic field can be very weak. In fact, the distance along the jet where most of the γ-ray flux is produced can be estimated from the gamma-ray variability timescale and from the location of the spectral break where the luminosity of the Compton component peaks, i.e. using the two equations $r = ct_{var}\frac{\delta}{1+z}$ and $\delta \sim \frac{1}{\gamma_b}\left(\frac{3}{4}(1+z)\frac{\nu_{EC}}{\nu_0}\right)^{\frac{1}{2}}$ (Equation 2.148). Typical timescales of γ-ray outbursts between 1-3 days, and the typical location of their spectral breaks in the 1–30 MeV range are consistent with production of γ-rays by Comptonisation off light from the Broad Emission Line (BEL) in the Broad Line Region (BLR) and dust clouds at distances 10^{17}–10^{18} cm (e.g. Błażejowski et al. (2000)). Sikora et al. (2002) also suggests that in the MeV-peaked gamma-ray sources, the γ-ray active region is significantly further from the centre and that in this case thermal photons and broad line emission play a crucial role in Compton scattering .

There are many variants of the external Compton radiation models. In some of them, radiation sources are approximated by homogeneous "blobs" propagating along the jet (Sikora et al. 1997), while in others they are approximated by an inhomogeneous flow (Blandford and Rees 1974). They also differ regarding the dominant diffuse ambient radiation field. For small distances, less than 10^{16}-10^{17} cm, the radiation can be provided directly by the accretion disk (e.g. Dermer and Schlickeiser (1993)), while at large distances, the Broad Emission Line (BEL) and the near-IR radiation from hot dust are likely to dominate. A comparison of the contributions of direct radiation from the disc with the radiation from the BEL and the IR radiation suggests that the contribution of the direct radiation from the accretion disk can be low as it is strongly redshifted, measured in the source co-moving frame (Sikora et al. 1994b, Celotti et al. 2007). In fact, since the highest temperature is reached in the innermost parts of the accretion disc, therefore the angle between the energetic disc photons and the moving shell is typically small, leading to almost a reflection back of the photons which will be in this way redshifted. It becomes relatively large only in the vicinity of the disc, but there the shell has not yet reached high bulk Lorentz factors. As a consequence, the observed typical frequency of the scattered disc photons will not increase much. On the contrary, photons from the BEL are always seen

head-on, and as such are maximally blueshifted (i.e. by the factor $\delta'\delta$). BL Lacertae (see Figure 1.8(b)) illustrates this case of the domination of the external Comptonisation from clouds (ECC), i.e. EC (BEL) and EC (IR) over the external Comptonisation of the direct radiation from the disc (ECD).

Sikora et al. (1994b) showed that the high energy gamma-rays detected by *EGRET* on board the *Compton Gamma-Ray Observatory* (*CGRO*) from FSRQs (or OVV quasars) can be produced by the Comptonisation off the broad emission line light as well as by Comptonisation of infrared radiation from dust heated by the disc radiation. Therefore, it is reasonable that the external Comptonisation model be evaluated (constrained) on our sample composed mostly by FSRQs. In fact, most of the selected sources show the gamma-ray luminosity, represented by $\nu F\nu$ in the SED, peaking in the MeV band.

The application of the EC model to *3EG J0500+2502*, *3EG J0706-3837*, *3EG J0724-4713*, *3EG J1659-6251*, *3EG J1709-0828* and *3EG J1813-6419* is justified by the fact that the SSC model failed to connect together the NIR to optical data and the γ-ray data considered to be the signatures of the synchrotron and of the inverse Compton scattering emission respectively (see Figure 5.4).

The six sources forming the third group, i.e. *3EG J0159-3603*, *3EG J0702-6212*, *3EG J1300-4406* , *3EG J1800-0146*, *3EG J1822+1641* and *3EG J1824+3441* showed no indication of the signature of the synchrotron emission at low frequencies by analysing the portion of their SEDs in the NIR and optical bands (see Figure 5.5).

More detail on the modelling aspect and on the constraining of parameters in the External Compton model can be found in Moderski et al. (2003), Sikora et al. (1994b; 1997) and Błażejowski et al. (2000). An appropriate code for this model was provided to us by Moderski R. and Sikora M.

In Section 4.4.1.3, it was shown that in some sources, the γ-ray spectra could not be fitted by a simple power-law model, as a turnover with a positive slope for energies above 1 GeV was observed. It was suggested that the transition could indicate an additional (different) mode of radiation mechanism. In fact, it appears that the External Comptonisation can be divided into two components: the "MeV" component that peaks in the 10–30 MeV energies, which can be interpreted as a result of the Comptonisation of the IR photons from dust heated by the disk radiation, and the "GeV" component, which peaks in the 1–10 GeV energies, can be interpreted as the Comptonisation of the UV Photons reprocessed and rescattered in the BLR region. Results of the constrained parameters of these sources are summarised in Table 5.3.

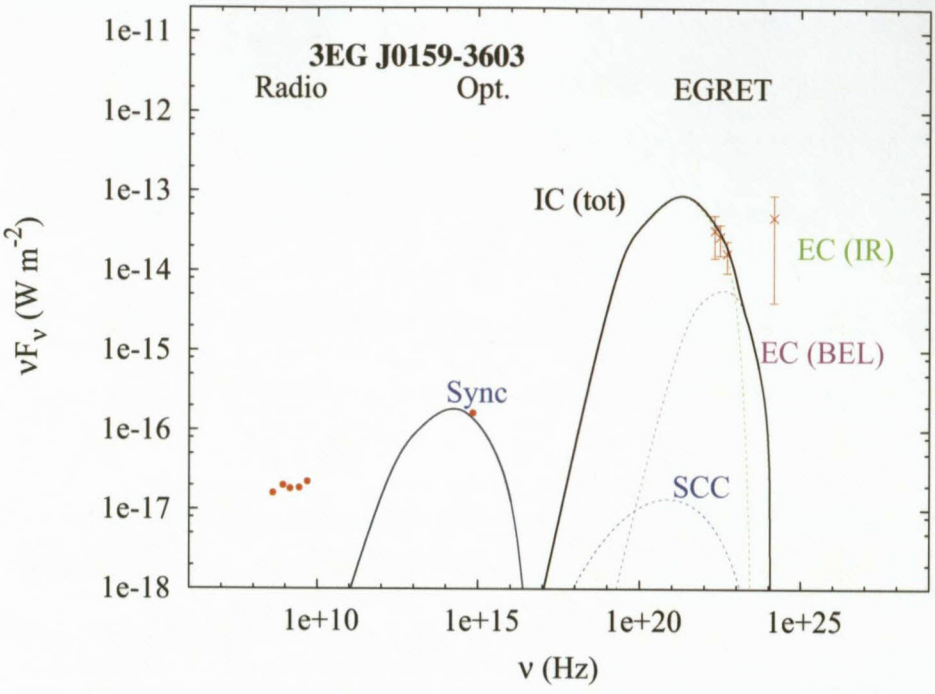

(a) *3EG J0159-3603*

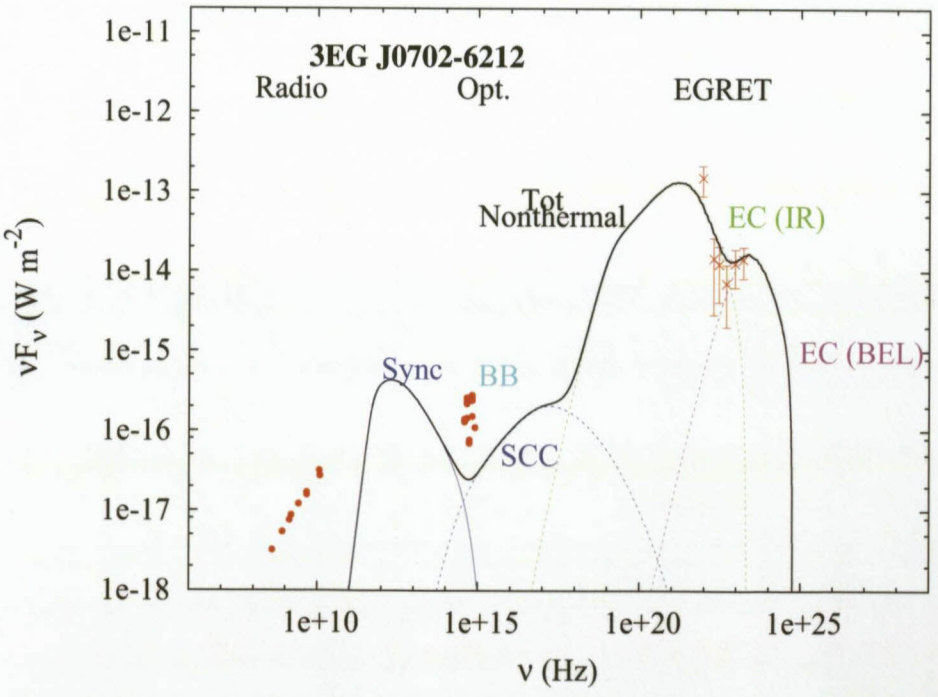

(b) *3EG J0702-6212*

Figure 5.5: Application of the EC model (Group II). For sources with no known redshift (e.g. *3EG J1659-6251* and *3EG J1709-0828*), the energy-fluxes were estimated using z = 1.

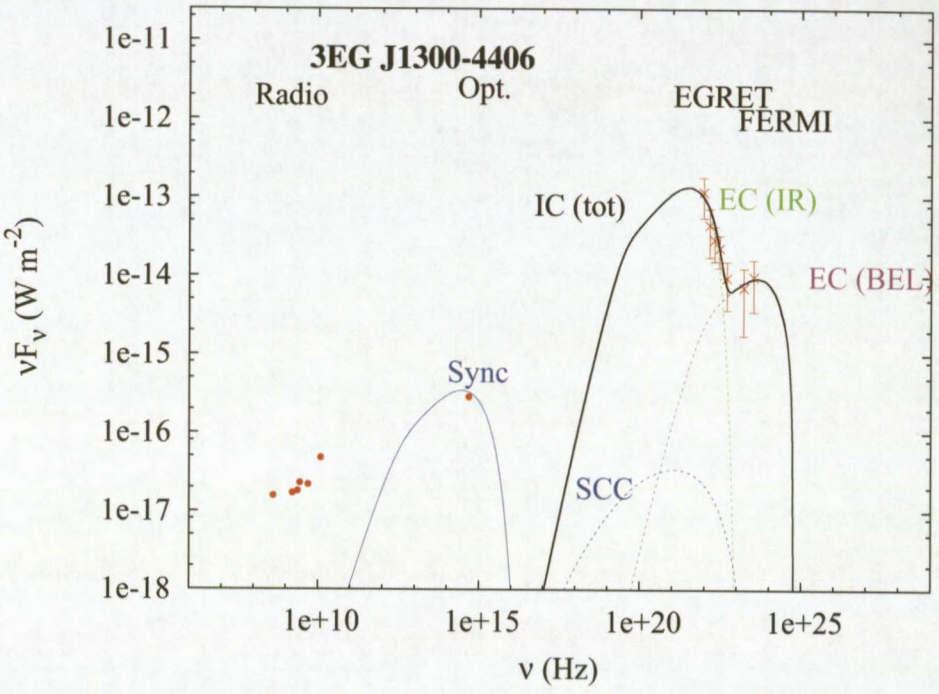

(c) *3EG J1300-4406*

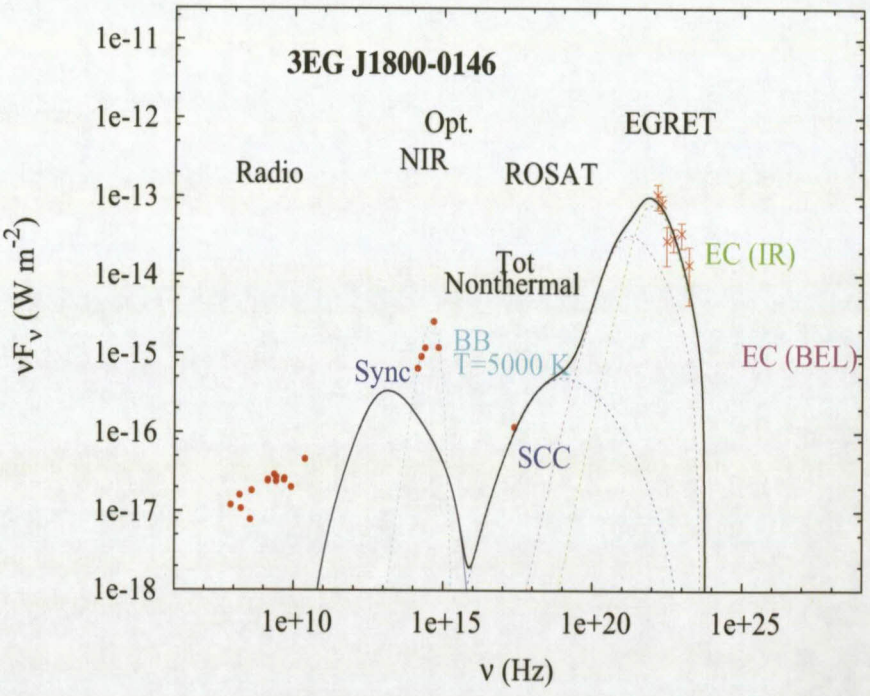

(d) *3EG J1800-0146*

Figure 5.5: Application of the EC model (Group II) (continued).

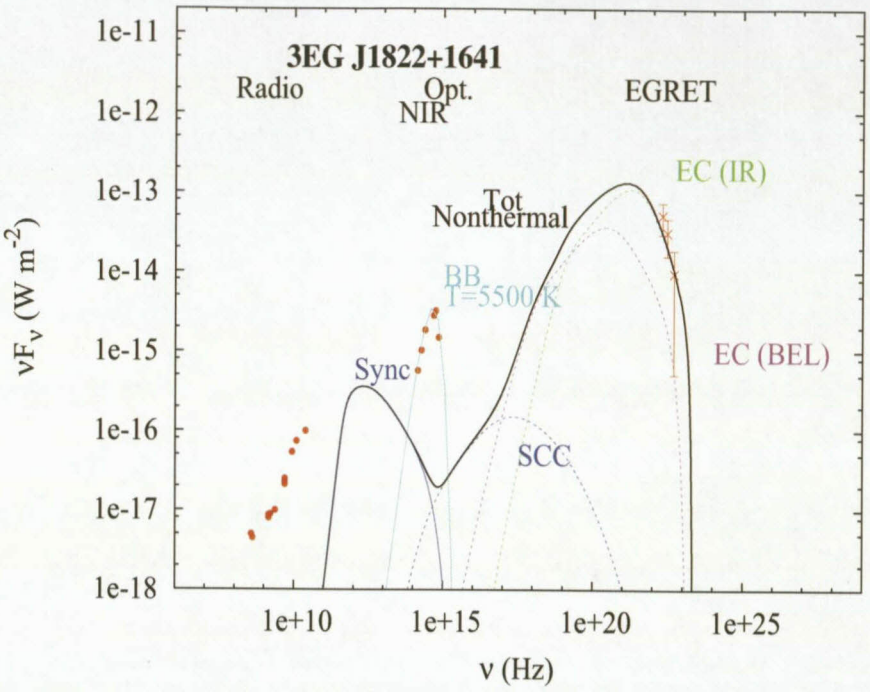

(e) *3EG J1822+1641*

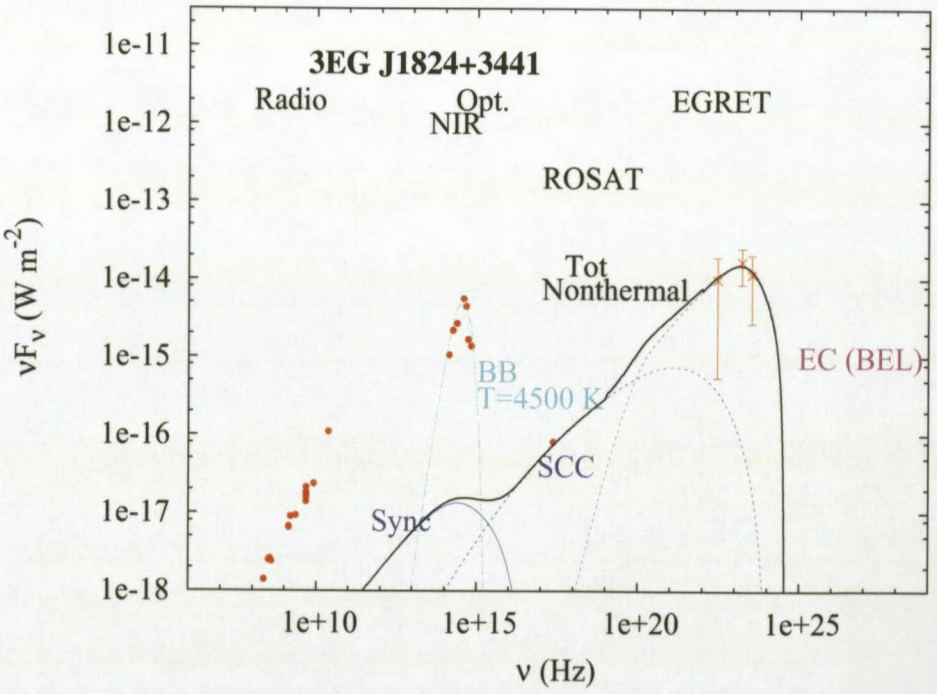

(f) *3EG J1824+3441*

Figure 5.5: Application of the EC model (Group II) (continued).

Source	R	Γ	θ_{obs}	B	$\gamma_{\rm min}$	$\gamma_{\rm br}$	$\gamma_{\rm cut}$	$\gamma_{\rm max}$	p_1	p_2	$K_{\rm e}$	$u_{\rm BEL}$	$\nu_{\rm BEL}$	$\alpha_{\rm BEL}$	u_{IR}	ν_{IR}
	(1)	(2)	(3)	(4)	(5)	(6)	(7)	(8)	(9)	(10)	(11)	(12)	(13)	(14)	(15)	(16)
3EG J0159-3603	1.0×10^{17}	15	1	15	2.0×10^{2}	2.5×10^{3}	1.0×10^{4}	1.0×10^{4}	2	4.2	5.0×10^{54}	3	10	-1	15	0.1
3EG J0500+2529	1.0×10^{17}	10	1	2.5	2.0×10^{2}	2.4×10^{3}	2.4×10^{4}	1.0×10^{5}	2	3.9	4.0×10^{53}	7	10	-1	15	0.1
3EG J0702-6212 (BEL)	1.0×10^{17}	15	1	15	4.0×10^{3}	9.0×10^{3}	5.0×10^{4}	5.0×10^{4}	2	3.8	9.0×10^{53}	7	1	-1	15	0.1
3EG J0702-6212 (IR)	5.0×10^{16}	15	1	15	1.0×10^{1}	2.0×10^{2}	2.0×10^{3}	2.0×10^{3}	2	4.4	1.0×10^{56}	4	1	-1	15	0.1
3EG J0706-3837	1.0×10^{17}	10	1	2.5	2.0×10^{2}	2.4×10^{3}	2.4×10^{4}	1.0×10^{5}	2	3.9	8.0×10^{52}	7	10	-1	15	0.1
3EG J0724-4713	1.0×10^{17}	10	1	2.5	2.0×10^{2}	2.0×10^{3}	2.4×10^{4}	2.4×10^{4}	2	3.9	4.0×10^{55}	7	10	-1	15	0.1
3EG J1300-4406 (BEL)	1.0×10^{17}	15	1	15	1.0×10^{3}	2.0×10^{4}	5.0×10^{4}	5.0×10^{4}	2	3.8	6.0×10^{53}	4	1	-1	15	0.1
3EG J1300-4406 (IR)	1.0×10^{17}	15	1	15	2.0×10^{2}	3.0×10^{3}	6.0×10^{3}	6.0×10^{3}	2	4.2	4.0×10^{54}	4	1	-1	15	0.1
3EG J1659-6251 (BEL)	1.0×10^{17}	10	1	2.5	2.0×10^{2}	2.0×10^{3}	1.0×10^{5}	1.0×10^{5}	2	2.6	6.0×10^{54}	4	10	-1	15	0.1
3EG J1659-6251 (IR)	1.0×10^{17}	10	1	2.5	2.0×10^{2}	2.0×10^{3}	1.0×10^{4}	1.0×10^{4}	2	4.2	3.0×10^{55}	4	10	-0.5	15	0.1
3EG J1709-0828	1.0×10^{17}	10	1	2.5	2.0×10^{2}	2.0×10^{3}	1.0×10^{4}	1.0×10^{4}	2	4.2	3.0×10^{55}	3	10	-1	15	0.1
3EG J1800-0146	2.5×10^{16}	15	1	15	2.1×10^{2}	5.0×10^{2}	5.0×10^{3}	5.0×10^{3}	2	4.2	3.0×10^{55}	4	1	-1	15	0.1
3EG J1813-6419	1.0×10^{17}	10	1	2.5	2.0×10^{2}	2.4×10^{3}	2.4×10^{4}	2.4×10^{4}	2	4.1	1.3×10^{55}	7	10	-1	15	0.1
3EG J1822+1641	5.0×10^{16}	15	1	15	1.0×10^{1}	2.0×10^{2}	2.0×10^{3}	2.0×10^{3}	2	4.4	1.0×10^{56}	4	1	-1	15	0.1
3EG J1824+3441 (BEL)	3.0×10^{15}	15	1	15	1.0×10^{2}	8.0×10^{3}	3.0×10^{4}	3.0×10^{4}	2	3.8	4.0×10^{54}	5.5	1	-1	15	0.1
3EG J1824+3441 (SSC)	1.8×10^{15}	15	1	15	1.0×10^{1}	2.0×10^{3}	1.0×10^{4}	1.0×10^{4}	2	3.8	1.0×10^{54}	7	1	-1	15	0.1

(1): Radius of the emitting region (in cm), (2): Bulk Lorentz factor of the jet, (3): Viewing angle (in degrees), (4): Magnetic field (in Gauss), (5): Minimal electron Lorentz, factor, (6): Electron Lorentz factor at spectral break, (7): Cut-off in electron energy , (8): Maximal electron Lorentz factor, (9): Electron distribution index ($\gamma < \gamma_{\rm br}$), (10): Electron distribution index ($\gamma > \gamma_{\rm br}$), (11): Electron normalization constant, (12): Energy density of BEL (in erg cm^{-3}), (13): Characteristic frequency of BEL (in eV), (14): BEL distribution photon index, (15): Energy density of dust IR radiation (in erg cm^{-3}) and (16): Radiation characteristic frequency of IR (in eV).

Table 5.3: Parameters of the External Compton (EC) model.

5.6 *PMN J0710-3850* versus *PMN J0708-3833*

The SED of *PMN J0708-3833* (see[6] Figure 5.6(b)), obtained by using the available online data, does not show any consistent indication that the γ-ray data belong to it rather than to *PMN J0706-3850*. In fact, the low-energy radio emission is too steep ($\alpha_r \sim> 1$ assuming $S_\nu \sim \nu^{-\alpha}$) and is unlikely to correlate with other radiation emission in other wavelengths, while the optical emission is fitted by a black body spectrum of temperature $T \sim 6700$ K. This has made it difficult to trace the existence of the synchrotron signature in the low energies of the spectrum of *PMN J0708-3833*, which is a property of the synchrotron self-Compton source. Therefore, *PMN J0710-3850* can be maintained to be the best radio counterpart of the *EGRET* source in the whole error box. If the source is confirmed, it will be the first Seyfert I galaxy discovered emitting the VHE γ-ray photons.

Parameter	Value
R (cm)	1.0×17
Γ	10
θ_{obs} (deg)	1
B (G)	2.5
$\gamma_{\rm min}$	2.0×10^2
$\gamma_{\rm br}$	2.4×10^3
$\gamma_{\rm cut}$	2.4×10^4
$\gamma_{\rm max}$	1.0×10^5
p_1	2
p_2	3.9
K_e	8.0×10^{52}
u_{BEL} (erg cm^{-3})	7
$\nu_{\rm BEL}$ (eV)	10
$\alpha_B EL$	-1
u_{IR} (erg cm^{-3})	15
ν_{IR} (eV)	0.1

Table 5.4: EC model parameters of *3EG J0706-3837$_b$ (PMN J0708-3833)*.

[6]Parkes-MIT-NRAO catalogue (PMN)

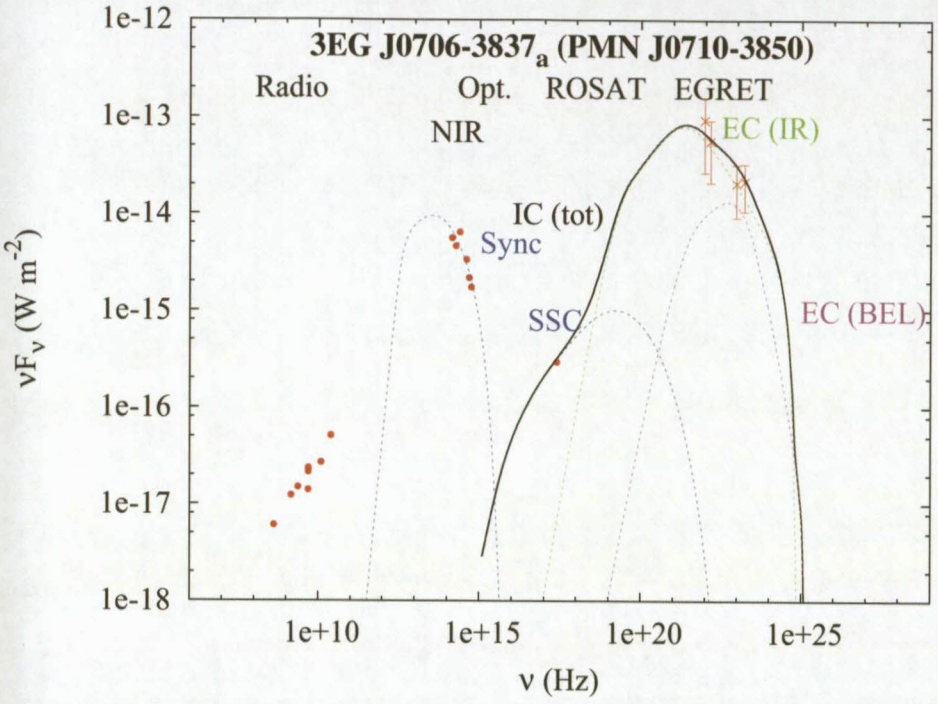

(a) *PMN J0706-3850*

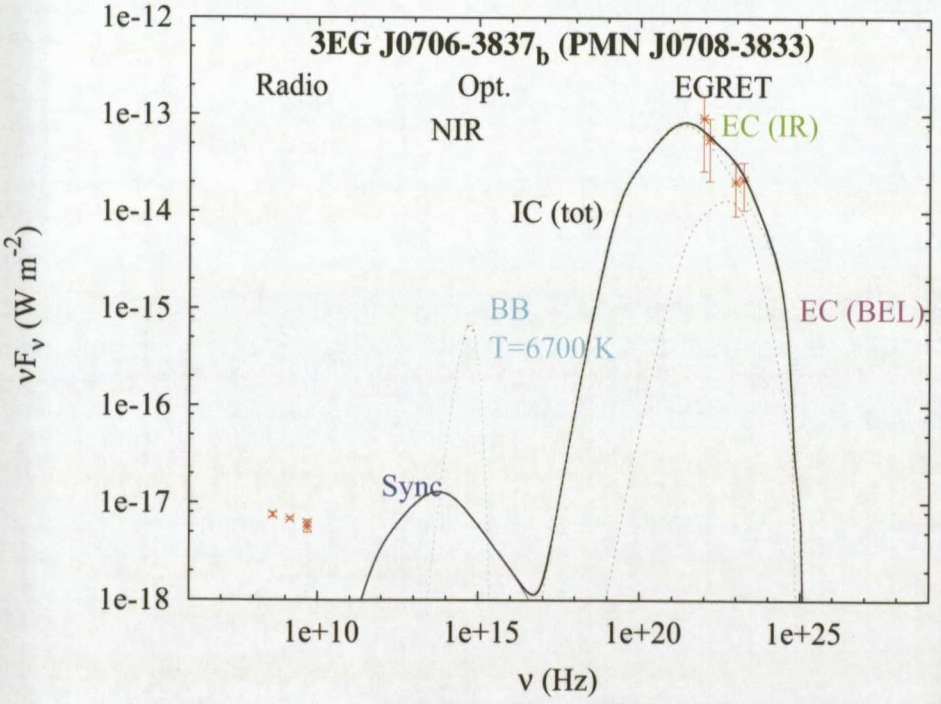

(b) *PMN J0708-3833*

Figure 5.6: The energy-fluxes for PMN J0708-3833 were calculated assuming z=0.128 (redshift for *3EG J0706-3837$_a$ (PMN J0710-3850)*).

Chapter 6

Discussion and Conclusions

The main purpose of this study was to search for possible synchrotron-Compton blazars among the southern high galactic latitude unidentified sources, detected by the *Energetic Gamma-Ray Experiment Telescope* (*EGRET*) on board the *Compton Gamma-Ray Observatory* (*CGRO*), during its 9 years of service between 1991 and 2000.

Synchrotron self-Compton-dominated blazars are assumed to be among the unidentified *EGRET* sources, especially those at high galactic latitudes, since the large majority of *EGRET*-detected sources have been associated with blazars (Hartman et al. 1999).

However, a serious complicating factor concerning possible identification of point sources that could possibly be associated with the *EGRET* γ-ray sources is the large field of view, i.e. between 0.5 and 1.5 degrees in the sky, implying that the *EGRET* field could harbour several potential sources, especially at low galactic latitudes.

The initial phase of this study constituted the tedious search for extra galactic flat spectrum radio counterparts in the online and published catalogues inside the *EGRET* error boxes of high galactic latitude sources, i.e. with $|b| > 10°$. The strategy was to select sources with $|\alpha| < 0.7$ for further multi-wavelength studies. To enable the utilization of the *HartRAO* radio telescope in this study, only sources with the declination range $-70° < \text{Dec} < +45°$ were considered. A further consideration was to single out only those flat spectrum sources with flux density above 200 mJy at 12.4 GHz, i.e. selecting those sources with rising nonthermal spectra (νF_ν versus ν) towards high energies. Based upon the above-mentioned criteria, a selection of 13 blazar-like candidates was made (see Table 3.4) for futher investigation.

6.1 Spectral Energy Distributions (SEDs)

The multi-wavelength observations conducted on these objects and subsequent data analysis were discussed in Chapter 4. Radio observations were conducted using the 26-m dish of the *Hartebeesthoek Radio Observatory (HartRAO)* during the year 2007. Due to the observing time

allocation, it was possible to conduct optical observations on only three sources *3EG J0702-6212*, *3EG J0821-5814* and *3EG J0706-3837*, with the aim of verifying their variability. This was performed using *SALT*, the 1.9-m and the 1.0-m telescopes, all operated by the *South African Astronomical Observatory* at Sutherland in South Africa, during 2008 and 2009 (first quarter).

Spectroscopic observations of the two objets, *3EG J0821-5814* and *3EG J0706-3837* were obtained from the *SOAR/Goodman* spectrograph during the night of 16/17 February 2009. One of the highlights of this study is the determination of the redshifts of these objects as well as their classification according to their spectral lines. It turned out that *3EG J0821-5814* and *3EG J0706-3837* have redshifts of 0.06 and 1.29 respectively and that the former is a Flat Spectrum Radio Quasar, while the latter is a Seyfert galaxy.

X-ray data were obtained from the *ROSAT* (0.2–2 keV), *XMM*(0–12 keV) and *EINSTEIN* (0.15-20 keV) X-ray satellites. However, in most of the cases, results were not for pointed observations, but transient, not allowing to estimate the X-ray spectral index, which is a measurement of the slope of the spectrum.

The high-energy γ-ray data from 30 MeV to 20 GeV were obtained from the *EGRET* telescope (thanks to David Thompson, former member of the *EGRET* team, for the link to the *EGRET* reduced data as the *EGRET* data reduction software was not made public), while another set of data of energy ranging from 100 MeV to 300 GeV was obtained from *Fermi-LAT*. In fact, in its first 11 months of operation, 4 sources, i.e. *3EG J0724-4713*, *3EG J1300-4406* , *3EG J1659-6251* and *3EG J1709-0828*, were detected. Most of the information used for these *Fermi-LAT* detected sources was in the recent published first catalogue of *Fermi-LAT* sources. However, a proper follow-up will be possible as the daily raw data can be accessed, being released by the satellite.

The Spectral Energy Distribution showed a peculiar behaviour, which needs to be mentioned here. In fact:

- The radio data of all sources are of nonthermal origin while the NIR-to-optical emission is for some sources a power law and for others a black body emission. Since the blazar's thermal emission comes mostly from the disc, where the nonthermal emission dominates it is an indication of the existence of relativistic jets, which are responsible for nonthermal radiation. Due to relativistic beaming, it is believed that this nonthermal radiation is beamed such that it swamps the disc emission.

- Due to the effect of self-absorption and inhomogeneity in the outer part of the jets, radio to mm fluxes of selected sources do not match the SED of the synchrotron self-Compton model of a beamed synchrotron and inverse Compton scattering from the same population of electrons resulting in a poor correlation between the radio to mm with γ-rays, as it was supposed to be in blazars and in particular in HBLs.

- The thermal NIR-to-optical emission in some sources suggests an additional high luminous

thermal dust component as a result of the heating by the accretion disk.

- The knowledge of the X-ray properties is of special relevance, because in this band both the synchrotron and inverse Compton processes contribute to the emission. The first mechanism is expected to produce a steep continuum in this band, while the second mechanism should give rise to a flat component ($\alpha \leq 1$, rising in a νF_ν plot). The shape of the X-ray spectrum can give a fundamental hint for disentangling the two components and inferring the respective peak frequencies (Fossati et al. 1998), i.e. the position of the X-ray data remains crucial for the determination of reliable peaks, for both synchrotron and inverse Compton radiation, which could help to classify sources in BL Lac subclasses.

6.2 Modelling

The total multi-wavelength emission of blazars from radio to γ-rays can be explained satisfactorily by a synchrotron self-Compton (SSC) model, which is a combined nonthermal synchrotron and inverse Compton scattering emission from highly relativistic electrons. It has been shown that the entire spectrum from radio to VHE γ-rays is reconcilable with processes within the jets, accelerating a large population of electrons to energies between $\gamma_e \sim 10^3$–10^4. The acceleration mechanisms in these objects are believed to be associated with strong shock waves in relativistic jet-like outflows originating from a region close to a compact object which is, in the case of blazars, a supermassive black hole. These shocks are believed to be accompanied by impulsive electrodynamic injection processes (Petrosian and Bykov 2008).

Interpretation of the observed Spectral Energy Distribution (SED) and identification of the involved interactions require not only high-quality observational data, but also a solid understanding of the contributing mechanisms. A model for the SSC process (Krawczynski 2004) is widely used to constrain physical parameters of the blazar-emitting region. However, due to the scarcity of the data, it was not possible to constrain all the relevant parameters satisfactorily in the sources under consideration for this study.

The model is successful, provided that there are sufficient data to pin down the observed parameters, such as the position of the peaks in emission as well the spectral indices in different parts of the SED. In the MeV to GeV energy range, consideration of the contribution of the external photons is highly recommended in the model due to the fact that the majority of the selected sources are confirmed FSRQs, in which this type of emission is believed to dominate. In most of the targets, data in this energy range were well fitted by the External Compton model, in which predominantly UV photons from the Broad Line Region and Near Infrared photons from the hot dust are inverse-Compton upscattered to γ-ray energies.

6.3 Classification

In Chapter 1, different criteria defining the blazar class have been described and were used later to classify the selected sources. The dividing criteria between radio loud and radio quiet are $\frac{f_{\rm radio}}{f_{\rm opt}} > 10$ for radio loud and $\frac{f_{\rm radio}}{f_{\rm opt}} < 10$ for radio quiet, which can be expressed in terms of energy flux as $\frac{\nu F_{\nu \rm opt}}{\nu F_{\nu \rm radio}} < 10^4$ for radio loud. It appears that except 3EG 0706-3837 which showed to be a Seyfert I galaxy, other 12 selected sources display properties of radio-loud AGNs.

In all sources, the SEDs extend from radio to the VHE γ-rays, but due to the quality of the data, in some sources of the sample, it is difficult to establish clearly the correlation between different components (e.g. synchrotron emission and inverse Compton scattering) when compared to blazars where the correlation is clearly defined. In all sources, it was found that there was no correlation between low-energy radio and high γ-ray emissions. This is interpreted by the fact that low-energy radio emission comes from the outer and inhomogeneous part of the jet while the gamma-rays are produced by upscattering off synchrotron-produced photons in the inner part of the jet or external photons from the BLR region and dust by relativistic relativistic electrons. The gamma-ray photon index of the selected sources ranges between 2 and 3.4 qualifying them to be either LBLs and FSRQs candidates. In published literature, already 4 sources from the list were classified FSRQs. These are *3EG J0500+2502* (e.g. Hewitt and Burbidge (1991) and Laing et al. (1983)), *3EG J0724-4713* (e.g. Véron-Cetty and Véron (2006)), *3EG J1813-6419* (e.g. Healey et al. (2008a)), and *3EG J1824+3441* (e.g. Zhang et al. (1998)).

Spectroscopic observations using the 4.1-m Goodman Spectrograph at the *Southern Observatory for Astrophysical Research* in Chile, of the sources PMN J0820-5705 and PMN J0710-3850, which were selected as radio counterparts of *3EG J0821-5814* and *3EG J0706-3837* respectively revealed that PMN J0820-5705 could be classified as an FSRQ, while PMN J0710-3850 as a Seyfert galaxy. Due to their relatively large viewing angle, Seyfert galaxies are not normally associated with blazar emission. This prompted re-analysis of another radio source in the same error box i.e. *PMN J0708-3833*. The SED of *PMN J0708-3833*, obtained using the available online data, does not show any consistent indication that the γ-ray data belong to it rather than to *PMN J0706-3850*. In fact, the low-energy radio emission is too steep ($\alpha_{\rm r} \sim> 1$ assuming $S_\nu \sim \nu^{-\alpha}$) and is unlikely to correlate with other radiation emissions in other wavelengths, while the optical emission is fitted by a black body spectrum of temperature $T \sim 6700$ K. This has made it difficult to trace the existence of the synchrotron signature in the low energies of the SED of *PMN J0708-3833*, which is a property of the synchrotron self-Compton sources. Therefore, *PMN J0706-3850* appears to be the best radio counterpart of the *EGRET* source in the whole error box. If the source is confirmed, it will be the first Seyfert I galaxy discovered emitting VHE γ-ray photons.

The photon indices of the high-energy γ-rays are between 2 and 3.4, maintaining these sources

in the class of either LBLs or FSRQs.

6.4 Future studies

A follow-up of the *F*ermi-LAT survey:

The high sensitive *Large Area Telescope* on board the *Fermi Gamma-Ray Large Area Space Telescope (Fermi/GLAST)*, already in operation surveying the high-energy gamma-ray universe, has started to provide high-quality data in the 20 MeV to 300 GeV energy band. During its 11 months of operation, 4 sources from the list have been already detected. It is expected that the rest of the sources on the list will possibly show up as a result of a long integration for faint sources. With its orbital period of 95 minutes, the *Fermi-LAT* is able to sweep out accross most of the sky about 16 times per day, which is suitable for studying the variability down to a time scale of 2 hours. This is particularly necessary to constrain the size on the emitting region and justify a continuous follow-up of the *Fermi-LAT* survey.

RSS spectroscopy:

In future studies in particular high-quality spectroscopy of weak-lined radio-loud AGN is needed, i.e. spectra with high resolution and good S/N, in order to detect even the faintest emission lines. It is believed that this will disentangle the FSRQ and LBL-like behaviour in these sources. In fact, it is necessary to measure with high accuracy the Ca break around 4000 Å (in the rest frame of the object), so that any confusion with radio galaxies be eliminated and then to make possible the measurement of the equivalent width down to any faintest line so that the problem of lack of emission lines in BL Lacs be addressed without confusion. In this regard, the *Robert Stobie Spectrograph (RSS)* at the *Southern African Large Telescope (SALT)* will play a vital role. A proposal in this regard has been submitted.

Magnetic field:

The jet magnetic field plays an important role in the synchrotron emission process. This can be constrained through polarization measurements.

Appendix A:

Finding Charts

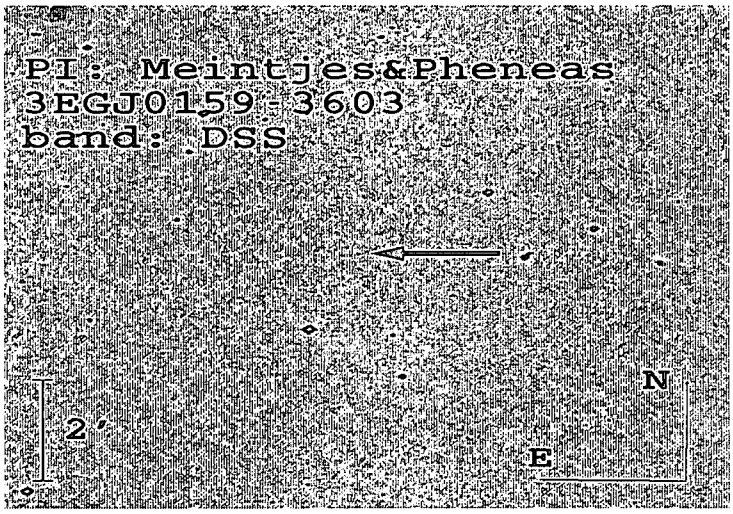

(a) *3EG J0159-3603*

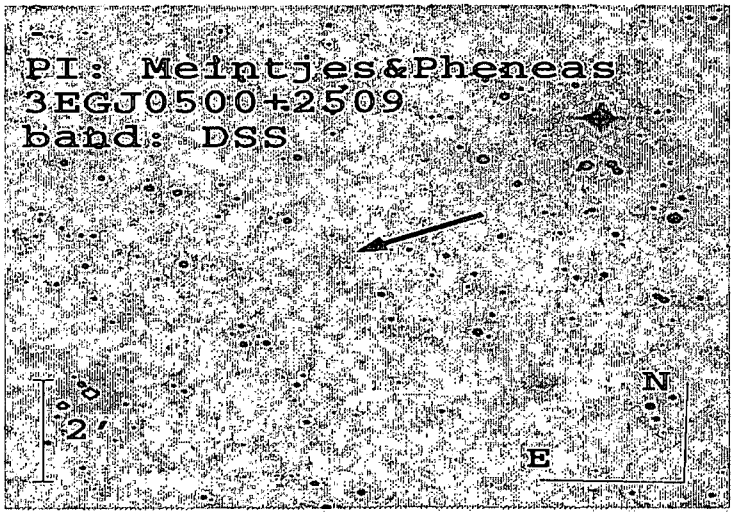

(b) *3EG J0500+2502*

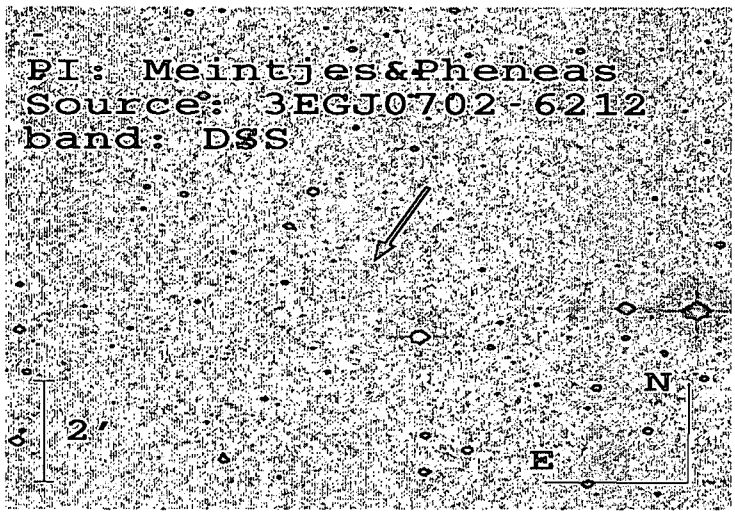

(c) *3EG J0702-6212*

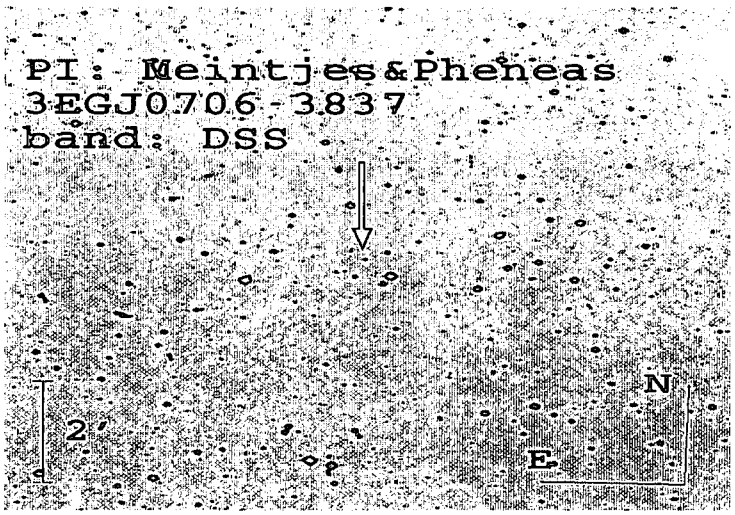

(d) *3EG J0706-3837*

Figure 1: Finding Charts (Continued).

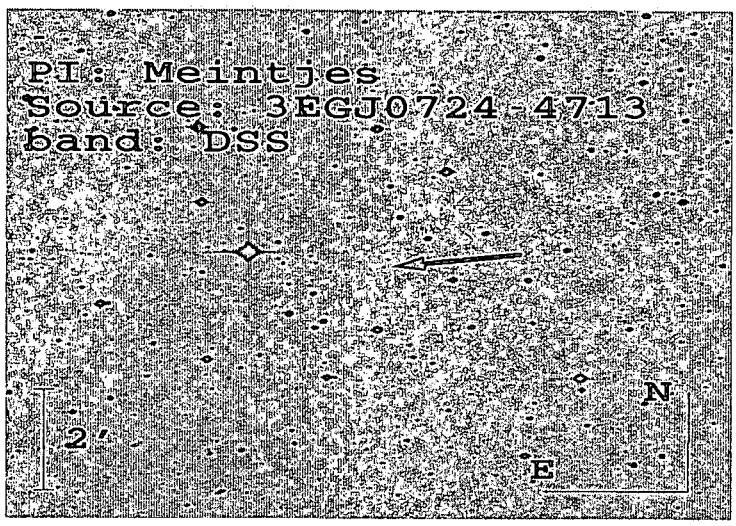

(e) *3EG J0724-4713*

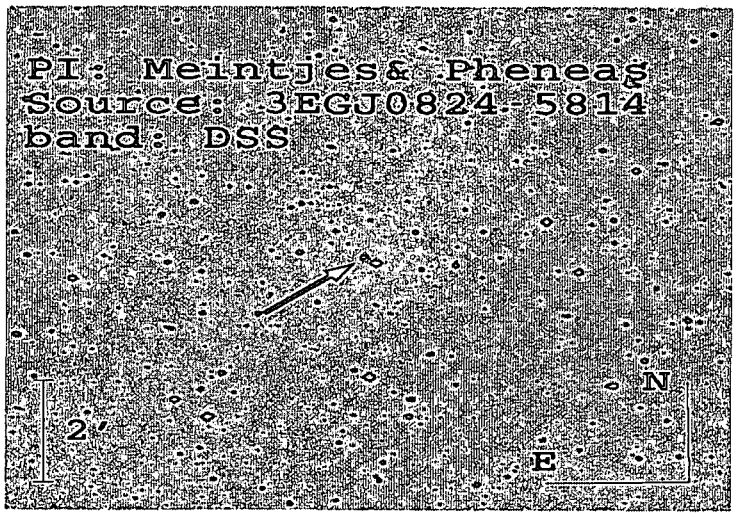

(f) *3EG J0821-5814*

Figure 1: Finding Charts (Continued).

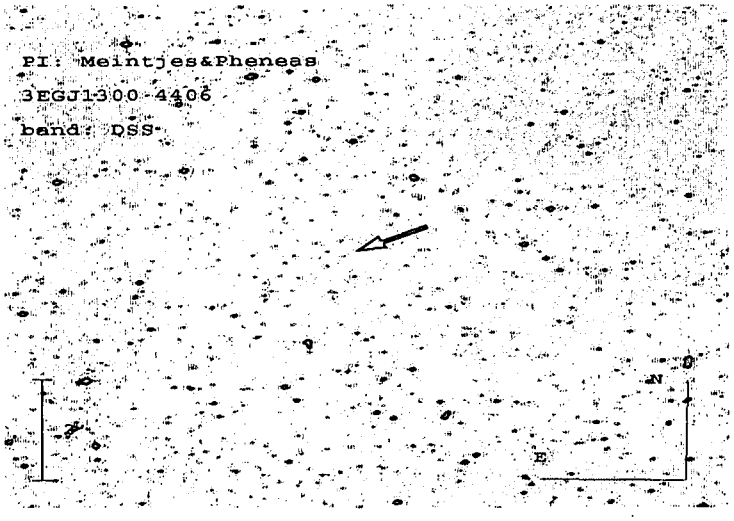

(g) *3EG J1300-4406*

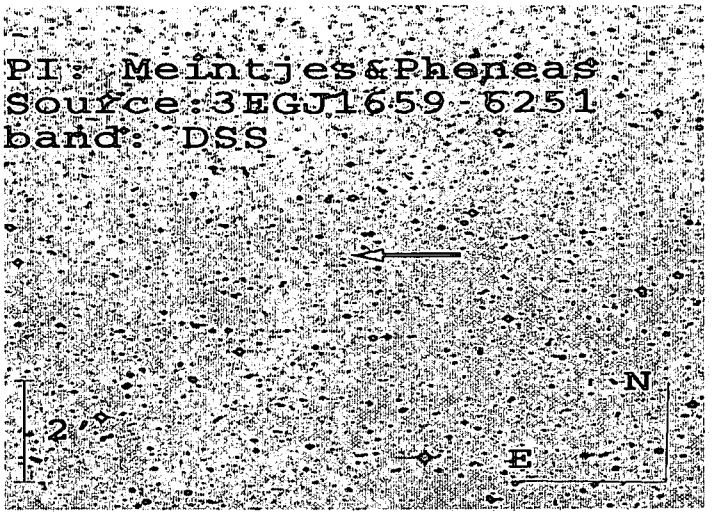

(h) *3EG J1659-6251*

Figure 1: Finding Charts (Continued).

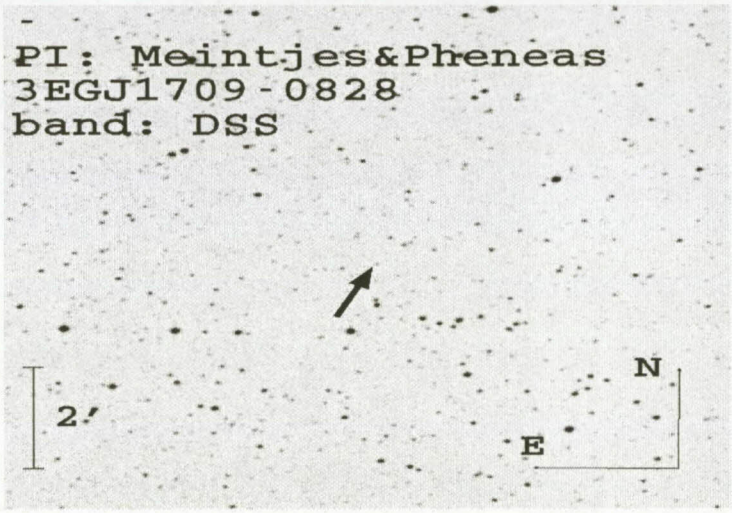

(i) *3EG J1709-0828*

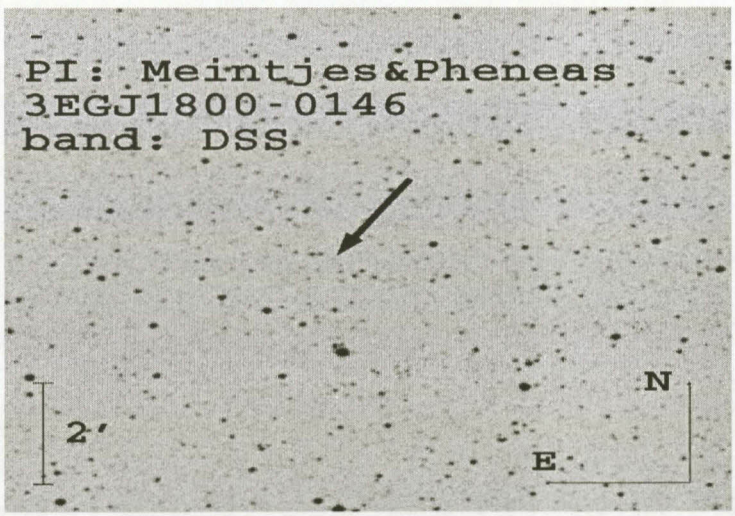

(j) *3EG J1800-0146*

Figure 1: Finding Charts (Continued).

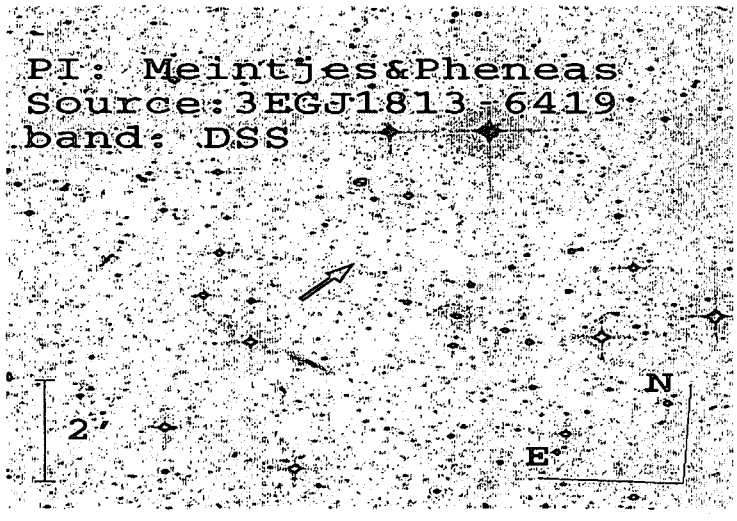

(k) *3EG J1813-6419*

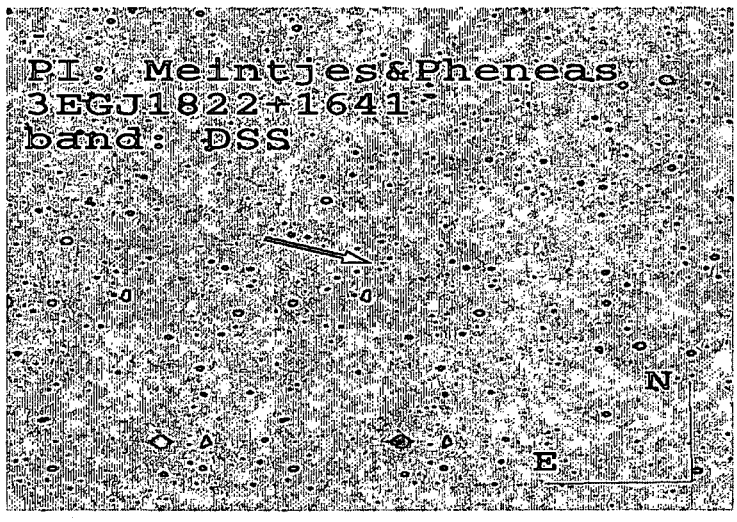

(l) *3EG J1822+1641*

Figure 1: Finding Charts (Continued).

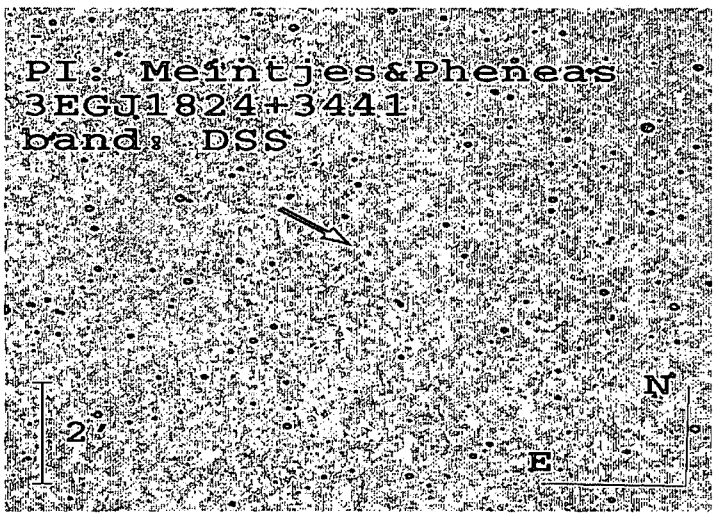

(m) *3EG J1824+3441*

Figure 1: Finding Charts (Continued).

Appendix B: Scientific Justification for the *SALT RSS* Proposal

Title: *Investigation on the Ca H & K Lines in the EGRET Southern Blazar Candidates*

P.I: P. Nkundabakura[1]
Co-I: Prof. P.J. Meintjes[1]

(1) *University of the Free State, Physics Department, P.O. Box 339, Bloemfontein, 9300, South Africa.*

Summary of observing runs requested for this project

Run	Telescope	Instrument	No. Nights	Moon	Optimal months	Acceptable
1	SALT	RSS	0.6n	dark	April-Oct	April-Dec

1. Abstract

Research is undertaken on 13 radio sources isolated from the error boxes of *EGRET* unidentified sources based on their similarities with blazars, in broadband multiwavelength properties. The recent spectroscopic data (acquired from the Goodman spectrograph at *SOAR/CTIO)* of two sources from this sample, i.e. *3EG J0821-5814* and *3EG J0706-3837*, opened a way to do a classification of these objects based on their spectroscopic features resembling blazars.

Blazars are flat-spectrum ($\alpha_r \leq 0.5$) radio sources (BL Lacs and FSRQs) with very narrow emission lines (or no lines at all) with rest-frame equivalent widths $EW_\lambda < 5$ Å (Stocke et al.1991). The narrowness of the lines ensures that the emission from the objects is dominated by a beamed nonthermal emission coming from their jets which are oriented to small angles with respect to the line-of-sight. Caccianiga et al. 1999 and Landt et al. 2008 showed that a source with Ca H & K break values $K_{4000} \leq 40\%$ was likely to have an extra component of nonthermal emission. The present observing proposal aims to investigate the possible domination of the nonthermal emission of the 6 Southern blazar candidates selected among the unidentified *EGRET* sources, as well as to determine their redshifts.

2. Feasibility

The V magnitudes of these sources range between 17 and 19 and therefore fall under the limits of *SALT RSS*. The observations will make use of the gratings pg3000 (resolving power $\sim$ 3000; Wavelength band covered: 3952-4683 Å) and pg0900 (resolving power $\sim$ 1000; Wavelength band covered: 4504-7589 Å) suitable for the measurements of the Ca depression in the UV and the redshift respectively, using the Balmer lines H_α and H_β. As sources seem to be faint, medium wide slits (of width 1.2" (on pg0900) and 1.5"(on pg3000) of height 8") have been selected to allow the entrance of enough light. With its high resolving power, pg3000 will be able to resolve the two nearest lines separated by 1.3 Å at 4000 Å, which is enough to resolve the two Ca H & K lines (separated by 63 Å in the rest frame) as mentioned above. The present proposal concerns 6 targets. The table below gives their coordinates as well as their visibility on *SALT*.

No	*EGRET* name	RA	DECL	V mag	Visibility on *SALT*	
	(3rd catalogue)	h m s	d m s		months	hours/day (*)
1	*3EG J0159-3603*	01 56 47	-36 16 14	18	Oct-Dec	2h
2	*3EG J0702-6212*	06 57 02	-61 39 26	18	Oct-Dec	1h
3	*3EG J1300-4406*	13 02 31	-44 46 52	19	May-August	1h
4	*3EG J1659-6251*	17 03 37	-62 12 38	18	May-August	2h
5	*3EG J1709-0828*	17 13 06	-08 17 01	19	Apr-Sept	1h
6	*3EG J1800-0146*	18 02 50	-02 07 44	17	Apr-Sept	1.5h

(*) These are slots of continuous availability with no interruption.

List of targets.

Each target will have its own block in which it will be cycled twice with the grating pg3000 (4 min exposure per cycle) and 4 times with the grating pg0900 (1 minute exposure per cycle). The total duration for all observations is about $\sim$ 19179 seconds $\simeq$ 5.3 h $\sim$ 0.6 n (where 1 n = 9 observing hours) to be calculated.

Exposure times were calculated by ensuring a reasonable S/N ratio 40–60. Calculations were done using the *RSS* simulator tool.

3. References

1. Stocke et al. 1991, APJ, Supplement series, 76: 813-874
2. Caccianiga et al.1999, APJ, 513, 51.
3. Landt et al. 2008, M.N.R.A.S., 391, 967985

Bibliography

Abdo, A. A., Ackermann, M., Ajello, ···+ Fermi/LAT Collaboration, Ghisellini, G., Maraschi, L., Tavecchio, F., and Angelakis, E.: 2009, *ApJ* **699**, 976

Abdo, A. A., Ackermann, M., Ajello, ···+ Fermi/LAT Collaboration, Ghisellini, G., Maraschi, L., Tavecchio, F., and Angelakis, E.: 2010a, *ApJ* **710**, 1271

Abdo, A. A., Ackermann, M., Ajello, M., Allafort, A., Antolini, E., Atwood, W. B., Axelsson, M., Baldini, L., Ballet, J., Barbiellini, G., and et al.: 2010b, *ApJS* **188**, 405

Achterberg, A.: 2001, in F. A. Aharonian & H. J. Völk (ed.), *American Institute of Physics Conference Series*, Vol. 558 of *American Institute of Physics Conference Series*, pp 392–404

Altavilla, G., Fiorentino, G., Marconi, M., Musella, I., Cappellaro, E., Barbon, R., Benetti, S., Pastorello, A., Riello, M., Turatto, M., and Zampieri, L.: 2004, *MNRAS* **349**, 1344

Axford, W. I., Leer, E., and Skadron, G.: 1977, in *International Cosmic Ray Conference*, Vol. 11 of *International Cosmic Ray Conference*, pp 132–+

Baars, J. W. M.: 1973, *IEEE Transactions on Antennas and Propagation* **21**, 461

Bell, A. R.: 1978, *MNRAS* **182**, 147

Bennert, N., Falcke, H., Schulz, H., Wilson, A. S., and Wills, B. J.: 2002, *ApJ* **574**, L105

Benz, A. O. and Courvoisier, T.: 1994, *Plasma astrophysics. Lecture notes 1994.*

Berezhko, E. G. and Ellison, D. C.: 1999, *ApJ* **526**, 385

Biskamp, D.: 1989, in K. Meisenheimer & H.-J. Roeser (ed.), *Hot Spots in Extragalactic Radio Sources*, Vol. 327 of *Lecture Notes in Physics, Berlin Springer Verlag*, pp 279–290

Blandford, R. D. and Konigl, A.: 1979, *ApJ* **232**, 34

Blandford, R. D. and Rees, M. J.: 1974, *MNRAS* **169**, 395

Blandford, R. D. and Rees, M. J.: 1978, *Phys. Scr* **17**, 265

Błażejowski, M., Sikora, M., Moderski, R., and Madejski, G. M.: 2000, *ApJ* **545**, 107

Boksenberg, A., Danziger, I. J., Fosbury, R. A. E., and Goss, W. M.: 1980, *ApJ* **242**, L145

Boksenberg, A. and Sargent, W. L. W.: 1978, *ApJ* **220**, 42

Böttcher, M.: 2002, *Bulletin of the Astronomical Society of India* **30**, 115

Caccianiga, A., della Ceca, R., Gioia, I. M., Maccacaro, T., and Wolter, A.: 1999a, in L. O. Takalo and A. Sillanpää (eds.), *BL Lac Phenomenon*, Vol. 159 of *Astronomical Society of the Pacific Conference Series*, pp 507–+

Caccianiga, A., Maccacaro, T., Wolter, A., della Ceca, R., and Gioia, I. M.: 1999b, *ApJ* **513**, 51

Carr, D.: 2005, *Measuring the Brightness Temperatures of Jupiter & Venus*

Casandjian, J.-M. and Grenier, I. A.: 2008, *A&A* **489**, 849

Celotti, A., Ghisellini, G., and Fabian, A. C.: 2007, *MNRAS* **375**, 417

Chiosi, C., Bressan, A., and Fagotto, F.: 1994, *Memorie della Societa Astronomica Italiana* **65**, 881

Condon, J., Cotton, W., Greisen, E., Yin, Q., Perley, R., Taylor, G., and Brodelick, J.: 1998, *AJ* **(115)**, 1693

Coppi, P. S. and Blandford, R. D.: 1990, *MNRAS* **245**, 453

Dermer, C. D. and Schlickeiser, R.: 1993, in *International Cosmic Ray Conference*, Vol. 1 of *International Cosmic Ray Conference*, pp 160–+

Dermer, C. D., Schlickeiser, R., and Mastichiadis, A.: 1992, *A&A* **256**, L27

Dreicer, H.: 1959, *Phys. Rev.* **115**, 238

Feigelson, E. D. and Berg, C. J.: 1983, *ApJ* **269**, 400

Fermi, E.: 1949, *Physical Review* **75**, 1169

Flesch, E. and Hardcastle, M. J.: 2004, *A&A* **427**, 387

Fossati, G., Maraschi, L., Celotti, A., Comastri, A., and Ghisellini, G.: 1998, *MNRAS* **299**, 433

Frank, J., King, A., and Raine, D.: 1992, *Accretion power in astrophysics: 2nd Edition.*

Frank, M. and Valenti, B.R., D.: 2007, *A&A* pp 165–+

Galbiati, E., Caccianiga, A., Maccacaro, T., Braito, V., Della Ceca, R., Severgnini, P., Brunner, H., Lehmann, I., and Page, M. J.: 2005, *A&A* **430**, 927

Georganopoulos, M., Kirk, J., and Mastichiadis, A.: 2001, Vol. 7 of *International Cosmic Ray Conference (ICRC)*, pp 2705–+

Ghisellini, G., Maraschi, L., and Dondi, L.: 1996, *A&AS* **120**, C503+

Giroletti, M.: 2005, *Baltic Astronomy* **14**, 385

Goldberg, L.: 1964, *ApJ* **140**, 384

Grenier, I. A., Casandjian, J.-M., and Terrier, R.: 2005, *29 th International Cosmic Ray Conference, Pune (2005)* **4**, 13

Haas, M., Chini, R., Meisenheimer, K., Stickel, M., Lemke, D., Klaas, U., and Kreysa, E.: 1998, *ApJ* **503**, L109+

Haerendel, G.: 1994, *ApJS* **90**, 765

Hartman, R., Bertsch, D., Bloom, S., A.W., C., Deines-Jones, P., Esposito, J., Fichtel, C., Friedlander, D., Hunter, S., McDonald, L., Sreekumar, P., Thomson, D., Jones, B., Lin, Y., Michelson, P., Nolan, P., Tompkins, W., Kanbach, G., Mayer-Hassel wander, H., Mucke, A., POHI, M., Reimer, O., Kniffen, D., Schneid, E., Montigny, C., Mukherjee, R., and Dingus, B.: 1999, *ApJS* **123**, 79

Healey, S. E., Romani, R. W., Cotter, G., Michelson, P. F., Schlafly, E. F., Readhead, A. C. S., Giommi, P., Chaty, S., Grenier, I. A., and Weintraub, L. C.: 2008a, *ApJS* **175**, 97

Healey, S. E., Romani, R. W., Cotter, G., Michelson, P. F., Schlafly, E. F., Readhead, A. C. S., Giommi, P., Chaty, S., Grenier, I. A., and Weintraub, L. C.: 2008b, *ApJS* **175**, 97

Hewitt, A. and Burbidge, G.: 1991, *ApJS* **75**, 297

Hubble, E.: 1929, in *Proceedings of the National Academy of Sciences*, Vol. 15

Inoue, S. and Takahara, F.: 1996, *ApJ* **463**, 555

Ivezić, Ž., Becker, R. H., Blanton, M., Fan, X., Finlator, K., Gunn, J. E., Hall, P., Kim, R. S. J., Knapp, G. R., Loveday, J., Lupton, R. H., Menou, K., Narayanan, V., Richards, G. R., Rockosi, C. M., Schlegel, D., Schneider, D. P., Strateva, I., Strauss, M. A., vanden Berk, D., Voges, W., Yanny, B., and The SDSS Collaboration: 2002, in R. F. Green, E. Y. Khachikian, and D. B. Sanders (eds.), *IAU Colloq. 184: AGN Surveys*, Vol. 284 of *Astronomical Society of the Pacific Conference Series*, pp 137–+

Jones, F. C.: 1968, *Physical Review* **167**, 1159

Kaspi, S., Smith, P. S., Netzer, H., Maoz, D., Jannuzi, B. T., and Giveon, U.: 2000, *ApJ* **533**, 631

Katarzyński, K., Sol, H., and Kus, A.: 2001, *A&A* **367**, 809

Kennicutt, Jr., R. C.: 2004, *VizieR Online Data Catalog* **7141**, 0

Khachikian, E. Y. and Weedman, D. W.: 1974, *ApJ* **192**, 581

Kirk, J. G., Duffy, P., and Gallant, Y. A.: 1996, *A&A* **314**, 1010

Kormendy, J. and Richstone, D.: 1995, *ARA&A* **33**, 581

Krawczynski, H.: 2004, *New Astronomy Review* **48**, 367

Krawczynski, H., Hughes, S. B., Horan, D., Aharonian, F., Aller, M. F., Aller, H., Boltwood, P., Buckley, J., Coppi, P., Fossati, G., Götting, N., Holder, J., Horns, D., Kurtanidze, O. M., Marscher, A. P., Nikolashvili, M., Remillard, R. A., Sadun, A., and Schröder, M.: 2004, *ApJ* **601**, 151

Krymskii, G. F.: 1977, *Akademiia Nauk SSSR Doklady* **234**, 1306

Kusunose, M., Takahara, F., and Kato, T.: 2003, *ApJ* **592**, L5

Laing, R. A., Riley, J. M., and Longair, M. S.: 1983, *MNRAS* **204**, 151

Landt, H.: 2003, *Ph.D. thesis*, University of Hamburg

Lebofsky, M. J.: 1981, *ApJ* **245**, L59+

Lesch, H.: 1991, in W. J. Duschl, S. J. Wagner, & M. Camenzind (ed.), *Variability of Active Galaxies*, Vol. 377 of *Lecture Notes in Physics, Berlin Springer Verlag*, pp 211–+

Longair, M.: 1992, *High Energy Astrophysics*, Vol. 1, Cambridge University Press

Longair, M.: 1994, *High Energy Astrophysics*, Vol. 2, Cambridge University Press

Maraschi, L. and Tavecchio, F.: 2001, in P. Padovani & C. M. Urry (ed.), *Blazar Demographics and Physics*, Vol. 227 of *Astronomical Society of the Pacific Conference Series*, pp 40–+

Martí, J., Paredes, J. M., Bloom, J. S., Casares, J., Ribó, M., and Falco, E. E.: 2004, *A&A* **413**, 309

Maslanka, K.: 2001, *ArXiv Mathematical Physics e-prints*

Mattox, J., Michelson, P. F., Nolan, P. L., Willis, T. D., Lin, Y. C., Jones, B., Tompkins, B., Twiggs, B., Yearian, M., Bloom, E. D., Atwood, W. B., Godfrey, G. L., Luebke, A., Wood, K. S., Johnson, W. N., Grove, J. E., Hertz, P. L., Lovellette, M., Suson, D., Oreglia, M., Ong, R., Mayer-Hasselwander, H. A., Merk, M., Scargle, J. D., Colavita, A., Barbiellini, G., Moreselli, A., Vacchi, A., Kamae, T., Kasahara, K., Nakano, G., Burnett, T., Johnson, R., and Cominsky, L. R.: 1996, *Memorie della Societa Astronomica Italiana* **67**, 607

Mattox, J. R., Wagner, S. J., Malkan, M., McGlynn, T. A., Schachter, J. F., Grove, J. E., Johnson, W. N., and Kurfess, J. D.: 1997, *ApJ* **476**, 692

Mc Laughlin, M., Mattox, J., Cordes, J., and Thomson, D.: 1996, *ApJ* **473**, 763

Meisenheimer, K., Haas, M., Müller, S. A. H., Chini, R., Klaas, U., and Lemke, D.: 2001, *A&A* **372**, 719

Moderski, R., Sikora, M., and Błażejowski, M.: 2003, *A&A* **406**, 855

Monet, D., Levine, S., and Casian, B.: 2003, *AJ* **125**, 984

Ochsenbein, F., Bauer, P., and Marcourt, J.: 2000, *A&A* 143(221)

O'Donoghue, D., Phil, A. C., and Homer, L.: 1999, *The UCT CCD Photometer, User & Technical guide, Version 2.0*, SAAO

Osterbrock, D. E.: 1987, in E. E. Khachikian, K. J. Fricke, & J. Melnick (ed.), *Observational Evidence of Activity in Galaxies*, Vol. 121 of *IAU Symposium*, pp 109–+

Osterbrock, D. E. and Veilleux, S.: 1986, *PASP* **98**, 1106

Ott, M., Witzel, A., Quirrenbach, A., Krichbaum, T. P., Standke, K. J., Schalinski, C. J., and Hummel, C. A.: 1994, *A&A* **284**, 331

Padovani, P. and Giommi, P.: 1996, *MNRAS* **279**, 526

Parker, E. N.: 1975, *ApJ* **202**, 523

Parker, E. N.: 1979, *ApJ* **233**, 1005

Petrosian, V. and Bykov, A. M.: 2008, *Space Sci. Rev.* **134**, 207

Ramanamurthy, P. V., Bertsch, D. L., Fichtel, C. E., Kanbach, G., Kniffen, D. A., Mayer-Hasselwander, H. A., Nolan, P. L., Sreekumar, P., and Thompson, D. J.: 1995, *ApJ* **450**, 791

Rees, M. J.: 1966, *Nature* **211**, 460

Rees, M. J.: 1978, *Nature* **275**, 516

Rosat, C.: 2000, *VizieR Online Data Catalog* **9030**, 0

Rybicki, G. and Lightman, A.: 2004, *Radiative processes in astrophysics*, Wiley-interscience

Safier, P. N.: 1992, *ApJ* **392**, 492

Saxton, R. D., Read, A. M., Esquej, P., Freyberg, M. J., Altieri, B., and Bermejo, D.: 2008, *A&A* **480**, 611

Sbarufatti, B., Ciprini, S., Kotilainen, J., Decarli, R., Treves, A., Veronesi, A., and Falomo, R.: 2008, in *Blazar Variability across the Electromagnetic Spectrum*

Schmitt, H. R. and Kinney, A. L.: 1996, *ApJ* **463**, 498

Sikora, M., Begelman, M. C., and Rees, M. J.: 1994a, *ApJ* **421**, 153

Sikora, M., Begelman, M. C., and Rees, M. J.: 1994b, *ApJ* **421**, 153

Sikora, M., Błażejowski, M., Moderski, R., and Madejski, G. M.: 2002, *ApJ* **577**, 78

Sikora, M., Madejski, G., Moderski, R., and Poutanen, J.: 1997, *ApJ* **484**, 108

Skrutskie, M. F., Cutri, R. M., Stiening, R., Weinberg, M. D., Schneider, S., Carpenter, J. M., Beichman, C., Capps, R., Chester, T., Elias, J., Huchra, J., Liebert, J., Lonsdale, C., Monet, D. G., Price, S., Seitzer, P., Jarrett, T., Kirkpatrick, J. D., Gizis, J. E., Howard, E., Evans, T., Fowler, J., Fullmer, L., Hurt, R., Light, R., Kopan, E. L., Marsh, K. A., McCallon, H. L., Tam, R., Van Dyk, S., and Wheelock, S.: 2006, *AJ* **131**, 1163

Sokolov, A. and Marscher, A. P.: 2005, *ApJ* **629**, 52

Sowards-Emmerd, D., Romani, R., and Michelson, P.: 2003, *ApJ* **590**, 109

Sowards-Emmerd, D., Romani, R. W., Michelson, P. F., and Ulvestad, J. S.: 2004, *ApJ* **609**, 564

Stecker, F. W., de Jager, O. C., and Salamon, M. H.: 1996, *ApJ* **473**, L75+

Stecker, F. W., Hunter, S. D., and Kniffen, D. A.: 2008, *Astroparticle Physics* **29**, 25

Stocke, J. T., Morris, S. L., Gioia, I. M., Maccacaro, T., Schild, R., Wolter, A., Fleming, T. A., and Henry, J. P.: 1991, *ApJS* **76**, 813

Strittmatter, P. A., Serkowski, K., Carswell, R., Stein, W. A., Merrill, K. M., and Burbidge, E. M.: 1972, *ApJ* **175**, L7+

Svestka, J.: 1976, *Ap&SS* **45**, 21

Takahashi, T., Kataoka, J., Madejski, G., Mattox, J., Urry, C. M., Wagner, S., Aharonian, F., Catanese, M., Chiappetti, L., Coppi, P., Degrange, B., Fossati, G., Kubo, H., Krawczynski, H., Makino, F., Marshall, H., Maraschi, L., Piron, F., Remillard, R., Takahara, F., Tashiro, M., Terasranta, H., and Weekes, T.: 2000, *ApJ* **542**, L105

Tavecchio, F., Maraschi, L., and Ghisellini, G.: 1998, *ApJ* **509**, 608

Tavecchio, F., Maraschi, L., and Ghisellini, G.: 1999, *Memorie della Societa Astronomica Italiana* **70**, 189

Terebey, S., Wehrle, A. E., and Zook, A. C.: 2002, in *Bulletin of the American Astronomical Society*, Vol. 34 of *Bulletin of the American Astronomical Society*, pp 1288–+

Thompson, D. J.: 2008, *Reports on Progress in Physics* **71(11)**, 116901

Thompson, D. J., Bertsch, D. L., Dingus, B. L., Esposito, J. A., Etienne, A., Fichtel, C. E., Friedlander, D. P., Hartman, R. C., Hunter, S. D., Kendig, D. J., Mattox, J. R., McDonald, L. M., von Montigny, C., Mukherjee, R., Ramanamurthy, P. V., Sreekumar, P., Fierro, J. M., Lin, Y. C., Michelson, P. F., Nolan, P. L., Shriver, S. K., Willis, T. D., Kanbach, G., Mayer-Hasselwander, H. A., Merck, M., Radecke, H., Kniffen, D. A., and Schneid, E. J.: 1995, *ApJS* **101**, 259

Thompson, D. J., Bertsch, D. L., Fichtel, C. E., Hartman, R. C., Hofstadter, R., Hughes, E. B., Hunter, S. D., Hughlock, B. W., Kanbach, G., Kniffen, D. A., Lin, Y. C., Mattox, J. R., Mayer-Hasselwander, H. A., von Montigny, C., Nolan, P. L., Nel, H. I., Pinkau, K., Rothermel, H., Schneid, E. J., Sommer, M., Sreekumar, P., Tieger, D., and Walker, A. H.: 1993, *ApJS* **86**, 629

Urry, C. M.: 1998, *Advances in Space Research* **21**, 89

Urry, C. M. and Padovani, P.: 1995, *PASP* **107**, 803

Véron-Cetty, M. and Véron, P.: 2001, *A&A* **374**, 92

Véron-Cetty, M. and Véron, P.: 2006, *A&A* **455**, 773

Visvanathan, N. and Wills, B. J.: 1998, *AJ* **116**, 2119

Voges, W., Aschenbach, B., Boller, T., Bräuninger, H., Briel, U., Burkert, W., Dennerl, K., Englhauser, J., Gruber, R., Haberl, F., Hartner, G., Hasinger, G., Kürster, M., Pfeffermann, E., Pietsch, W., Predehl, P., Rosso, C., Schmitt, J. H. M. M., Trümper, J., and Zimmermann, H. U.: 1999, *A&A* **349**, 389

Voges, W., Aschenbach, B., Boller, T., Brauninger, H., Briel, U., Burkert, W., Dennerl, K., Englhauser, J., Gruber, R., Haberl, F., Hartner, G., Hasinger, G., Pfeffermann, E., Pietsch, W., Predehl, P., Schmitt, J., Trumper, J., and Zimmermann, U.: 2000, *VizieR Online Data Catalog* **9029**, 0

Vollmer, B., Davoust, E., Dubois, P., Genova, F., Ochsenbein, F., and van Driel, W.: 2005, *A&A* **436**, 757

Wallace, P., Griffis, N., Bertsch, D., Hartman, R., Thomson, D., Kniffen, D., and Bloom, S.: 2000, *ApJ* **540**, 184

Wehrle, A. E., Zacharias, N., Johnston, K., Boboltz, D., Fey, A. L., Gaume, R., Ojha, R., Meier, D. L., Murphy, D. W., Jones, D. L., Unwin, S. C., and Piner, B. G.: 2009, in *AGB Stars and Related Phenomenastro2010: The Astronomy and Astrophysics Decadal Survey*, Vol. 2010 of *Astronomy*, pp 310–+

White, R. L.: 1985, *ApJ* **289**, 698

Woo, J. and Urry, C. M.: 2002, *ApJ* **579**, 530

Wright, A. E. and Otrupcek, R.: 1996, *VizieR Online Data Catalog* **8015**, 0

Yang, J.-H. and Fan, J.-H.: 2005, *Chinese Journal of Astronomy and Astrophysics* **5**, 229

Yepez, J., Vahala, G., Vahala, L., and Soe, M.: 2009, *Phys. Rev. Lett.* **103(8)**, 084501

Zacharias, N., Monet, D. G., Levine, S. E., Urban, S. E., Gaume, R., and Wycoff, G. L.: 2005, *VizieR Online Data Catalog* **1297**, 0

Zhang, J., Bai, J.-M., Chen, L., and Yang, X.: 2009, *ApJ* **701(1)**, 423

Zhang, X., Zhu, W., Wei, J., Hu, J., and Ma, Z.: 1998, *Acta Astrophysica Sinica* **18**, 453